The structure and evolution of galaxies via their bulges and disks in the nearby Universe

Louis Quilley

▶ **To cite this version:**

Louis Quilley. The structure and evolution of galaxies via their bulges and disks in the nearby Universe. Astrophysics [astro-ph]. Sorbonne Université, 2023. English. NNT : 2023SORUS400 . tel-04390957

HAL Id: tel-04390957

https://theses.hal.science/tel-04390957v1

Submitted on 12 Jan 2024

HAL is a multi-disciplinary open access archive for the deposit and dissemination of scientific research documents, whether they are published or not. The documents may come from teaching and research institutions in France or abroad, or from public or private research centers.

L'archive ouverte pluridisciplinaire **HAL**, est destinée au dépôt et à la diffusion de documents scientifiques de niveau recherche, publiés ou non, émanant des établissements d'enseignement et de recherche français ou étrangers, des laboratoires publics ou privés.

Sorbonne Université

École doctorale 127: Astronomie et Astrophysique d'Île-de-France

Institut d'Astrophysique de Paris

The structure and evolution of galaxies via their bulges and disks in the nearby Universe

Doctoral thesis in Astrophysics

Author:
Louis Quilley

Supervisor:
Dr. Valérie de Lapparent

Presented and publicly defended on the 22^{nd} of September 2023
in front of the following jury

Véronique Buat	Professor at Laboratoire d'Astrophysique de Marseille	President & Referee
Steven Bamford	Associate professor at Nottingham University	Referee
Dmitry Makarov	Director of the Special Astrophysical Observatory	Examiner
Clotilde Laigle	Deputy Astronomer at Institut d'Astrophysique de Paris	Examiner
Valérie de Lapparent	Senior researcher at Institut d'Astrophysique de Paris	Supervisor

Institut d'Astrophysique de Paris
Unité mixte de recherche 7095 CNRS - Sorbonne Université

Abstract

Edwin Hubble was the first astronomer to classify galaxies according to their shapes and features. It led to the establishment of the famous Hubble sequence, describing the morphological classes that are ellipticals (E), lenticulars (S0), spirals (Sa to Sm), and irregulars (Im). The formation of the present-day Hubble sequence raises a challenge to galaxy formation theories, as they must explain how arose such a diversity of objects. Addressing this issue requires to characterize the morphology of statistically representative samples of galaxies, in order to gain insight into their formation history.

In this thesis, I use SourceXtractor++ and design a procedure for reliable modeling of the luminosity profiles of the dominant galaxy components, the bulges and disks, for the 4458 nearby galaxies of the EFIGI morphological database. I also perform spectral fitting with ZPEG of the bulges and disks multi-band fluxes in order to derive stellar masses and star formation rates. The absolute $NUV - r$ color versus mass diagram shows the known bimodality and the intermediate Green Valley. The new result is that they are spanned by the consecutive morphological types of the Hubble sequence. Galaxies across the Green Valley undergo a systematic disk reddening and a marked bulge growth by a factor of 2 to 3, excluding a quick quenching scenario. By examining bulges, disks, bars, rings and spirals arms, we paint a picture of galaxy evolution suggesting that internal dynamics, likely triggered by mergers or flybys, may be the key to galaxy aging. The Hubble sequence can then be considered as an inverse sequence of galaxy physical evolution.

The profile modelings also allow me to revisit the scaling relations between size, luminosity and surface brightness of bulges and disks as a function of morphology. I show that the Kormendy relation for E galaxies extends to the bulges of S0 to Sb types, whereas fainter and smaller bulges of later Hubble types depart from it with decreasing bulge-to-total ratio (B/T) and Sérsic indices. I provide evidence that there is a continuous transition from pseudo-bulges to classical ones, rather than a dichotomy between them. I derive new convex size-luminosity relations for both the bulges and disks of EFIGI galaxies, that prevent over or under estimates of bulge, disk and galaxy sizes at all magnitudes. These are crucial for generating realistic mock galaxy fields which include all existing types, which are necessary to control the systematic effects related to galaxy shapes in the measurement derived from very large surveys, such as those performed with the recently launched Euclid space telescope. Moreover, I obtain the unprecedented result that the effective radii of both the bulges and disks of either spirals or lenticulars increase as power-laws of B/T.

The analysis for the EFIGI morphological catalog can be extended to MorCat, a magnitude limited survey to $g \leq 15.5$, from which EFIGI is a comparable Hubble type frequency sub-sample, hence allowing to derive distributions of morphological parameters that are representative of the local Universe.

This study of nearby galaxies provides us with an evolutionary picture across Hubble types that can be parameterized in terms of bulge and disk properties. The analysis of morphology as a function of redshift is however needed for direct evidence on the establishment of the Hubble sequence over cosmic times. To pursue this avenue of research, the methodology I developed during my thesis can be adapted to galaxy surveys at high redshift obtained from either space or ground-based telescopes, in particular the forthcoming Euclid data, the CFHT Legacy Survey Deep fields, or the Hyper Suprime-Cam Deep fields.

I also intend to locate the morphological types along the sheets, filaments and nodes of the cosmic web, in order to further study the role of the local and large-scale environment in the morphological transformations from the Blue Cloud to the Red Sequence.

Abstract

L'astronome Edwin Hubble classa les galaxies selon leurs formes, créant ainsi la séquence de Hubble, qui décrit les classes morphologiques des elliptiques (E), des lenticulaires (S0), des spirales (de Sa à Sm) et des irrégulières (Im). La formation de la séquence de Hubble pose un défi aux théories de formation des galaxies, qui doivent expliquer comment une telle diversité d'objets a pu se former. Répondre à cette question demande de caractériser la morphologie d'échantillons représentatifs de galaxies afin de comprendre leur histoire de formation.

Dans cette thèse, je développe avec SourceXtractor++ une procédure de modélisation fiable des profils de luminosité des composantes dominantes des galaxies, les bulbes et les disques, pour les 4458 galaxies proches du catalogue morphologique EFIGI. Avec ZPEG, j'ajuste des spectres sur leurs flux multi-bandes afin de déterminer leurs masses stellaires et leurs taux de formation d'étoiles. Dans le diagramme de couleur absolue $NUV-r$ versus masse, je retrouve la bimodalité en couleur et la zone intermédiaire de la Vallée Verte, et montre qu'elles sont parcourues par les types morphologiques successifs de la séquence de Hubble. Les galaxies situées dans la Vallée Verte subissent un rougissement systématique du disque et une croissance marquée du bulbe par un facteur de 2 à 3, ce qui exclut un scénario d'extinction rapide. En examinant les bulbes, disques, barres, anneaux et bras spiraux, nous dressons un schéma de l'évolution des galaxies suggérant que la dynamique interne, sous l'effet d'interactions ou de fusions, pourrait être la clé du vieillissement des galaxies. La séquence de Hubble peut alors être considérée comme une séquence inverse de l'évolution physique des galaxies.

Je réexamine les relations d'échelle entre la taille, la luminosité et la brillance de surface des galaxies, bulbes et disques en fonction de leur morphologie. Je montre que la relation de Kormendy pour les galaxies elliptiques s'étend aux bulbes des types S0 à Sb, tandis que les bulbes moins brillants et plus petits des types plus tardifs s'en écartent, avec une diminution du rapport bulbe-sur-total (B/T) et des indices de Sérsic. Je mets en évidence une transition continue des pseudo-bulbes aux bulbes classiques, plutôt qu'une dichotomie entre ces deux classes. Je dérive de nouvelles relations convexes entre taille et luminosité pour les bulbes et disques des galaxies EFIGI, améliorant l'estimation de leur taille à toutes les magnitudes. Cet aspect est crucial pour générer des images synthétiques réalistes comprenant tous les types de galaxies existants, qui sont nécessaires pour contrôler les effets systématiques liés à la forme des galaxies dans les mesures qui sont déduites des grands relevés de galaxies, tels qu'avec Euclid. De plus, j'obtiens le résultat inédit que les rayons effectifs des bulbes et des disques des spirales ou des lenticulaires augmentent selon des lois de puissance du B/T.

L'analyse du catalogue morphologique EFIGI peut être étendue à MorCat, un relevé limité en magnitude apparente à $g \leq 15.5$, dont EFIGI est un sous-échantillon de fréquence comparable des types de Hubble, ce qui permet de dériver des distributions des paramètres morphologiques représentatives de l'Univers proche.

Cette étude des galaxies proches dresse un scénario d'évolution pour les types de Hubble paramétré par les propriétés des bulbes et des disques. Toutefois, l'analyse directe de la morphologie en fonction du temps cosmique est nécessaire pour comprendre comment la séquence de Hubble s'est mise en place. Pour cela, ma méthodologie peut être adaptée à d'autres relevés de galaxies, comme avec Euclid, ou les champs profonds du CFHT Legacy Survey ou de Hyper-Suprime Cam.

Je compte également localiser les types morphologiques parmi les feuillets, filaments et nœuds de la toile cosmique, afin d'explorer le rôle de l'environnement local et à grande échelle dans les transformations du Nuage Bleu vers la Séquence Rouge.

Résumé long

Cette thèse intitulée “La structure et l'évolution des galaxies des galaxies via leurs bulbes et disques dans l'Univers proche” a pour objet l'étude de la morphologie des galaxies, un axe de recherche aussi ancien que l'étude même des galaxies, tous deux ayant débuté avec les travaux de l'astronome américain Edwin Hubble dans les années 1920.

Dans le chapitre 1, des éléments de contexte généraux, nécessaires à la compréhension des travaux de thèse, sont rappelés. Il s'agit d'abord d'introduire le modèle standard de la cosmologie moderne : le modèle ΛCDM, qui décrit l'Univers depuis le Big Bang il y a 13.7 milliards d'années, dans lequel ont émergé et évoluent les galaxies. Je rappelle ensuite les principales propriétés des galaxies et comment elles sont observées. La notion de relevé de galaxies est présentée, ainsi que le choix de ses caractéristiques en fonction des contraintes techniques et objectifs scientifiques fixés. On distingue les relevés photométriques qui mesurent la luminosité des objets dans différentes plages de longueur d'onde du spectre électromagnétique, des relevés spectroscopiques qui produisent directement les spectres des sources observées . Des relevés récents qui ont fortement contribué aux connaissances en astronomie extragalactique sont brièvement présentés et une description plus exhaustive est faite du Sloan Digital Sky Survey (SDSS), étant donné que ces images sont exploitées dans cette thèse. Je discute aussi de l'intérêt des simulations de galaxies pour modéliser l'évolution des galaxies au cours du temps et les confronter aux observations, permettant ainsi de tester les modèles théoriques et phénoménologiques de formation et d'évoluion des galaxies.

Ensuite, les différentes propriétés permettant de décrire toute la diversité des galaxies observées sont présentés, et permettent de faire un état des lieux des connaissances établies à leur sujet. La séquence de Hubble permet de décrire les différentes classes morphologiques des galaxies, à savoir elliptique, lenticulaire, spirale (subdivisées en types) et irrégulière. Après avoir défini la magnitude d'une galaxie, les fonctions de masse et de luminosité sont présentées comme indicateur statistique majeur pour contraindre les modèles de formation des galaxies. Le calcul de la taille des galaxies permet par ailleus de mettre en évidence une relation entre leur taille et leur luminosité.

L'utilisation d'observations à différentes longueurs d'onde permet de calculer les couleurs des galaxies, qui nous renseignent notamment sur les différentes populations stellaires qui les constituent, et permettent de comprendre la formation d'étoiles en leur sein. La définition du redshift ou décalage vers le rouge des galaxies est introduite pour calculer la distance d'une galaxie, et ainsi permettre de reconstituer notre univers en 3D à partir de la vue en projection sur le ciel. Grâce à la cartographie à grande échelle des galaxies, il est possible de connaître leur environnement et donc d'étudier quel est son impact sur l'évolution des galaxies : la relation morphologie-densité indique que les galaxies aux morphologies tardives (spirales) sont situées dans les zones de plus faible densité, tandis que les environnements les plus denses contiennent majoritairement des galaxies aux morphologies dites précoces (elliptiques et lenticulaires notamment). La dynamique interne des étoiles dans ces types de galaxies a été rendue possible par les spectrographes à champ intégral, améliorant notre compréhension de leurs mécanismes de formation.

Les galaxies sont le lieu de naissance des étoiles et comprendre ce qui favorise la formation des étoiles dans les galaxies, ou pourquoi certaines galaxies cessent de former de nouvelles étoiles,

sont des questions majeures en suspens dans la thématique. Les étoiles se forment à partir de nuages de gaz moléculaire suffisamment refroidi pour permettre un effondrement gravitationnel qui déclenche la fusion de l'hydrogène. La diversité et le nombre relatif des différents types d'étoiles, qui se forment dans ces pouponnières stellaires est décrite par la fonction de masse initiale, une loi de puissance pour les masses supérieures à celle du Soleil faisant consensus, mais sa forme pour les plus faibles masses n'étant pas encore contrainte précisément. La loi de Kennicutt-Schmidt d'abord prédite théoriquement par Schmidt en 1959, puis confirmée observationnellement par Kennicutt en 1998, permet d'établir un lien entre la densité locale de gaz et la densité de formation d'étoiles. Enfin, je liste et décris et brièvement les différents mécanismes physiques qui ont été proposés pour expliquer l'arrêt de la formation d'étoiles dans certaines galaxies, notamment les galaxies les plus massives et/ou situées dans les environnements les plus denses, comme par exemple la rétroaction des noyaux actifs de galaxies, en distinguant les processus réduisant ou interrompant l'apport en gaz de la galaxie de ceux qui empêchent la transformation du gaz en étoiles.

Dans le chapitre 2, je poursuis en d'écrivant l'état de l'art sur la connaissance des galaxies, cette fois-ci uniquement axé sur l'aspect morphologique. Cela passe par la description des composantes que sont le bulbe et le disque des galaxies, le premier étant une concentration centrale de lumière, et donc de matière, au sein du second, dans lequel les étoiles sont en rotation, mais aussi de structures secondaires (barres, anneaux, ...). La classification morphologique des galaxies s'est d'abord faite visuellement, depuis Edwin Hubble jusqu'aux catalogues récents, pour lesquels des astronomes ont décrit des dizaines d'attributs pour des échantillons de plusieurs milliers de galaxies. C'est notamment le cas d'EFIGI - pour Extraction des Formes Idéalisées de Galaxies en Imagerie - le catalogue morphologique qui sera étudié tout au long de cette thèse, et qui contient des informations morphologiques détaillées sur 4458 galaxies proches, donc aux images bien résolues, avec leur type Hubble et 16 attributs décrivant leur forme et aspect, leurs composantes dynamiques (bras spiraux, barres, anneaux, etc.) et leur texture (floculence, poussière, etc.). La morphologie visuelle est complémentée par des méthodes de mesure automatiques de la morphologie qui permettent d'obtenir d'une part des mesures quantitatives, ainsi que de caractériser d'autre part de plus grands échantillons. La modélisation des profils de luminosité ajuste des fonctions mathématiques, et notamment le profil de Sérsic, aux variations observées de la brillance de surface d'une galaxie afin de caractériser sa taille, la raideur du profil et le flux total observé. Des mesures non-paramétriques ont aussi étéévelopppées, telles que le système CAS qui décrit la concentration (C), l'asymétrie (A) ou la régularité ("S" pour "smoothness") du profil de lumière d'une galaxie. Récemment, les méthodes basées sur l'apprentissage automatique ou l'intelligence artificielle ont démontré leur capacité à produire des classifications morphologiques robustes, avec des temps de calcul réduits par rapport aux méthodes précédemment décrites, qui seront indispensables pour traiter les données massives des grands relevés à venir de milliards de galaxies (Euclid, LSST).

Dans le chapitre 3 de cette thèse, je décris la méthodologie employée. Le travail mené dans cette analyse s'appuie sur la modélisation des images multi-bandes des 4458 galaxies du catalogue EFIGI afin d'en caractériser la morphologie de manière automatique et quantitative, avec exhaustivité et précision. Pour cela, j'ai effectué une décomposition multi-bande en bulbe et disque des profils de lumière *gri* en utilisant SourceXtractor++, un logiciel en cours de développement pour Euclid, avec un profil de Sérsic et un profil exponentiel pour le bulbe et le disque, respectivement. Les innovations significatives de cet outil de modélisation (ajustement simultané de profils multi-bande, pose de contraintes à priori - ou " priors" - sur tout paramètre, entre des paramètres distincts d'une même bande, ou entre les bandes) me permettent de réduire les

dégénérescences inhérentes à une telle modélisation : sans priors, 20% des galaxies voient leur rayon effectif de bulbe surestimé par un facteur de 5, et 75% d'entre elles voient également leur rapport de flux bulbe-sur-total B/T surestimé par un facteur de 2. Je complémente aussi la photométrie optique *ugriz* du SDSS par la photométrie ultraviolette NUV obtenue avec le satellite GALEX. Les magnitudes ainsi obtenues sont corrigées de manière à compenser l'extinction due à l'atmosphère terrestre, ainsi que l'extinction lors de la traversée de notre galaxie la Voie Lactée. Une fois cette photométrie multi-bande obtenue, j'ai utilisé ZPEG pour effectuer un ajustement de distributions modélisées d'énergie spectrale (SED) et ainsi dériver les magnitudes absolues et les paramètres physiques (taux de formation d'étoiles, masses stellaires, etc.) de toutes les galaxies EFIGI, ainsi que pour leur bulbes et disques séparément.

Dans le chapitre 4, je localise les différents types de Hubble dans le diagramme couleur $NUV - r$ versus masse stellaire, et je montre un changement monotone de type morphologique qui traverse la bimodalité déjà connue. Je suggère donc que la séquence de Hubble est une séquence inverse de l'évolution physique des galaxies : la morphologie change de manière continue depuis les irrégulières, à travers les spirales, jusqu'aux types lenticulaires et elliptiques, tandis que les galaxies croissent en masse stellaire et que leur formation d'étoiles s'atténue pour devenir inactive. Il est important de noter que la tendance continue du type de Hubble à travers le diagramme couleur-masse peut être caractérisée par une augmentation continue des rapport de luminosité du bulbe sur le total B/T, ainsi que le rapport en masse stellaire, de 10^{-2} à $\lesssim 1$, accompagné d'un rougissement des couleurs du disque de 0.6 magnitude en $g - r$.

J'approfondis également l'étude des propriétés morphologiques des galaxies dans la Vallée Verte, située dans la zone de transition entre le Nuage Bleu et la Séquence Rouge, et montre que l'évolution vers des types morphologiques plus précoces correspond à une croissance de la masse stellaire d'environ ~ 5 dex. En revanche, la Vallée Verte concentre la plupart des changements de couleur dans un intervalle de masse stellaire d'environ ~ 1 dex, commun à tous les types de Sb à S0. Cependant, l'augmentation graduelle observée de B/T et le rougissement de la couleur du disque le long de la séquence de Hubble sont significatifs dans la Vallée Verte, avec un doublement de B/T et un rougissement de 0.4 magnitude en $g - r$. Les échelles de temps significatives nécessaires pour de tels changements morphologiques, en particulier plus d'un doublement de B/T dans cette région, plaident contre des scénarios d'extinction rapide, par exemple via la rétroaction des noyaux actifs de galaxies, invoqué dans les simulations numériques pour limiter le nombre de galaxies très massives produites.

Mon étude met également en évidence le rôle des fusions à toutes les étapes de l'évolution des galaxies. En effet, les 4 ordres de grandeur de croissance de la masse stellaire à travers le Nuage Bleu ne peuvent pas être expliqués uniquement par le réapprovisionnement et la consommation de leur réservoir de gaz. De plus, la croissance du bulbe décrite précédemment est concomitante à un changement de profil vers des bulbes plus concentrés (avec un indice de Sérsic plus grand), et elle est donc probablement causée par des fusions mineures. Enfin, l'existence d'elliptiques très massives au-delà de la limite de masse pour les spirales $M_{\rm lim} = 10^{11.7} M_\odot$ ne peut s'expliquer que par des fusions pauvres en gaz, car les première forment peu ou pas d'étoiles et ne peuvent donc pas augmenter leur masse stellaire en convertissant le gaz en étoiles.

De plus, je note une sur-représentation des anneaux internes et externes dans les galaxies de la Vallée Verte, en comparaison au reste du diagramme couleur-magnitude. Celle-ci est en accord avec de précédentes études, tant observationnelles que basées sur des simulations. Les anneaux peuvent se former sous l'effet d'une barre, ou suite à une fusion de galaxies. La légère sur-représentation des anneaux dans les galaxies barrées mesurée dans EFIGI tend à confirmer la validité du premier mécanisme, mais semble insuffisant pour expliquer l'existence de nombreux anneaux dans des galaxies sans barre. Pour expliquer ces anneaux dans la Vallée Verte, il a été

noté dans les simulations que la présence de gaz permet la formation d'anneaux lors des fusions, tandis qu'un bulbe prépondérant assure leur persistance dans le temps. Or ces deux conditions ne sont remplies simultanément que dans la Vallée Verte, les galaxies du Nuage bleu ayant de trop petits bulbes tandis que les lenticulaires de la séquence Rouge sont dénuées de gaz. Ce nouvel élément s'inscrit donc bien dans notre scénario d'une évolution séculaire sous l'effet de fusions.

Dans le chapitre 5, je réexamine les relations d'échelle des bulbes et des disques à l'époque actuelle, qui permettent de relier leurs rayons effectifs à leurs brillances de surface apparentes et leurs magnitudes absolues. Je montre que les bulbes des types S0$^-$ à Sab suivent les relations de Kormendy et taille-luminosité dérivées pour les galaxies elliptiques, et interprétées comme résultant d'une formation par relaxation violente. En revanche, les bulbes de types Sbc à Sdm s'écartent des deux relations et sont donc susceptibles d'être des pseudo-bulbes, formés par une accrétion progressive au sein du disque, et donc probablement maintenus dynamiquement par rotation.

En ce qui concerne les disques, je montre qu'ils suivent des relations d'échelle similaires aux bulbes, avec des rayons effectifs plus grands que pour leurs bulbes d'un facteur d'environ 5 pour les types S0 à approximativement 15 pour les spirales tardives. De plus, je montre qu'il existe des lois de puissance entre les rayons effectifs des bulbes et des disques et le rapport de luminosité du bulbe sur total B/T, ce qui fournit des informations sur la manière dont les galaxies transfèrent de la masse entre les deux composantes au cours de leur évolution. Ces relations sont également cruciales pour générer des catalogues synthétiques (ou " mocks") à partir de ces deux ingrédients essentiels des galaxies, le bulbe et le disque.

Dans le chapitre 6, je mets en évidence des gradients de couleur dans les bulbes et disques des galaxies EFIGI. En effet, les variations des rayons effectifs des profils de lumière ajustés dans les différentes bandes indiquent que les disques des spirales intermédiaires sont relativement plus bleus à leur périphérie qu'en leur centre, tandis que leurs bulbes montrent l'effet inverse, avec des profils plus bleus au centre. Après avoir vérifié que ces tendances ne sont pas induites par un bais de modélisation, j'interprète ces variations observées le long de la séquence de Hubble en terme de populations stellaires.

D'une part, les bulbes ont des couleurs rouges du fait qu'ils sont formés de vielles étoiles et il n'est donc pas attendu qu'ils forment de nouvelles étoiles de manière significative. Toutefois, les gradients mesurés dans ceux-ci indique des profils plus bleus au centre donc des étoiles jeunes y sont présentes. La présence de bras spiraux nucléaires dans de nombreuses galaxies spirales permet d'acheminer du gaz au coeur des bulbes, ce qui pourrait y permettre la formation d'étoiles et expliquer les gradients observés. Cet effet n'est visible que dans les spirales de types intermédiaires, qui sont riches en gaz et dont les bulbes ne sont pas encore massifs.

D'autre part, dans les disques, les gradients observées correspondent à des profils de lumière plus bleus en périphérie des disques, donc une formation d'étoiles relativement plus intense en leur périphérie. Cela pourrait être la conséquence du fait que le gaz du milieu circumgalactique est accrété sur les bords du disque, en accord avec la croissance de la taille du disque dans les galaxies spirales. Ce gradient est visible dans les galaxies formant activement des étoiles mais tend à disparaître pour les types de Hubble plus précoces, au fur et à mesure que le formation d'étoiles s'éteint. Les scénarios de "inside-out quenching" décrivant un arrêt de la formation d'étoiles partant du centre et s'étendant à la périphérie des disques seraient donc une interprétation erronée de ces gradients. En effet, lors de la transformation des spirales intermédiaires en types plus précoces jusqu'aux lenticulaires, on part d'un disque formant des étoiles activement, et encore plus en périphérie, puis le rougissement indique une baisse de la

formation d'étoiles, visible dans tout le disque, mais plus marqué en périphérie, où l'excès relatif se fait moins important, jusqu'à arriver à un disque uniformément éteint en formation détoiles pour les galaxies lenticulaires.

Tous les résultats décrits ci-dessus sont synthétisés dans la conclusion qui montre comment leur combinaison amène au scénario d'évolution dessiné au cours de cette thèse. Dans ce scénario, une évolution séculaire des galaxies, sous l'effet de fusions et interactions, les fait traverser continûment la séquence de Hubble, qui peut donc être considérée comme une séquence inverse de l'évolution des galaxies. Une croissance en masse et en taille a lieu des galaxies irrégulières aux spirales intermédiaires, puis la formation d'étoiles s'arrête, conduisant au rougissement du disque, lors du passage des spirales précoces vers les lenticulaires, enfin les galaxies elliptiques - les plus massives observées - se forment par des fusions majeures pauvres en gaz.

Enfin, le travail de recherche mené ici appelle d'autres projets permettant de mieux comprendre le rôle prépondérant de la morphologie dans l'évolution des galaxies. Dans les perspectives sont présentés les axes futurs de la recherche que je mènerai dans les années suivant ma thèse.

Il est d'abord question de ré-appliquer la méthodologie construite ici au catalogue complet en magnitude MorCat, dont est extrait EFIGI, afin d'obtenir un recensement des morphologies de galaxies dans l'Univers local. Les informations obtenus lors de l'étude d'EFIGI et notamment l'identification du rapport B/T et de la couleur du disque comme traceurs du type de Hubble servira de base à l'établissement d'une séquence "morphométrique". Le caractère complet en magnitude de MorCat donnera aussi l'opportunité de calculer des fonctions de taille et de luminosité en fonction de B/T, et séparément pour les bulbes et les disques.

En parallèle, je m'intéresserai aux galaxies à plus grand décalage vers le rouge, pour étudier leur évolution au cours du temps cosmique. Le calcul de la relation taille-luminosité sera reproduit à différentes époques, permettant de construire des catalogues mock fiables pour les prochains grands relevés de galaxies, et notamment pour Euclid. Grâce à ce télescope spatial, la caractérisation de dizaines puis centaines de milliers de galaxies au cours des 10 derniers milliards d'années de l'Univers sera possible et constituera un test critique du scénario d'évolution inféré dans cette thèse à partir de la diversité des galaxies actuelles. Il devrait ainsi être possible d'observer les fusions transformant les galaxies vers des morphologies plus précoces, dictant la variation du taux de formation d'étoiles dans l'Univers.

Je m'intéresserai aussi aux liens entre la morphologie des galaxies et leur position au sein de la toile cosmique, car cette information est liée à l'histoire des interactions et fusions des galaxies.

Remerciements

Cette thèse aura été mon quotidien pendant 3 années et représente à ce titre un chapitre important de ma vie. Je souhaiterais ici remercier toutes les personnes qui y ont joué un rôle et m'ont accompagné dans cette aventure.

Je commence par remercier ma famille qui m'a soutenue dans ma thèse comme elle m'a toujours soutenue dans ma vie et dans mes études. Je remercie mes parents qui ont toujours voulu me proposer leur aide et qui se sont toujours plus inquiétés que moi de tous les problèmes que j'ai pu rencontrer et de toutes les dates de rendus se rapprochant trop vite. Je remercie ma soeur à qui je tiens bien plus que ce que laisse penser le faible nombre de fois où on s'est vus ces trois dernière années.

Ensuite, je tiens à remercier Valérie, ma directrice de thèse, pour sa bienveillance et son aide précieuse au cours de ces 3 années de travail ensemble. Tout le travail accompli ici a été un effort conjoint à deux, et sa disponibilité et ses nombreux conseils ont été clés tant dans la réalisation des projets que dans mon développement en tant que jeune chercheur. Je remercie aussi Clotilde pour l'intérêt qu'elle a porté à mon travail de thèse, et son soutien continu, notamment en me mettant en contact avec ses collaborateurs pour aller présenter mes résultats à des séminaires ou pour rechercher un contrat postdoctoral. Je remercie aussi Gary, qui a été le premier à m'accueillir à l'IAP en stage de M2, et qui est toujours aussi passionné d'échanger sur des questions scientifiques. J'étends mes remerciements à toutes les personnes avec qui j'ai eu l'opportunité d'échanger à l'IAP, et qui participent à l'atmosphère vivante de ce laboratoire.

Je remercie aussi mes amis avec qui j'ai passé les heures en dehors du travail. Car si ma thèse a eu lieu au 98 bis Boulevard Arago, une bonne partie de mes souvenirs de ces 3 dernières années a pour décor le reste de Paris, avec une préférence notable pour le Quartier Latin, ses salles de cinémas, ses restaurants et ses bars. Je remercie donc Amaury, Cyril, Arnaud, JB, Antoine, Nathan et Naïla pour tous ces bons moments passés ensemble, et qui continueront d'avoir lieu dès qu'au moins deux d'entre nous seront à Paris (ou ailleurs) en même temps.

Je remercie tout particulièrement Amaury avec qui en plus de partager de nombreuses séances de cinéma, restaurants (sichuanais) et parties de jeux de société, j'ai aussi partagé un bureau pendant 2 ans. J'attends avec impatience notre prochaine rencontre, que ce soit à ton retour en France ou si je viens te rendre visite au Japon.

J'en arrive maintenant à remercier tous les nouveaux amis que je me suis faits au cours de cette thèse: j'ai nommé les doctorants de l'IAP. Ça a été un plaisir chaque matin de venir au travail car j'étais certain de retrouver la bonne ambiance qui règne toujours à l'entresol et d'être bien accompagné pour prendre des pauses, aller à la cantine, ou prolonger notre bonne entente en dehors de l'IAP. Je remercie Naïavec qui on s'est soutenus pour garder le moral quand les soirées au bureau traînaient en longueur, et pour ses divines pâtes carbonara. Je remercie Aline pour son énergie et sa folie communicative, ainsi que pour son manque de sens de l'orientation quand on rentrait ensemble le soir. Je remercie Pierre d'avoir toujours été là depuis les "Bonjour Joe" dans mon premier bureau jusqu'aux *morning tea* de 3ème année, en passant par les midi escalade. Je remercie Marko pour les les tennis du jeudi matin, les excellentes pizzas, et les inoubliables soirées du 52 rue Damesme.

Et enfin, pour tous les autres, si je suis plus bref ou ne cite pas d'anecdotes à vos côtés soyez assuré que c'est par souci de ne pas écrire plus de remerciements que de contenu scientifique dans cette thèse, mais que j'en garde bien précieusement le souvenir. Je remercie donc aussi Clément (blagues et référérences toujours percutantes), Louise (Taylor et les catalogues), Étienne (sans rancune à Complots), Émilie (les scans One Piece, le tarot et l'escalade), Denis (toujours très bon public), Simon D. (encore plus d'escalade), Marie, Emma, Mathieu, Axel, Simon C., Alice, Ira, Chi An, Hugo et David, sans oublier ceux déjà partis vers de nouveaux horizons: Julien, Virginia, Mike, Eduardo, Lukas, Quentin, et Dani.

Merci à tous pour ces trois années pleines de vie.

Contents

List of Figures

P.2 From left to right: *gri* composite color image of the galaxy and of the bulge, model-fitting and residual of the bulge in the g band with a single Sérsic profile, and with two Sérsic profiles, for PGC0010108 and PGC0047678 in the top and bottom rows, respectively. Both examples show that with a single Sérsic profile there remains an excess of light in the very center of the bulge whereas the level of flux in its outskirts is over-estimated by the model. The modeling with two Sérsic profiles displays an improvement, as the amplitude of the residual structures at the location of the bulge are significantly lower. 142

List of Tables

Introduction

Trying to understand how these immense structures of stars, gas, and dust that we call galaxies assembled over the history of the Universe has remained a broad, complex and open question for astronomers over the last century. Each new generation of telescopes allowed us to probe with more details and in greater number the galaxies covering the night sky, therefore gaining further insight into the complex machinery driving their evolution. The use of morphological classification is as old as galaxy science itself and remains relevant up to this day, as sorting galaxies into an array of various shapes is a logical and effective way to map the striking diversity of their inner structures, which carries a lot of information about the physical phenomena that have been and still are building each kind of galaxy.

However, many more tools have been created to complement the difficult visual classification process performed by famous astronomers such as Edwin Hubble, Gérard De Vaucouleurs or Allan Sandage, and take advantage of the ever-increasing computation power to better interpret the light we receive from galaxies. Automatic processing of astronomical images progressed so that the morphologies of hundreds of thousands of galaxies can be analyzed, and softwares were developed to characterize them through various quantitative parameters, whose statistical analysis leads to a wider perspective on the issue of galaxy formation and evolution.

The work pursued in this thesis comes in the continuity of this progress as it is mainly based on the morphological database EFIGI: a catalog of 4458 nearby galaxies that have been visually classified by a team of experts astronomers to obtain as much qualitative information about the shapes and features constituting these objects as possible. The results of this classification serve to develop and are confronted to an automated and quantitative description, that takes the form of a robust and precise bulge and disk decomposition, i.e. a modeling of the multi-band light profiles of the galaxy's two main components, making the most of the new capabilities of the SourceXtractor++ software.

Chap. 1 gives an overview of galaxy formation and evolution, focusing mainly on the galaxy surveys from which we extract information, and the main properties that characterize galaxies.

Chap. 2 review the discoveries of a century of astronomical research, this time only regarding the morphology of galaxies. It also introduces the EFIGI morphological catalog, whose galaxies are studied throughout this thesis.

Chap. 3 presents the methodology developed to study galaxy images. It contains the description of the model-fitting procedure of galaxy light profiles using SourceXtractor++, and details the various implemented steps based on the use of priors, in order to obtain a proper characterization of the bulge and disk morphological parameters. It also describes the corrections that need to be applied to the apparent magnitudes, and finally introduces the SED model-fitting method that has been applied on the obtained photometry to retrieve absolute magnitudes, as well as to estimate stellar masses and star formation rates.

Chap. 4 relates the color bimodality of galaxies (either red or blue) to the Hubble sequence, by putting into context and presenting the results of Quilley & de Lapparent (2022), as well as introducing unpublished works on galactic rings. This chapter discusses the dependence between the morphology of a galaxy and its star forming state, and advocates in favor of a merger-driven evolution. Its main conclusion is that the Hubble sequence can be considered as an inverse evolutionary sequence.

Chap. 5 presents the photometric scaling relations of the bulges and disks of the EFIGI galaxies performed in Quilley & de Lapparent (2023). New computations of historic landmark relations are presented for the different Hubble types, and the variations between them are discussed. It also

introduces new power-law relations between the sizes of the bulges and disks, and the bulge-to-total ratio of galaxies. The use of these relations is considered, on the one hand to build realistic galaxy mock catalogs, and on the other hand to gain insight into the formation of bulges and disks.

Chap. 6 reports on the colors and color gradients of bulges and disks along the Hubble sequence. It therefore sheds light on the distribution of different stellar populations within the bulge and disk, and allows a discussion on how the star formation activity is distributed and varies during the joint evolution of bulges and disks, and how the dynamical interactions and internal perturbations such as bars may play a role in this evolution.

Chapter 1

Overview of galaxy formation and evolution

A galaxy is a gravitationally bound system containing a large number of stars, from 10^6 to 10^{12}, but also stellar remnants, dust, and gas. Beyond this simple definition, the term galaxy actually encompasses a very large diversity of objects. Indeed, galaxies come in many sizes, shapes, and colors, hence a large number of parameters is needed to properly characterize them. Studying galaxies consist mostly in measuring and understanding the full probability distribution function of all these parameters, so as to explain how such a diversity of objects arose in the Universe. In this chapter, we provide the historic context of how studying galaxies came to be, and present the ΛCDM model describing the Universe in which galaxies evolve. We introduce the methods used to observe galaxies and acquire knowledge on these objects. Then we review the most remarkable properties of galaxies, and especially those that will be relevant to the studies conducted in this thesis. Finally, we present galaxies as the birthplace of stars.

1.1 The rise of extra-galactic astronomy

The word Galaxy comes from the Greek galaxias (γαλαξίας), literally milky, a term used to denote the visual appearance of our very own galaxy the Milky Way, which appears in the sky as a hazy band of light formed by stars indistinguishable to the naked eye. A few galaxies are bright enough to be observed without the help of any instrument, such as our neighbor the Andromeda galaxy, whose first recorded observation dates back to 964 by Persian astronomer Al-Sufi. With the invention of the telescope, and its first use to observe the sky by Galileo Galilei in 1609, astronomy entered a new era in which many more galaxies were to be observed. One can mention the work of French astronomer Charles Messier and more specifically his catalog containing the 109 brightest celestial objects having nebulous appearance, or subsequently William Herschel's catalog of 5000 nebulae. However, until the end of the 19th century, if those objects could be distinguished from stars their nature remained unknown and highly debated by the astronomical community. In 1920 took place the "Great Debate" between astronomer Harlow Shapley and Heber Curtis, who confronted their views on the nature of the spiral nebulae and the size of the Universe. The former argued that the Milky Way was the whole Universe, and that spiral nebulae were laying within its outskirts, while the latter considered that spiral nebulae were "island universes", so galaxies on their own, similar to the Milky Way and located at greater distances. The debate was finally settled a few years later by Edwin Hubble, thanks to the improved capacities of the new Mount Wilson telescope, that allowed him to resolve outer parts of spiral nebulae and to identify Cepheid variables. Using these standard candles, he measured the distance to the spiral nebula M31 (Andromeda), which he proved to be far too distant to be part of the Milky Way, thus demonstrating that it was indeed a galaxy (Hubble 1926, 1929).

Since then, our knowledge on galaxies has been regularly increasing with each new generation of ground-based and more recently spatial telescopes, allowing astronomers to probe wider and deeper areas of the sky, and increasing the number of galaxies observed by several orders of magnitudes, from the 40 galaxies appearing in Messier's *Catalogue of Nebulae and Star Clusters* to the expected 20

billion galaxies that will be observed by the Vera C. Rubin Observatory, who will carry out a synoptic astronomical survey: the Legacy Survey of Space and Time (LSST).

1.2 Cosmological context

Before focusing on galaxies, it is both interesting and helpful to briefly introduce the Universe in which they are observed, or more precisely our understanding of it so far.

The current cosmological framework describing the evolution of our Universe is the Lambda Cold Dark Matter (ΛCDM) model. In this model, the Universe is homogeneous and isotropic at large scales, and expanding at a time-varying rate $H(t)$. It is constituted of three main components : (i) ordinary baryonic matter[1]; (ii) cold dark matter, which dominates the matter content and the Universe, is invisible ("dark"), only interacts through gravity, and is best modeled by non-relativistic ("cold") particles (Bertone et al. 2005); (iii) dark energy, represented by the cosmological constant λ, which is the mysterious component responsible for the acceleration of the expansion of the Universe over the last 5 Gyr (Riess et al. 1998; Perlmutter et al. 1999).

In this framework, small matter overdensities resulting from the quantum fluctuations of the early Universe assembled over time to form larger and larger structures through gravitational instability, until regions of high density collapsed to first form dark matter halos. Within these potential wells, hydrogen gas clouds also collapsed when their mass overcame their internal pressure, as they reached the Jeans mass ($M_{\rm J} \sim 10^4 M_\odot$). This process was the birth of the first stars (called Population III stars) in the history of the Universe, which also led to the first generations of galaxies (Loeb & Barkana 2001). This scenario of hierarchical evolution continued to reach the present day Universe in which galaxies are distributed along large-scale structures that were first predicted through theoretical models and numerical simulations (Zeldovich et al. 1982; Klypin & Shandarin 1983; Blumenthal et al. 1984; Davis et al. 1985). Then the extension of the Center for Astrophysics Redshift Survey (Huchra et al. 1983) confirmed the existence of large-scale- structures by providing the first observational evidence for walls, filaments and voids separating clusters of galaxies, forming the Cosmic Web (de Lapparent et al. 1986; Geller & Huchra 1989).

In this thesis, we adopt the ΛCDM model with the following parameters: a Hubble constant $H_0 = 70$ km s^{-1} Mpc^{-1} (Freedman et al. 2001), and density parameters $\Omega_m = 0.258 \pm 0.030$ for the matter density, $\Omega_\Lambda = 0.742 \pm 0.030$ for the dark energy density(Dunkley et al. 2009).

1.3 Observing galaxies

1.3.1 Galaxy surveys

Because the relevant timescales of galaxy evolution are all orders of magnitude longer than human life, no observer can have the luxury to decipher galaxy evolution by looking at the evolution of a galaxy over time. Instead, evolution must be inferred from the evolution of the statistical properties of galaxy populations in the Universe with cosmic time. Galaxy surveys are designed to probe the sky, looking at as many galaxies as allowed by the current technological advancements. Then the application of 3 fundamental principles ensures that the knowledge gained from a large enough patch of the sky can be considered valid for the whole Universe: (i) the Copernican principle states that the Earth and more generally the Milky Way, so us as observers, do not occupy a special place in the Universe, (ii) the cosmological principle assumes that on large scales the matter distribution in the Universe is both homogeneous and spatially isotropic, (iii) the ergodicity principle states that the measured statistics on a large volume is equivalent to the statistics of the whole Universe.

One can distinguish two kinds of surveys:

- Deep surveys that allocate long exposure time to one or several patches of the sky, so as to be able to detect galaxies to faint apparent fluxes, hence probing higher redshifts, at the expense of the area covered

[1] see https://astronomy.swin.edu.au/cosmos/b/Baryonic+Matter

- Wide surveys on the contrary span large fractions of the sky to brighter apparent flux limits, and consequently will be more limited in their redshift range as well

The scientific purposes of a survey arbitrate this inescapable compromise between width and depth. Among the parameters that measure the "quality" of a survey are its area on the sky, its wavelength coverage (see below), its resolution (see below), its sensitivity, which is the magnitude of the faintest object detected, and its completeness limit. Completeness is the fraction of objects seen by the survey compared to the number of objects in the probed region of the sky, and depends on apparent magnitude. It is often evaluated by measuring the departure from the extrapolation of the power-law number counts of galaxies at bright magnitudes. To obtain a better estimate, artificial galaxies can be generated into images, with random positions and mimicking statistically the photometric properties of a real galaxy population, while "observing" them through the full telescope and instrument setup (Carassou et al. 2017). The number of detected galaxies can then be compared to the number of input galaxies as a function of apparent magnitude.

Moreover, surveys can be photometric, spectroscopic, or spectro-photometric when they combine both types of observations, allowing for different and complementary information on galaxy properties (see Sects. 1.3.2 and 1.3.3 below).

In the nearby Universe, it is also common to perform in-depth observations of specific galaxies, and not only surveys, so as to characterize them in full detail, with the best accuracy attainable. When a galaxy or a small sample of galaxies is detected in a survey, showing properties worth of interest, it is also common practice to do follow-up observations, with additional instruments and telescope time allocated to further probe these objects.

1.3.2 Photometry

With photometry, the gathered data take the form of images for which the value in each pixel represents the amount of flux received from a given position in the sky. Photometric surveys are very commonly multi-band surveys, meaning that a given pointing in the sky is repeated in several bands of the electromagnetic spectrum. From the photometric data, it is possible to measure their surface brightness profiles, their sizes and luminosities as a function of band, that is to study their morphology and how it articulates with the underlying stellar populations, as different types of stars emit in different wavelengths (see Sects. 1.3.3 and 1.4.4).

The angular resolution of a photometric survey determines its ability to distinguish neighboring objects, or to sample more thoroughly a light profile, thus providing more precise images of the galaxies observed. It depends on the pixel resolution, which is the solid angle of the celestial sphere covered by a pixel, but also the seeing of the observing site (defined as the full width at half maximum of a long-exposure image of a star, that is spread due to the turbulent motions in the atmosphere), which both determine the point-spread function (PSF) describing the response of the telescope and instrument to a point-source. Ideally the PSF should be sampled by at least 3 pixels.

As the light received in different wavelength ranges of the electromagnetic spectrum correspond to different emitters within a galaxy, the more bands are obtained for a given patch of the sky, the greater are the number of physical phenomena probed for the galaxies observed in that region. Therefore, it has become common for several instruments to observe the same region of the sky in order to combine their data, while also permitting cross-verification of the measured properties.

We provide below a list of photometric surveys, with no intent of exhaustivity, but to present briefly those that are used or mentioned in this thesis:

- The Sloan Digital Sky Survey, see Sect. 1.3.4 for a detailed description
- The Galaxy Evolution Explorer (GALEX, Martin et al. 2005) was a NASA space telescope operated by the California Institute of Technology. Between 2003 and 2012, this survey in the near and far ultraviolet (nUV and fUV, see Fig. 1.1) bands observed around 75% of the sky, in order to measure the emission of young stars in the UV without the strong atmospheric extinction nor Rayleigh scattering that otherwise considerably degrade observations[2].

[2] https://skyandtelescope.org/astronomy-resources/transparency-and-atmospheric-extinction/

- The Two Micron All-Sky Survey (2MASS, Jarrett et al. 2000) observations covered the whole sky between 1997 and 2001, hence providing a large photometric catalog of 1.5 million galaxies in the near-infrared (IR) bands.
- The Cosmic Evolution Survey (COSMOS, Scoville et al. 2007) is a deep-field survey designed to probe the evolution of galaxies with both cosmic time (redshift) and environment. Initiated with HST observations, it includes photometric data from X-ray to radio bands, as well as spectroscopic follow-up (see Sect. 1.3.3), thanks to the many space and ground based instruments that observed this 2 deg^2 equatorial field, with now over 2 million galaxies detected.
- The Cosmic Assembly Near-IR Deep Extragalactic Legacy Survey (CANDELS, Koekemoer et al. 2011) provides Hubble Space Telescope (HST) observations of 250,000 high redshift galaxies ($1.5 < z < 8$) at optical and near-IR wavelengths, within a wide field of 0.2 deg^2 and a deep field of 0.04 deg^2,in order to study galactic evolution in the first Gyrs after re-ionization.
- The Canada-France-Hawaï Telescope Legacy Survey (CFHTLS) consists of four deep fields for a total sky area of 4 deg^2 and four wide fields covering 171 deg^2, observed with the CFHT 3.6 m telescope and its MegaCam imager at the *ugriz* optical wavelengths (Hudelot et al. 2012) and complemented by the WIRCam Deep Survey (WIRDS) in the JHK IR bands (Bielby et al. 2012). See more details in Sect. 6.2
- The Great Observatories Origins Deep Survey (GOODS, Dickinson et al. 2003; Giavalisco et al. 2004) covers two fields, each of 10 arcmin x 16 arcmin, centered on the Hubble Deep Field North and the Chandra Deep Field South respectivley. It was obtained through the combined observations of NASA's space telescopes Spitzer, Hubble and Chandra, ESA's Herschel and XMM-Newton, as well as several ground-based telescopes (VLT, Keck, Gemini, etc). The extensive coverage of these north and south fields in X-ray, radio, submillimeter, near-IR and optical make them the most extensively studied deep survey areas of the sky.

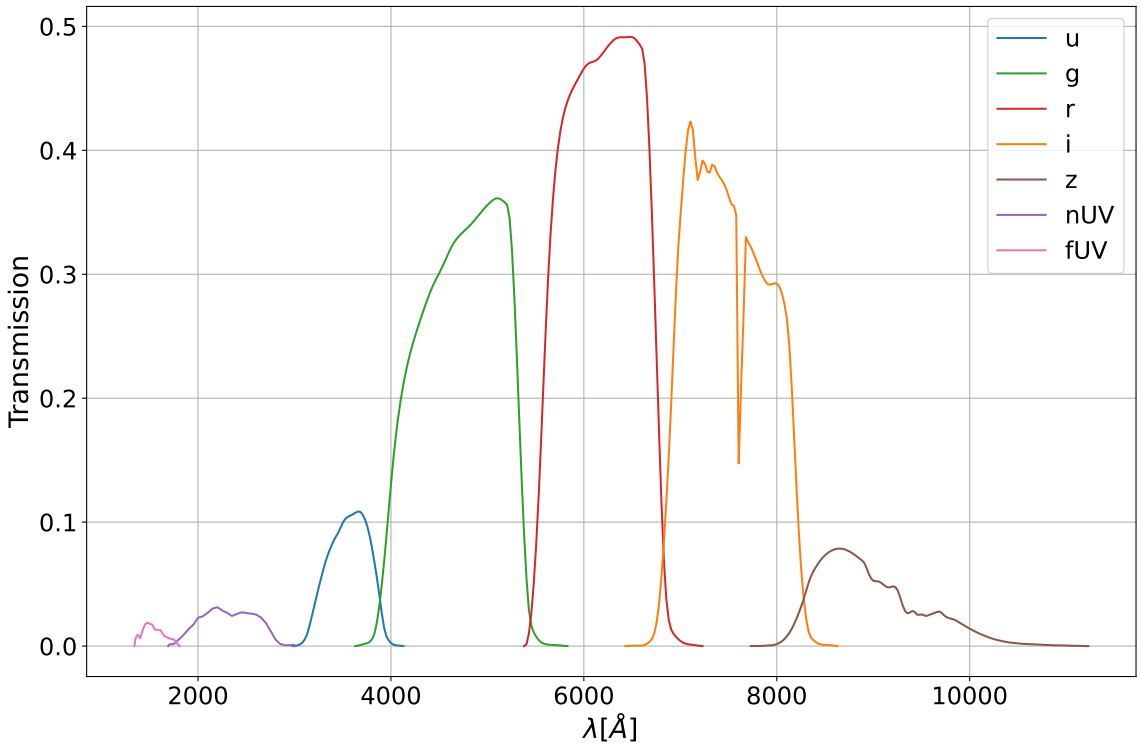

Figure 1.1: Transmission curves for the *ugriz* SDSS bands as well as the nUV and fUV bands of GALEX, which are the two surveys whose photometric data will be exploited in this thesis work. SDSS and GALEX bands cover the optical and ultraviolet wavelength range respectively.

1.3.3 Spectroscopy

Spectroscopy probes the spectral energy distribution (SED) of the observed sources. It can be used to measure the redshift of galaxies by analyzing emission and absorption lines (see Sect. 1.4.5). The redshift measures the velocity of an object relative to us, the observer, which is the sum of the result of the expansion of the Universe and of the peculiar velocity of a galaxy. This allows one to study the movement of galaxies, along the line of sight, and relatively to their neighbors. For instance, Zwicky (1937) measured the orbit velocities of galaxies in clusters, which was in disagreement with the value predicted by gravitation from the luminous mass of the cluster and led to the hypothesis of the additional presence of a significant mass of non-luminous matter, which we attribute to the dark matter halo.

The spectra of a galaxy is the sum of the spectra of all of its stars as well as the nebular emission from the gas, and the absorption and emission from the dust, so analyzing a galaxy's spectra provides information on its constituents. Therefore, it allows for instance to derive the metallicity of a galaxy, or its star formation rate, which is linked to the number of very young stars.

There are three types of spectroscopic surveys: fiber spectroscopy in which one fiber is positioned usually on the density peak of the object, and the sky is measured with one or several fibers positioned outside the object, long-slit spectroscopy, with the slit providing several spectra of the object along a single direction, as well as sky spectra outside the object, and integral field spectroscopy which divides a field of view into smaller sections and retrieves a spectrum for each of them, allowing, for instance, to analyze the stellar population at different positions within an extended galaxy (Kreckel et al. 2018, 2019; Erroz-Ferrer et al. 2019).

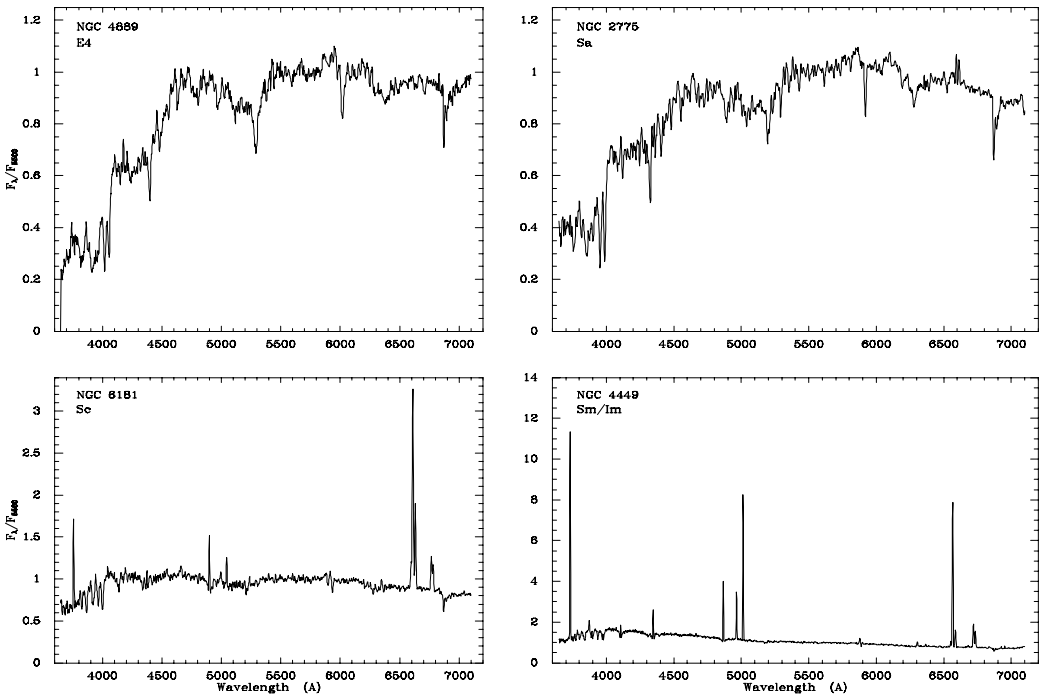

Figure 1.2: Integrated spectra of elliptical, spiral, and irregular galaxies. The fluxes are normalized to unity at 5500Å. From Kennicutt (1998a), adapted from Kennicutt (1992) data.

Here again, I provide a list of spectroscopic surveys, with no intent of exhaustivity, but to introduce those that are of interest in this thesis:

- The Sloan Digital Sky Survey, see Sect. 1.3.4 for a detailed description
- The VIRMOS-VLT Deep Survey (VVDS, Le Fèvre et al. 2005) consists of 4 fields covering a total sky area of 3.5 deg^2 and uses the VIMOS and NIRMOS wide field multi-object spectrographs

installed on the 8.2m Very Large Telescope (VLT) to measure the redshifts of 150,000 galaxies in the $0 < z < 5$ redshift range, in order to probe the evolution of galaxies, large scale-structures and AGNs.

- zCOSMOS (Lilly et al. 2007) is a redshift survey undertaken in the COSMOS field with the VIMOS spectrograph on the 8m VLT. It provides spectroscopic redshifts for COSMOS galaxies, with the magnitude-limited sample zCOSMOS-bright containing 20,000 galaxies with $0.1 < z < 1.2$ over the whole 1.7 deg^2 COSMOS ACS field, and zCOSMOS-deep observing 10,000 color-selected galaxies to have $1.4 < z < 3.0$ within the central 1 deg^2. The survey is designed to probe the diversity of environments of COSMOS galaxies as well as to provide diagnostic information on both galaxies and AGN.

- The Galaxy and Mass Assembly survey (GAMA, Driver et al. 2011) started operating in 2008 on the 3.9-m Anglo-Australian Telescope using the AAOmega fibre-fed spectrograph facility to acquire spectra with a resolution of $R \sim 1300$, initially of 120,862 SDSS selected galaxies, and has now observed around $\sim 300,000$ galaxies over a sky area of ~ 286 deg^2.

- Mapping Nearby Galaxies at Apache Point Observatory (MaNGA, Bundy et al. 2015) is an SDSS-IV integral-field spectroscopic survey started in 2014 to investigate the internal kinematic structure and composition of gas and stars in 10,000 nearby galaxies.

1.3.4 The Sloan Digital Sky Survey

The Sloan Digital Sky Survey (SDSS, York et al. 2000)[3] is an imaging and spectroscopic survey using a dedicated 2.5 wide-angle meter optical telescope located at Apache Point Observatory (APO), in New Mexico state (USA). On the one hand, the imaging is performed by a 120-megapixel camera that observes in the 5 optical bands u, g, r, i, and z 1.5 square degrees of sky at a time (about eight times the area of the full moon). On the other hand, two spectrographs fed by optical fibers are able to measure the spectra of more than 600 sources in a single observation, allowing to derive their redshifts. SDSS strongly influenced the research in astrophysics at the start of the 21st century, and notably in galaxy evolution by obtaining deep multi-band images of an unprecedented number of galaxies. The survey is still ongoing and is now in its fifth phase of operations: SDSS-I from 2000 to 2005, SDSS-II from 2005 to 2008, SDSS-III from 2008 to 2014, SDSS-IV from 2015 to 2020, and now SDSS-V until 2025. At the end of the third phase, it had observed about a third of the sky, covering ~ 14555 deg^2, so that its data set contains about $\sim 4.7\ 10^8$ cataloged objects and more than $1.8\ 10^6$ galaxy spectra (SDSS-DR12, Alam et al. 2015). Since 2017, the du Pont telescope at Las Campanas Observatory (LCO) complements the northern sky SDSS with a view of the southern hemisphere sky (Abdurro'uf et al. 2022).

1.3.5 Simulated galaxies

As it will be developed in the following section, galaxy evolution is a complex interplay of many physical phenomema acting on a wide range of scales, from the details of star formation within molecular clouds (see Sect. 1.5.1), up to the environmental effects linked to the galaxy positions within the Cosmic Web (see Sect. 1.4.6). In order to obtain theoretical predictions that can be confronted with observations, N-body numerical simulations represent a powerful tool to integrate all the already understood aspects of galaxy formation.

Cosmological simulations aim at recreating typically a cube of the Universe and use it as a computational laboratory for astrophysical tests. They start from the initial conditions and use the ΛCDM model to reproduce the large-scale structures of the dark matter distribution. While some N-body simulations, such as Millenium (Springel et al. 2005c), are only limited to dark matter particles, hydrodynamical simulations, such as Illustris (Vogelsberger et al. 2014), IllustrisTNG (Springel et al. 2018) or Horizon-AGN (Dubois et al. 2014), use both dark matter and baryons, hence adding the whole range of baryonic physical processes, from gas cooling to star formation and then stellar feedback, but also

[3] https://classic.sdss.org/

modeling the interstellar medium (ISM), supermassive black holes and active galactic nuclei (AGN), as well as introducing magnetic fields, radiation fields and cosmic rays (Vogelsberger et al. 2020).

Similarly to the issue of a finite observing time that can be devoted to a given survey, which raises the issue of making a choice between depth and width (angular area), the finite memory of computing systems constrains the numerical astrophysicists to arbitrate between larger cosmological volumes and finer spatial resolution.

The large number of galaxies found in the cosmological boxes of these simulations makes them well-fitted to study the statistics of galaxy populations. Comparisons can be made between the simulated galaxy population, whose properties are fully known, and the observed galaxy population, whose properties are measured by observational surveys, as long as observational biases, such as completeness, limit in surface brightness, etc., are properly taken into account. For instance, using a light-cone from the Horizon-AGN simulation, a photometric catalog of 750.000 galaxies at redshifts $0 < z < 4$ was produced to provide apparent magnitudes in COSMOS, Dark Energy Survey, LSST-like, and Euclid-like filters at depths comparable to these surveys, and therefore forecast the performance of these imaging surveys in deriving galaxy physical parameters (Laigle et al. 2019; Davidzon et al. 2019).

Among the recent successes of N-body numerical simulations, one can mention their ability to reproduce the stellar mass function of low redshift galaxies (see Sect. 1.4.2, Kaviraj et al. 2017; Pillepich et al. 2018), the galaxy color bimodality (see Chap. 4, Trayford et al. 2015; Nelson et al. 2018), and some of the main scaling relations of galaxies, such as the size-mass relation (see Sect. 1.4.3), the supermassive black hole mass-stellar velocity dispersion relation (Kormendy & Ho 2013), and the mass-metallicity relation (Tremonti et al. 2004; Davé et al. 2017; De Rossi et al. 2017; Torrey et al. 2019).

While large cosmological volumes are needed to properly survey the statistical properties of galaxies and how they are arranged within the large-scale structures, it can be also insightful to do high-resolution simulations of a limited number of galaxies. Using full cosmological simulations with spatial and mass resolutions increased in a specific "zoom-in" region is nowadays frequently used to better model the galaxy physics at scales closer to those of groups of stars and molecular clouds, and how the different zoom level can impact the results of the simulations (Katz & White 1993; Governato et al. 2004; Semelin & Combes 2005; Martig et al. 2009). If "Zoom-in" N-body or smoothed-particle hydrodynamics (SPH) simulations are easier to set up and require less computing time than cosmological simulations, they present the disadvantage to disconnect the studied galaxies from their large-scale environment.

In the context of morphology (see Chap. 2), it is of particular interest to study in-depth the dynamical evolution of the bar and its impact on the secular evolution of a galaxy (see for instance Combes & Sanders 1981; Athanassoula 2013 among many other works, notably by the same authors), the interplay between the bulge and the disk in spiral and lenticular galaxies (Athanassoula 2005), in particular for the Milky Way (Di Matteo et al. 2014, 2015; Fragkoudi et al. 2018), or the formation and persistence of spiral arms (D'Onghia et al. 2013). Moreover, these simulations are tools to study the effects of galaxy mergers, or even fly-bys (Kumar et al. 2021), and to see how the properties of the progenitors and conditions of the interaction determine the merger remnant characteristics (Springel & Hernquist 2005; Hopkins et al. 2009; Athanassoula et al. 2016).

1.4 Characterizing galaxies

1.4.1 Hubble sequence and morphological features

Edwin Hubble, an american astronomer at the Mount Wilson Observatory (California, USA), was the first to classify galaxies according to their shapes and features (Hubble 1926). It led to the establishment of the famous Hubble sequence, also known as the Hubble tuning fork diagram due to its shape, and later the Hubble-de Vaucouleurs sequence, following noteworthy contribution to morphological classification by french astronomer Gérard de Vaucouleurs, the at the Mount Stromlo Observatory (Australia) (de Vaucouleurs 1959). The Hubble sequence comprises the following types:

- **Ellipticals (E)** have smooth and regular 2D luminosity profiles making them appear as ellipses

on images. In the original Hubble classification, they are ordered from left to right by increasing ellipticity, denoted by a number n, which is ten times the ellipticity value, rounded to the closest integer. Ellipticity is defined as $e = 1 - \frac{b}{a}$ with a and b the semi-major and semi-minor axis of the ellipse respectively. The ellipcity seen on the sky however differs from the true 3D ellipticty of the galaxy, thus reducing the relevancy of this parameter. Ellipticals have been shown to be mostly oblate systems (Costantin et al. 2018).

- **Spirals (S)** consist of a flattened disk, within which stars form a spiral structure (hence their name) as well as a central concentration, named bulge. The tuning-fork comes from the separation between barred (SB) and unbarred (S) spirals, and about two-thirds of spiral galaxies host a bar (de Lapparent et al. 2011). Many classes of spiral galaxies exist, from the original Sa, Sb and Sc defined by Hubble, according to the fraction of galaxy light enclosed in the bulge, and how tightly wound are the spiral arms (both increasing from Sc to Sa). Intermediate classes, such as Sab in between Sa and Sb, were then added, and the sequence was also extended (see Irr, below) towards the Sd type (very loose arms and very weak bulge) and even Sm (some indication of arms and very weak bulge).

- **Lenticulars (S0)** are found in between the elliptical and spiral galaxies in the Hubble sequence. They are made of a bright central bulge and a disk, similarly to spirals, except that the latter does not host any spiral arm. Lenticular and spiral galaxies taken together can be referred as disk galaxies.

- **Irregulars (Irr)** include galaxies whose shapes are too irregular to fall in any of the previous classes. When extending the Hubble sequence, and after the discovery of a faint spiral structure within the Large Magellanic Cloud, G. de Vaucouleurs further divided the irregular galaxies into those showing some evidence for spiral structure (as Sm) and those that have no obvious structure, such as the Small Magellanic Cloud, denoted Im (for Magellanic irregulars) and placed them after the spirals at the right end of the morphological sequence.

For historical reasons, galaxies on the left of the diagram (ellipticals and lenticulars) are called early-type galaxies (ETG), whereas those on the right (spirals) are called late-type galaxies (LTG). A similar distinction exist within spirals, with early spirals (Sa-Sb) and late spirals (Sc-Sm).

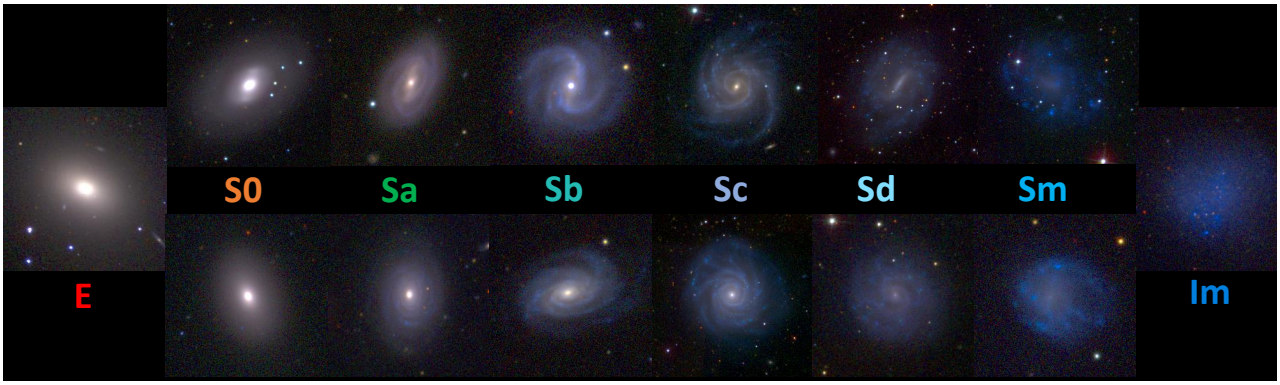

Figure 1.3: The Hubble-de Vaucouleurs sequence illustrated by EFIGI galaxies (see Sect. 2.2.3). It starts from the left with the elliptical galaxies (E). then contains the lenticular galaxies (S0), with a bulge and a disk, but no spiral arms. The spiral galaxies have a bulge of decreasing prominence, a disk and spiral arms more loosely wound as one moves to the right of the sequence, from types Sa to Sm. The upper arm shows the same types as the lower one, but with a bar across the bulge. The irregular galaxies (Im) end the sequence, with no bulge nor spiral arms. Credits: SDSS, AstrOmatic.net, V. de Lapparent

1.4.2 Magnitudes and stellar masses

To measure the brightness of a celestial object, astronomers use magnitudes. Their scale is logarithmic, they decrease as an object gets brighter, with a factor $\sqrt[5]{100} \sim 2.51$ of the received flux, so that an object A 100 times brighter than an object B has a magnitude 5 less than B: $m_A = m_B - 5$. This also requires the definition of an object of reference which is assigned a defined magnitude, so that all magnitudes are then computed as:

$$m - m_{\rm ref} = -2.51 \log_{10} \frac{F}{F_{\rm ref}} \tag{1.1}$$

with m ($m_{\rm ref}$) and F ($F_{\rm ref}$) the magnitude and flux (in units of power per surface area) of the (reference) object respectively. Magnitudes are usually defined in a specific wavelength band, depending of the instrument of measure.

Two different kinds of magnitudes are defined. Apparent magnitudes m measure the brightness of an object as seen in the night sky, which depends on the object luminosity, its distance to us, and the extinction reducing its brightness along the line of sight. Absolute magnitudes M measure the object intrinsic luminosity, by defining it as the apparent magnitude of the object if it was at a fixed distance of Earth (usually 10 pc) with no extinction. Therefore one has :

$$m - M = 5 \log D_{\rm lum}[\text{Mpc}] + 25 + A \tag{1.2}$$

with $D_{\rm lum}$ the luminosity distance given in Megaparsec, and A (≥ 0) the extinction.

Galaxies span many order of magnitudes in luminosity with the brightest elliptical galaxies having luminosities around $10^{12} L_\odot$, with $L_\odot$ the luminosity of the Sun, whereas dwarf galaxies, such as the dwarf spheroidals orbiting the Milky Way, can have luminosities as low as $10^3 L_\odot$ (Kirby et al. 2013; Simon 2019). The optical luminosity of a galaxy is mostly the sum of the luminosities of all its stars, so the luminosity of a galaxy is related to its stellar mass, with the difference in stellar populations inducing some dispersion. Therefore, galaxies also span several orders of magnitudes in terms of stellar mass (see Chap. 4).

To constrain theories of galaxy formation, the number of galaxies of a certain luminosity, or equivalently mass, that exist in the Universe, or at least in a representative subset of the Universe (assuming the cosmological principle), at a given time, is used to compare surveys between them and with numerical simulations. The luminosity and mass functions, that represent the number of galaxies per unit of magnitude and mass, respectively, are consequently key statistical indicators of the galaxy populations. It is well established that there are more faint (or low-mass) galaxies than bright (high-mass) ones (see Fig. 1.4), so they dominate the number counts, but in such a way, that neither the numerous faint galaxies nor the rarer bright galaxies actually dominate the total luminosity, and instead galaxies with an intermediate luminosity, close to that of the Milky Way, actually do (Mo et al. 2010).

The luminosity function is usually fitted by a Schechter function (Schechter 1976), which is defined by:

$$\phi(L) dL = \phi^* \left(\frac{L}{L^*}\right)^\alpha \exp\left(-\frac{L}{L^*}\right) \frac{dL}{L^*} \tag{1.3}$$

where $\phi(L)dL$ represents the comoving number density of galaxies in the luminosity range L to $L + dL$, ϕ^* is the normalization factor, L^* is the characteristic luminosity scale and α is the faint-end slope parameter. It can be also expressed equivalently in terms of magnitude as:

$$\phi(M) dM = 0.4 \ln 10 \; \phi^* 10^{-0.4(M-M^*)(\alpha+1)} \exp\left(-10^{-0.4(M-M^*)}\right) dM \tag{1.4}$$

The total luminosity function summed over all galaxy types is well constrained in the nearby Universe, at $z = 0.1$, thanks to the results of the SDSS survey, which provided best-fit parameters for ϕ^*, L^* and α at different stages of the survey (Blanton et al. 2003; Montero-Dorta & Prada 2009), with the results for the sixth data release (DR6) presented in Fig. 1.4.

In contrast, the mass function can be approximated by a double Schechter function with a single break mass (Pozzetti et al. 2010; Baldry et al. 2012), which is defined by:

$$\phi(M) dM = \exp\left(-\frac{M}{M^*}\right) \left[\phi_1^* \left(\frac{M}{M^*}\right)^{\alpha_1} + \phi_2^* \left(\frac{M}{M^*}\right)^{\alpha_2}\right] \frac{dM}{M^*} \tag{1.5}$$

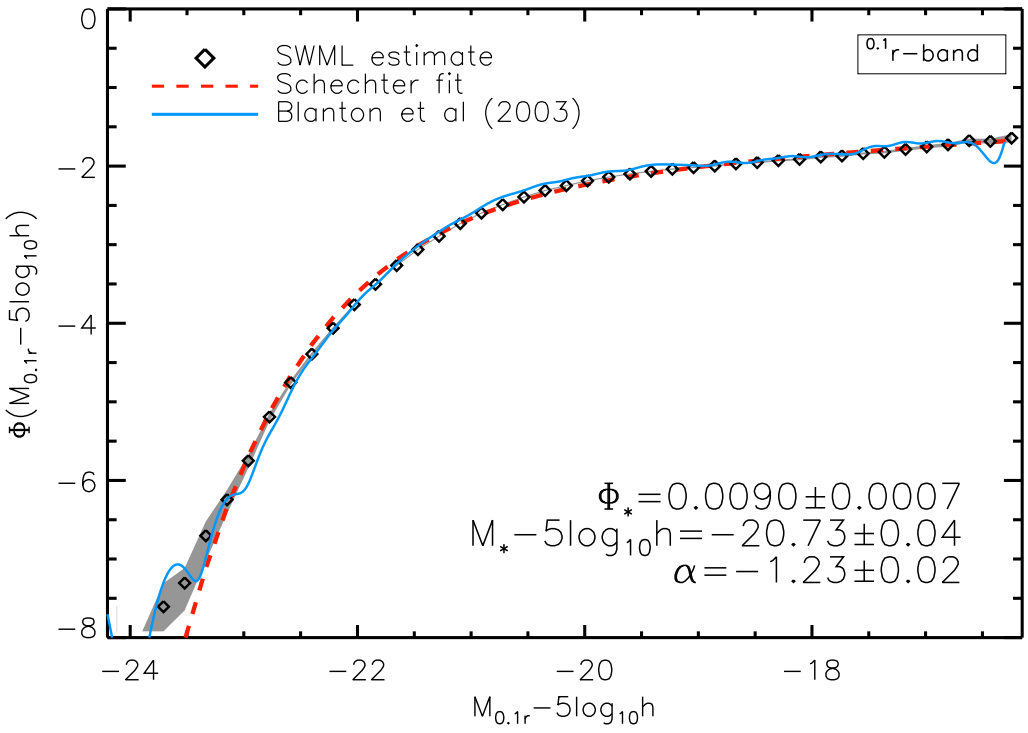

Figure 1.4: Luminosity function for the SDSS DR6 (Adelman-McCarthy et al. 2008). From Montero-Dorta & Prada (2009)

where $\phi(M)dM$ represents the comoving number density of galaxies in the mass range M to $M+dM$, M_* is the characteristic (or break) mass, ϕ_1^* and ϕ_2^* are the normalization factors, and α_1 and α_2 are the faint-end slope parameters, for the two Schechter components respectively. The best fit-parameters obtained by Baldry et al. (2012) from the Galaxy And Mass Assembly (GAMA) survey (Driver et al. 2011) are presented in Fig. 1.5. The luminosity functions per galaxy morphological type are however poorly known, despite recent surveys with morphological classification. This is nevertheless an important issue as the different types have distinct functions in their luminosity range and ratio of bright to faint galaxies (de Lapparent 2003).

1.4.3 Sizes

The boundaries of a galaxy are difficult to define, as most light profiles tend to decrease in intensity at their outskirts until the distance at which they are fainter than the background sky, hence cannot be measured. It is therefore not straightforward to determine the size of a galaxy from an image. The isophotal diameter D_{25} defined as the length of the projected major axis of a galaxy at the isophotal level 25 mag/arcsec^2 in the B-band, can be used, but it is unclear what fraction of a galaxy light it encloses. It is therefore common to measure sizes using the radius that encloses half of the galaxy total luminosity, or "effective radius" R_e. The relation between the angular size θ of a galaxy seen across the sky and its intrinsic physical size R is given by:

$$D_{\rm ang} = \frac{R}{\theta} \tag{1.6}$$

where $D_{\rm ang}$ is the angular diameter distance.

Similarly to luminosity and mass functions, one can examine the size distribution of galaxies, depending on their morphological type, or mass, to put further constraints on galaxy formation scenarii. The size distribution of spiral galaxies at a given magnitude was shown to follow a log normal law, by de Jong & Lacey (2000). Later on, Shen et al. (2003) argued that even though all galaxies showed a

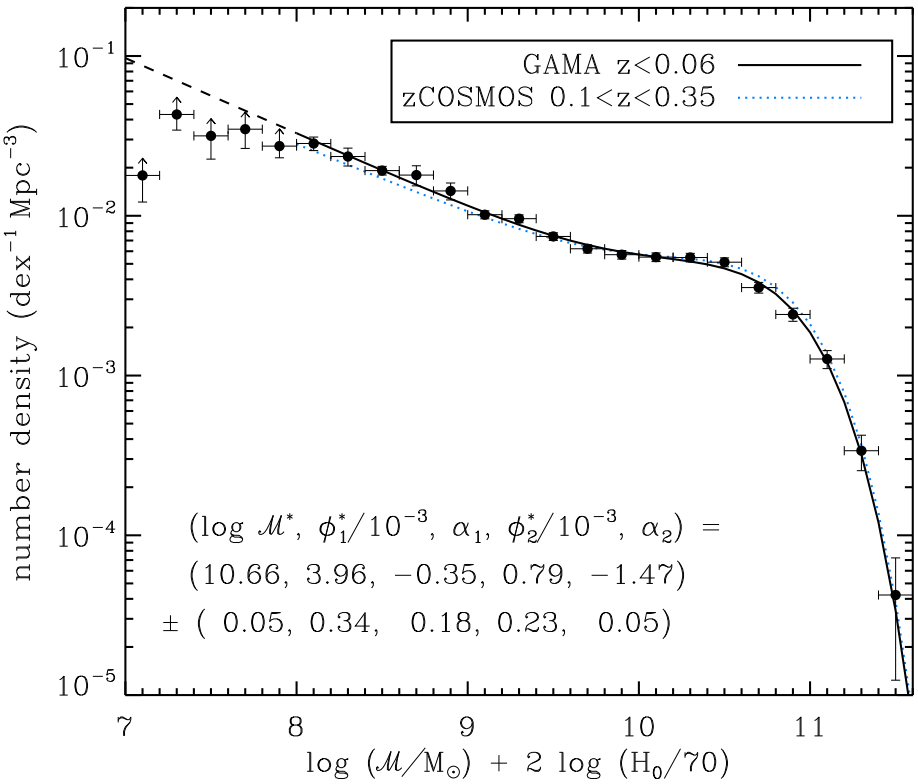

Figure 1.5: Mass function for 5210 galaxies from the GAMA survey and comparison with previous results from Pozzetti et al. (2010) based on ∼ 8500 zCOSMOS galaxies. From Baldry et al. (2012)

correlation between size and luminosity/mass, with brighter/more massive galaxies being larger in size, this "size-mass" relation was dependent on morphology. On the one hand, ETG follow a power-law:

$$\overline{R_e} \propto {M_*}^{0.55} \tag{1.7}$$

where $\overline{R_e}$ is the median effective radius in the z band, and M_* the stellar mass, and with a scatter of $\sigma_{\ln R} \sim 0.35$ dex. On the other hand, LTG show two different behaviors at magnitudes fainter and brighter than $M_{r,0} = -20.5$ (corresponding to $M_{*,0} = 10^{10.6} M_\odot$) with:

$$\begin{aligned} \overline{R_e} &\propto {M_*}^{0.40} \text{ for } M_* > M_{*,0} \\ \overline{R_e} &\propto {M_*}^{0.15} \text{ for } M_* < M_{*,0} \end{aligned} \tag{1.8}$$

with a scatter of $\sigma_{\ln R} \sim 0.35$, 0.45 dex for the high and low mass galaxies, respectively. One of the goal of the present thesis is to remeasure these relations for the various morphological types of well-resolved nearby galaxies (see Chap. 5).

1.4.4 Color, stellar populations, and star formation

When one has access to multi-band data for a galaxy, it becomes possible to compare the amount of light emitted in different wavelength bands. Colors are usually defined as the difference between the magnitudes in two distinct bands, and galaxies are said to be red (or blue) if they emit more light in the redder (bluer) band, i.e. at higher (lower) wavelengths than in the bluer one, in comparison to other galaxies. Thanks to the SDSS, it was observed that the color distribution of galaxies is bimodal between red and blue galaxies, with fewer galaxies having intermediate colors (Strateva et al. 2001). This question is addressed in more details in Chap. 4, with a broader review on color bimodality presented in Sect. 4.1. It was also observed by Strateva et al. (2001) that elliptical galaxies are red, and so are lenticulars, whereas spirals are blue. Within spirals, it is also noted from color images that

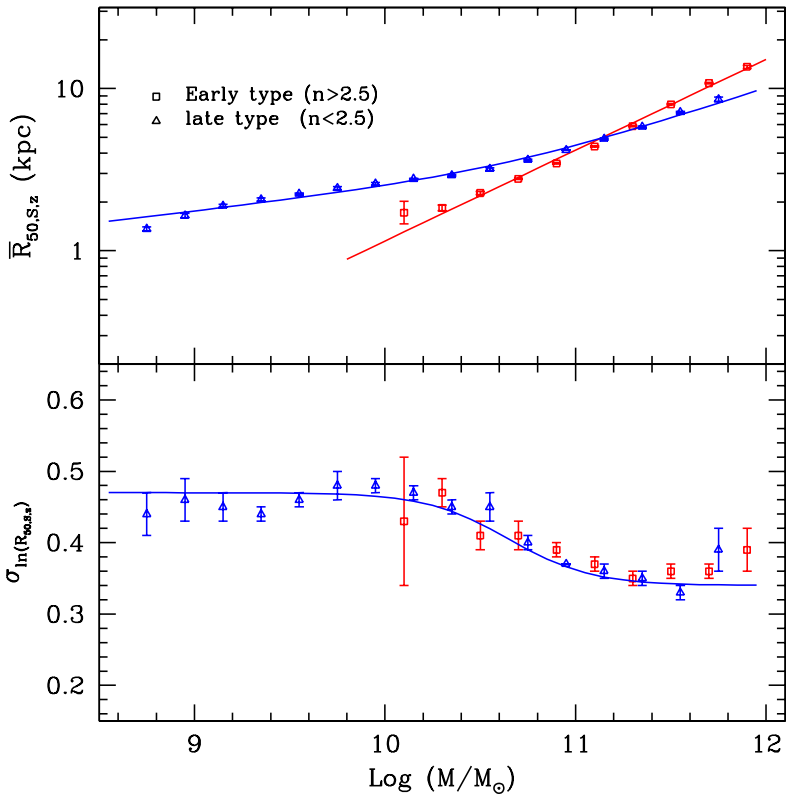

Figure 1.6: Mass-size relation for 140,000 galaxies from the SDSS. From Shen et al. (2003)

the disk appears blue whereas the bulge has redder colors, resembling more those of ellipticals and lenticulars.

The color holds very valuable information about the stellar populations present within each type of galaxy. Indeed, young stars, hence newly-formed stars, emit a bluer light than their older counterparts, so actively star-forming galaxies show bluer colors than the red and so called "dead" galaxies which have stopped forming stars and are consequently made up of old stars. The color of galaxies thus testifies of their star-forming activity.

1.4.5 Redshift and distances

Galaxies are distributed all across the sky but also at different distances from us. The images astronomers use to study galaxies are 2D projections of the 3D space they probe. Fortunately, it is possible to reconstitute this missing 3rd dimension by measuring the distance to the galaxy. In order to do so, one analyzes the spectrum of a given galaxy and looks for specific spectral lines. By measuring the wavelength $\lambda_{\rm obs}$ of each of these lines and comparing it to the known rest-frame wavelength $\lambda_{\rm em}$ of the same atomic element, one can compute the redshift z of a spectrum, which is given by :

$$z = \frac{\lambda_{\rm obs} - \lambda_{\rm em}}{\lambda_{\rm em}} \tag{1.9}$$

In practice, redshifts are measured by cross-correlation of each observed spectrum with various spectral templates, in order to take into account all possible emission and absorption lines (Bellanger et al. 1995).

The redshift is due to the expansion of the Universe which causes distant galaxies to move away from us, at a speed increasing with their distance, provoking a Doppler-Fizeau effect on the observed photons. From the history of the expansion of the Universe, one can compute a distance associated with each redshift. Four types of distances are used in astrophysics (physical, comoving, luminosity and angular diameter) depending on the quantity that is under study (Hogg 1999).

The speed of light $c = 3\ 10^8$ ms^{-1} is finite. As a result, when one observes distant objects in the Universe, they are actually seen as they appeared in the past. Astrophysicists use the concept of

look-back time to account for this phenomenon, which is the duration between the actual emission of light from an object and the moment it is observed. Nearby objects have a negligible look-back time, but for extremely distant objects, the look-back time can be billions of years or even more, up to the limit set by the age of the Universe (Riess et al. 1998). This means that looking at galaxies at various redshifts, or equivalently distances, allows us to unravel the evolution of galaxies during the last few billion years.

1.4.6 Environment

Galaxies are not randomly distributed across space, but rather cluster in different kinds of structures. Galaxies can reside in high-density clusters that contain hundreds of galaxies, in smaller groups containing only a few to tens of galaxies, or they can also be located within lower density environments, such as the filaments and sheets of the Cosmic Web (Mo et al. 2010). Many of these structures are bound together by gravity and have likely played significant roles in the formation and evolution of galaxies. This significance becomes apparent when considering the distribution of different galaxy types. Elliptical galaxies are more frequently observed in cluster environments, whereas spiral galaxies are often found in filaments, sheets, or in relative isolation. This morphology–density relation was quantified by Dressler (1980) who showed decreasing/increasing fraction of late/early-type galaxies with increasing local density, while Weinmann et al. (2006) found similar results with either increasing halo mass or increasing distance to the halo's center. This effect is thought to reflect enhanced dynamical interaction in denser environments. Moreover, denser environments also host galaxies that are on average more massive, redder, more centrally concentrated, less gas-rich, and have lower specific star-formation rates (Kauffmann et al. 2004; Baldry et al. 2006). But as these parameters are all correlated with each other, one must be careful in concluding a causality link between one of these quantities and the environment. For instance, the lower specific star-formation rates measured in clusters of galaxies compared to other environments could be simply the consequence of more predominant early-type morphology, as ETG are often quiescent, while LTG are star-forming. But Kauffmann et al. (2004) also finds lower sSFRs for galaxies in denser environments at fixed stellar mass and morphology, hence indicating an effect of the environment on the star formation activity of galaxies (see the description of galaxy strangulation in Sect. 1.5.3).

1.4.7 Kinematics

Using long-slit spectrographs to measure stellar rotation in elliptical galaxies, it was shown that the massive ellipticals tend to rotate slowly Illingworth (1977), while less massive ones (Davies et al. 1983) and galaxy bulges (Kormendy & Illingworth 1982) appear to rotate faster. With the development of CCD photometry, it became possible to differentiate within E galaxies those with disky and boxy isophotes. This dichotomy matches the one seen in magnitude and rotation speed, with giant slow-rotating E galaxies having boxy ispohotes, while fainter fast-rotating E show disky isophotes. These observations led Kormendy & Bender (1996) to propose a revision of the Hubble sequence that would take into account these varying physical properties for E instead of their isophote elongation. Starting from lenticulars, disky and then boxy ellipticals would continuously extend the sequence in a physically meaningful way.

More recently, thanks to the development of integral-field spectroscopy, it became possible to probe the orbit of stars within galaxies for large samples, hence allowing more robust statistical analysis. Such kinematical analyses have shown that early-type galaxies can indeed be separated into two classes of objects between slow and fast rotators (Emsellem et al. 2007, 2011), depending on the overall level of rotation of their stellar orbits. There is a dichotomy between these two classes, rather than a continuous transition, made of slow rotators that dominate above a critical mass of $10^{11.7} M_{\odot}$, while fast rotators, having a disk component, are more numerous below this mass limit and show properties similar to spirals (Cappellari 2016). Most ETG are fast rotators, with respective fractions of $86 \pm 2\%$ (224/260) and $14 \pm 2\%$ for fast and slow rotators in the volume-limited sample ATLAS^{3D} (Emsellem et al. 2011). Fast and slow rotators are often associated to lenticulars and ellipticals, respectively, but Emsellem et al. (2011) found that even if 93% of S0s are fast rotators, 20% of fast rotators are actually

E galaxies, so that 66% of E galaxies are fast rotators. Moreover, Cappellari et al. (2011) examined the morphology-density relation (see Sect. 1.4.6) in terms of slow and fast rotators instead of ellipticals and lenticulars, and found that it leads to a tighter correlation with the environment density.

The different properties of fast and slow rotators also imply different formation mechanisms. Their position within the mass-size relation (see Sect. 1.4.3) was examined by Cappellari et al. (2013), who derived two evolutionary channels. On the one hand, fast rotators would begin as star-forming disks, they would accrete gas that would sink towards the galaxy center, so they would increase in mass and grow a bulge, which would lead them to being quenched (see Sect. 1.5.3, and the discussion on bulge growth in Quilley & de Lapparent 2022, presented in Chap. 4), therefore forming a passive fast rotator with a disk component. On the other hand, galaxies near the center of massive halos may, through intense star formation at high redshift, reach the critical mass above which the infalling gas is shock heated (Dekel & Birnboim 2006, see Sect. 1.5.3 and Sect. 4.1) therefore suppressing their star formation. Such objects would constitute the progenitors of current slow rotators that were built through dry mergers in a hierarchical formation scenario (see Sect. 4.2).

1.5 Galaxies as the birthplace of stars

1.5.1 Star formation

It was observed that in the Milky Way, and other nearby galaxies, star formation takes place within dense molecular clouds (Blitz 1993; Williams et al. 2000). The virial theorem states that for a system to maintain equilibrium, its gravitational potential energy must be equal to twice the internal thermal energy $E_g = -2E_{th}$. As a consequence, clouds of gas within a galaxy disk remain in hydrostatic equilibrium as long as the kinetic energy of the gas pressure balances the potential energy of the internal gravitational force. However, if cooling mechanisms are efficient enough for the interstellar medium (ISM) gas to cool down, then it moves out of equilibrium and gas clouds can then collapse under their own self-gravity, leading to cold and dense gas clouds within which star formation will occur. It is also possible for a gas cloud to be compressed by an external force, which leads to its gravitational collapse, and trigger star formation. For instance, tidal forces during galaxy interactions (mergers or fly-bys) can agitate and collide molecular clouds, leading to intense starburst episodes.

The gas of the interstellar medium is the fuel of star formation within a galaxy. Therefore, its star formation rate depends on the availability of this gas, and more specifically cold gas that can be transformed into stars. Current star formation depends on the thermal and dynamical conditions within the gas disk, while future star formation will also depend on the replenishment of the gas reservoir. Lilly et al. (2013) built a simple model of gas regulation in order to understand star formation in galaxies, as shown in Fig. 1.7, in which the gas reservoir is replenished by the accretion of external gas, from cosmic flows or the surrounding halo, but suffers losses from stellar wind feedback mechanisms (see Sect. 1.5.3). Gas is turned into stars with an unknown efficiency, while stars at the end of their evolutionary tracks return their gas to the ISM, with increased metallicity. Analyzing this interplay between gas and stars is the key in deciphering star formation in galaxies.

The formation of stars in a galaxy is usually described by the following parameters:

- the star formation rate is defined as the time derivative of the stellar mass $SFR = \dot{M}_*$ and measures the mass of stars formed by unit of time. Because gas is turned into stars, one also has $\dot{M}_* = -\dot{M}_{\rm gas}$

- the specific star formation rate is defined as the star formation rate divided by the galaxy stellar mass $sSFR = \frac{SFR}{M_*} = \frac{\dot{M}_*}{M_*}$. Its inverse is the time needed to form the galaxy stellar mass with its current star formation rate.

- the star formation efficiency SFE (or ϵ) is defined as the ratio between the star formation rate and the mass of gas present in the galaxy $SFE = \frac{SFR}{M_{\rm gas}}$. Its inverse is the depletion time τ_{SF} that quantifies the time needed to deplete the galaxy gas reservoir, if the current star formation rate could be maintained.

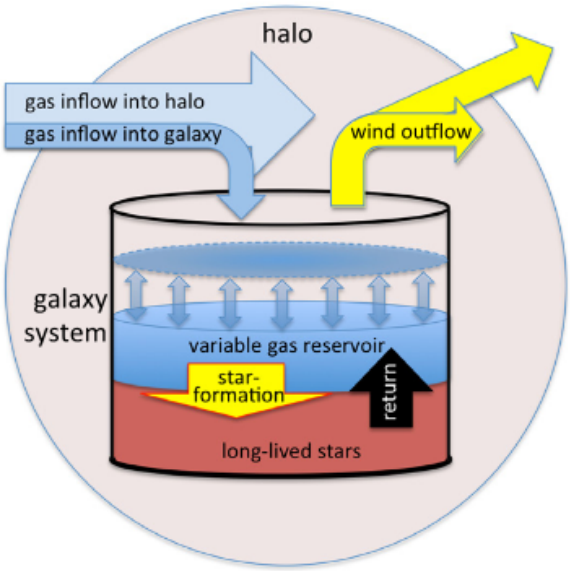

Figure 1.7: Illustration of a simple model of gas regulation in and around a galaxy. Gas flows into the halo in which the galaxy is embedded and directly into the galaxy, thus replenishing its gas reservoir. Within the galaxy, star formation turns gas into stars, while dying stars redistribute their gas (with higher metallicity) into the gas reservoir. Outflow mechanisms (see Sect. 1.5.3) can expel gas outside of the galaxy. The different rates and efficiencies of these processes dictate the evolution of the gas reservoir and of star formation within the galaxy. Figure adapted from Lilly et al. (2013).

In this regard, a key result is the Kennicutt-Schmidt relation, an empirical law that relates the local star formation, measured by the star formation rate surface density Σ_{SFR}, or more simply said the mass of stars formed by unit of time and of area , to the gas surface density Σ_{gas}, which parametrizes the amount of gas available to form stars per unit of area within the galaxy. It states that a power law of index n exists between the two quantities:

$$\Sigma_{SFR} \propto {\Sigma_{gas}}^{n} \tag{1.10}$$

Schmidt (1959) first proposed this law and estimated $n \sim 2$. Almost 40 years later, Kennicutt (1998b) analyzed a sample of 61 spiral and 36 starburst galaxies, covering altogether 5 order of magnitudes in gas surface density, and showed that the distribution of Σ_{SFR} versus Σ_{gas} of the sample was well fitted by a Schmidt law with $n = 1.4 \pm 0.15$. This relation provides a simple and convenient way to relate gas content and star formation in numerical simulations.

1.5.2 Initial Mass Function

When stars form in a cloud gas cloud, they can take a wide range of masses, but not all masses are equally probable. The initial mass function (IMF) describes the distribution of masses for a newly formed stellar population. It can also be seen as a probability density function that gives the probability for a newly formed star to be of a certain mass. Constraining this empirical function is particularly important as stars of different masses have different evolutionary tracks and different spectral types. Knowledge of the IMF is pivotal to correctly interpret the light emitted by galaxies, seen as a collection of stars. The historical IMF was proposed by Salpeter (1955) as the following decreasing power-law:

$$\psi(m)dm = A\, m^{-\alpha} dm \tag{1.11}$$

where $\psi(m)dm$ is the number of stars formed in the mass interval $m \pm dm/2$, with m the stellar mass, A the normalization constant, and α the power-law index. The Salpeter IMF typically has a value of $\alpha \approx 2.35$.

Further developments have argued in favor of an IMF slightly deviating from a pure power law, using log normal distributions, of broken power-laws with increasingly steeper indexes for higher masses.

They all describe a flatter shape for masses below one solar mass, and slightly steeper at the high mass end (Miller & Scalo 1979; Kroupa 2001; Chabrier 2003).

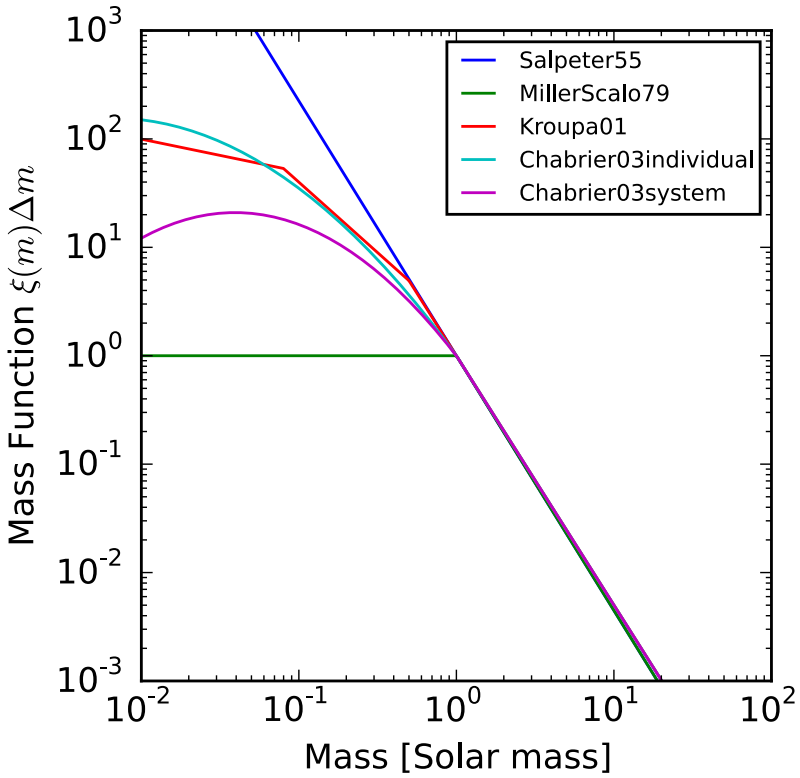

Figure 1.8: Comparison between different initial mass functions. The y-axis is a scaled version of $\phi(m)$. Credit: By Johannes Buchner - Own work, CC BY-SA 4.0, https://commons.wikimedia.org/w/index.php?curid=44779435

1.5.3 Quenching mechanisms

If all galaxies have formed stars at some epoch(s) during their existence, a significant number of galaxies are observed to form few or no stars. These are called "passive", as their star formation is not active anymore, or "quiescent", in the sense that they have been quenched of their star formation fuel: cold gas.

In publications, there is often confusion between the decrease in star formation (the symptom) and the quenching (the cause), by invoking the latter when only observing the former. Here we make the distinction and, when appropriate, specifically refer to the symptom as **star formation fading**.

To understand how star formation is shut down in galaxies, many phenomena have been proposed, but no consensus was reached on their relative preponderance. Galaxy quenching is mainly dependent on two parameters, mass and environment, as the fraction of quenched galaxies was shown to significantly increase with both stellar mass and local over-density (Peng et al. 2010b). Some mechanisms are particularly relevant for massive galaxies, while other are only effective in galaxies residing in dense environments. More generally, multiple mechanisms contribute in parallel to the quenching of a galaxy, but deciphering their relative preponderance remains a challenge.

Quenching refers to any process that prevents a galaxy from forming stars, and any of the conditions needed to form stars, as described in Sect. 1.5.1, can be affected. Therefore one can separate quenching mechanisms in two broad classes: those that prevent the building up of the gas reservoir, and those preventing the transformation of gas into stars.

On the one hand, processes acting on the gas reservoir include:

- Cosmological starvation refers to a reduced gas accretion from the cosmic environment onto the galaxy halo, thus stopping the replenishment of the gas reservoir. However, it is not a

self-sufficient mechanism as it cannot explain why the gas replenishment from internal stellar evolution does not lead to star formation.

- Active Galactic Nuclei (AGN) feedback, in its kinetic mode (Silk & Rees 1998; Di Matteo et al. 2005), refers to the gas being expelled from the galaxy by the strong momentum produced by accretion onto the supermassive black hole (SMBH) of a galaxy.

- Ram-pressure stripping happens when galaxies are moving inside a galaxy cluster, through the intra-cluster medium (ICM). They are then subject to a ram pressure $P_{\rm ram} \sim \rho_{\rm ICM} v^2$ with $\rho_{\rm ICM}$ the ICM gas density and v the speed of the galaxy relative to the ICM, which can strip the gas out of the galaxy if this pressure overcomes the gas gravitational binding, hence for $\rho_{\rm ICM} v^2 > 2\pi G \Sigma_* \Sigma_{ICM}$, where Σ_* and Σ_{ICM} are the mean surface densities of the galaxy disk stellar mass and ICM, respectively (Gunn & Gott 1972).

- Galaxy strangulation is in the continuity of ram-pressure stripping, but concerns the gas surrounding a galaxy that can be accreted to replenish its gas reservoir, and continue forming stars. As this "available" gas is even less gravitationally bound than the gas within a galaxy, it can be easily stripped off, causing the galaxy to gradually run out of gas. It can also be consumed without being replenished, both effects leading to a slow decline of the star formation rate (Larson et al. 1980). Galaxy strangulation thus explains the strong anti-correlation between environment density and specific star formation rate that is observed for galaxies of similar mass and structure (Kauffmann et al. 2004), if the morphology-density relation effect is removed.

On the other hand, mechanisms that can prevent gas from turning into stars are the following:

- Virial shock heating designates the heating of the gas by virial shocks as it collapses onto a dark matter halo (Birnboim & Dekel 2003; Kereš et al. 2005; Dekel & Birnboim 2006). Shocks form in halos of mass $M \geq 10^{12} M_\odot$, which coincide with the mass limit over which galaxies are predominantly quiescent. However, this phenomenon only explains the onset of quenching and further, more long term heating processes are needed to prevent the gas from cooling, for the galaxy to stay quiescent.

- AGN feedback, in its thermal mode (Croton et al. 2006) refers to radiatively inefficient accretion onto supermassive black holes, that heats up the gas, and prevents it from cooling, mainly in massive halos. It is widely invoked in simulations as it allows to reduce the number of massive galaxies produced and thus reproduces the high-mass end of the observed galaxy mass functions (Bower et al. 2006; Kaviraj et al. 2017).

- Gravitational heating is a proposed alternative to AGN feedback to explain the long-term quenching in massive dark matter halos ($M \geq 7\ 10^{12} M_\odot$). In this mechanism, the gravitational energy of cosmological accretion is transferred to the inner halo hot gas by cold flows, and cold clumps (in the mass range 10^4-$10^8 M_\odot$), via ram-pressure drag, local shocks and dynamical friction (Dekel & Birnboim 2008).

- Stellar feedback is another source of gas heating, mainly due to Type Ia supernovae (SNIa) and red giants of the asymptotic giant branch (Ciotti et al. 1991).

- Morphological quenching refers to the halt of star formation in galactic disks when they become dominated by a stellar spheroid, which stabilizes the disk against the fragmentation into bound, star-forming clumps. This does not require neither gas removal nor gas supply termination, so a gas disk can still persist in the red early type galaxy that is formed. This is particularly interesting to explain the quenching of lenticulars and ellipticals in dark matter halos with masses below $10^{12} M_\odot$ as quenching mechanisms acting on the gas content such as gas stripping, AGN feedback, virial shock heating, and gravitational heating are only effective in halos more massive than this limit (Martig et al. 2009).

For an exhaustive review, see Man & Belli (2018), from which this section was based on.

Chapter 2

The morphology of galaxies

In Sect. 1.4.1, we have introduced the landmark classification system of the Hubble sequence, as the morphological type is among the main properties for characterizing galaxies. Because this thesis is focused on galaxy morphology, we dive here into more detail in the morphological properties of galaxies, discussing the two components - bulge and disk - that play a key role in the establishment of the Hubble sequence, as well as the features that fall outside of it. Then we present the two approaches of morphological analysis, which are the visual classification, including most notably the EFIGI morphological catalog that is used throughout this thesis, and the quantitative measurements that can be performed on galaxy images.

2.1 In-depth galaxy morphology

2.1.1 Bulge

Bulges are nested in the inner regions of spiral and lenticular galaxies. They correspond to the excess of light, hence stellar mass, found at the center of galaxies when extrapolating inwards the surface brightness exponential profiles of the disk. One can differentiate two kinds of bulges (Kormendy & Kennicutt 2004). Classical bulges (cB) are spheroidal systems, which are pressure-supported, dynamically hot and build by violent relaxation. Their properties are close to those of the elliptical galaxies, in terms of kinematics, and they reproduce some relations of elliptical galaxies, such as the luminosity-metallicity relation (Jablonka et al. 1996) or the Kormendy relation (see Chap. 5, Gadotti 2009). The similar kinematics led Renzini (1999) to see bulges as ellipticals embedded in a disk, or ellipticals as bulges without disk, even though the picture is actually more complex, with bulges having different formation history than ellipticals (Gadotti 2009). The formation processes that are thought to explain the growth of classical bulges are mergers (Aguerri et al. 2001; Sachdeva et al. 2017; Tacchella et al. 2019), mostly numerous minor mergers (see Sect. 4.2 for a definition), but their number and mass ratios remain poorly constrained, and also clump migration (Noguchi 1999; Bournaud et al. 2007).

On the other hand, pseudo-bulges (pB) are rotation-supported systems, that are flatter in shape, i.e. disk-like (Kormendy 1993). Among the pseudo-bulges, one can further differentiate disky bulges that are within the disk and built through secular evolution, from boxy/peanut bulges that also show circular orbits but are vertically more extended than the disk, and thought to be built by the buckling of the bar (Combes et al. 1990; Athanassoula 2005, 2008, 2013; Debattista et al. 2006).

The dichotomy between classical and pseudo-bulges is further explored in Chap. 5 in the light of previous analyses as well as results from Quilley & de Lapparent (2023, presented in Sect. 5.2 and shown in Sect. 5.3). The review by Fisher & Drory (2016) presents the many observational properties that allow them to be distinguished, with relative reliability.

2.1.2 Disk

Disks form the outer regions of spiral and lenticular galaxies. They are composed of stars, gas, and dust and can be described by two scale-lengths: a height (or width) and a radius (note that in the absence

of perturbations, galaxy disks are circular[1]), with the former being one or two orders of magnitudes smaller than the latter. Within the disk, stars are on circular orbits, which allows one to compute rotation curves $V_{\rm rot}(r)$. The discrepancy between the flat rotation curves measured by Rubin et al. (1980) and the decrease with radius expected from Newtonian mechanics, was one of the first indications of the existence of dark matter. Another landmark result regarding rotation curves is the Tully-Fisher relation, which shows a correlation between the absolute magnitude of a spiral or lenticular galaxy, and its asymptotic rotation velocity, thus providing a method to estimate extra-galactic distances from rotation curves (Tully & Fisher 1977).

For spirals, disks are the locus of star formation and host a spiral structure made up of several arms. If those arms were material structures, then they would become increasingly more tightly wound as time passes, because the matter nearer to the center of the galaxy rotates faster than the matter at the edge, so the arms would disappear after a few orbits. To solve this so-called winding problem, Lin & Shu (1964) proposed that spiral arms were density waves propagating with fixed angular velocity, that revolves across the galaxy at a speed different from that of the galaxy's gas and stars. As gas clouds move into the density wave, the local mass density increases, making them more likely to collapse and form stars, thus leading to enhanced star formation. The disk can be further decomposed into two components: the thin disk and the thick disk. Thin disks are composed of younger stars, are more metal-rich, and have shorter scale heights and scale lengths, with factors of $\sim 1/2$ and $\sim 4/5$ respectively, than the thick disks (Yoachim & Dalcanton 2006).

2.1.3 Additional morphological features

Some other morphologies exist but are not described within the Hubble sequence, this is most notably the case for the faintest galaxies observable: dwarf galaxies (Mo et al. 2010). Some of them show irregular shapes and are thus referred to as dwarf irregulars, while some exhibit regular surface brightness profiles, with no arms, and are called dwarf spheroidal elliptical (dE), and may exhibit a nucleus (dEn). One can also mention peculiar galaxies which are highly distorted galaxies with either tails or filamentary structures, and are often associated with a recent merger or tidal interaction, thus explaining their complex and uncommon structure (Mo et al. 2010).

Moreover, not all morphological features are taken into consideration when classifying a galaxy onto the Hubble sequence. Extra dimensions of morphological classification can be added by adding an indicator on the presence or absence, and relative strength if present, of the following features:

- Rings or pseudo-rings
- Nuclear rings and nuclear bars
- Lenses
- Dust lanes

There is no limit to the degree of complexity that can be added to a morphological description. One can try to count the number of spiral arms, analyze the shape of a galactic bar or investigate the relative size between different morphological features, with for instance the outer rings of early-type barred galaxies whose radius is roughly twice the bar length (Buta 2011). But the parameters used for the Hubble sequence already provide a satisfying classification system, that has been the standard used over the last century.

2.1.4 Morphology across the electromagnetic spectrum

We emphasize that classification methods can be extended beyond optical imaging, as examining galaxies across the electromagnetic spectrum can lead to different and complementary descriptions. The $H\alpha$ line or UV imaging provides information on the youngest stars, and thus trace star formation within a galaxy (Buta 2011). On the other side of the optical domain, infrared (IR) imaging, even though it loses information about star formation, presents the advantage of being less sensitive to

[1]The analysis of Sect. 3.1.1 shows that the aspect ratio of unperturbed face-on galaxies has a median value of 0.90

both internal and external extinction, and thus provides smoother-looking images allowing for a better mapping of the stellar mass in a galaxy (Rix & Rieke 1993; Block et al. 1994). Beyond stars, the gas content of a galaxy can also be visualized using the 21cm fine structure emission line that traces neutral atomic HI gas, while molecular gas is generally mapped using the ^{12}CO J=1-0 rotational transition at a wavelength of 2.6mm, assuming a specific CO and hydrogen mix (Buta 2011).

2.2 Visual classification

2.2.1 A century of visual classification

The pioneering work of Edwin Hubble was based on a visual classification, the American astronomer classified galaxies according to the shapes and features he saw in the images taken by the Mt Wilson telescope (Hubble 1926). This approach persisted in the next decades with the improvement of the classification system brought by de Vaucouleurs (1959) and Sandage (1961). Later on, the deep images obtained by the Hubble space telescope that opened a new window on past and distant galaxies, have also led to visual classifications (Dressler et al. 1994; van den Bergh et al. 1996; Lee et al. 2013; Mortlock et al. 2013). Very recently, the stupendous images of the JWST have been visually inspected in order to measure the proportion of spheroids and disks at unprecedented redshifts, up to $z = 8 - 9$, leading to the conclusion that the Hubble sequence was already in place very early in the history of the Universe (Ferreira et al. 2022; Jacobs et al. 2023; Kartaltepe et al. 2023). The obvious drawbacks of visual classification are the human dependence that can introduce biases, the low time efficiency that limits the analysis to hundreds or thousands of galaxies when performed by professional astronomers (but see next sub-section for the use of citizen science). Human visual classifications are also discrete , hence can only assign classes and categories, but no continuous quantitative parameter. However, visual classification remains useful as it allows one to perform a richer description of the very complex morphological features of galaxies, and provide the astrophysical community with databases that can used for comparison of automated processes and algorithms.

2.2.2 Morphological catalogs

The Third Reference Catalogue of Bright Galaxies (de Vaucouleurs et al. 1991, RC3) has long been the reference for the morphological types, as well as information on the presence of bars and rings for nearby galaxies. It contains a total of $\sim$ 23000 galaxies with an apparent photographic magnitude limit $B_T \leq 15.5$, which have been identified from photographic plates. Complementary catalogs exist to study some specific morphological features, such as bars, rings or lenses (Kormendy 1979; Buta 1995), but are limited to one or several properties for small samples and/or in preferred regions of the sky.

Thanks to the Sloan Digital Sky Survey (see Sect. 1.3.4), the amount of data available to study galaxy morphology has reached new heights. Because the process of visual classification is long, the Galaxy Zoo initiative (Lintott et al. 2008) had the idea of inviting the general public to perform such task. Anyone accessing the Galaxy Zoo website (`https://www.zooniverse.org/projects/zookeeper/galaxy-zoo`) is presented with composite color galaxy images and is guided through the process of visual classification through simple questions on elements such as the smoothness of the profile, the presence of features (bar, arms, rings, etc.). It allowed for nearly 900,000 SDSS galaxies with $z \leq 0.25$ to be visually classified by more than 100,000 volunteers (Lintott et al. 2011). This citizen science project shows robustness thanks to the large number of classifications per object, which allows one to associate an uncertainty to each classification, and by showing a satisfying agreement between the classification made by amateurs through the internet to previous classifications made by professional astronomers.

Also based on the SDSS images, the classification of $\sim$ 14000 galaxies by Nair & Abraham (2010) into a Hubble type with secondary attributes indicating the presence of bars, rings, lenses, distortions, tidal tails, spiral arms, and dust can be compared to the EFIGI catalog, on which is based this thesis (see next sub-section). The classification is based on the g image only, and uses the r and i images to define flags (see Baillard et al. (2011, Sect. 6) for a comparison of this catalog with EFIGI, indicating general agreement for the perturbation, bar and ring attributes). The morphological catalog built by

Ann et al. (2015) that visually classified 5836 galaxies according to the RC3 sequence using *gri* color images from the SDSS DR7, forms a representative sample of local galaxies with $z \leq 0.01$, by being almost complete for galaxies brighter than $r_{pet} = 17.77$. This classification also distinguishes the fine features of dwarf elliptical galaxies into 5 sub-classes, as well as their nucleation. This catalog provides estimates that in this region of the Universe, dwarf ellipticals, lenticulars, dwarf elliptical, spirals and irregulars contribute 1.5%, 5%, 19%, 32% and 43% respectively of galaxies.

2.2.3 The EFIGI morphological catalog

EFIGI, which stands for "Extraction de Formes Idéalisées de Galaxies en Imagerie", is a morphological catalog of 4458 nearby ($z < 0.08$) galaxies selected from the Principal Galaxy Catalogue (Paturel et al. 1995). It is based on imaging data from the whole area of the 4th Data Release (DR4) of the Sloan Digital Sky Survey (SDSS) (Adelman-McCarthy et al. 2006), which corresponds to a solid angle of 6670 deg^2 in the northern galactic cap (see Fig. 2.1). EFIGI galaxies are selected so that their imaging is available in all 5 optical bands u, g, r, i and z.

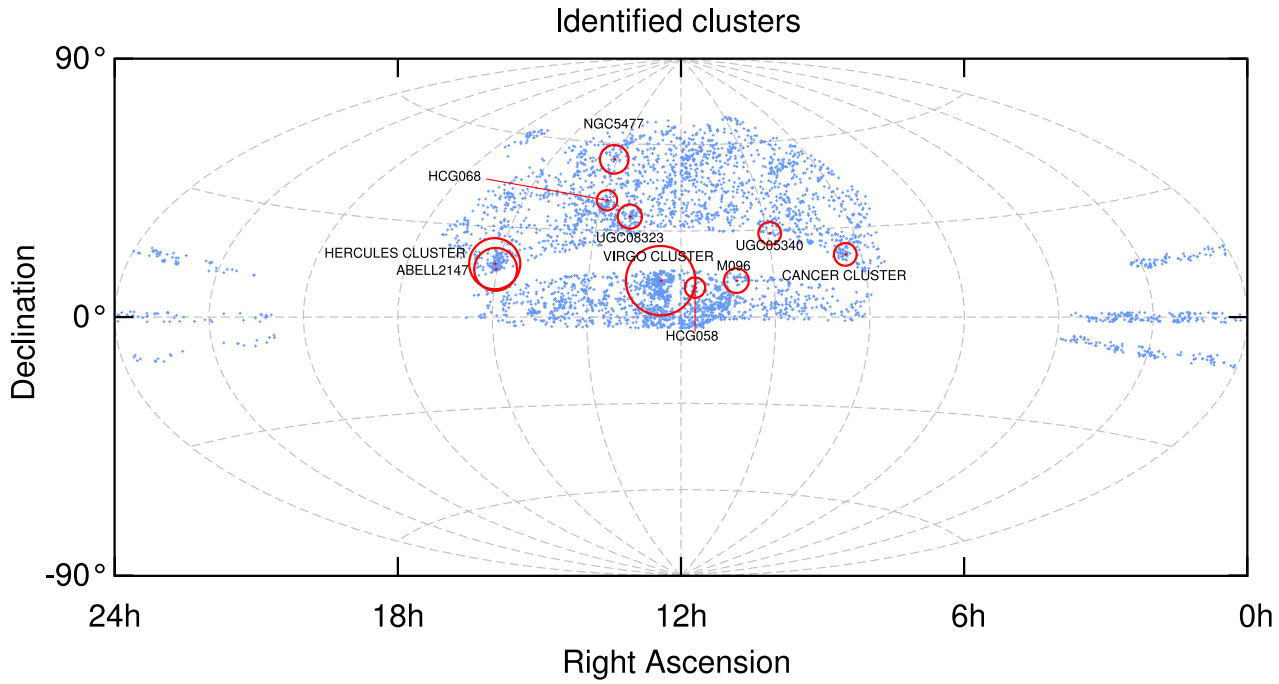

Figure 2.1: Positions of EFIGI galaxies on the celestial sphere, shown as blue dots. Clusters of galaxies are identified as red circles, whose center is given by its NED coordinates, and their enclosed area is proportional to the number of cluster members. From Baillard et al. (2011).

The EFIGI catalog was created to be a tool of morphological analysis and therefore includes a few hundred objects for each morphological type, except for some rare types for which it is not possible. It is also apparent-diameter limited with $D_{25} > 1$ arcmin, where D_{25} is the diameter of the isophote at which the surface brightness is 25mag.arcsec^{-2}. This is the limit beyond which visual identification becomes challenging. Therefore, EFIGI does not provide a representative picture of the sky as it is not a magnitude limited catalog, and it probably over-samples late-type spirals (Sd, Sdm, Sm) compared to magnitude-limited catalogs.

All EFIGI galaxies, and more specifically their composite color images, were visually examined by a team of astronomers who assigned to each of them a Hubble type and also 16 morphological attributes on a five-scale level, as well as a confidence level for each of them. These attributes allow for a more exhaustive description of the morphology of the galaxies in terms of structure, texture, environment and appearance and quantify the following elements :

- the bulge-to-total luminosity ratio of the object

- the length of the bars and the intensity of the internal and external rings
- the intensity of the spiral arms, their curvature and their direction of rotation
- the presence and dispersion of dust
- the significance of "flocculent" features due to scattered HII regions ("Flocculence"), and regions of intense star formation ("Hot Spots")
- the perturbation of the profile compared to rotational symmetry
- the contamination of the profile by foreground sources, and the number of neighboring galaxies.

(note that intensity means the fraction of flux enclosed in the component compared to the total flux of the galaxy). The objective of these attributes is to define the specific features that contribute to the morphological type of a galaxy, or that make the galaxy deviate from the Hubble types (for example when a galaxy is contaminated by another object). They also relate the shape of a galaxy to the underlying physical phenomena, by characterizing the stellar, gaseous, and dusty components, as well as the dynamic structures, while taking into account the impact of the immediate environment and observational biases on the apparent shape of a galaxy.

The EFIGI morphological sequence is based on the 3rd revised catalog (RC3) Hubble sequence (de Vaucouleurs et al. 1991), with the following differences :

- the EFIGI sequence only has one elliptical type, as the different elongation stages of elliptical galaxies in the RC3 are measured by the EFIGI `Inclination` attribute
- the RC3 non-Magellanic irregulars (I0 type) are not considered as a separate type in EFIGI, but as galaxies of some other Hubble type which undergo some perturbation as measured by the corresponding attribute
- in EFIGI, the dwarf elliptical and dwarf spheroidal galaxies are together in one separate class from the ellipticals.

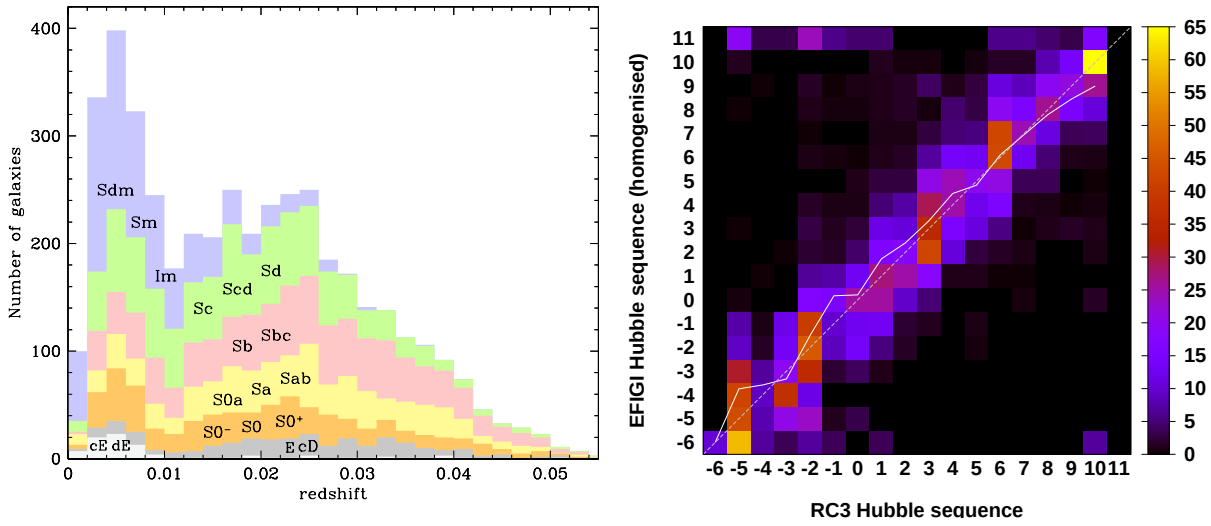

Figure 2.2: **Left:** Redshift distribution of the EFIGI galaxies separated by morphological type. The peak at $z \sim 0.004$ corresponds to the Virgo Cluster. Figure from de Lapparent et al. (2011). **Right:** Confusion matrix between the EFIGI Hubble sequence and the RC3 Hubble sequence. The solid line represents the average EFIGI Hubble type per PGC type bin. Extracted from Baillard et al. (2011).

There is good agreement between both classification as shown by the confusion matrix of Fig. 2.2 left panel, thus confirming its reliability to be used for morphological analysis. Buta (2019) examined the EFIGI catalog from the standpoint of the comprehensive de Vaucouleurs revised Hubble sequence

and also found good agreement with the classification of Baillard et al. (2011), while also arguing that the EFIGI catalog is very valuable: on the one hand for its many examples of specific morphological features (skewed bars, blue bar ansae, bar-outer pseudo-ring misalignment, extremely elongated inner SB rings etc.) that are pivotal to understanding secular evolution and internal dynamics; on the other hand, it can be used as a training set for supervised learning methods that will be needed to exploit forthcoming large surveys (Euclid, LSST).

As mentioned previously, EFIGI is not a magnitude limited sample. This can lead to statistical biases if one wants to use EFIGI to infer morphological statistics in the nearby Universe. To address such issues, it is essential to note that EFIGI is included in a larger catalog called MorCat (for Morphological Catalog) which is magnitude-limited with $g \leq 15.5$ and contains 20,126 galaxies (see Sect. 6.2 for considerations regarding its exploitation).

2.3 Quantitative and automatic morphological measurements

Automatic extraction of galaxies from astronomical images started in the 1980's with the use of optical digital detectors (CCD's) in replacement of the non linear photographic plates. Open-source software for detecting and measuring sources in stellar and galaxy fields became essential astronomical tools.

2.3.1 Surface brightness profile-fitting

In order to quantitatively measure the morphology of a galaxy, the first attempt was made by de Vaucouleurs (1948) who used the aperture photometry measurement at different radii to build the integrated light profile of elliptical galaxies and proposed a functional form. The derived profile, deemed after his inventor the de Vaucouleurs profile has long been used to model spheroids (Kormendy 1977b), such as elliptical galaxies, or bulges. It was generalized by the Sérsic profile (Sérsic 1963), which has since then become a standard luminosity profile, widely used to model the light of galaxies, or of their bulges and disks.

The Sérsic profile is given in the case of circular symmetry by the Sérsic function :

$$I(r) = I_{\rm e} \exp\left\{-b_n\left[\left(\frac{r}{r_{\rm e}}\right)^{1/n} - 1\right]\right\} \tag{2.1}$$

where r is the angular radius to the profile center, r_e is the effective radius that encloses half of the total light of the profile, that is

$$\int_0^{r_e} I(r)\, 2\pi r {\rm d}r = \frac{1}{2}\int_0^{+\infty} I(r)\, 2\pi r {\rm d}r. \tag{2.2}$$

$I_e = I(r_e)$ is the intensity at this radius, n is the Sérsic index that defines the steepness of the profile, with higher n corresponding to steeper profiles, and b_n is a normalization parameter depending on n only. Graham & Driver (2005) provides an exhaustive description of the circular Sérsic profile. The analytical function for a profile with elliptical isophotes can be derived from Eq. 2.1.

The de Vaucouleurs profile corresponds to the specific case where the Sérsic index is equal to 4. Similarly, the exponential profile, another standard profile, is simply the Sérsic profile where the Sérsic index is equal to 1. The de Vaucouleurs profile is suited for spheroids whereas the exponential profile has been widely and successfully used to model the disk of galaxies (Freeman 1970; Kormendy 1977b; de Jong 1996).

The standard approach that has arisen over the past decades is to model a galaxy as the sum of a bulge and a disk, using either a Sérsic or a de Vaucouleurs profile for the bulge, and an exponential profile for the disk (see for instance de Jong 1996; Allen et al. 2006; Huertas-Company et al. 2007; Simard et al. 2011; Dimauro et al. 2018, among many others). It is therefore called a bulge and disk decomposition and allows to account for the different structural properties between these two components (see Sect. 2.1.1 and 2.1.2). However, single-profile modeling remains used to model galaxies, for instance for elliptical galaxies with no visible disk, or when image resolution does not allow for two components to be fitted. On the contrary, more complicated models can be created by adding as many

components as computationally possible, to model bars, lenses, or rings (Kruk et al. 2018; Gao et al. 2019).

The SourceXtractor software (formerly SExtractor, Bertin & Arnouts 1996) that was developed by two PhD students at the Institut d'Astrophysique de Paris (IAP), first took the lead, due to its accessibility, easy use, and high execution speed, but many softwares have been subsequently developed to perform this profile-fitting task on images, including among others GIM-2D (Simard 1998), GALFIT (Peng et al. 2002, 2010a), Morfometryka (Ferrari et al. 2015), ProFit (Robotham et al. 2017), DeepLeGATo (Tuccillo et al. 2018), Galapagos-2 (Häußler et al. 2022), and finally SourceXtractor++ (Bertin et al. 2020; Kümmel et al. 2020) that we use in this work (see Sect. 3.1).

2.3.2 Non-parametric morphological measurements

With the previous methodology, one has to assume that the light profile of any galaxy can be approximated by a combination of analytical functions. However, it can be interesting to quantify the morphology of galaxies without any prior assumption, and this is what non-parametric approaches attempt to do.

Regarding galaxy sizes, the Petrosian radius R_P (Petrosian 1976) is defined as the radius for which the ratio $\eta(R)$ of the local surface brightness $I(R)$ divided by the mean surface brightness within this radius $\langle I(< R)\rangle$ reaches a certain value, usually $\eta(R_P) = 0.2$. In practice, the local surface brightness $I(R)$ is integrated over an annulus of a certain width so we have:

$$\frac{\int_{\alpha R_P}^{\beta R_P} 2\pi r I(r)\, dr / \left[\pi(\beta^2 - \alpha^2){R_P}^2\right]}{\int_0^{R_P} 2\pi r I(r)\, dr / \left[\pi {R_P}^2\right]} = \eta(R_P) = 0.2 \tag{2.3}$$

where the width of the annulus is characterized by α and β, chosen to be 0.8 and 1.25 respectively in the SDSS catalogs. (Blanton et al. 2003; Shen et al. 2003).

To quantify the inner structure of a galaxy, the CAS system, for concentration (C), asymmetry (A) and clumpiness - or smoothness - (S) was developed by Conselice (2003), which is based on the following parameters. The concentration C measures the fraction of light at the center of the galaxy compared to its outer parts. A common definition used is:

$$C = 5 \log \frac{r_{\text{outer}}}{r_{\text{inner}}} \tag{2.4}$$

where r_{outer} and r_{inner} are the radii containing a certain fraction of the total galaxy flux (e.g. 80% and 20%). Petrosian radii can also be used. The asymmetry index measure the share of a galaxy light which is located in non-symmetric parts of the galaxy. It is defined by measuring the fractional difference in flux between the galaxy image $I_{x,y}$ and the same image rotated by 180° $I_{-x,-y}$, so that:

$$A = \frac{\sum_{x,y} |I_{x,y} - I_{-x,-y}|}{\sum_{x,y} I_{x,y}} \tag{2.5}$$

Proper computation of this quantity raises several challenges, including the determination of the center and the estimation of the background noise. The clumpiness (or smoothness) S measures the fraction of light within clumpy structures. To measure it from a galaxy image $I_{x,y}$, a blurred image $I^{\sigma}_{x,y}$ is created (for example by convolution with a Gaussian filter of r.m.s. σ), so that subtracting the latter from the former creates a residual map containing only the high spatial frequency structures of the galaxy (this depends on the blurring procedure). I write here the reduced formula for a null background image:

$$S = 10 \frac{\sum_{x,y} (I_{x,y} - I^{\sigma}_{x,y})}{\sum_{x,y} I_{x,y}} \tag{2.6}$$

(the exact formula takes into account the background noise of both images, and also eliminates from the sum the central pixels of galaxies due to their unresolved high-spatial frequency light).

Mapping galaxies in the 3-dimensional CAS space allows one to identify galaxy classes according to their morphology, and to separate them based on a few parameters. For instance, E galaxies have

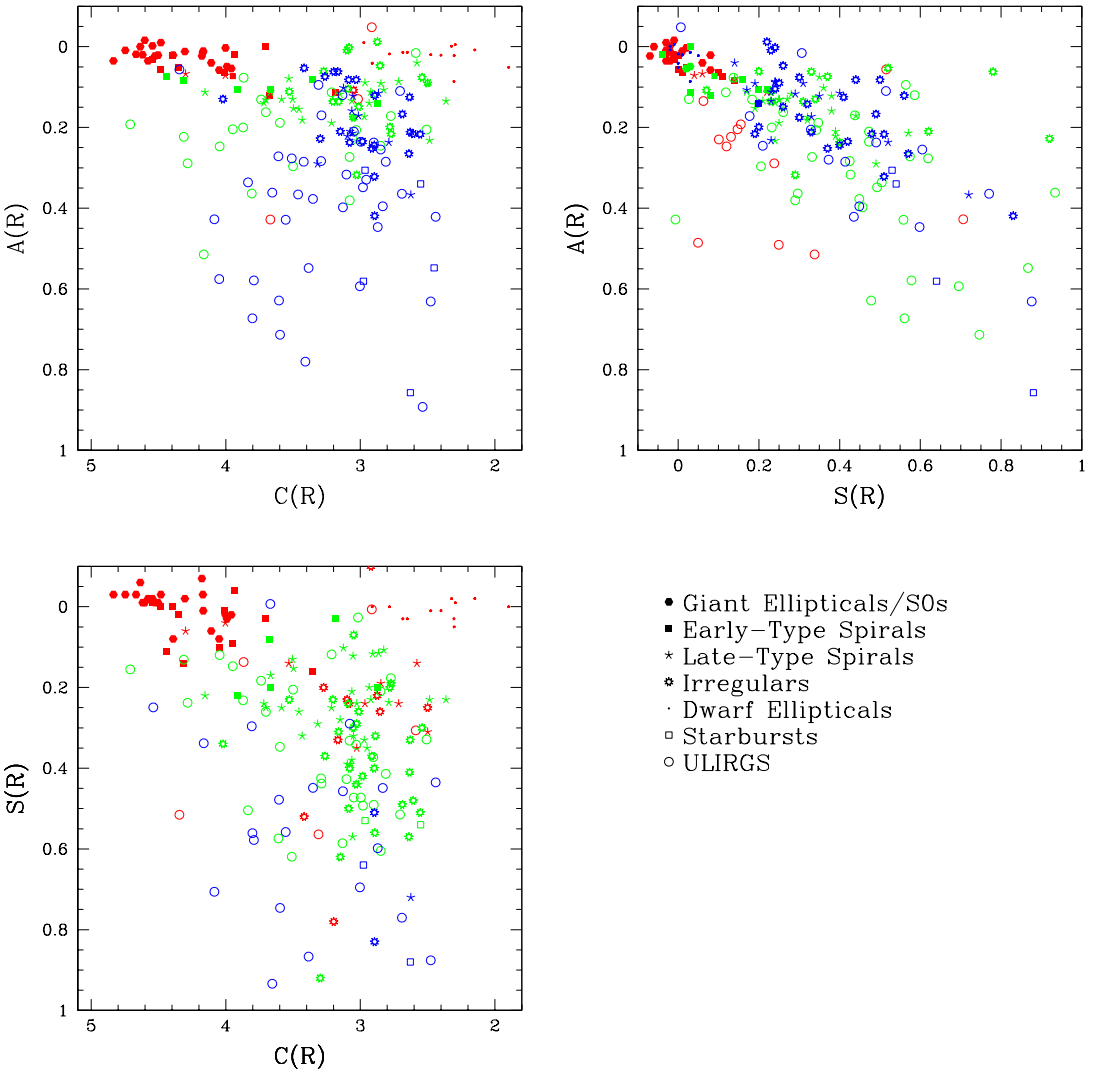

Figure 2.3: The three projections of the CAS parameter space are shown for a sample of galaxies of various types, denoted by their symbols. The color of the points represent the third dimension: in the $A-C$ diagram, red is for $S < 0.1$, green for $0.1 < S < 0.35$ and blue for $S > 0.35$; in the $A-S$ diagram, red is for $C > 4$, green for $3 < C < 4$ and blue for $C < 3$; in the $S - C$ diagram, red is for $A < 0.1$, green for $0.1 < A < 0.35$ and blue for $A > 0.35$. Taken altogether, these 3 morphological parameters succeed in discriminating between the different morphological types. From Conselice (2003).

the highest concentration value with $4 < C < 5$ but very low assymetry and clumpiness, with very small A and S values (< 0.1). Whereas early-type spirals (Sa and Sb) have lower concentrations ($3.5 < C < 4.5$) than the ellipticals, slightly higher asymmetries ($A \sim 0.1$), and clumpiness values $S \sim 0.1$. Late-type galaxies (Sc and Sd) have even lower light concentrations ($C < 3.5$)), higher asymmetries ($0.1 < A < 0.3$) and large clumpiness values ($S > 0.1$) (Conselice 2003).

Other non-parametric measurements have been developed for quantifying galaxy morphology such as the Gini index G which is the relative distribution of the galaxy pixel flux values, and the second-order moment of the brightest 20% of the galaxy's flux M20 (Lotz et al. 2004).

2.3.3 Machine Learning

With the numbers of galaxies observed by telescopes skyrocketing with each new generation of instruments, and especially with the next generation of wide-field surveys that will be gathered by Euclid, the Vera Rubin Observatory and WFIRST (Wide Field Infrared Survey Telescope), containing billions of galaxies, even automatic profile-modeling methods of analysis will end up taking unreasonable com-

puting times. In that regard, "Machine Learning" presents itself as a solution to treat these data in the future.

As in other scientific fields, machine learning can be used to analyze highly-correlated data from a large parameter space, with for instance neural networks (Ball et al. 2004), principal component analysis (Scarlata et al. 2007), support vector machines (Huertas-Company et al. 2008) or random forests (Bluck et al. 2022). However, to actually solve the computing time issue of morphological analysis, one is mostly interested in learning methods that directly extract features from galaxy images, without requiring a pre-processing step to extract any parameters such as, e.g. profile-fitting or CAS measurements.

Morphological classification is a task well-fit for machine learning, and many attempts at creating pipelines to infer a morphological type from a galaxy image have been designed over the last few years, with samples of increasing sizes, from the 50,000 CANDELS galaxies classified by Huertas-Company et al. (2015), to $\sim$ 21 millions and $\sim$ 27 million DES galaxies classified by Cheng et al. (2021a) and Vega-Ferrero et al. (2021) respectively.

The machine learning can be supervised if one provides the computer with a labeled training set, so that it learns to map the inputs (here galaxy images) given the desired outputs (morphological classification), so the morphological catalogs described in Sect. 2.2.2 and in Sect. 2.2.3 are needed as training sets. Because training sets of at last 10^5 objects are necessary, way more than there are nearby galaxies in the Universe, mock galaxy images can be created in order to augment the training sets. This nevertheless poses the challenge to simulate realistically the full diversity of galaxies in both their large-scale components (bulge, disk, spiral arms, bars, rings, etc.), as well as their possible distortions (due to mergers), and the texture within them (scattered HII regions, dust). In unsupervised machine learning, the data is provided without prior labeling, and let the machine construct a classification as it seems fit. In the context of galaxy morphology, this can lead to classifications that do not follow the Hubble sequence, thus raising the challenge of measuring the relevance of the obtained classification, without the possibility of a direct comparison with labeled data, but also providing at the same time the opportunity to yield classifications with new physical significance (Cheng et al. 2021b).

So far, convolutional neural networks (CNN) have proven to be the most effective method in extracting morphological information from galaxy images (Cheng et al. 2020). However, even if these state-of-the-art methods yield very satisfactory results to provide simple or even binary classifications, such as LTG versus ETG, they still struggle to reach a higher precision in the morphological characterization encompassing many classes, with for instance lenticulars not being properly identified (Cheng et al. 2023). In that regard, a very recent work by Domínguez Sánchez et al. (2022) have used deep learning to yield the morphological type of 670,000 SDSS galaxies. On parallel, simulation-based machine learning techniques, that perform massive data transformation and compression while maximizing information using neural networks, also showed to be able to distinguish the statistical properties of ETG and LTG (for example their luminosity functions), hence their different bulge and disk morphologies, directly from deep galaxy fields (Livet et al. 2021).

Deep learning can also be used to infer a set of morphological parameters describing the galaxy rather than a single Hubble type, and in particular, which characterize the profile. For instance, DeepLeGATo (Tuccillo et al. 2018) succeeds in retrieving from galaxy images the full set of parameters of one-component Sérsic models, with similar accuracy as GALFIT, and its extension to more complex models, more specifically bulge and disk decomposition, could be of great value in the exploitation of future surveys.

Chapter 3

Methodology

3.1 Luminosity profile-fitting with SourceXtractor++

SourceXtractor++ (Bertin et al. 2020) is a new open-source software package for detecting and measuring sources in astronomical images, that was developed for the Euclid satellite project. It comes with enhanced performance and new capabilities such as complex priors over SourceXtractor. I have therefore based my thesis work on this tool, and spent the first year of my PhD mastering it while it was still being developed by the team of developers Kümmel et al. (2020), in frequent interaction with that team using the GitHub page of the software[1], on which I reported anomalies and confirmed the need for some useful options. I also developed during that first year the zoom-in approach allowing to reduce the degeneracies in the bulge and disk modeling of nearby galaxy profiles (see Sect. 3.1.2). I wrote python programs and shell scripts to process the data and execute SourceXtractor++ runs via condor on a dedicated computing cluster (called *Morpho*) installed at IAP and maintained by Emmanuel Bertin.

3.1.1 Generalities on the use of SourceXtractor++

The processing of an image by SourceXtractor++[2] is made of the following steps: background estimation, source detection and deblending, isophotal measurement and model-fitting.

To detect sources, the challenge is to identify the pixels corresponding to the galaxy that one wants to model, all of them and them exclusively. To detect sources, it is essential to properly sample the background sky. This requires images that are large enough around the galaxy to contain enough pixels non contaminated by other sources. In my case, I used images centered on each galaxy to be analyzed and resized to 5 $D_{15,g}$, defined as the major diameter in the g band to the elliptical approximation of the galaxy isophote at 1.5σ of the background root-mean-square noise previously measured by my thesis supervisor, Valérie de Lapparent, using SourceXtractor on the EFIGI sample. $D_{15,g}$ was found by V. de Lapparent to be a good match to the $D25$ historical isophotal diameter (defined in Sect. 1.4.3) for the SDSS g images of EFIGI galaxies. For estimating the background, SourceXtractor++ scans the pixel data of the filtered data image (see details below), and estimates the local background in each cell of a square grid through a combination of $\kappa\sigma$ clipping and mode estimation. The choice of the background-cell-size parameter will determine the quality of the produced background map. If it is too small, part of the flux of the most extended sources can be absorbed into the background map, and this issue is particularly important for nearby galaxies with large angular sizes.

We therefore used images of size $5D_{15,g}$ and a background-cell-size of the size of the full image, with this factor of 5 scaling determined by stabilization in the number of pixels of the detected source, identified as the central galaxy, in a sample of EFIGI test objects. Using larger images would have taken more memory and slightly increased computing time for no gain. As many sources stand above the background sky, I used the fact that I knew precisely the central coordinates of the EFIGI galaxies and could then use SourceXtractor++ in association mode once it became available, in April 2021.

[1] https://github.com/astrorama/SourceXtractorPlusPlus
[2] https://sourcextractorplusplus.readthedocs.io/en/latest/

The association mode allows to provide a specific position within the image (here the image center) and a maximal distance, so that sources identified at a further distance are automatically discarded. In the meantime, I used another criterion such as the minimum number of pixels for the source to be accepted, defined empirically as ${D_{15}}^2/20$, hence using the additional information that I was studying galaxies with large apparent diameter.

A major issue remained, which was the contamination by either foreground sources, mostly Milky Way stars, or neighboring galaxies, which are too close for a gap to be visible. However, the contrast parameter of SourceXtractor++ can here be used to detect overlapping sources whose contaminated pixels differ strongly from the rest of the profile. This is particularly effective to remove foreground stars. To deblend neighboring galaxies whose light profile merges with the galaxy of interest in the image, it is possible to reduce the background cell size, which is the mesh size over which the background sky intensity is computed at each location of the filtered image. This leads to a higher background sky estimation and therefore reduce the size of the isophotal print of each galaxy, as the detection isophote level is defined as the contour delineating pixels that are above the local background by 1.5 times the background noise, thus allowing to separate the luminosity profiles. This leads to an underestimation of the central galaxy isophotal flux, but the flux determined by profile fitting is less affected, provided the contamining galaxy overlaps only a fraction of the central galaxy.

Regarding the model-fitting step, the user provides a configuration file in which are specified a list of parameters (see Sect. 3.1.3 for the ones I used), as well as the models to be fitted to the image, which take these parameters as arguments. The parameters are either "free" and therefore vary freely during the fitting procedure aiming at minimizing the distance between the data and model images, while dependent parameter are determined as functions of other parameters. All parameters must be defined, and free parameters are all given an initial value as well as an authorized range of values, in order to ensure that the explored parameter space is finite.

The parameters of the Sérsic model are: x and y positions of the center of the model, a total flux, an effective radius, a Sérsic index, an elongation or aspect ratio characterizing the ellipticity of the profile, and an angle indicating the direction of the semi-major axis. The parameters of the exponential profile are identical, the Sérsic index being excluded as it is fixed to 1 for this profile.

Multiple models can be added by the user to model the light profile within an image. I could have used a de Vaucouleurs profile for the modeling of the bulge, but forcing $n = 4$ means adding a constraint on the modeling, so it remains better to let n vary freely and compare the resulting values with 4. Many bulge and disk decompositions yielded a wide range of Sérsic indexes ($\sim [1; 4]$) for the bulges (Allen et al. 2006; Kim et al. 2016; Gao et al. 2019), which led to a better characterization of the bulge (see Sect. 4.1 and Sect. 5.3 for discussion of Allen et al. 2006 and Fisher & Drory 2008 results respectively, which explain why the use of the de Vaucouleurs profile over Sérsic has become uncommon).

For the model-fitting step, we have made three main runs:

- a single-Sérsic profile to model the whole galaxy
- a bulge and disk decomposition that uses a Sérsic profile for the bulge and an exponential profile for the disk, without priors on their parameters, which we refer to as the "no prior" method ("np")
- a similar bulge and disk decomposition, with priors to reduce the degeneracies between both components (see Sect. 3.1.2), which we refer to as the "with priors" method ("np")

All of them are applied to the 5 $D_{15,g}$ images centered on each EFIGI galaxy, using a 9x9 gaussian convolution mask of a with a 5 pixel full width half maximum (FWHM) filtering (this 2D convolution operator is used to "blur" images, hence removes details and noise). The identification of the source is made on the g band image while the model-fitting is done simultaneously on the g, r and i band images, with the associated weight maps and PSF files.

The PSF was calculated prior to the start of my thesis by my supervisor Valérie de Lapparent using PSFex on a sufficient number of stars around each of the 4458 EFIGI galaxy and in the 5 *ugriz* bands. The PSF in each band is provided to SourceXtractor++ with each image in the same band, in order to be convolved with the model before computing the distance to the data image during the

model-fitting process. Because 77% of the EFIGI galaxies have $D_{15} \geq 1$ arcminute (and 90% and 99% are above 0.8 and 0.5 arcmin, respectively), the PSF has little impact except in the central parts of steep profiles, and for texture (HII regions, dust) on scales on the order of the seeing of the SDSS images ($\sim$ 1.3 arcsec FWHM).

3.1.2 Defining the priors for the model-fitting

A new capability introduced by SourceXtractor++ compared to its predecessor is the use of priors. In this section I present the priors used to improve the model-fitting, the methodology to determine them, and finally evaluate their impact on the measure of bulge and disk parameters.

The aim of the priors we developed is to ensure that the Sérsic profile for the bulge component in the bulge and disk decomposition does actually model the bulge. A galaxy bulge is defined for disk galaxies as the central concentration of light surrounded by the disk, and/or common disk features such as spiral arms, bars, rings. On a test sample of 100 lenticular and spiral galaxies, we found that this can be achieved by choosing adequate starting values and limiting the range of possible bulge parameter values. The presence of a central bar for nearly half of spiral and lenticular galaxies (de Lapparent et al. 2011, more specifically 70% of S0 and 40% of spirals) can lead to the Sérsic model designed to fit the bulge to actually fit both the bulge and the bar. Examples are shown in Fig. 3.8. In these cases, the aspect ratio is significantly larger than that of the bulge, and the effective radius is overestimated by a factor of 3 to 6. Foreground sources, significant amounts of visible dust for inclined galaxies, and inner rings are other features that can bias the bulge measured in a bulge and disk decomposition.

3.1.2-a Zoom-in procedure

In order to obtain adequate values to be used as priors of the bulge parameters, we had the idea of developing a zoom-in procedure that takes advantage of the high resolution of the EFIGI images to model the bulge only, and then use the output of this model for the galaxy model-fitting as the sum of a bulge and a disk. When zooming into the bulge, several small scale structures as the internal parts of the bar, of spiral arms, nuclear rings, HII regions etc., complicate the determination of a pseudo-background above which one would like to detect the bulge and only it, in order to model it. These small scale structures are different from a bulge because they are more diffuse. They can be modeled by using a background mesh size comparable to their typical angular size. We found that calculating the isophotal size of the bulge detected at 2.5σ above a background modeled with an initial mesh size of 2 pixels, then iterating with MeshSize $= \sqrt{A}/2$, with A the isophotal area, would succeed in a few iterations to partition the object from the spurious neighboring structures, and to allow its modeling with minimal contamination, using a Sérsic profile (see Fig. 3.1). This process was first tested and its parameters empirically defined on a sample of 100 spiral and lenticular galaxies with `Inclination`≤ 2, `Contamination`≤ 1 and `Multiplicity`≤ 1, then applied to the full EFIGI sample.

The bulge zoom-in procedure applied to all galaxies was the following:

1. I create zoomed-in images of the galaxy bulge by cropping the initial galaxy image around its center and fixing a new size of $2\lfloor\frac{0.25(a+b)}{2}\rfloor$ where a and b are the isophotal major and minor axis diameters of the full galaxy, respectively; the 2 factors are here to ensure an even number of pixels as the center of the image is located at the corner of 4 pixels. I examine the images to make sure that our objective of framing the whole bulge and a part of the disk was fulfilled (for very inclined galaxies, this inevitably includes some sky background on each side of the disk).

2. I apply the iterative process described above to determine the adequate bulge "background" measured on the disk and in the resulting background subtracted image of the bulge, I perform an isophotal analysis and then a luminosity model-fitting of the created image, using a Sérsic profile.

3. I create another zoomed-in image of the bulge using this time a_b and b_b, the isophotal major and minor axes diameters of the bulge, respectively, with image size $2\lfloor\frac{5(a_b+b_b)}{2}\rfloor$, in order to ensure that the bulge background determination and profile fitting are performed in similar conditions

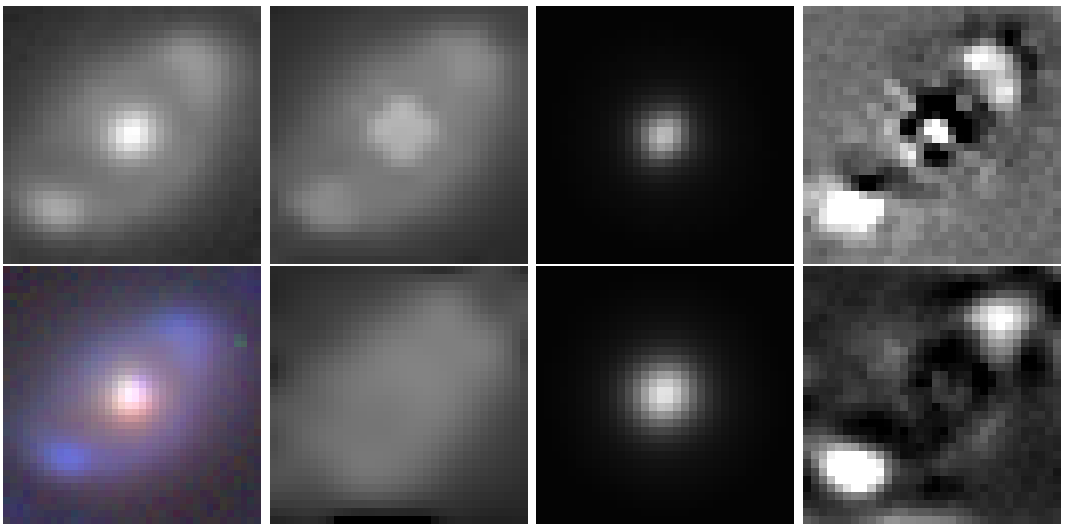

Figure 3.1: Zoom-in bulge modeling of PGC0054039. Left column: g-band data image (top) and gri composite color image (bottom). From left to right: background estimation, model-fitting and residual of the bulge for a meshsize of 2 and 4 pixels for the top and bottom rows, respectively. The iteration starts with a meshsize of 2 pixels, which gives a poor modeling of the bulge, as its profile is included in the background map. The loop on the meshsize stops at 4 pixels, which yields a satisfying modeling, as seen in the residual map: the bulge has almost completely disappeared.

for all bulges. I examined these new images and especially those that had different sizes from the previous step, and noticed the use of this improved zoom level in particular for galaxy with prominent bulges that, with the zoom level in step1, occupied too many pixels of the sub-image to allow a background determination.

4. I repeat the step 2 on the image created in step 3.

I performed some checks on the success of the zoomed-in bulge fits in the g band, by analyzing the sets of measures for the bulge that I had obtained at the end of the process, but also comparing it to the intermediate measurements done at the second step. In order to make sure that the zoom-in bulge modeling is functional, I defined warning flags of the cases that were most likely to provide incoherent values, as follows:

- a B/T value is computed by dividing the flux of the second bulge model by the isophotal flux of the galaxy. If it is below 0.005, it is flagged as too low for a bulge to be measured;

- the mean values $\overline{B/T}$ and r.m.s. standard deviations σ of the quantitative B/T are computed for 5 sub-samples of EFIGI corresponding to each of the 5 levels of the visually classified `B/T` attribute. If a galaxy B/T deviates by more than 3σ away from the mean for its `B/T` value, it is flagged as an outlier;

- if the aspect ratio of the bulge profile is below 0.25, it is flagged as too eccentric to correspond to a bulge;

- if between the two bulge profiles modeled, either the Sérsic index, the effective radius, the flux level or the aspect ratio, varies by more than 100%, the bulge is flagged;

- the distance between the center of the bulge and disk profile and the center of the image is computed and compared to the mean offset (~ 0) using the associated r.m.s. standard deviation, that are computed over all EFIGI galaxies. If the distance offset of a galaxy is higher than 3 times the r.m.s. deviation, the light profile is flagged as it may differ from the bulge zoom-in profile;

We then visually examined the zoom-in bulge modeling of all the flagged objects, as well as a random sub-sample of ~ 100 non-flagged galaxies, and a posteriori verified that the bulge zoom-in process was reaching its goal of appropriately modeling the bulge when feasible. Due to disk inclination, absence of bulge (for very late-type spiral galaxies), or contamination by foreground sources, the automatic detection of a bulge in the zoom-in procedure is sometimes not possible and we ensure that the flag levels did include these cases, whereas moderately inclined spirals and lenticulars, as well as elliptical galaxies, would be properly treated. For the barred galaxies among these objects, we verified that this process succeeds in measuring the bulge radius and aspect ratio with a limited impact from the bar (see Fig. 3.6).

The described bulge process is then repeated in all three g, r, i bands with satisfying signal-to-noise ratio, and the median values of the second bulge model are computed in order to be used as priors for the subsequent bulge and disk decomposition. We denote them as $p_{\rm prior} = median(p_g, p_r, p_i)$ for p being any parameter of the Sérsic function.

3.1.2-b Gaussian priors for consistency between bands

Another set of priors aims at making the simultaneous multi-band fitting coherent across the different observing bands. This takes the form of a Gaussian prior between the r and i bands in reference to the g band, the most sensitive of the three in the SDSS (the combination of filter transmission and exposure time yields the deepest images compared to the other bands).

These band-to-band priors are mainly set up with the intent that the bulge and disk models are coherent between the different filters, while taking into account the different distributions of stellar populations of different ages within galaxies, as these emit light at shifted wavelengths. Forcing the same bulge or disk parameters in different bands is not realistic, but letting them completely free would lead to incoherent component modeling (see Sect. 3.1.4 and Fig. 3.8). Gaussian band-to-band priors therefore contribute to yield reliable color gradients for the bulges and disks that are discussed in Chap. 6. From these measurements, I confirm that the ratios of effective radii between bands systematically differ from unity by $\lesssim 20\%$ for bulges and $\lesssim 10\%$ for disks, hence validating a posteriori the 0.1 r.m.s. deviation in these priors (see Tab. 3.1). However, for studies involving more bands over a larger wavelength coverage, applying the priors between subsequent bands, rather than compared to a reference band, could be another method to ensure color consistency. To keep using g as a reference band and applying priors to UV or IR bands for instance could require to measure the color gradients, in order to shift the peak value of the Gaussian at the actual ratio of the parameters if it deviates significantly from 1.

The set of priors we applied in the simultaneous multi-band model-fitting is listed in Tab. 3.1.

Parameter [unit]	Value expected to be of zero-mean	σ
Bulge position x_B [pixels] (same for y_B)	$x_{B1} - x_{B2}$	0.3
Effective radius (both bulge and disk) [pixels]	$\log(R_{e1}/R_{e2})$	0.1
Aspect ratio (both bulge and disk)	$\log((b/a)_1/(b/a)_2)$	0.1
Position angle of the major axis (both bulge and disk)	$\theta_1 - \theta_2$	$5/2\pi$
Sérsic index	$n_1 - n_2$	0.1

Table 3.1: Gaussian priors applied in the bulge and disk decomposition between the g band (used as reference and denoted by the 1 index) and both the r and i bands (denoted by the 2 index).

3.1.3 Configuration of the different model-fitting methods

In Sect. 3.1.2-a, I obtained estimations of the bulge parameters, which I used as priors when performing the bulge and disk decomposition, in which the Sérsic profile intended to model the bulge is defined with the starting values and ranges presented in Tab. 3.2.

To evaluate the interest of the bulge zoom-in and band-to-band priors, I also performed for each galaxy a model-fitting with no such prior. The initial values as well as the bounds still must be set up for the bulge parameters, they are listed in Tab. 3.3.

Regarding the disk priors, the exponential profile and the same parameter setup is used for the runs with the full set of priors, and those without. The initial values and boundaries are listed in Tab. 3.4.

Note that for both bulge and disk decomposition, the total flux f is defined using the built-in function `get_flux_parameter` that takes as initial value the isophotal flux and bounds it by factors of 10^{-3} and 10^{3}. Two dependent parameters $flux_B$ and $flux_D$ are created for the Sérsic and exponential profiles respectively and are defined as $flux_B = B/T * f$ and $flux_D = (1 - B/T) * f$, with f and B/T simultaneously fitted with the bulge and disk profiles by SourceXtractor++.

Finally, I also performed on all galaxies a single Sérsic profile model-fitting using the parameters values listed in Tab. 3.5. The flux is here simply defined by the built-in function `get_flux_parameter`. The Gaussian priors between bands presented in Sect. 3.1.2-b and Table 3.1 are also used in these runs. The results of these runs are useful for E and Im galaxies (see Sect. 5.3).

3.1.4 Comparison between runs

To measure the improvements brought by the simultaneous bulge zoom-in and band-to-band priors, we compare the parameters of the fitted models for the bulge and disk decompositions, with and without priors respectively. In this section, all results are based on the sample of EFIGI spiral and lenticular galaxies (types S0$^-$ to Sm) with `Inclination`≤ 2, because they are the galaxies for which the bulge prior setup procedure was extensively tested on (see Sect. 3.1.5 for discussing the perspectives of running it on inclined galaxies).

3.1.4-a Consistency between bands

We start by assessing independently the results of both modeling methods by examining their consistency between bands. One expects that the values of bulge and disk parameters slightly change between subsequent bands, I therefore added Gaussian prior to help ensure this in the run with priors (see Sect. 3.1.2). In that regard, I compute the median value between the g, r and i bands and the deviations between each band value and this median for the effective radii and magnitudes of both bulges and disks, as well as the B/T ratio, (the deviations are therefore differences for magnitudes and the logarithm of the ratio for the other quantities). I then compute the mean deviation associated r.m.s. dispersion σ for the EFIGI sample defined above, and flag values (for each band and each parameter examined) that deviate more than 3σ away from the mean. A galaxy model is then considered as band-to-band coherent if none of its parameters is flagged. I emphasize that such criterion is used throughout the following analyses, except that the B/T parameter is excluded, as another method to identify inconsistent bulges is presented in Sect. 4.3.1 of Quilley & de Lapparent (2022) using the flux of the bulge measured in the zoom-in procedure (see Sect. 3.1.1).

This verification process allow us to put aside inconsistent fits, while already advocating in favor of the modeling with priors, as 89.9% of the galaxies have band-to-band coherent models with this method against 85.2%. Removing the galaxies contaminated by a foreground source or a neighboring galaxy, i.e. applying the conditions `Contamination`≤ 1 and `Multiplicity`≤ 1, lead to even higher success rates of 91.7% and 86.2%, with and without priors respectively, as these effects may impact the fits differently in different bands.

3.1.4-b Comparison of the fitted parameters before and after adding priors

I now further compare the "np" and "wp" fits (for "no prior" and "with priors", respectively). To this end, we limit the sample to the 2022 spiral and lenticular EFIGI galaxies with low-inclination (`Inclination`≤ 2) whose modeling is band-to-band consistent in both methods in order to compare the results of fits that seem successful.

A first important thing to note is that the total galaxy magnitude is weakly affected by the use of priors, it is the decomposition of the total light into bulge and disk components that is at stake. Indeed, left panel of Fig. 3.2 shows the difference in the g magnitudes between the two methods for

Bulge zoom-in priors

Parameter [unit]	Range Type	Initial value	Lower limit	Upper limit
B/T	Exponential	0.5	0.001	1.0
Position x and y [pixels]	Linear	$x_{\rm prior}$	$x_{\rm prior} - 5$	$x_{\rm prior} + 5$
Effective radius [pixels]	Exponential	$R_{e\rm prior}$	$R_{e\rm prior}/3$	$3R_{e\rm prior}$
Aspect ratio	Exponential	$(b/a)_{\rm prior}$	$0.9(b/a)_{\rm prior}$	$1.1(b/a)_{\rm prior}$
Position angle [radians]	Linear	`o.get_angle()`$^{(a)}$	$-\pi/2$	$\pi/2$
Sérsic index	Linear	$n_{\rm prior}$	$min(0.4, n_{\rm prior} - 1)$	$n_{\rm prior} + 1$

Table 3.2: Free parameters defining the Sérsic model component in the bulge and disk decomposition using the bulge priors from the zoom-in procedure (see Sect. 3.1.2-a).

Bulge modeling parameters without priors

Parameter [unit]	Range Type	Initial value	Lower limit	Upper limit
B/T	Exponential	0.5	0.001	1.0
Position x and y [pixels]	Linear	`get_pos_parameters()`$^{(a)}$		
Effective radius [pixels]	Exponential	3	0.1	100
Aspect ratio	Exponential	1	0.1	10
Position angle [radians]	Linear	`o.get_angle()`$^{(a)}$	$-\pi/2$	$\pi/2$
Sérsic index	Linear	4	0.5	10

Table 3.3: Free parameters defining the Sérsic model component in the bulge and disk decomposition that do not use the priors derived in the zoom-in procedure.

Disk modeling parameters

Parameter [unit]	Range Type	Initial value	Lower limit	Upper limit
Position x and y [pixels]	Linear	`get_pos_parameters()`		
Effective radius [pixels]	Exponential	`o.get_radius()`$^{(a)}$	0.1 `o.get_radius()`	10 `o.get_radius()`
Aspect ratio	Exponential	`o.get_aspect_ratio()`$^{(a)}$	0.5 `o.get_aspect_ratio()`	2 `o.get_aspect_ratio()`
Position angle [radians]	Linear	`o.get_angle()`	$-\pi/2$	$\pi/2$

Table 3.4: Free parameters defining the exponential model component in both methods of bulge and disk decomposition.

Single-Sérsic profile modeling parameters

Parameter [unit]	Range Type	Initial value	Lower limit	Upper limit
Position x and y [pixels]	Linear	`get_pos_parameters()`		
Effective radius [pixels]	Exponential	`o.get_radius()`	0.1 `o.get_radius()`	10 `o.get_radius()`
Aspect	Exponential	1	0.1	10
Angle [radians]	Linear	`o.get_angle()`	$-\pi/2$	$\pi/2$
Sérsic index	Linear	4	0.1	10

Table 3.5: Free parameters defining the Sérsic profile in the single profile model-fitting.

Note:

(a) SourceXtractor++ built-in functions `get_pos_parameters`, `o.get_radius`, `o.get_aspect_ratio`, `o.get_angle` are all based on the isophotal analysis of the objects. `get_pos_parameters` return a free parameter initialized at its center coordinates and linearly limited to ± its major axis radius. The functions with the `o` prefix respectively return the values of its major axis radius, its aspect ratio, and the angle between the direction of the major axis of the isophotal profile and the x-axis in the $[-\pi/2; \pi/2]$ interval.

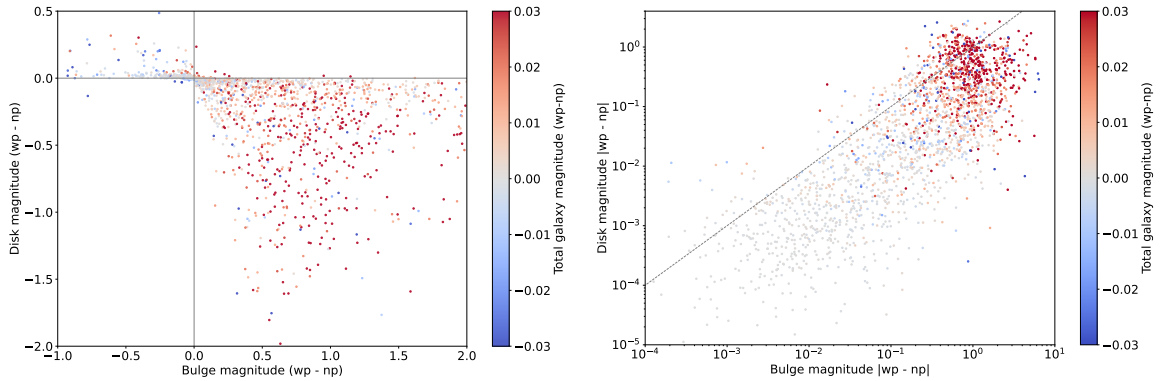

Figure 3.2: Difference between the two modeling methods for the disk magnitudes versus for the bulge magnitudes, in linear (left) and logarithmic scale of the absolute value (right), color-coded by the difference in total galaxy magnitude.

the disk versus the bulge, color-coded with the difference in the total galaxy magnitude: bulge and disk magnitudes can vary by several magnitudes whereas the galaxy magnitude remains stable, with a mean difference of 0.005 and associated dispersion of 0.011 over the sub-sample of 2022 galaxies. The difference of the bulge magnitudes has a mean value of 0.48 and a r.m.s. dispersion of 0.87, whereas for the difference in disk magnitudes, the mean is -0.19 and the dispersion is 0.39. Therefore, bulge magnitudes tend to be overestimated, and disk magnitudes underestimated without priors. Indeed, 70% of the galaxies have a brighter bulge and a fainter disk without prior than with them, and there is a factor of ~ 10 larger flux ratio for bulges than for disks when considering the absolute values (see right panel of Fig. 3.2).

The fact that the bulge profile is more affected than that of the disk by the degeneracy in the absence of bulge zoom-in priors also reflects in the effective radii. The right panel of Fig. 3.3 shows an overall stability of the disk radii, whereas strong variations for the bulge radii are observed in the left panel of Fig. 3.3. Both panels present the ratio of the effective radii between the two modeling methods, for the bulge (left) and disk (right), as a function of the value derived with priors, and color-coded with the B/T value also obtained with priors. The stability of the disk radii is such that 50% of the sample exhibit ratios in the interval $[0.95; 1.01]$ and 90% in the interval $[0.71; 1.32]$. This distribution has a geometric mean of 0.99, a median at 1.00 and a dispersion of 0.13 dex. We also note that deviating points always correspond to high values of B/T, meaning that a strong bulge is needed to disrupt the disk profile measure. For the bulge radii, the situation is completely different with large discrepancies between the effective radii returned by the two methods. The prior-less modeling tends to return values systematically higher than the ones using priors, with 42% of the bulge radii being overestimated by a factor of 2, against only 3% for which it is underestimated by the same factor. The overestimation by the prior-less method is even above a factor of 10 for 11% of objects. The diagonal line that appears in this plot is the result of the bulge effective radii hitting the maximal value of the available range, which is set at 100 pixels.

The larger bulge profiles of the prior-less method also correspond to larger amount of fluxes assigned to the bulge than to the disk, as seen in Fig. 3.2. The overestimation of the bulge flux in the prior-less approach impacts the measure of the B/T ratio that is one of the major parameter for characterizing the morphological evolution of galaxies, as shown in this thesis. Left panel of Fig. 3.4 shows the comparison between the derived B/T for both methods, color-coded by the EFIGI visual attribute `B/T`, that helps us here in identifying wrong B/T measurements. Indeed, the 173 galaxies (8.6%) visually classified with `B/T`≤ 1 and having $B/T < 0.1$ with priors but $B/T > 0.1$ without priors are wrong overestimates, for which the addition of prior lead to a correction. This systematic overestimation is such that adding priors decreases on average the measured B/T by a factor of 0.65. We can also focus on specific regions of the left panel of Fig. 3.4, with for instance the galaxies visually classified with prominent bulges (`B/T`=3 or 4) and notice that the overestimation by the prior-less method yields B/T values over 0.8, which are not expected for lenticular or spiral galaxies. The right panel of Fig. 3.4 presents

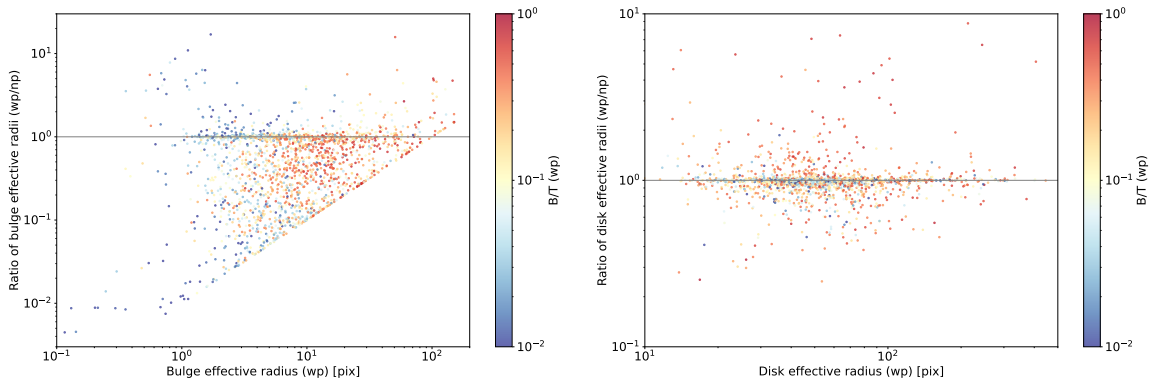

Figure 3.3: Ratio between the effective radii of the two modeling methods ("wp" for "with priors" divided by "np" for "no prior") as a function of the value obtained with priors, for the bulge (left) and disk (right) components. Adding priors leads to smaller bulge effective radii, whereas disk effective radii are overall stable.

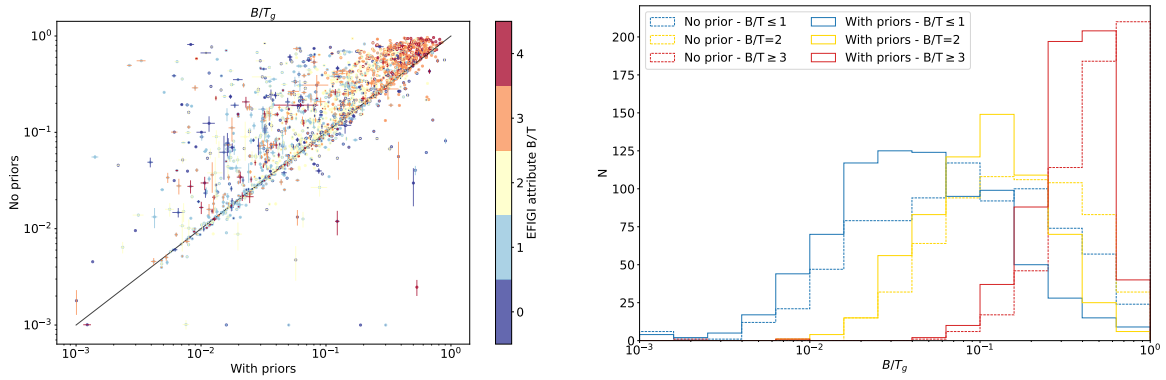

Figure 3.4: **Left:** Comparison between the B/T values measured with both methods of the bulge and disk decomposition, color-coded by the EFIGI visual attribute `B/T`. **Right:** Histograms of the B/T values measured for each method, separated according to classes of the `B/T` attribute values. There is a systematic overestimation of the B/T when no prior is used.

the distributions of the measured B/T for each method for different classes of the EFIGI attribute `B/T`. We do see that for `B/T`=3 or 4, the measured B/T peaks either at $\gtrsim 0.7$ or at ~ 0.4 without and with priors respectively, so the addition of priors lead to a better agreement with previous studies (Kim et al. 2016; Gao et al. 2019). For lower values of the visual `B/T`, the tail of measured B/T above 0.5 without priors is equally concerning and points towards wrong measurements.

Furthermore, this discrepancy between the bulges measured by the two modeling methods also appears when comparing the obtained Sérsic indexes. Indeed, left panel of Fig. 3.5 shows that the Sérsic indexes are overestimated without the use of priors. The Sérsic index seems to be a more volatile parameter as larger discrepancies are seen here, that do not follow any trend and appear as dispersion. The difference between the prior and prior-less case has a mean value of -1.66, a median of -0.57, and a dispersion of 2.64. Bulges are supposed to stand out from the disk exponential profile, hence to have $n \geq 1$, but have been shown to have lower Sérsic indexes than E galaxies, whose standard value is often considered to be $n = 4$, as in the de Vaucouleurs profile (Fisher & Drory 2008; Kim et al. 2016; Gao et al. 2019). Regarding the most prominent bulges that are supposed to have the highest Sérsic indexes, left panel of Fig. 3.5 shows that EFIGI galaxies with a visual attribute `B/T`≥ 3 have Sérsic indexes mainly in the $[2; 5]$ and $[2; 10]$ intervals, with and without priors respectively. This large tail of high n for the prior-less modeling is also seen in the right panel of Fig. 3.5, that presents the distribution of the Sérsic indexes for both methods, for two ranges of B/T values, in order to isolate very faint bulges whose measure is more difficult. For these objects (dashed lines), the distribution peaks at the lower bound values and sharply decrease for larger Sérsic indexes, with a secondary peak

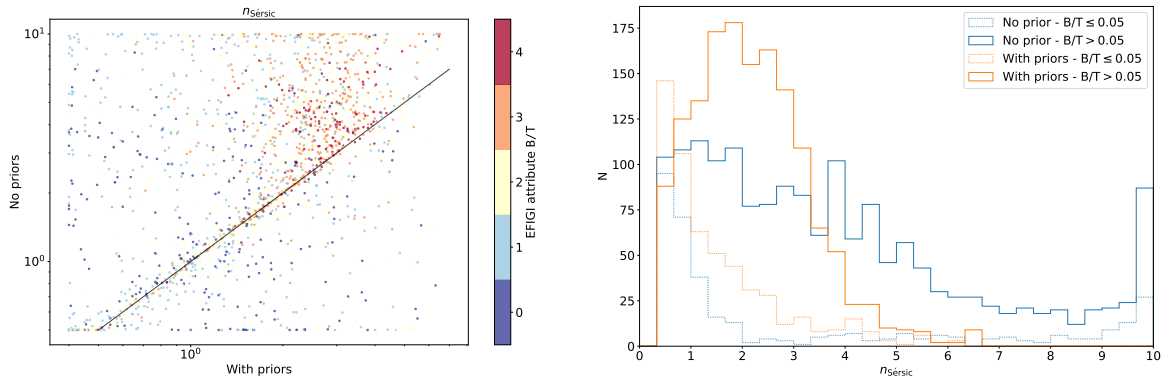

Figure 3.5: **Left:** Comparison between the $n_{\text{Sérsic}}$ indexes measured with both modeling methods, color-coded by the EFIGI attribute `B/T`. **Right:** Histograms of the Sérsic indexes measured for each method, for sub-samples depending on the B/T value measured for the same model. There is a systematic overestimation of $n_{\text{Sérsic}}$ when no prior is used.

at the upper bound for the np method. For the bulges with $B/T > 0.05$ that are supposed to be more properly modeled, there is a strong discrepancy between the two modeling methods, with values spanning the whole $[0.5; 10]$ interval, with a slowly decreasing fraction towards higher indexes and a peak at the higher bound, whereas the distribution of n obtained with priors peaks around 2.

We specifically examine the cases in which, without the bulge zoom-in priors, the bar is taken into account and biases the bulge modeled by the Sérsic profile. We examine in Fig. 3.6 the ratio between the effective radii with the two methods, as in the left panel of Fig. 3.3, but as a function of the ratio between the effective radius calculated with priors, and the D_{15} which estimates galaxy full size; points are color-coded with the `Bar` attribute (estimating the bar length). I measured an overall trend of more frequent over-estimations of the bulge prior-less radii for increasing `Bar` attribute values. Indeed, for $R_e/D_{15} < 0.1$, the fraction of bulges for which the ratio of effective radii is below 0.7 is $50.4 \pm 3.1\%$, $49.7 \pm 4.7\%$, $46.9 \pm 4.6\%$, $62.8 \pm 6.9\%$, $70.0 \pm 12.2\%$ for `Bar` attribute values of 0, 1, 2, 3, 4, respectively. Therefore, when a long bar and a small bulge are coexisting in a galaxy, there is more often over-estimation of the bulge radius than when no bar is present, which is explained by the fact that the bar biases the bulge model making it very elongated, as seen in Fig. 3.8. This effect might be stronger if we could also take into account the relative bar and bulge fluxes, in addition to their sizes.

When examining in more detail Fig. 3.6, one can see that for bulges smaller than $R_e/D_{15} \lesssim 0.5$, there is a large fraction of galaxies with none or very small bars (`Bar`≤ 1) for which the effective bulge wp/np radii ratio is ~ 1, and a tail of overestimated prior-less bulge radii up to a factor of more than 10; intermediate barred galaxies with `Bar`$= 2$ cover the whole range of wp/np radii ratio, from 1 to below 10^{-1}; in contrast, long barred galaxies with `Bar`≥ 3 predominantly have overestimated prior-less bulge radii. For bulges in the overlapping $0.4 \lesssim R_e/D_{15} \lesssim 0.8$ interval, galaxies with bars of all lengths have a nearly flat distribution of bulge wp/np radii ratio at a value of 1 and below, hence a large fraction of prior-less radii are overestimated by a factor from 1 to ~ 15. For larger bulges with $R_e/D_{15} \gtrsim 0.8$, a large fraction of the long bars `Bar`≥ 3 show similar values of the prior-less and with-prior radii, probably because the bulges are so dominant that the bar is a weaker perturbation to their profile. This analysis therefore demonstrates that the zoom-in bulge prior succeeds in many cases in avoiding the degeneracies in the bulge fit that naive bulge and disk decomposition may suffer due to the presence of a bar. The inclusion of a bar component would in principle be preferable, but this represents a technical challenge (see Sect. 6.2).

We have therefore quantified the differences between the bulge and disk decomposition with and without the bulge zoom-in priors, and shown that without them, there is a systematic overestimation of the bulge effective radius, total flux, and bulge-to-total ratio. This is due to the fact that more light than the actual bulge profile is taken into account by the model, for instance by including a bar as well (see Fig. 3.8). Priors provide a priori information about the bulge identification and properties, therefore allow us to avoid many cases of degeneracies. Typical examples of prior-less model-fitting

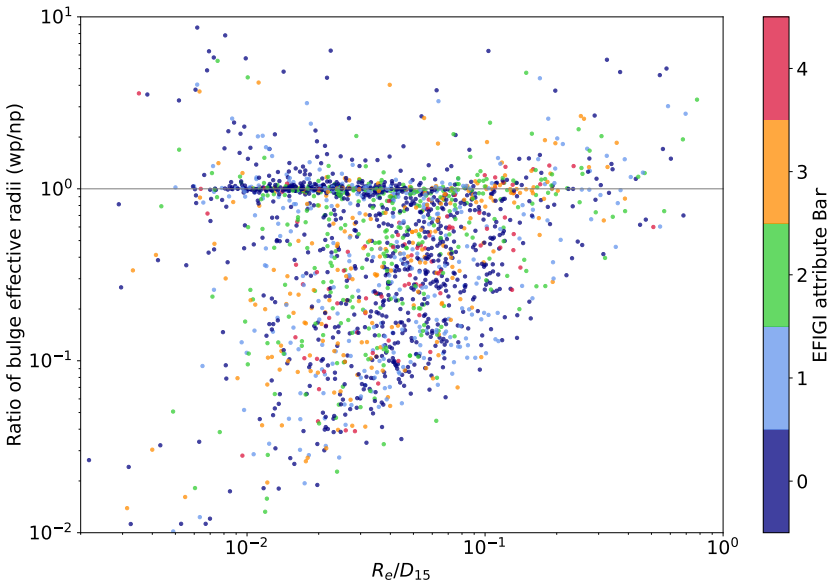

Figure 3.6: Ratio between the effective radii of the two modeling methods as a function of the ratio between the bulge and galaxy sizes, defined as the effective radii with priors and the $D15$ respectively. The color of the points represent the EFIGI `Bar` attribute which estimates the length of the bar compared to the galaxy size. For small bulges measured with the bulge zoom-in priors, there is a higher fraction of small ratios, hence over-estimations without these priors, for long bars, indicating that those are modeled instead of the bar, or at least bias the bulge model.

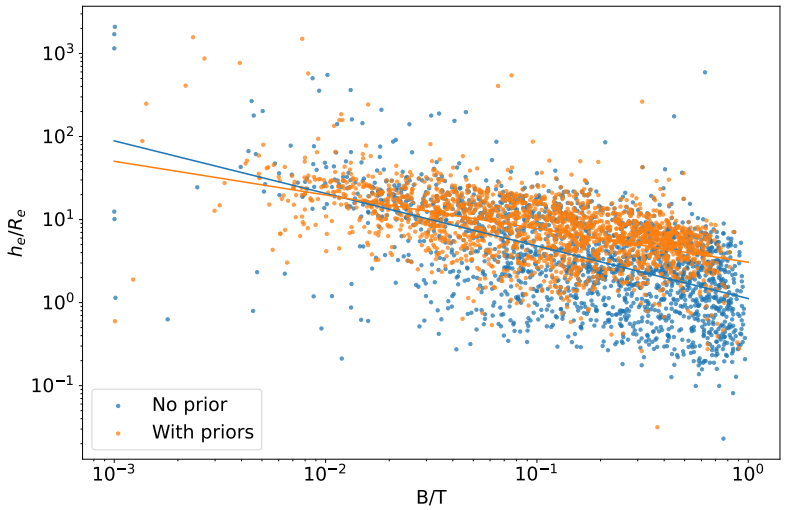

Figure 3.7: Ratio of the disk and bulge effective radii as a function of the B/T ratio, for both modeling methods. The results of the model-fitting with priors allow to derive a power-law between these size and luminosity ratios (see Chap. 5.3). Without priors the many galaxies with a disk effective radius smaller than their bulge effective radius drive the relation downwards and add dispersion.

in which the bulge modeling appears to fail for various reasons are shown in Fig. 3.8, along with the successful bulge and disk decomposition performed thanks to the use of priors.

We also provide in Fig. 3.7 the example of one of the graphs that appears in Quilley & de Lapparent (2023, see Sect. 5.3), and shows the ratio of the disk and bulge effective radii as a function of B/T, for both modeling methods, in order to illustrate how the results regarding the physical characterization of galaxies that are obtained in this thesis would have been impacted by a naive bulge and disk

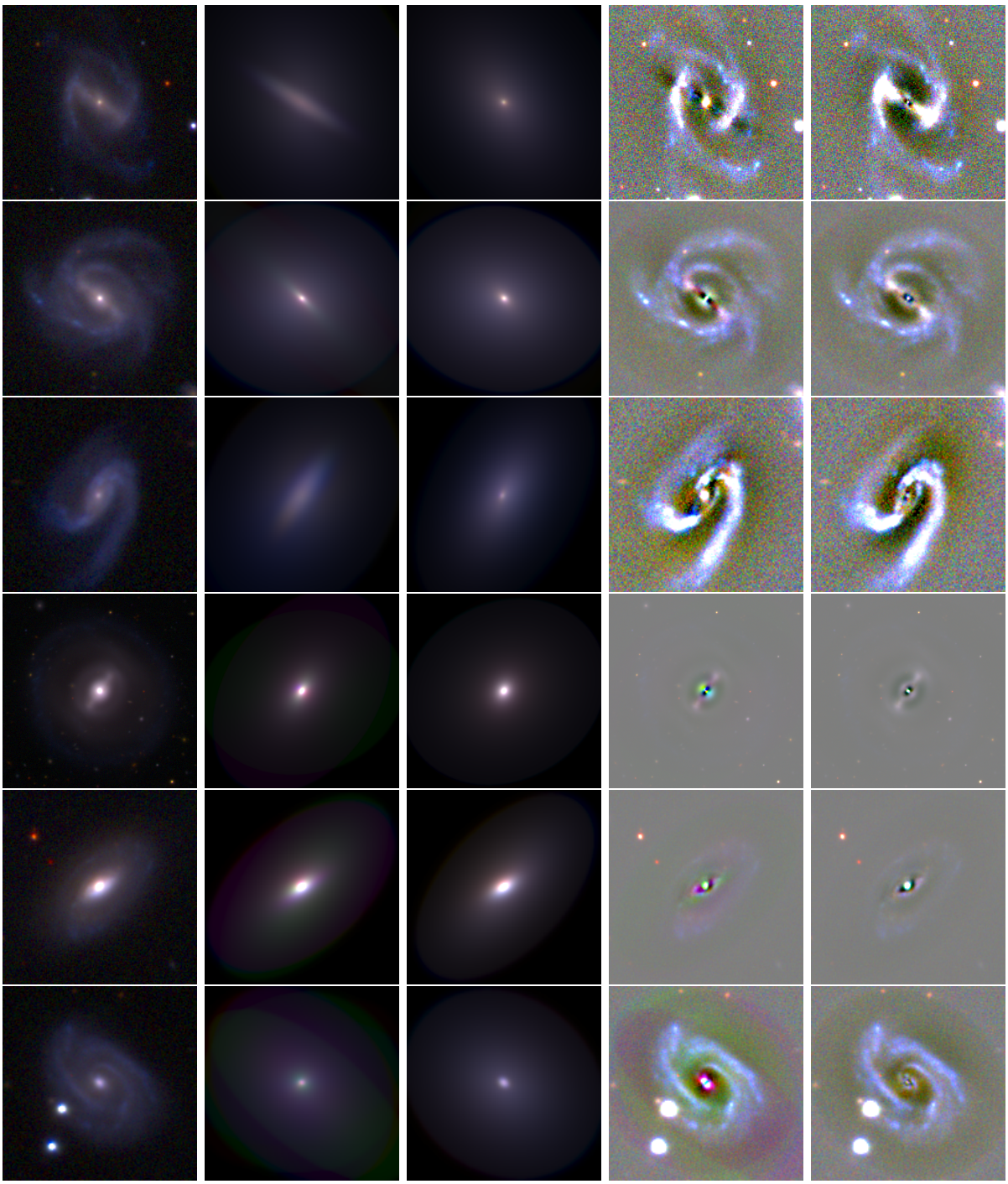

Figure 3.8: Examples of galaxies for which the addition of prior correct the luminosity profile-fitting. Each line represents a different galaxy, with from left to right the data image, the model images without and with priors, and the associated residual images. Typical issues were chosen to illustrate the variety of cases in which our use of prior brings improved accuracy in the modeling. From top to bottom: PGC0020886 and PGC0043288 are examples of barred galaxy where the bulge prior allows to model the bulge instead of the bar; for PGC0035964, the prior-less model fits the central lens-shaped low surface brightness region delineated by the spiral arms, but fails to fit the much smaller bulge within it; PGC0011670, PGC0022314 and PGC0036187 are examples of fits inconsistent between bands that are corrected by the use of priors. Note also that the successful model fits reproduce the color gradient from red in the part of the disk seen above the bulge, to blue on the opposite side, that is seen in the data image of PGC0022314, and is probably due to dust.

decomposition. Indeed, the power-law exhibited between the size and luminosity ratios, which is an unprecedented result derived in this thesis, shows a steeper exponent, with a difference of 0.23, hence 9σ, between the slopes of the two linear regressions performed in log-log scale. Moreover, the root mean square dispersion around these fits is 45% larger without the bulge zoom-in priors. The predicted ratio between bulge and disk radii at high values of B/T would be underestimated due to the presence of 391 galaxies with a bulge effective radius larger than that of their disk, against only 38 such galaxies using the bulge priors. Therefore, without the use of priors the results that are described in this thesis would be significantly affected, in particular the size-luminosity relations, and the mock distributions that could be generated from them would be biased.

3.1.5 Future improvements

3.1.5-a Addition of u and z bands

We limited ourselves to the simultaneous model-fitting of the g, r and i images, but data was available in the u and z bands as well. This choice was motivated by the fact that in these bands the images are noisier, thus jeopardizing a joint multi-band profile fitting. But going forward, I could model them separately, by also using the zoom-in bulge priors determined in the gri bands and applying them to the bulge and disk decomposition of the u and z images, without activating the band-to-band Gaussian priors. We would have to assess the reliability of the derived bulge and disk parameters. However, the total magnitudes would likely be robust, as they are here proven to be less impacted than other morphological parameters by the intricacies of the profile-fitting procedure, and will be of value for the SED-fitting step (see Sect. 3.3).

3.1.5-b Fitting inner truncated disk profiles

With the release of the 0.16 the version of SourceXtractor++ was introduced the use of ad hoc models. This means that in addition to the point-source, Sérsic and exponential profiles already provided by the software, any user can create a model based on a function of his choice, thus allowing more flexibility in the model-fitting.

I took advantage of this functionality to test the use of truncated disk profiles. Indeed, it is a physically motivated hypothesis to consider that within the bulge region, the layout of stars are different than from the disk and orbits are rearranged, hence disrupting the exponentiality of the disk profile. This argument is more appropriate for classical bulges which are pressure supported system with random orbits, while for disky pseudo-bulges, the disk profile could remain, with an added central density constituting the bulge (Sect. 2.1.1 and Sect. 5.3). Baggett et al. (1998) performed bulge and disk decomposition on 659 spiral and lenticular galaxies using the inner truncated exponential function introduced by Kormendy (1977b):

$$I_D(r) = I_0 \exp\left\{-\left[\frac{r}{r_0} + \left(\frac{r_\mathrm{h}}{r}\right)^{n_\mathrm{h}}\right]\right\} \tag{3.1}$$

where r_h is the radius of the central cutoff of the disk (or "hole" radius), which is expected to be similar to the bulge radius, and n_h defines the steepness of this cutoff. We note that we retrieve the exponential profile for $r_\mathrm{h} = 0$. The fits are made on the major axis cut, so a lot of information is lost from the full image. Baggett et al. (1998) adopted $n_\mathrm{h} = 3$, following the results of Kormendy (1977b) and used a de Vaucouleurs profile (i.e. a Sérsic profile with $n_\mathrm{Sérsic} = 4$) for the bulge and found that for 25% of the successfully fitted galaxies (156 out of 620), the inner truncation provided a better fit, with a more than 10% improvement on the weighted r.m.s. Similarly, Anderson et al. (2004) found that the inner truncated disks allowed for better bulge and disk decomposition for 28% of its sample of 218 spiral and lenticular galaxies. More recently, Breda et al. (2020) also questioned the validity of the exponentiality of disk profiles, using integral field spectroscopy to show that removing a purely exponential disk lead to unphysical bulge spectra for up to 30% objects, while that issue could be circumvented by having centrally decreasing disk profile. In these studies, only a minority of the galaxies are better fitted with an inner truncation, and no explanation is given as to why some galaxies would maintain their disk dynamics and the associated profile within the bulge, while other would not.

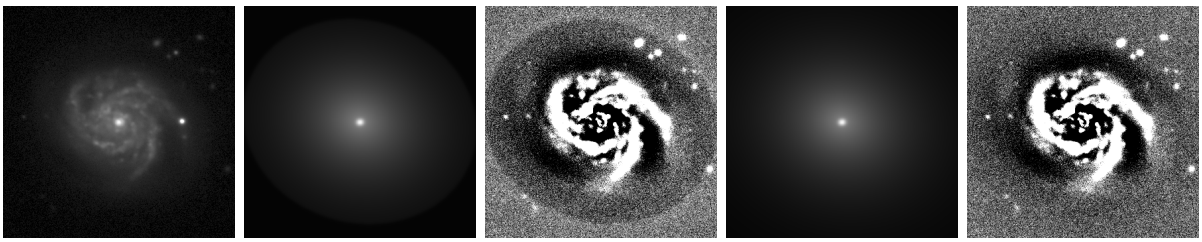

Figure 3.9: From left to right: g-band data image, model-fitting and residual of PGC0002600 for a bulge and disk decomposition with an exponential disk, and with an inner truncated exponential disk, respectively (both using the bulge zoom-in priors). The residuals are similar for the two modeling methods, so the added complexity of the inner truncated disk does not appear justified.

I implemented the inner truncated exponential in SourceXtractor++ and run tests on a small sample of spiral galaxies. More specifically, I found examples of galaxies better fitted with the inner truncation in Baggett et al. (1998) that are also present in EFIGI (PGC0002035, PGC0002600 and PGC0002691 are also named NGC0151, NGC0234 and NGC0245 respectively) and tried to retrieve this result. However, the increased complexity of inner-truncated disks did not result in an improvement of the model-fitting of these galaxies, with similar residuals (see Fig. 3.9). With the model-fitting of inner truncated disks proving to be inconclusive, I decided to give up this track.

The above modeled galaxies are of types Sbc, Sc, Sb respectively, whose bulges are usually at the transition between pseudo and classical (see Quilley & de Lapparent 2023 in Sect. 5.3), may not be the ideal test cases due to their small B/T values. It would be interesting to test inner-truncated profiles on galaxies of earlier types hosting more prominent bulges that are unequivocally observed to be classical bulges, to test if the disruption of the exponentiality of the disk profile occurs in the bulge region in this case.

3.2 Removing extinction effects

Extinction refers to the absorption and scattering of the light emitted by an astronomical object by the dust and gas present along its travel towards an observer. In order to obtain rest-frame magnitudes (see Sect. 1.4.2), the model magnitudes I obtained from the luminosity profile-fitting of the images must be corrected for both atmospheric $A_{\rm atm}$ and galactic $A_{\rm gal}$ extinction, so that the apparent magnitudes I will use moving on are given by:

$$m_{{\rm new},band} = m_{{\rm old},band} - A_{{\rm atm},band} - A_{{\rm gal},band} \tag{3.2}$$

3.2.1 Atmospheric Extinction

As our SDSS imaging data comes from a ground-based telescope, it is affected by atmospheric extinction, which is the extinction effect caused by the gas and dust constituting our atmosphere. This extinction is mainly due to the Rayleigh scattering by air molecules, the scattering by particulates, and the molecular (often referred as telluric) absorption, with molecular oxygen and ozone absorbing UV light, and water absorbing IR photons. To correct for this effect, empirical linear relations have been found between the air mass and the atmospheric extinction when the galaxy is observed at the zenith. So I use the kk coefficients multiplied by the airmasses provided for the SDSS DR7 (Abazajian et al. 2009), to obtain the atmospheric extinction in the g, r and i bands:

$$A_{{\rm atm},band} = kk_{band}{\rm airmass}_{band} \tag{3.3}$$

3.2.2 Galactic Extinction

There is also galactic extinction, caused by the gas and dust forming the interstellar medium of the Milky Way, that needs to be taken into account. To correct for this effect, I use the dust reddening galactic maps from Schlegel et al. (1998) to obtain color excess $E(B-V)$ values for each galaxy from

its sky coordinates. The color excess, here for the $B-V$ color, is defined as the difference between the observed color and the intrinsic color of a source: $E(B-V) = (B-V)_{obs} - (B-V)_{intrinsic}$. Then, Table 6 of Schlafly & Finkbeiner (2011) provides us with the conversion factors between $E(B-V)$ and the extinction $A_{\mathrm{gal},band}$ in the nUV, g, r, i bands, which are given for different configurations. We choose the coefficients listed for a Milky Way reddening law with an extinction to reddening ratio $A_V/E(B-V) = 3.1$.

3.3 Spectral energy distribution fitting with ZPEG

3.3.1 Generalities on SED fitting

The Spectral Energy Distribution (SED) of a galaxy is shaped by the many properties of its stellar populations: star formation history, stellar mass, initial mass function, stellar metallicity and abundance patterns; these are related to the time variations of its gas and dust content (Tinsley 1972; Bruzual 1981; Guiderdoni & Rocca-Volmerange 1987). The aim of SED fitting is to infer all the physical parameters describing these properties from the analysis of either the galaxy spectra, or multi-band photometric data, that provides integrated information about the spectra in the available wavelength ranges, thus working as very-low resolution spectra.

In order to infer, or at least constrain, these parameters, the observed SED is compared to a matrix of template SEDs that were generated by varying the relevant parameters, and are redshifted to the possible values for the data. Codes following a frequentist approach, like ZPEG[3] (Le Borgne & Rocca-Volmerange 2002), provide the best-fitting model, while other using a Bayesian approach, such as BEAGLE (for BayEsian Analysis of GaLaxy sEds, Chevallard & Charlot 2016) and CIGALE (for Code Investigating GALaxy Emission, Boquien et al. 2019), return a probability distribution (Pacifici et al. 2023).

The generation of these templates is based on spectral population synthesis, which generates a galaxy spectra as the sum of the spectra of its many stars. It is based on simple stellar population (SSP) models, that describe the evolution with time of the SED of a single coeval stellar population, at a given metallicity and abundance pattern. This step requires a precise knowledge of stellar evolution, including spectral stellar libraries providing SED of all kind of individual stars, isochrones locating stars with a common age and metallicity within the Hertzsprung-Russell (HR) diagram, hence tracking their luminosity and spectral type evolution, and the initial mass function (Conroy 2013). Then, SSP models are summed according to the star formation history, and metal enrichment history, to obtain the cumulative spectra of all the galaxy stars. The effect of dust attenuation is also taken into account. Matching the observed SED with the templates also yields the most probable redshift of the object, which is called photometric redshift when only multi-band data is available to define the observed SED. Then for each observed object, one obtains a full theoretical galaxy spectrum as it would ideally be observed, and that best matches the observed SED.

3.3.2 Objectives: K-corrections, stellar masses and SFR

In the context of this thesis, I needed to derive the rest frame or absolute magnitudes from the apparent magnitudes obtained from the profile-fitting of the EFIGI galaxy images (see Sect. 3.1).

As the measure of magnitude for astronomical objects is done in one (or multiple) wavelength band(s), one must take into account the fact that the light received in a band was emitted at different wavelengths, due to redshift. To directly measure the light emitted in a band defined by its response function $\lambda \to R(\lambda)$ by a galaxy at redshift z, one would need to measure the light received in the band defined by $\lambda \to R((1+z)\lambda)$. To circumvent this issue, knowledge about the overall shape of the galaxy SED is required and takes the form of the k-correction K_{corr}, which thus depends on the redshift, the band considered and the SED of the galaxy. Therefore, while Eq. 1.2 remains valid for bolometric magnitudes, in the case of magnitudes in a wavelength band, it becomes (assuming no extinction):

$$m - M = 5 \log D_{\mathrm{lum}}[Mpc] + 25 + K_{\mathrm{corr}} \tag{3.4}$$

[3] http://imacdlb.iap.fr/cgi-bin/zpeg/zpeg.pl

with m and M the apparent and absolute magnitudes in the given band and $D_{\rm lum}$ the luminosity distance in megaparsecs.

The process of SED-fitting provides me with the necessary information about the galaxy SED to compute the k-corrections in the different bands, and consequently derive absolute magnitudes. Furthermore, the process of SED fitting also constrains many physical parameters regarding the stellar populations within the galaxy, and most notably the total stellar mass M_* and the current star formation rate SFR of the galaxy. This provides complementary information from the morphological analysis and will allow us to relate the morphological evolution of galaxies with their mass growth and star-forming state in Chap. 4.

3.3.3 ZPEG software and PEGASE templates

With the intent to work on galaxy morphology, and to make the most out of the information provided by the EFIGI visual classification, we choose to perform SED-fitting with the ZPEG software (Le Borgne & Rocca-Volmerange 2002), as the PEGASE[4] (Projet d'Étude des GAlaxies par Synthèse Évolutive, in French) templates it uses are build using evolutionary scenarii depending on the morphological type of the considered galaxy (see Fioc & Rocca-Volmerange 1997, 1999, 2019 for the three generations of PEGASE templates).

3.3.4 Details of the fitting procedure

The configuration files we used for the different runs of ZPEG whose results are exploited in this thesis contain the following parameters:

- the redshift is used here as a fixed parameter, using the value provided by Hyperleda (de Lapparent et al. 2011)
- the templates of the following types: E, S0, Sa, Sab, Sb, Sbc, Sc, Sd, Im and starburst, that all use a Salpeter IMF
- no mass constraint was enforced
- the age constraints were between 0.01 and 20 Gyr for all templates, except the starburst templates for which it was between 0.01 and 0.1 Gyr.

Another parameter of ZPEG is the internal dust extinction, that I did not activate as my attempts to use it led to poorer results. Using for instance a configuration for dust extinction consisting of 6 increments of 0.05 for $E(B-V)$ between 0 and 0.25 (other configurations were tried which led to similar results), we obtain that 43% and 19% of EFIGI galaxies are best fitted by an Im or a starburst template respectively, when Im represent only 5% of EFIGI. For E and lenticular types, the Im template is obtained for 37% to 59% of galaxies, and more than 80% of the best-fit templates are of type Sb or later. With dust added to the spectrophotometric evolution model, there is a systematic shift toward templates of later-types, whose younger stellar populations emit bluer light, compensated by dust, causing a reddening of the observed light. Therefore, the inclusion of internal dust in the ZPEG fitting was not conclusive, surely due to the fact that 3 optical bands and 1 UV band do not provide enough information for a more complex model (with more free parameters), especially for dust, which is constrained by IR data (this is further discussed in the next sub-section). The ZPEG run without dust extinction that we kept shows an overall good agreement between the morphological and spectral types, with, for all Hubble types, a maximum shift of two types for the spectral type of the most frequently obtained template.

For the ZPEG runs using the galaxy total magnitudes derived from the three profile-fitting methods (see Sect. 3.1), the three model magnitudes in g, r, and i only were used. The nUV magnitudes from GALEX were used for the 1848 galaxies for which a cross-match by 5 arcsec with the catalogue by Bianchi et al. (2017) was successful. For the runs using the separate bulge and disk magnitudes, we only used the three model magnitudes in g, r, and i, as the nUV magnitudes from GALEX were not separated into bulge and disk components.

[4] http://www2.iap.fr/pegase/

3.3.5 Future improvements

The more bands for which photometric data is available, and the wider the wavelength range they cover, the better is the quality of the SED fits. Because we are working with nearby SDSS galaxies that have been widely observed by different surveys and instruments, the EFIGI catalog benefits from observations in other wavelength bands. It was essential to complement the SDSS optical photometry with GALEX UV photometry as it provides key information on the star formation rate. In the analysis of the forthcoming complete MorCat catalog, we plan to add the u and z magnitudes, that I will obtain for whole galaxies as well as bulges and disks (see Sect. 6.2). It will be most interesting to also cross-match the optical data with an infrared (IR) survey to cover a wider wavelength range, such as the J, H, K_s bands of the 2MASS Large Galaxy Atlas (Jarrett et al. 2003). Besides, as dust tends to absorb and scatter the UV light, and re-radiate it in the IR (Conroy 2013), adding photometry in IR bands would surely prove valuable to allow for variable dust extinction estimates by the spectral template fitting procedure with ZPEG. Another robustness check would be to use a different SED-fitting code (see Sect. 3.3.1) and compare its results to the ones obtained with ZPEG.

Chapter 4

Color bimodality across the Hubble sequence

4.1 Color bimodality

To follow the evolution of how galaxies acquire their stars, grow in mass, and then transition towards quiescence, we can look at their distribution in both color and absolute magnitude. Indeed, the absolute magnitude is linked to the total number of stars shining within the galaxy, while an adequate choice of color will testify of the relative preponderance of young and old stars, respectively emitting more light in the bluer and redder wavelengths of the spectrum respectively.

Using the SDSS imaging data (see Sect. 1.3.4), Strateva et al. (2001) first showed that for a magnitude limited sample of 147,920 galaxies ($g^* \leq 21$), galaxies were displaying a bimodal distribution within the $g^* - r^*$ vs $u^* - g^*$ color-color diagram, with an optimal color separator of $u^* - r^* = 2.22$. Furthermore, Strateva et al. (2001) highlighted that these blue and red populations correspond to LTG (Sb, Sc, and Irr) and to ETG (E, S0 and Sa), using visually classified sub-samples. The study also made the link between color and morphological parameters describing the concentration of the radial luminosity profile, with red galaxies having higher concentration and being more likely fitted by a de Vaucouleurs profile than an exponential profile, compared to blue galaxies. This latter point is expected from the correlation between color and morphology. Later on, still using SDSS data, Baldry et al. (2004b) further explored this color bimodality by showing it in the color $u^* - r^*$ - magnitude M_r diagram. They also quantified the bimodality by fitting a double Gaussian to the color distributions in magnitude bins.

This bimodality of the galaxy population has been strengthened by later studies which reproduce it, using different parameters. A very common representation is based on the intrinsic physical parameters describing the stellar mass evolution, which are the total stellar mass M_* and its time derivative the star formation rate $\dot{M}_* = SFR$. These can be estimated using SED fitting (see Sect. 3.3). The specific star formation rate $sSFR = SFR/M_*$ is also often used. In the $SFR - M_*$ diagram, the blue galaxies make up the Main Sequence (MS) of star-forming galaxies (SFGs), with starbursts galaxies located above it due to their higher SFR, and a high-mass tail of red and low SFR galaxies forming the second population of the bimodality (Brinchmann et al. 2004).

A key development in regard to the color bimodality came with the space mission Galaxy Evolution Explorer (GALEX, Martin et al. 2005), a 50 cm diameter telescope in orbit around the Earth from 2003 to 2013 with the goal to probe star formation in galaxies by observing them in the ultraviolet (UV), so as to measure the emission of their very young stars, without suffering from the Earth atmospheric absorption. The color-magnitude diagram obtained using UV to optical color (Wyder et al. 2007) reproduced the blue-red bimodality but with a clearer color separation between the two distributions, and revealed an intermediate low-density area within this plane: the "Green Valley", as its color is intermediate between those of the two strong peaks of red and blue galaxies. The intermediate location of Green Valley galaxies lent them high interest as they allow one to probe the transition between star formation and quiescence.

To explain the origin of the bimodality, the effect of environment was highlighted with the fraction

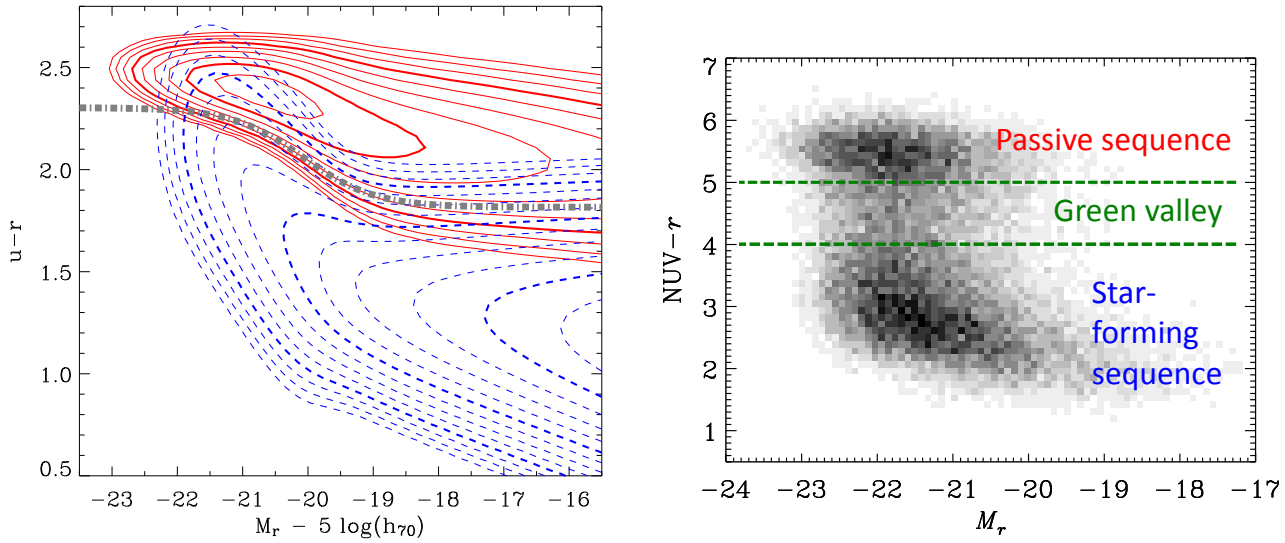

Figure 4.1: Color-magnitude diagrams for SDSS galaxies using $u-r$ color (left), and GALEX data with $NUV-r$ color (right). The optical color shows a bimodality with two density peaks, red and blue. The wider magnitude range encompassed by galaxies in $NUV-r$ color (~ 5 vs ~ 2 for $u-r$) allows for a clear separation of the blue and red populations, therefore bringing to light the intermediate Green Valley. From Baldry et al. (2004b) (left) and Salim (2014) (right).

of red galaxies being shown to be a strong function of local density, at all magnitudes, increasing from $\sim 10\% - 30\%$ of the population in the lowest density environments to $\sim 70\%$ at the highest densities (Balogh et al. 2004). Baldry et al. (2004b) used a simple merger model to explain the transition from blue to red galaxies, and Baldry et al. (2004a) further showed that the fraction of red galaxies could be predicted by a combination of local projected density (estimated using a surface density given by $\Sigma_5 = 5/(\pi r^2)$, where r is the projected distance to the fifth-nearest spectroscopically-confirmed neighbor) and the absolute magnitude, which they related to the probability of transformation events such as mergers or galaxy harassment. Dekel & Birnboim (2006) proposed to explain the bimodality and its associated observed features (luminosity and mass functions, color-magnitude diagrams, star formation history etc.) by the accretion of cold gas flows that enhance star formation below a critical halo mass $M_{\rm shock}$, but that are shock heated above it (see Sect. 1.5.3). For masses below this threshold, supernovae feedback regulates star formation, while above it, AGN feedback maintains the gas hot enough for galaxies to stay quiescent, as shown in the semi-analytical model of Cattaneo et al. (2006). The importance of AGN feedback was further corroborated by Baldry et al. (2006) as it allowed to reproduce the dependence of the red fraction with both mass and environment when incorporated in the semi-analytical models, based on the Millenium N-body simulation, developed by Croton et al. (2006) and Bower et al. (2006), the latter showing even better agreement.

There are also morphological parameters that play a part in shaping this bimodality. Indeed, the color bimodality is a bimodality in star formation activity between blue star-forming galaxies and red quiescent ones, and the star formation rate is itself correlated to the morphology of galaxies (Kennicutt 1998a). In that regard, using a visually classified sub-sample of 287 bright galaxies ($g^* < 16$), Strateva et al. (2001) studied the color distributions for four morphological categories: E/S0, Sa, Sb, and Sc/Irr. They found that the $u-r$ red peak was composed of E/S0 and Sa galaxies, with the former sample having the reddest average color, while Sb galaxies were spread between the two peaks and in the under-dense region between them, and finally that Sc/Irr occupy the blue peak. Gil de Paz et al. (2007) then used GALEX data to locate galaxies according to their morphological type from the RC3, in color-color and color-magnitude diagrams using UV, optical, and IR bands, and showed that in $FUV - K$, the E and S0 were forming the Red Sequence, while spirals were forming the Blue Cloud, with later types being increasingly bluer. The authors found some dispersion in the relation, with for instance early spirals also showing red colors similar to E and S0. However, both of these morphological

sub-samples are limited in size, and the link between star formation and morphology requires a large and complete (with all Hubble types) morphological sample in order to decipher the causality of the measured correlations between the aforementioned parameters.

Using different parameters to explore the color bimodality allows one to gain insight into the fundamental differences between these two populations. For instance, Allen et al. (2006) used bulge and disk decomposition on a sample of 10,095 galaxies from the Millenium Galaxy Catalog to show a bimodality in the color concentration plane, the Sérsic index of the bulge modeling quantifying the profile concentration. By reproducing a strong color-concentration bimodality, they linked the color of the population to the prominence of their bulge, hence providing more details on the relation between color and morphology already seen in the SDSS analysis of Strateva et al. (2001).

By design, the EFIGI morphological catalog provides good statistics for all Hubble types and a finer and extensive classification than the previously used catalogs, with intermediate types and additional features (see Sect. 2.2.3), which make it well-fitted to explore in-depth how the morphological properties vary across the galaxy bimodality. As explained in Sect. 1.4.1, the Hubble sequence shows a continuity in the individual morphological features between subsequent types. For example, the fraction of light within the bulge, changes gradually along the Hubble sequence. Moreover, the morphological features have specific colors: bulges and bars are generally redder than the disks (Kruk et al. 2018), due to older stellar populations, the spiral arms and regions of scattered or strong HII regions that these contain are bluer than the disk due to star formation, whereas rings can be either blue or red (see Sects. 4.5 and 6.2). Therefore, with its 16 shape attributes (see Sect. 2.2.3), the EFIGI sample bears promise for studying how morphology shapes the color bimodality, hence gaining further insight into the link between star formation and morphology.

4.2 Merger driven evolution

In the ΛCDM paradigm, the growth of structures happens through hierarchical assembly, which in the case of galaxies manifests itself by mergers. Galaxy mergers occur when two galaxies collide with each other, to form a single more massive galaxy whose properties will highly depend on many of the conditions of the merger: speeds, impact parameters, collision angle, and the relative properties (mass, gas, and dust content, structure ...) of the merging galaxies. For instance one can differentiate between major and minor mergers that are defined according to the mass ratio between the two merging galaxies, with major mergers involving similar mass objects whereas minor mergers are encounters in which one galaxy is significantly less massive than the other one, with a mass ratio threshold usually defined at 1:10. One can also distinguish between wet and dry mergers, involving gas-rich and gas-poor galaxies respectively. Simulations have shown that major mergers of spirals lead to elliptical galaxies while minor mergers tend to preserve the disk (Bournaud et al. 2004, 2005; González-García & Balcells 2005; Martin et al. 2018). The impact of mergers on star formation remains debated, as the violent mixing of gas and dust can greatly enhance star formation through starburst episodes (Barnes & Hernquist 1991; Teyssier et al. 2010), but can also trigger stellar and black hole feedback mechanisms after coalescence thus suppressing star formation in the remnant (Springel et al. 2005b,a). All these results paint a picture of galaxy evolution in which minor gas-rich mergers contribute to star formation in spiral galaxies, while major and/or dry mergers form massive quiescent ellipticals.

Therefore, the formation of the Hubble sequence in the low redshift Universe, which we are concerned with in this thesis, is expected to be dependent on the merger histories of galaxies. At higher redshifts, peculiar and disk systems, that are blue and heavily star-forming are more numerous than at present times, when a growing number of massive ETG also exist. A combination of secular evolution and mergers have to explain this morphological evolution (Abraham & van den Bergh 2001; Steinmetz & Navarro 2002). In that regard, constraining the rate of merger over cosmic time would prove very valuable, but is very difficult to perform observationally, due to the difficulty to estimate the mergers rate in surveys. Indeed, galaxies can be in a large variety of states throughout a merger that can last several billion years: the approaching and distancing phases that precede the actual mixing of the two galaxies, are difficult to account for observationally, and the starburst phase that follows the merger may be similar to those produced by a fly-by or an increased gas inflow via the cosmic streams.

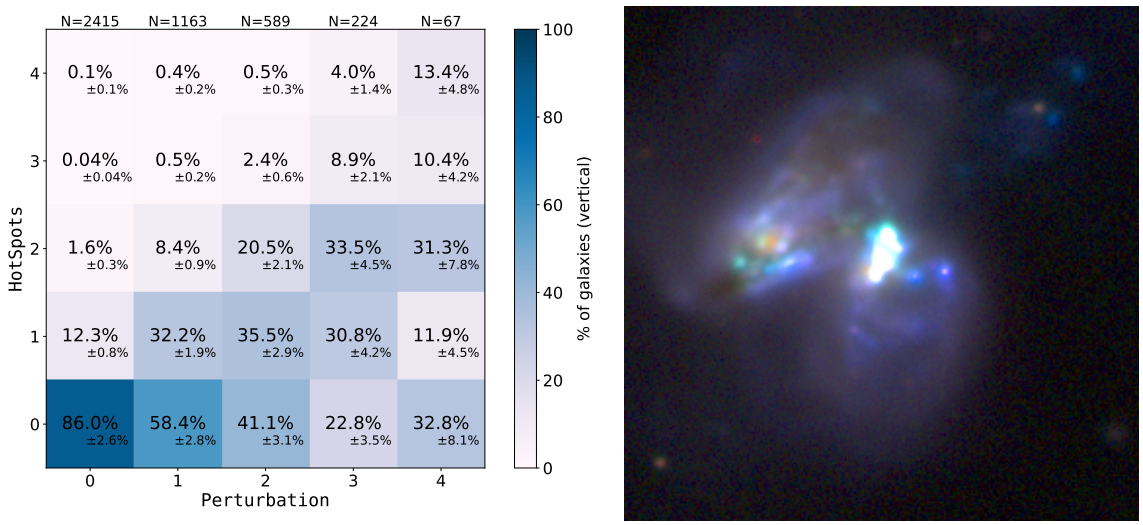

Figure 4.2: **Left:** Percentages of galaxies with a given value of the `Hot Spots` attribute among all galaxies having a certain value of `Perturbation`. The number of galaxies per value of `Perturbation` is given at the top of each column. **Right:** *gri* composite image of PGC0035326 (center) and PGC0035321 (left), a pair of merging galaxies. Both have a `Perturbation` attribute labeled at 4 and `Hot Spots` values of 4 and 3 respectively.

Whereas in a numerical simulations, the fraction of galaxies in the process of merging at a given time, or the frequency of mergers during the history of a galaxy can both be defined unequivocally. Still, merger rates have been estimated from surveys, trying to decipher between the different kinds of mergers, with an overall agreement that the merger rate increases with redshift, but some discrepancies between the evolution measured in different studies, which are difficult to assess as they not only use different methods, but also mass limits or redshift range (Conselice et al. 2003; Lin et al. 2004; Bower et al. 2006; Bluck et al. 2009; López-Sanjuan et al. 2009; Bridge et al. 2010; Conselice et al. 2022).

The EFIGI catalog is limited to nearby galaxies, and the rate of mergers decreases at lower redshifts (Bridge et al. 2010), especially major mergers (López-Sanjuan et al. 2009). There are 557 out of 4458 EFIGI galaxies with `Multiplicity` ≥ 1, i.e. 12.5% that have at least one neighboring galaxy with a magnitude difference less than 5 and centered within 75% of their isophotal diameter. Moreover, if two galaxies will interact or have started interacting but are seen too distant from each other (for EFIGI, beyond the threshold distance for the `Multiplicity` attribute to be non null), the merger event will not be counted. One should therefore be able to estimate the dynamical timescale over which a merger can be identified and the typical spread of the orbits during the pre-merger interaction in order to derive an observational merger rate from interacting systems counts.

Another evidence of a galaxy-galaxy interaction in the form of a recent merger or fly-by event is the distortion of a galaxy's isophotes compared to rotational symmetry. The EFIGI `Perturbation` attribute was designed to this end. The impact of interactions and mergers on scattered or localized star formation in galaxy disks can be measured by the intensity of scattered HII regions (`Flocculence`[1] attribute), and giant and high surface brightness regions (`Hot Spots` attribute).

Other EFIGI attributes can be used as clues of interactions and mergers of galaxies, which are the dynamical features, with attributes measuring the bar length (`Bar`), the spiral arms intensity (`Arm Strength`), the spiral arms pitch angle (`Arm Curvature`), the inner (`Inner Ring`) and outer ring intensities (`Outer Ring`, see Sect. 4.5). Disentangling the impact of merger events on the inner dynamics of galaxy structures from their secular evolution remains a challenge, and examining attributes related to these phenomena and their correlations is the first step in tackling this issue. The EFIGI catalog proves to be of great value in that regard with its large variety of individual morphological attributes on a five-level scale. For instance, to identify a merger in its post-mixing phase, we expect that the recently formed merger remnant is still asymmetric and shows enhanced star formation (starburst),

[1] All attributes are described in Sect. 2.2.3

therefore has non-zero to high values of both `Perturbation` and `Hot Spots`. Fig. 4.2 shows indeed that the fraction of galaxies with high values of the `HotSpots` attribute is higher for galaxies selected to have higher values of the `Perturbation` attribute.

Therefore, using the EFIGI catalog, it remains possible to study how our characterization of Hubble types along the color-mass diagram fits into the picture of a "hierarchical origin of galaxy morphologies" (Steinmetz & Navarro 2002).

4.3 Synthesis

In this section, we refer to the sections and figures of the article by Quilley & de Lapparent (2022), presented in Sect. 4.4.

In this article, to cleanly relate the morphology of galaxies to their star-forming state, we chose to plot the color-magnitude diagram using the $NUV - r$ absolute color. We then analyze the relation between the absolute magnitude and stellar mass (Fig. 11), and between the $NUV - r$ color and the $sSFR$ (Fig. 12) of EFIGI galaxies, taking into account the limited number of bands we use to derive the physical quantities from the SED-fitting (see Sect. 3.3). This allows us to switch from the color-magnitude to the color-mass diagram (Fig. 13), the latter being almost a mirrored version of the former, and focus the rest of the analysis on the evolution of morphological parameters along this 2D plane, analyzing the trends observed in view of the location of the different Hubble types (Fig. 20).

We use the additional information of the `HubbleType` which is given by the EFIGI visual classification and obtain that each type occupies a specific location of this graph (Fig. 4). Moreover, when looking at the mean positions per type, we highlight that the Hubble sequence spans monotonously the diagram with the Im at the faint end of the Blue Cloud, and spirals of type Sm to Sb forming the Blue Cloud (earlier types being brighter). Sab types mark the transition towards the Green Valley, populated by types Sa and S0a, while the remaining early-type galaxies constitute the Red Sequence, with ellipticals being brighter than lenticulars (Fig. 5). Consequently, the EFIGI results contradict the first part of the claim by Salim (2014) that "The red sequence should not be equated with early-type galaxies, which, in turn, must not be equated with the spheroids (elliptical galaxies)" the second part is correct as we show using EFIGI that the Red Sequence also includes lenticular galaxies. We confirm that the low density of points seen in the Green Valley is not originating from selection effects in the EFIGI catalog, by using the magnitude-limited sample of MorCat (Fig. 6). We propose to rename this region the "Green Plain" because of its significant width and low and nearly flat density over ~ 2 mag. in $NUV - r$, and we show that it is caused that it is caused by a wide color shift (due to a strong fading of star formation) between the corresponding morphological types, rather than by a decrease in their number density. We also emphasize the need for UV to optical colors to probe the Green Plain, as optical colors do not allow a clear enough separation of blue and red galaxies. Indeed, Green Valley galaxies identified through their $NUV - r$ color are mainly located in the $u - r$ color interval $[2.0; 3.0]$ which also contains Blue Cloud galaxies at $2.0 \lesssim u - r \lesssim 2.5$ and Red Sequence galaxies at $2.5 \lesssim u - r \lesssim 3.0$, making the under-dense Green Valley almost disappear (Figs. 8 and 9).

We identify two key morphological parameters whose variations in the color-mass diagram replicate the monotonous span of the subsequent Hubble types, meaning that these parameters actually vary along the Hubble sequence and can be consequently seen as proxies of the Hubble type: the B/T (both the luminosity and mass ratios can be used, Figs. 16 and 17), and the disk $g - r$ color (Fig. 21). We also quantify the variations of these parameters across the Green Plain, with an increase by a factor of more than 2 in B/T and a disk reddening of ~ 0.2 mag, which provides new and quantitative measures of how galaxies change in color and morphology while their star formation fades.

The Blue Cloud extends over 4 order of magnitudes in stellar mass. Explaining this growth only by the consumption of the HI gas reservoir would require massive gas inflows and long-term intensive star-formation , with $sSFR$ orders of magnitudes higher than what is measured in the Blue Cloud. Therefore we suggest that galaxy mergers play a key part in the mass growth across the Blue Cloud, either by enhancing the star formation of these galaxies, or more simply through the addition of the stellar masses of the merged galaxies. To gain insight on star-formation and stellar mass growth within the Blue Cloud, we investigate the variation of some EFIGI attributes along the color-mass

diagram and find that the scatter in star formation rate observed across the main sequence of star-forming galaxies (i.e. the Blue Cloud) can be related to variations in the prominence of spiral arms (`Arm Strength`, Fig. 23), the presence of scattered HII regions within the disk (`Flocculence`, Fig. 23), and the presence of giant regions of star formation (`Hot Spots`, Fig. 25). We obtain that all of these attributes, which correspond to enhanced star formation within the disk, show a vertical gradient within the Blue Cloud, with bluer galaxies having higher attribute values. We also note a similar variation for the attribute measuring the distortions in the galaxy profile (`Perturbation`, Fig. 24) that we interpret as a marker of a recent tidal interaction, which may also temporarily boost star formation. Based on previous studies, we also discuss the influence of mergers and fly-bys in contributing to the bulge growth of galaxies, especially through the Green Plain, and in the formation of the most massive elliptical galaxies. Interestingly, the EFIGI galaxies display a common mass limit for early to intermediate spirals (Sa to Sc) at $\log(M_*/M_\odot) = 11.7$, which also approximately matches the transition mass between the E galaxies dominating the high-mass end of the Red Sequence, and S0s its low mass end.

All of these elements put together allow us to paint a picture of galaxy evolution in which the Hubble sequence can be seen as an inverse evolutionary sequence, with Im and spirals merging to form spirals of earlier and earlier types, that eventually merge to produce lenticular and elliptical galaxies. These morphological transformations are related to the mass growth across the Blue Cloud for the different types of spirals, the fading of star formation through the Green Valley from early spirals to lenticulars, and the mass growth between S0s and Es within the Red sequence. Growth of the bulge and reddening of the disk occur all along these processes, thus characterizing the aging of galaxies along the Hubble sequence. We emphasize that galaxies do not necessarily go through all the Hubble types during their evolution, and neither is this evolution linear along the morphological sequence, because it depends on the details of the merger history and the environment. We also mention that backwards evolution to later types may occur in the context of star-formation bursts, but it remains marginal compared to the global evolution of the galaxy populations. Finally, an isolated galaxy not going through any interaction could stay in a spiral state for as long as its gas reservoir allows it, and redden into a lenticular when star formation eventually fades after its gas exhaustion.

Our derived evolutionary picture is also confronted to the results of cosmological simulations that allow one to directly track galaxies over time and identify the formation mechanisms responsible for the different Hubble types. We find good agreement with the study of Deeley et al. (2021) regarding the formation of lenticulars, mainly through mergers. But we also express concerns about the findings of Park et al. (2021) in which the star-formation fading and morphological transformations needed to turn a star-forming spiral into a massive quiescent elliptical are decoupled, as these appear to occur in parallel in the EFIGI data.

4.4 Article

"Aging of galaxies along the morphological sequence, marked by bulge growth and disk quenching"
Louis Quilley & Valérie de Lapparent
Astronomy & Astrophysics, Volume 666, id. A170, 24 pp.
Submitted 7 June 2022 / Accepted 3 August 2022
24 pages, 27 figures, 1 table
10.1051/0004-6361/202244202
10.48550/arXiv.2206.04707
https://ui.adsabs.harvard.edu/abs/2022A%26A...666A.170Q/abstract

Astronomy & Astrophysics manuscript no. output
December 21, 2023
© ESO 2023

Aging of galaxies along the morphological sequence, marked by bulge growth and disk quenching

Quilley, L.⋆ de Lapparent, V.⋆⋆

Institut d'Astrophysique de Paris, CNRS, Sorbonne Université, 98 bis boulevard Arago, 75014 Paris, France

Received 8 June 2022 / Accepted 3 August 2022

ABSTRACT

Aims. We revisit the color bimodality of galaxies using the extensive EFIGI morphological classification of nearby galaxies.
Methods. The galaxy profiles from the Sloan Digital Sky Survey (SDSS) *gri* images were decomposed as a bulge and a disk by controlled profile modeling with the Euclid SourceXtractor++ software. The spectral energy distributions from our resulting *gri* SDSS photometry complemented with Galaxy Evolution Explorer (GALEX) NUV photometry were fitted with the ZPEG software and PEGASE.2 templates in order to estimate the stellar masses and specific star formation rates (sSFR) of whole galaxies as well as their bulge and disk components.
Results. The absolute $NUV - r$ color versus stellar mass diagram shows a continuous relationship between the present sSFR of galaxies and their stellar mass, which spans all morphological types of the Hubble sequence monotonously. Irregular galaxies to intermediate-type Sab spirals make up the "Blue Cloud" across 4 orders of magnitude in stellar mass but a narrow range of sSFR. This mass build-up of spiral galaxies requires major mergers, in agreement with their frequently perturbed isophotes. At high mass, the Blue Cloud leads to the "Green Plain," dominated by S0a and Sa early-type spirals. It was formerly called the "Green Valley," due to its low density, but we rename it because of its wide stretch and nearly flat density over ~ 2 magnitudes in $NUV - r$ color (hence sSFR), despite a limited range of stellar mass (1 order of magnitude). The Green Plain links up the "Red Sequence," containing all lenticular and elliptical galaxies with a 2 order of magnitude mass interval, and systematically higher masses for the ellipticals. We confirm that the Green Plain cannot be studied using $u - r$ optical colors because it is overlayed by the Red Sequence, hence NUV data are necessary. Galaxies across the Green Plain undergo a marked growth by a factor 2 to 3 in their bulge-to-total mass ratio and a systematic profile change from pseudo to classical bulges, as well as a significant reddening due to star formation fading in their disks. The Green Plain is also characterized by a maximum stellar mass of $10^{11.7} M_{\odot}$ beyond which only elliptical galaxies exist, hence supporting the scenario of ellipticals partly forming by major mergers of massive disk galaxies.
Conclusions. The EFIGI attributes indicate that dynamical processes (spiral arms and isophote distortions) contribute to the scatter of the Main Sequence of star-forming galaxies (Blue Cloud), via the enhancement of star formation (flocculence, HII regions). The significant bulge growth across the Green Plain confirms that it is a transition region, and excludes a predominantly quick transit due to rapid quenching. The high frequency of bars for all spirals as well as the stronger spiral arms and flocculence in the knee of the Green Plain suggest that internal dynamics, likely triggered by flybys or (mainly minor) mergers, may be the key to the bulge growth of massive disk galaxies, which is a marker of the aging of galaxies from star forming to quiescence. The Hubble sequence can then be considered as an inverse sequence of galaxy physical evolution.

Key words. Galaxies: star formation – Galaxies: evolution – Galaxies: bulges – Galaxies : elliptical and lenticular, cD – Galaxies : spiral – Galaxies : irregular

1. Introduction

The study of galaxy morphology started with Edwin Hubble classifying the different galaxies he observed according to their shapes and features (Hubble 1936). This process led to the Hubble sequence being established, which was then improved by De Vaucouleurs (de Vaucouleurs 1959). This system of visual classification has several drawbacks: it is a long and tedious work that requires prohibitive amounts of human time to be performed on large surveys; galaxies should be well resolved, hence at a limited distance depending on the telescope and instrument; it is based on the human eye, so the results are prone to errors, as well as systematic drifts across the sample.

To survey the diversity of galaxy population, establishing color-magnitudes diagrams have become a standard workaround approach, because it can be performed on all kinds of galaxies, even distant and poorly resolved ones, and it is a quantitative method that is significantly faster than visual classification. Using such diagrams, it was shown that early-type galaxies (ellipticals and lenticulars) are predominantly red, whereas late-type galaxies (spirals and irregulars) are blue (Gil de Paz et al. 2007). This dichotomy was first shown using the optical color $u - r$ (Strateva et al. 2001, Baldry et al. 2004, Conselice 2006), and it became even clearer when complementing the optical data with an ultraviolet (UV) band. Color-magnitude diagrams were proved to convey physical information about galaxies: for example, SED model-fitting showed that UV to optical color (in particular the $NUV - r$ color) is a tracer of star formation (Salim et al. 2007, Kauffmann et al. 2007, Kaviraj et al. 2007).

The star formation rate (SFR) of a galaxy is linked to its morphology (Kennicutt 1998): elliptical and lenticular galaxies are generally quiescent and composed of old stars, whereas spiral galaxies show significant star formation in their disks, characterized by young stellar populations and HII regions delineating

⋆ email: louis.quilley@iap.fr
⋆⋆ email: valerie.de_lapparent@iap.fr

their spiral arms. The analysis of the UV-optical color magnitude diagram (Martin et al. 2007, Wyder et al. 2007, Salim et al. 2007) shows a physical bimodality between the star-forming galaxies of the Blue Cloud, and the so-called quiescent (or passive) galaxies of the Red Sequence, that is with very low or no star formation. The intermediate region between them was originally named the Green Valley because of its low number density of galaxies in the color-magnitude diagram.

Uncertainties remain as to how the individual Hubble types are located along these sequences, in particular for Green Valley galaxies. For example, the Galaxy Zoo (Lintott et al. 2011) greatly expanded the number of classified galaxies, but the poor angular resolution of the majority of the galaxies (up to redshifts $\lesssim 0.1$) only allows for a rough classification into ellipticals, spirals, or mergers. More recently, Bait et al. (2017) studied the star-forming state of galaxies with a visual morphological classification (Nair & Abraham 2010), and show the strong interdependence between SFR and morphology, being stronger than with the local density for both parameters. Studies based on bulge and disk decomposition of galaxies at redshifts from 0 to ~ 2.5 show the role of bulge growth (Lang et al. 2014, Bluck et al. 2014, Bremer et al. 2018, Bluck et al. 2022, Dimauro et al. 2022) and disk reddening (Bremer et al. 2018) in the transformation of galaxies from star-forming to quiescent.

In the present article, we analyze a sample of nearby, well-resolved galaxies extracted from the Sloan Digital Sky Survey images (SDSS), a subsample of which were thoroughly studied to create a visual morphological classification ("Extraction de Formes Idealisées de Galaxies en Imagerie" - EFIGI), and we examine them in terms of absolute colors and magnitudes. We complement the SDSS optical photometry with UV photometry obtained by the Galaxy Evolution Explorer (GALEX). In addition, we perform bulge and disk decomposition to further relate colors and the morphology.

In Sect. 2, we present the data used for this study. In Sect. 3, we detail the methodology used to perform model-fitting of the luminosity profiles using SourceXtractor++ (Bertin et al. 2020), as well as of the spectral energy distribution (SED) using ZPEG (Le Borgne & Rocca-Volmerange 2002). We then analyze our results in Sect. 4, by locating morphological types and their characteristics within the color-absolute magnitude diagram, as well as the color-stellar mass diagram. In Sect. 5, we question the nature of the transition between star-forming and quiescent galaxies in view of additional EFIGI morphological attributes, and well as other published relevant analyses, and discuss the implications of our findings.

2. Data

2.1. MorCat

The Morphological Catalogue (MorCat) is a complete catalog of galaxy images extracted from the Sloan Digital Sky Survey (SDSS) Data Release 8 (DR8) (Aihara et al. 2011) in its five bands u, g, r, i and z, to an apparent magnitude limit of $g \leq 15.5$. To avoid solving the complex segmentation problem of identifying large galaxies (and all of them) directly from the images, we assume that all galaxies to that g limit are included in HyperLeda (Makarov et al. 2014) to $B_T \leq 18.0$. After restricting this HyperLeda sample to a sky mask corresponding to the SDSS northern galactic cap, extracting the images of each galaxy from the SDSS image database, measuring their photometry by bulge and disk modeling using SExtractor (Bertin & Arnouts 1996), and discarding spurious sources (unresolved objects and image artifacts), a total of 20126 MorCat galaxies with $g \leq 15.5$ are obtained.

2.2. EFIGI

Within the intersection of their masks over the northern sky and the northern galactic cap (see Quilley & de Lapparent, (*in prep.*), EFIGI ("Extraction de Formes Idéalisées de Galaxies en Imagerie") is a subsample of MorCat (EFIGI contains 657 galaxies outside this intersection, and located mostly within the southern galactic hemisphere of the northern sky). It contains 4458 galaxies with known morphological types and uncertainties from the RC3 Revised Hubble sequence (RC3-seq hereafter) (de Vaucouleurs et al. 1991).

A systematic visual classification process by a group of astronomers led to a new catalog with 16 morphological attributes: `B/T` (as bulge over total flux ratio), spiral `Arm Strength`, spiral `Arm Curvature`, `Bar Length`, `Inclination-Elongation` (hereafter shortened to `Incl-Elong`), `Perturbation`, `flocculence`, `Hot Spots` and `Visible Dust` are the 9 attributes used here; the other 7 attributes not directly used in the present analysis are `Contamination`, `Multiplicity`, spiral `Arm Rotation`, `Inner Ring`, `Outer Ring`, `Pseudo-ring`, and `Dust Dispersion` (Baillard et al. 2011). These attributes allow to better understand the nature of the Hubble sequence (de Lapparent et al. 2011), and can be useful to understand some trends (or biases) in the results of analyses as a function of morphology.

The stage of each galaxy on a morphological sequence based on the RC3-seq, and which we call the EFIGI morphological sequence (EFIGI-seq hereafter), has also been measured for each EFIGI galaxy, with the following specificities: contrary to the RC3-seq, the EFIGI-seq only has one elliptical type, as the different elongation stages of elliptical galaxies in the RC3-seq are measured by the EFIGI `Incl-Elong` attribute; the RC3-seq non-magellanic irregulars (I0 type) are not considered as a separate type in the EFIGI-seq, but as galaxies of some other Hubble type which undergo some perturbation as measured by the corresponding attribute; in the EFIGI-seq, the dwarf elliptical (dE) and dwarf spheroidal (dSph) galaxies are in a separate class from the Ellipticals, named dE. The various types along the EFIGI-seq are listed in Table 1. Table 1 also shows the mean difference of RC3 and EFIGI type for EFIGI galaxies grouped by EFIGI type: except for the difference due to different definitions (for types cE and dE), there is an overall agreement between RC3-seq and EFIGI-seq, as shown by the rather small mean difference and moderate dispersion of these differences (see also Baillard et al. 2011, Fig. 19).

We note that the EFIGI sample was built with the goal of having a few hundreds of galaxies of each Hubble type, and mostly include galaxies with apparent diameter ≥ 1 arcmin (de Lapparent et al. 2011). Therefore EFIGI is not magnitude limited and is not a representative sample of nearby galaxies, which MorCat is. Their largely overlapping masks in the sky allows to interpret MorCat results with EFIGI morphology information, and to generalize EFIGI results using MorCat.

2.3. GALEX cross-match

In order to complete the SDSS optical photometry with UV photometry, we perform a cross match between the EFIGI or MorCat catalog and the Galaxy Evolution Explorer (GALEX) catalog, which covers the whole sky, except for the plane of the

Table 1: Means and standard deviations of the difference between the RC3 and EFIGI Hubble types for EFIGI galaxies.

EFIGI Hubble Type	cE	E	cD	S0$^+$	S0	S0$^-$	S0a	Sa	Sab	Sb	Sbc	Sc	Scd	Sd	Sdm	Sm	Im	dE
RC3 number	-6	-5	-4	-3	-2	-1	0	1	2	3	4	5	6	7	8	9	10	11
Mean difference	2.964	1.334	0.388	-0.048	0.276	-0.292	-0.021	0.111	0.251	0.206	-0.173	-0.41	-0.538	-0.653	-0.936	-1.22	-0.818	-9.775
Standard deviation	3.96	1.267	1.703	1.386	1.552	1.733	1.645	1.349	1.303	1.664	1.604	1.46	1.468	1.403	1.989	2.306	1.85	5.38

Milky Way. To retrieve GALEX data, we used VizieR[1] and performed a cross-match on celestial position, with a maximum distance of 5 arcsec, between two GALEX tables from the revised catalog of GALEX UV sources (GUVcat_AIS DR6+7, Bianchi et al. 2017): (i) the sample of the revised GALEX catalog of UV sources (GUVcat_AIS) from DR6+7, providing magnitudes of all detected sources in the FUV (1350 − 1750Å) and NUV (1750 − 2800Å) bands; (ii) the list of galaxies larger than 1 arc minute included in the GUVcat footprint. Another cross match is then performed between the resulting GALEX table and the MorCat galaxies, based on the galaxy name list provided by HyperLeda (Makarov et al. 2014) for each MorCat object.

Among the 4458 EFIGI galaxies, 1848 have NUV data, while only 1754 of the 16327 of MorCat galaxies outside of EFIGI do. In the FUV band, we obtain magnitudes for 1301 EFIGI galaxies and for 1255 MorCat galaxies (outside of EFIGI). As we show below, the GALEX NUV band is sufficient to estimate the star formation rate, whereas using instead the FUV band would reduce the EFIGI and MorCat subsamples with UV photometry by 29.6% and 29% respectively. We therefore only make use of the NUV data in the present analysis, and note EFIGI ∩ GALEX and MorCat ∩ GALEX to refer respectively to the EFIGI and MorCat subsamples with GALEX NUV photometry. GALEX photometry is given only for the whole galaxies, it is not separated into bulge and disk components. While SDSS photometry is subject to splitting issues (see Sect. 5.3 and Fig. 24 in Baillard et al. (2011)), hence the need to remeasure magnitudes ourselves (see Sect. 3.1), we keep the magnitudes provided by the pipeline in GALEX. Indeed, Bianchi et al. (2007) explain that the shredding issue only applies to a few objects in GALEX AIS catalog, so it cannot jeopardize our results.

3. Methodology

3.1. Galaxy profile-fitting with SourceXtractor++

SExtractor bulge and disk photometry is performed for all MorCat and EFIGI galaxies, and displays on synthetic images of galaxies with similar properties, a high accuracy in the modeled total apparent magnitudes. However the EFIGI morphological attributes allow one to detect systematic biases due to degeneracies between the bulge and disk components, and which affect the separate bulge and disk photometry.

To obtain more reliable bulge and disk magnitudes for EFIGI galaxies, we use the SourceXtractor++ software (Bertin et al. 2020) on EFIGI galaxies only, which is a followup to SExtractor (Bertin & Arnouts 1996) developed in the context of the Euclid space mission (Scaramella et al. 2021). The great advantage of this new software is the possibility to perform simultaneous multiband model-fitting for as many Sérsic (or exponential) profiles as desired for each object, and with a control on all the model parameters: one can put priors on the Sérsic index, the effective radius or the aspect ratio (= b/a with a, b the major and minor axis of the profile respectively), and one can also control the relative values of a given aforementioned parameter between the bulge and disk components, or across filters. In particular, we make sure that values of both the bulge and disk effective radii are similar (within some adjustable margin) between filters (details on the adopted priors are provided in Quilley & de Lapparent (*in prep.*). Because many SDSS images of the EFIGI galaxies in the u and z bands are noisier than in the higher signal-to-noise g, r, and i bands, and therefore degrade the multiband bulge and disk model-fitting when included, we limit here these fits with SourceXtractor++ to the 3 bands g, r and i (and, as already mentioned, do not include the NUV band in this decomposition).

We use and compare two different methods to model the galaxy profiles as sums of disks and bulges with SourceXtractor++. On the one hand, we have a prior-less two-component model as the sum of a Sérsic profile (intended for the bulge) and an exponential profile (intended for the disk). On the other hand, we develop a two-component model with priors defined by automatically zooming into the galaxy disk in order to model specifically the bulge with a Sérsic profile in the g, r and i bands separately, while treating the disk as a background component. The level of zoom is a function of the minor and major axis of the segmented area for the galaxy, and in any case smaller than 1/2 of the smallest of the two. We then use the derived median bulge parameters over the g, r, and i bands as bulge priors for the two-component bulge and disk model. These two-component models are performed simultaneously in the g, r and i bands, with Gaussian priors on ratios or differences of profile parameters between bands. More information on the SourceXtractor++ configuration will be given in Quilley & de Lapparent (*in prep.*) For consistency between the EFIGI and MorCat results derived below, we calculate that the distribution of difference between SourceXtractor++ and SExtractor apparent magnitudes of EFIGI galaxies per apparent magnitude intervals ([8, 12], [12, 14], [14, 16] and [16, 18]) in the g, r, and i bands, peaks between 0.02 and 0.06 when more than 100 galaxies per interval, and with an r.m.s. dispersion varying between 0.1 and 0.2 for all 3 bands for the 3 most luminous intervals, and reaching 0.4 for g in the magnitude interval [16, 18] (this bin is too poorly populated in the r and i bands, with less than 100 galaxies). These differences may result from the use of an adaptive mesh size for estimating the sky background in the SourceXtractor++ analysis (5 times the isophotal diameter up to 2048 pixels), whereas the mesh size is fixed to 1024 pixels in the SExtractor analysis (except for heavily contaminated galaxies in both analyses).

The PSF is calculated using a sufficient number of stars around each galaxy using PSFEx, and is provided to SourceXtractor++ with each image in order to be convolved with the model before computing the distance to the data image, that is used to perform the model-fitting. Because the EFIGI galaxies are typically larger than 1 arcmin, the PSF has little impact except in the central parts of steep profiles, and for texture (HII regions, dust) on scales on the order of the seeing (∼ 1.3 arcsec) of the SDSS images.

[1] https://vizier.u-strasbg.fr/

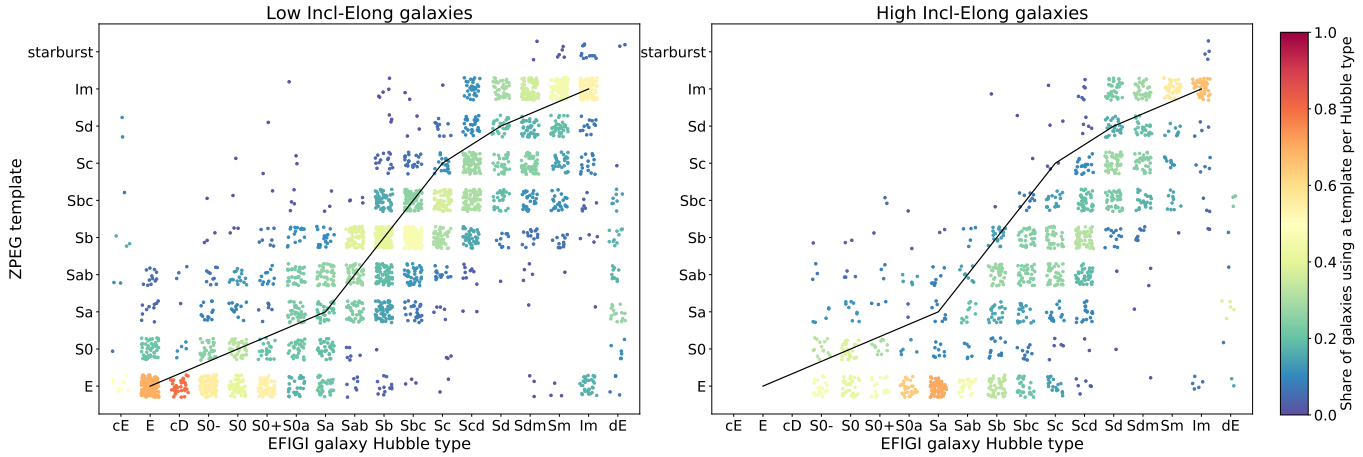

Fig. 1: Comparison of the EFIGI Hubble type to the spectral type defined by the SED template found by ZPEG to match the measured apparent magnitudes and redshift. The black solid line is the type identity line. The color represents the fraction of galaxies of a specific Hubble type that is best fitted by a given spectral template (sum of vertical fraction is 1 for each Hubble type). The left and right panels are restricted to EFIGI galaxies with `Incl-Elong` ≤ 2 and `Incl-Elong` ≥ 3 respectively, showing a dispersion between the morphological and spectral type as well as a systematic shift toward later spectral types for a given morphological type, due to disk inclination and internal dust.

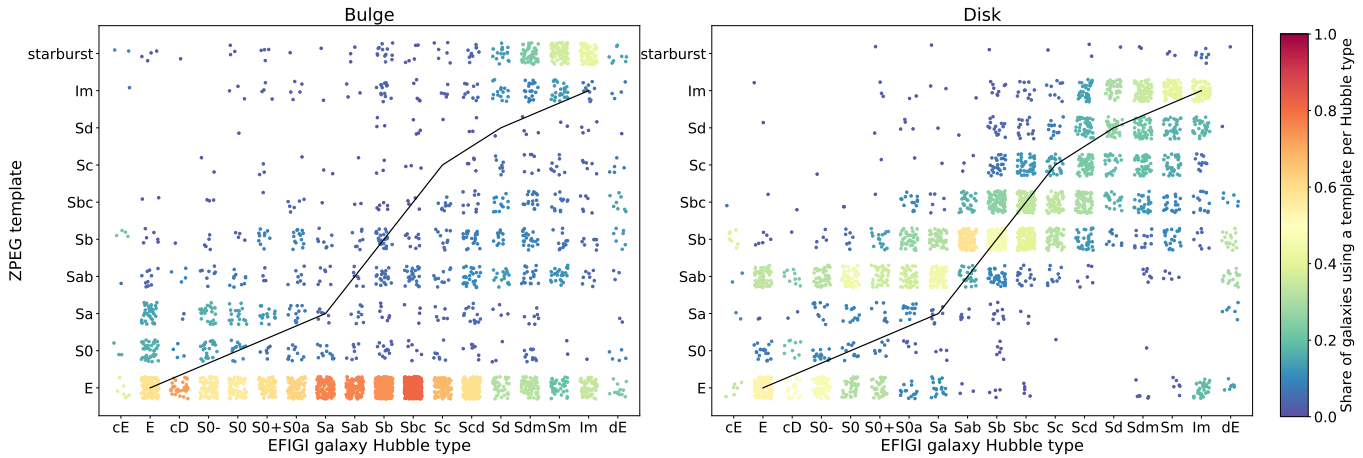

Fig. 2: Same as Fig. 1 for the bulges (left) and the disks (right) of EFIGI galaxies with `Incl-Elong` attribute values of 0, 1 or 2. For the bulges SED model-fitting, the E template is largely favored to fit the bulge magnitudes of all Hubble types having a bulge component, from E to Sc; while the later types Sd to Im are shared between the E and the starburst template. For the disks, there is a wider distribution around the identity line, as for whole galaxies in Fig. 1.

3.2. SED model-fitting with ZPEG

3.2.1. Absolute magnitudes, stellar masses and star formation rates

To obtain the absolute (rest-frame) magnitudes and colors of EFIGI and MorCat galaxies, we use ZPEG (Le Borgne & Rocca-Volmerange 2002). This software receives as inputs the apparent magnitudes in the NUV, g, r, i bands for EFIGI galaxies measured by SourceXtractor++ (with NUV only when available from GALEX) and in the NUV, u, g, r, i and z bands for MorCat galaxies measured by SExtractor, as well as the HyperLeda redshifts corrected for Virgocentric infall (see Sect. 2.2 of de Lapparent et al. 2011). ZPEG fits to these apparent magnitudes the SEDs of families of templates from the PEGASE.2 library (Fioc & Rocca-Volmerange 1999), including all scenarios adjusted to the major galaxy types; they are mainly characterized by specific functions for the evolution of the star formation rate with time: E, S0, Sa, Sab, Sb, Sbc, Sc, Sd, Im, starburst. There is an age constraint on these templates with all types from E to Sd, Im and starburst having a minimum age of 11 Gyr, 9 Gyr and 0 Gyr respectively. ZPEG offers the option for a variable internal extinction; we however deactivated this option because it leads to larger discrepancies between the spectral and morphological types (see below). Through this SED model-fitting, ZPEG yields the age of the scenario corresponding to the best-fit template, as well as several galaxy parameters including the mean stellar age, the stellar mass M_* and the star formation rate SFR, from which we derive the specific star formation rate sSFR = SFR/M_*.

To test the robustness of this SED model-fitting, Fig. 1 compares the Hubble types as classified in EFIGI to the spectral type of the best fit template determined by ZPEG, which we note "spectral type" hereafter. Because the presence of dust and the inclination of a galaxy disk are two factors that lead to its reddening, we split EFIGI galaxies at an `Incl-Elong` at-

tribute value of 2, corresponding to an inclination of 70° for disks and an elongation of 0.7 for disk-less galaxies (see Baillard et al. 2011). The left panel of Fig. 1 is restricted to galaxies with `Incl-Elong` ≤ 2 and show that face-on and galaxies with intermediate `Incl-Elong` have a spectral type approximately "aligned" with their morphological type with some scatter and a systematic offset toward earlier spectral types for a given morphological type, likely to be due to internal reddening. For edge-on and nearly edge-on galaxies corresponding to `Incl-Elong` ≥ 3, shown in the right panel, the stronger systematic shift toward earlier spectral types illustrates the additional effect of disk inclination, which also increases the reddening due to dust.

3.2.2. SED of bulges and disks

To evaluate whether the multiband bulge and disk apparent magnitudes obtained by the SourceXtractor++ bulge and disk profile-fitting can be used to perform ZPEG SED model-fitting to derive separate parameters for these components, one must evaluate whether the PEGASE.2 SED templates make sense for a bulge and a disk across all types in the Hubble morphological sequence. The following arguments favor this unconventional use of the PEGASE.2 templates :

1. For elliptical galaxies, the bulge component dominates the galaxy profile with B/T close to 1, the disk component is essentially used in the fits to correct some irregularities in the observed profile compared to the Sérsic profile, or to account for a disk component that was not visible from SDSS images during the visual classification (these objects may be of type S0$^-$).
2. For lenticular galaxies, the SourceXtractor++ photometry shows that the bulge and disk colors are similar (Quilley & de Lapparent, *in prep.*), so the S0 PEGASE.2 template should be appropriate for both components as long as it is appropriate for the whole galaxy.
3. For early-type spirals, Allen et al. (2006) showed that the light profile of bulges are similar in terms of color and profile slope (Sérsic index) to those of elliptical galaxies, which justifies the use of the E template for these central components.
4. For the early and intermediate type spirals (Sa to Scd), we assume that the presence of a bulge simply shifts the disk template to a later type compared to that for the whole galaxy, and we use the a posteriori quality of the SED fits to validate this argument (see below).
5. For very late-type spirals (Sd, Sdm, Sm) and irregulars, with very weak or no bulge, SourceXtractor++ yields very low values values of $B/T \leq 0.01$, so the disk component constitutes the whole galaxy and can be modeled by the Sd or Im scenarios. In the cases where a strong HII region is modeled by a bulge component, it is expected to be best fit with the Im or starburst template.

We therefore apply the ZPEG SED model-fitting on the bulge and disk apparent magnitudes in the g, r, and i bands derived from the SourceXtractor++ bulge and disk modeling with the same PEGASE.2 templates as for the entire galaxy, which allows us to obtain estimates of absolute magnitudes and stellar masses for the bulge and disk components separately. Fig. 2 shows that bulges are better fitted by E spectral templates down to spiral Hubble types Sd, but the E template competes with the Im or starburst spectral templates for Sdm, Sm and Im Hubble types, in agreement with the fact that these very late types have very weak or no bulge, hence a star-forming region is sometimes modeled as such. In contrast the disk of S0 and Sa Hubble types are best fitted by E or Sab spectral types, and those of Sab to Im Hubble types by Sb or later spectral types. The 1-type mismatch between the Hubble types and PEGASE.2 templates may call for a readjustment of the PEGASE.2 scenarios, as the EFIGI catalog was not available when the scenarios were designed. Fig. 2 is further discussed in Sect. 4.3.3.

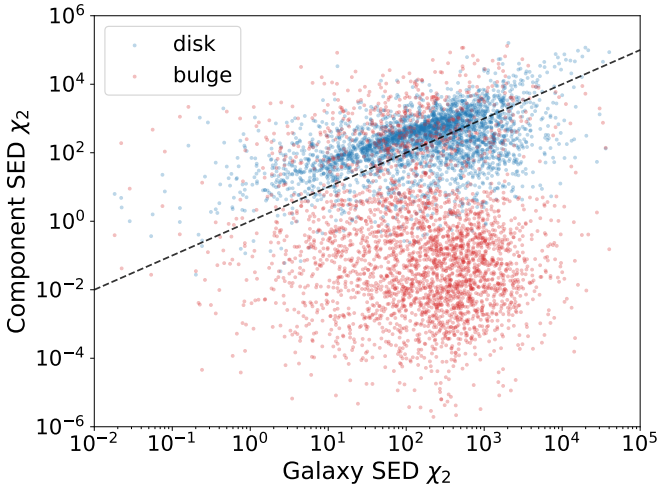

Fig. 3: Distribution of χ^2 of ZPEG best-fit PEGASE.2 template with the EFIGI *NUVgri* photometry (or only *gri* when *NUV* is not available) for whole galaxies compared with the χ^2 obtained with the *gri* only photometry of the bulge and disk components extracted with SourceXtractor++ by bulge and disk modeling. The 1 to 3 order of magnitude lower χ^2 for the bulges compared those for the whole galaxies, and the factor of 2-3 higher for disks validate the use of templates designed for whole galaxies.

Fig. 3 shows the distribution of χ^2 derived by ZPEG for the best-fit template to each EFIGI galaxy compared to the χ^2 for the best-fit templates to the bulge and disk components separately. First, it is noteworthy that the χ^2 of the majority of bulges (in red), that are best-fit by the E template (as shown in the left panel of Fig. 2), is $\sim 2-5$ orders of magnitude lower than the χ^2 for the whole galaxy-template match, reinforcing the fact that the PEGASE.2 elliptical template is an appropriate description of any real bulge of all morphological types in EFIGI (only galaxies with a very small, hence unreal bulge, enclosing a few percents of the galaxy light have a ratio of bulge to total SED χ^2 in the range 0.1 to 100 - see Sect. 4.3.3). The blue cloud of points in Fig. 3 shows that the χ^2 for the disk is predominantly higher than for the whole galaxy, by a factor 3 to 4, but there are only 3% of galaxies for which the disk to galaxy χ^2 ratio is $\gtrsim 10$, and 22% of galaxies for which the ratio is $\lesssim 0.1$. Using templates outside of their intended range of application explain these slightly poorer fits. Note also a tail of 5% of galaxies for which the disk to galaxy χ^2 ratio is $\lesssim 0.01$, indicating that for these galaxies there is an important gain in the bulge and disk decomposition in terms of SED fitting. Altogether, these results lend joint credibility to our bulge and disk decompositions using SourceXtractor++, and to their SED fitting using ZPEG and PEGASE.2 templates.

4. Results

4.1. How galaxy fluxes and colors change with morphology

In the left panel of Fig. 4, we plot the $NUV - r$ absolute color versus the absolute r magnitude (denoted M_r hereafter) for the 1848 EFIGI galaxies with GALEX NUV photometry. Galaxies are grouped in three main regions: on one hand, the Red Sequence around $NUV - r = 6$ and the Blue Cloud containing galaxies bluer than $NUV - r = 4$ and extending toward very faint, and very blue galaxies; both regions define the well-known galaxy population bimodality, with specific characteristics like the greater extent of the Blue Cloud compared to the Red Sequence; on the other hand, one can observe between the two high density regions a low density one, originally named Green Valley, and first studied by Martin et al. (2007), Wyder et al. (2007) and Salim et al. (2007). We note that the EFIGI Green Valley (that we define in Sect. 4.1.2 as $NUV - r \in [3.77, 5.71]$) extends further up than the [4, 5] interval quoted in the review of this region by Salim (2014): this author finds a Red Sequence at lower, hence bluer values of $NUV - r$ than in our analysis, with an approximate shift of $\Delta_{NUV-r} \simeq 0.75$, whereas there is no shift in our respective Blue Clouds. This prevents a simple interpretation in terms of difference between our respective samples, or the SDSS photometry and ours (using SourceXtractor++). We point out that the errors in the absolute magnitudes and colors are plotted on all graphs of this study: they are mostly very small and indistinguishable from the points except for objects with a low NUV flux, hence predominantly in the Red Sequence.

The left panel of Fig. 4 suggests that each Hubble type populates a specific part of the color-magnitude plane. Because disk inclination tends to redden galaxy colors (Driver et al. 2007), we show in the right panel of Fig. 4 the same graph restricted to EFIGI galaxies with `Incl-Elong` ≤ 2: this corresponds to face-on or intermediate inclination galaxies for disks, that is $\leq 70°$, and elongation ≤ 0.7 for disk-less galaxies; this removes highly inclined disks, but keeps all E galaxies as their values of `Incl-Elong` are between 0 and 2 (Baillard et al. 2011). This leads to a "cleaner" sample in which galaxies of each morphological type are less dispersed in $NUV - r$: for example, Sc galaxies shown as cyan symbols in Fig. 4 mostly have $NUV - r \lesssim 3.7$ in the right panel of Fig. 4, whereas they spread above $NUV - r = 5$ in the left panel. We therefore choose to focus on galaxies with `Incl-Elong` ≤ 2 hereafter.

The right panel of Fig. 4 better shows a remarkable coherence of the morphological sequence along the color-magnitude diagram: types occupy specific ranges of color and magnitudes, with these ranges being contiguous and overlapping. This can be better seen using the mean colors and magnitude of each morphological type with `Incl-Elong` ≤ 2, plotted in Fig. 5. All ellipticals and $S0^-$, S0 and $S0^+$ lenticulars populate the Red Sequence. Note also the presence of dwarf ellipticals (dE) at absolute magnitude $M_r \sim -18$, as faint as Sm galaxies, whereas they have $NUV - r \sim 5$, as red as S0a galaxies. The Green Valley is dominated by galaxies of the intermediate type between lenticulars and spirals, that is S0a, as well as of the earliest spiral type, Sa, with fractions of 57.5% and 72.4% resp. of these types in the $NUV - r$ interval [3.77, 5.71] (see right panel of Fig. 4 and Fig. 5). The S0a galaxies have a morphology similar to lenticulars in terms of bulge-to-total ratio and old stellar population, with some additional evidence for tenuous and blue portions of spiral arms, hence star formation, within the disk. Moving along the color-magnitude diagram, Figs. 4 and 5 show that the Blue Cloud is populated by immediately later spiral types, that is from Sab all the way to Sm, followed by the Magellanic Irregulars (Im; referred to as irregulars hereafter), each type being bluer and fainter as one advances along the Hubble sequence.

Altogether, the Hubble sequence displays an "S" shape in the color-magnitude diagram. Both panels of Fig. 4 show that moving back up the Hubble Sequence starting from the irregulars, the "S" shape results from a strong increase in M_r over 8 magnitudes across the Blue Cloud, with a progressive but weak reddening from $NUV - r = 2$ to 3.5. Then there is an abrupt and vertical change of $NUV - r$ color between 4 and 5.5 across the Green Valley. The third and final trend is again a strong luminosity increase by 4 magnitudes along the Red Sequence, when going from S0 to ellipticals, correlated to a weak reddening. Moreover, lenticulars have redder colors (in the interval [5.5, 6.5]) than early spiral types (Sa-Sab), but they are spread over the same magnitude range with $M_r \in [-23.0, -20.0]$, spanning the Green Valley; on the other hand, ellipticals have slightly redder colors in the interval [5.75, 7] and significantly brighter magnitudes ($M_r \in [-24, -21]$) compared to lenticulars and early spirals. There is, however, a lower luminosity tail in lenticular galaxies than in the Sa type dominating the Green Valley. Indeed, the mean magnitude of S0a, $S0^+$, $S0^-$ galaxies are 0.73, 0.58 and 0.57 magnitude fainter respectively than for Sa galaxies. van den Bergh (1990) already noticed the lower-luminosity of S0 galaxies and inferred that only a fraction of lenticular galaxies, the most luminous ones, could be seen as an intermediate state between E and Sa galaxies, and that the S0 class was likely to group objects with different evolution histories. See Barway et al. (2007), Barway et al. (2009), and Barway et al. (2013) for further characterization of faint and bright S0 galaxies.

Importantly, Fig. 5 shows that the S shape of the color-magnitude diagram could be parameterized with the mean Hubble type: displacements along the diagram can be defined as a monotonous function of the Hubble type. This smooth and continuous transition between morphological properties and types of galaxies was already shown by van den Bergh (2007), but the use of only optical colors prevents this analysis from detecting the Green Valley (see Sect. 4.1.3). Hereafter, we refer to the **knee** of the Green Valley as the region of the graph where the most luminous and bluest Sab, Sb, Sbc, Sc, and Scd galaxies reside, that is for $M_r \in [-23, -21]$ and $NUV - r \in [2.3, 3.5]$, as it is the pivotal region of the S shape color-magnitude sequence between variations dominated by a change in magnitude (Blue Cloud) and by a change in color (Green Valley; see also Sect. 4.1.2).

Moreover, the equality we find between the Red Sequence and the early-type galaxies of the Hubble Sequence (E+S0) contradicts the statement made by Salim (2014) that the Red Sequence can not be equated to early-type galaxies because it includes almost all of Sa and Sb galaxies. However, he refers to the results of Gil de Paz et al. (2007), in which the considered Sa-Sb galaxies, from the GALEX Ultraviolet Atlas of Nearby Galaxies, do have intermediate $FUV - K$ colors, in agreement with the results obtained here for EFIGI sample. Conselice (2006) also show that Green Valley galaxies are predominantly of Sa and Sab types, using $U - B$ colors of RC3 galaxies, however within the limitations of using only optical colors (see Sect. 4.1.3). Bremer et al. (2018) also describes the Green Valley population as dominated by early-type spirals.

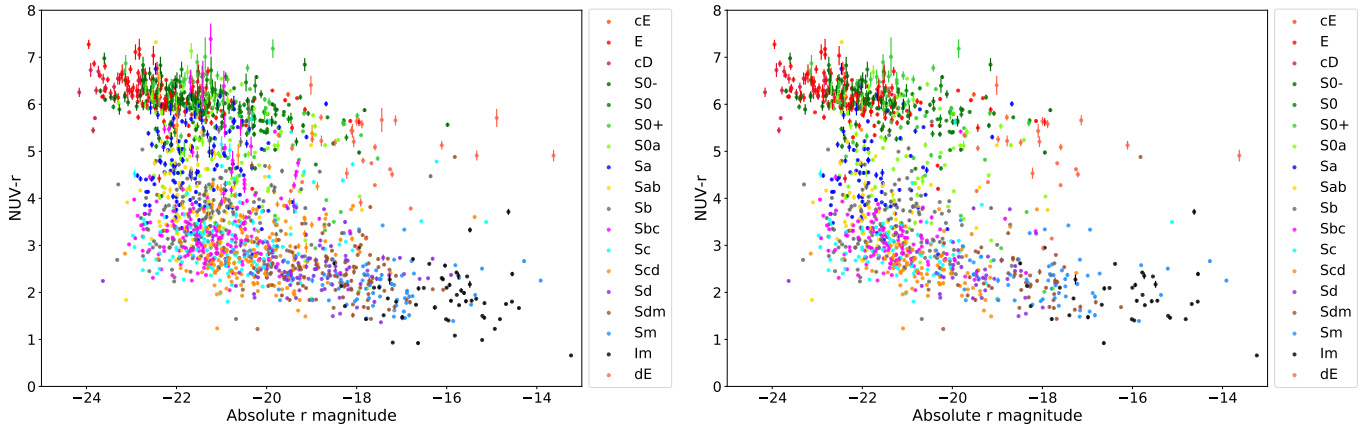

Fig. 4: Color-magnitude diagram defined as $NUV - r$ absolute color versus r absolute magnitude for the 1848 EFIGI ∩ GALEX galaxies at all inclinations (**left panel**), and with `Incl-Elong` ≤ 2 (**right panel**). The color of the points indicates their Hubble Type as classified in the EFIGI morphological catalog. The distributions of galaxies in both graphs exhibit the bimodality between the ellipticals and lenticulars in the upper region (the Red Sequence), and spirals of type Sab and later in the lower region (the Blue Cloud). A lower density region (the Green Valley) connects both structures, with galaxies of types S0a and Sa.

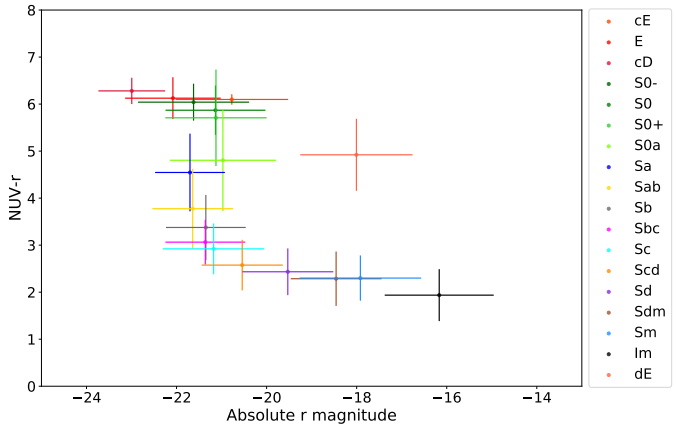

Fig. 5: Mean absolute color $NUV - r$ versus mean r absolute magnitude for each Hubble type for EFIGI ∩ GALEX galaxies with `Incl-Elong` ≤ 2; the error bars represent the r.m.s. deviation within each type. The Hubble sequence draws an "S" shape that could be parameterized monotonously by the mean Hubble type, with the exception of dE at $(-18, 4.9)$.

4.1.1. From EFIGI to MorCat: The representative galaxy density

In order to evaluate how the relative galaxy densities seen in the Red Sequence, Green Valley and Blue Cloud of Fig. 5 are affected by the type selection biases of the EFIGI morphological sample, we use the magnitude-limited MorCat sample (see Sect. 2). One must correct for the fact that only 3149 of the 20,126 MorCat galaxies have a NUV magnitude in GALEX, and that the fraction of galaxies with NUV data varies with absolute r magnitude (M_r). We thus compute the distribution of M_r for both MorCat and MorCat ∩ GALEX and for each bin of M_r (of width 1, between -24 and -14) we randomly draw galaxies from MorCat ∩ GALEX to create a subsample with a similar M_r distribution as the full MorCat sample (based on a constant fraction of galaxies with NUV equal to that in the bin where it is the lowest). The resulting $NUV - r$ distribution is shown in the left panel of Fig. 6. The three major features of the EFIGI S shape color-magnitude diagram (Fig. 4) remain present when using the magnitude-limited MorCat sample, with similar characteristics: the Red Sequence has higher density than the Blue Cloud, and they are separated by an under-dense region, the Green Valley.

As the dispersion in the $NUV - r$ color for the EFIGI data can be reduced using the `Incl-Elong` attribute (see Fig. 4), we use the aspect ratio of the isophotal profiles of MorCat galaxies measured by SExtractor to identify highly inclined disk galaxies. To this end, we perform a polynomial fit of the aspect ratio as a function of the `Incl-Elong` attribute for EFIGI galaxies. We obtain that `Incl-Elong` ≤ 2 can be approximated by an aspect ratio ≥ 0.61, and show in the right panel of Fig. 6 the resulting color-magnitude distribution for the corresponding MorCat subsample. The lower density of the Green Valley compared to the two dense regions appears accentuated.

Fig. 7 shows the $NUV - r$ histograms for the right panels of Figs. 4 and 6 (restricted to weakly elongated or weakly inclined galaxies): the peaks of the Red Sequence and Blue Cloud are located at identical $NUV - r$ colors in both EFIGI and MorCat, hence are not sensitive to the EFIGI type selection effects. If one considers only bins with more than ∼ 10 galaxies, they are represented in similar proportions for MorCat and EFIGI for $NUV - r \in [3.5, 6.0]$. However, the bluest EFIGI galaxies, with $NUV - r \lesssim 3.5$ (that is spiral types later than Sb) are overrepresented compared to MorCat. This is due to the fact that EFIGI was created so as to represent densely every morphological type, including the rarer late spirals and irregulars.

4.1.2. Abrupt reddening across the Green Plain

In the right panel of Fig. 6, we delineate as dashed lines regions of the Red Sequence, Green Valley, and Blue Cloud in the common $M_r \in [-22.5, -20]$ interval: comparison of their $NUV - r$ extent and galaxy densities shows that the Green Valley is characterized by a significant width and low and nearly flat density over ∼ 2 magnitudes in $NUV - r$. We therefore rename it the "Green Plain" hereafter, and further characterize this region and justify this name change.

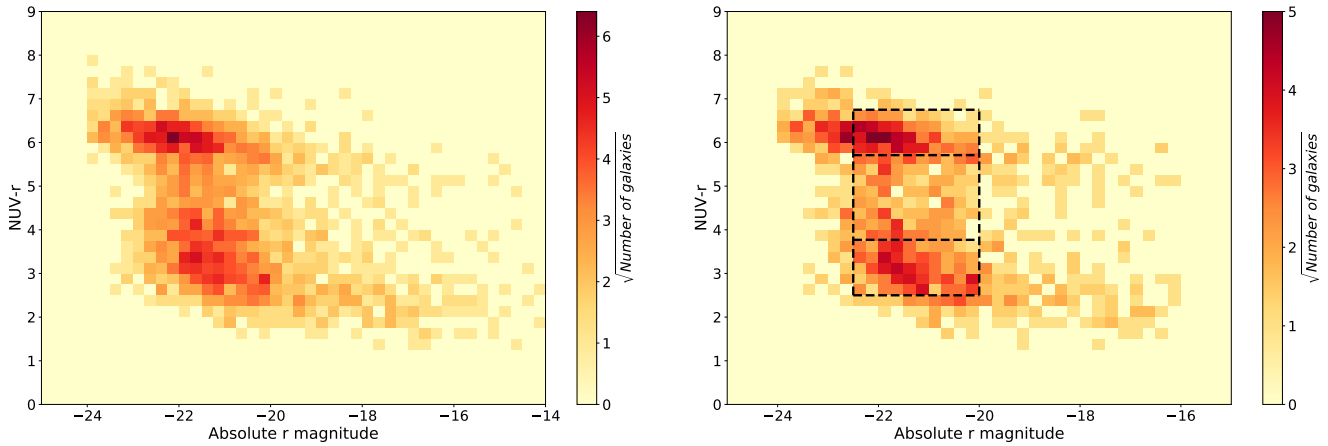

Fig. 6: MorCat color-magnitude diagrams in square cells of color and magnitude of length 0.25. To retrieve a representative picture of nearby galaxies, galaxies were randomly drawn from the MorCat ∩ GALEX sample in 1 magnitude intervals of M_r, in order to match the M_r distribution of MorCat. **Left panel** shows the distribution of all MorCat galaxies, whereas the **right panel** is restricted to galaxies with an aspect ratio ≥ 0.61, in order to exclude highly inclined and edge-on disks. Both graphs display the bimodal distribution of galaxy population with the two density peaks of the Red Sequence and the Blue Cloud, separated by the Green Valley or Green Valley. The dashed lines in the right panel delimit the regions of the Red Sequence, the Green Valley, and the Blue Cloud that are respectively used in Sect. 4.1.2 to illustrate the stretching of the $NUV - r$ that generates the Green Valley, and lead us to rename it Green Plain.

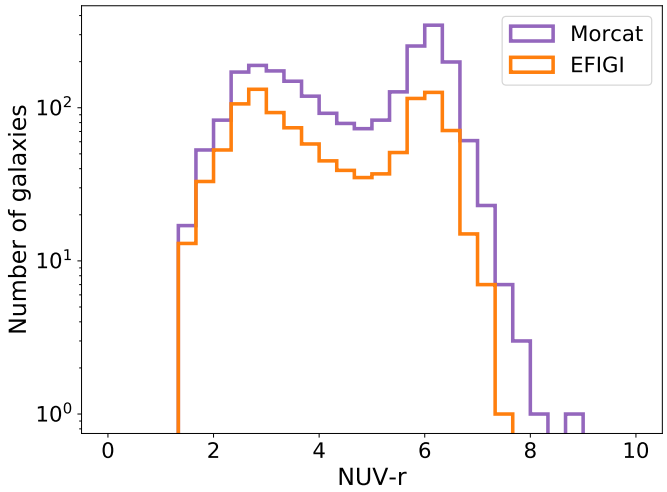

Fig. 7: $NUV - r$ color distribution for all MorCat ∩ GALEX galaxies with aspect ratio ≥ 0.61 (purple), and for all EFIGI ∩ GALEX with `Incl-Elong` ≤ 2 (orange). One can see that the galaxy bimodality is present in both samples with two peaks of density at $NUV - r \sim 2.5$ for the Blue Cloud, and ∼ 6.0 for the Red sequence, while the Green Valley corresponds to the under-density for $NUV - r \in 3.7, 5.7]$.

Let us scrutinize the mean colors of morphological types across the Green Plain in Fig. 5. In the approximate center of the Green Plain lie the S0a and Sa types (from top to bottom; order also used hereafter), separated by only 0.26 in $NUV - r$. Immediately above and below are types $S0^+$ and Sab, respectively separated by 0.90 and 0.78 from the $S0^+$ and Sab respectively. These wide steps cause the large color extent of the Green Plain. Then the next color steps to the outside types shrink to 0.16 and 0.40 for types S0 and Sb, respectively; the average of these steps is 0.28, comparable to the step between the central types. If one scales down both stretched intervals $S0^+$-S0a and Sa-Sab to 0.28, the full $NUV - r = [3.77 - 5.71]$ interval from the mean Sab to the mean $S0^+$ color shrinks from 1.94 down to 0.84, that is by a factor of 2.36.

The mean colors 5.71 and 3.77 of types $S0^+$ and Sab, respectively, are those used to split regions of the Red Sequence ($NUV - r \in [5.71, 6.75]$), Green Plain ($NUV - r \in [3.77, 5.71]$) and Blue Cloud ($NUV - r \in [2.5, 3.77]$), using the dashed lines in the right panel of Fig. 6. The number of galaxies within these color intervals and the common $M_r \in [-22.5, -20]$ interval are 377, 174 and 317 respectively. As such, the density of galaxies per color-magnitude cells is smaller in the Green Plain than in either the Blue Cloud or the Red Sequence by a factor of 1.8 or 2.2 respectively. Squeezing of the $NUV - r$ interval by the 2.36 factor proposed above would then increase the number density of MorCat Green Plain galaxies to levels similar or higher than in the Red Sequence or the Blue Cloud. With this higher density of galaxies in the color-magnitude graph, this region would therefore not appear anymore as a Plain, but as a "bridge" connecting the Blue Cloud and the Red Sequence, with a region of similar galaxy density as both regions.

This rough calculation illustrates that the Green Plain is caused by a strong reddening rather than by a decrease in the number density of the corresponding morphological types. We show in turn in Sect. 4.2 that this reddening results from a strong fading in the specific star formation rate of the corresponding Hubble types. The larger $NUV - r$ color range seen in Fig. 5 for the Green Plain compared to the other 2 sequences could also be contributed to by a larger dispersion in color for the Green Plain morphological types that for other types. At last, the fact that S0a, and even more so, Sa and Sab galaxies may have a strong dust content visible in the optical, as shown in EFIGI (de Lapparent et al. 2011) could introduce an additional dispersion in the color to that due only to the star formation rate. The EFIGI classification shows a high dust content for Sb types (de Lapparent et al. 2011), which may also explain the stronger dispersion in color of the morphological types at the bright end of the Blue Cloud.

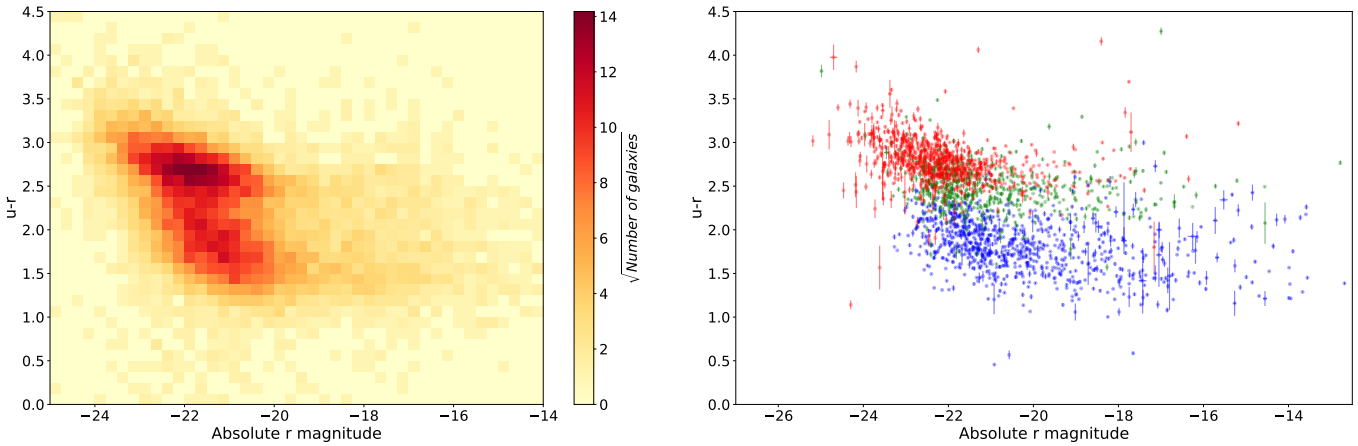

Fig. 8: Color-magnitude diagram for all MorCat galaxies with aspect ratio ≥ 0.61 using the absolute optical color $u-r$ and the absolute magnitude in the r band, from the SExtractor photometry. **Left:** number of galaxies in cells of both color and magnitude. Each cell has a width of 0.25 and a height of 0.125 dex. **Right:** Individual galaxies are plotted in blue for the Blue Cloud ($NUV-r < 3.77$), green for the Green Plain ($NUV-r \in [3.77, 5.71]$) and red in the Red Sequence ($NUV-r > 5.71$). The dichotomy between the Red Sequence and the Blue Cloud is still present but the Green Plain seen in $NUV-r$ (Fig. 4) has disappeared, being superimposed on the Red Sequence.

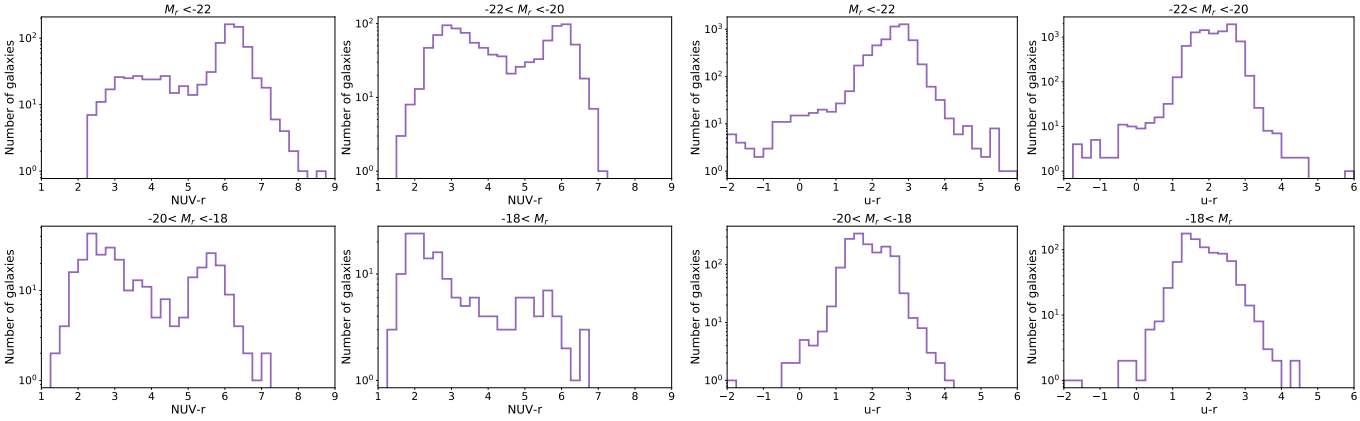

Fig. 9: Comparison of the $NUV-r$ and $u-r$ absolute color distributions for all MorCat ∩ GALEX galaxies with aspect ratio ≥ 0.61, in bins of absolute r band magnitude, using SExtractor photometry data. **Left:** The distribution of $NUV-r$ colors shows the bimodality caused by the presence of the Green Plain for all absolute magnitude intervals. **Right:** The Green Plain, hence the bimodality disappear in the distributions of $u-r$ colors for all r intervals.

4.1.3. Ultraviolet band for detecting the Green Plain

Optical-optical colors are often used to study the color-magnitude bimodality of galaxies (Strateva et al. 2001; Baldry et al. 2004; Schawinski et al. 2014), but Salim (2014) warns that the Green Plain can only be seen using an UV to optical color. For direct comparison of both approaches with a single sample, we examine the SDSS $u-r$ colors for MorCat, that are available for all galaxies, and compare with the colors based on the NUV data from GALEX, that are available for only $\sim 1/7$ of MorCat.

The left panel of Fig. 8 shows that for MorCat galaxies with aspect ratio ≥ 0.61, there is only one dense cloud of points extending from $u-r \sim 3$ to $u-r \sim 2.5$, with a diffuse tail of bluer galaxies down to $u-r \sim 1.5$. Both features extend to faint galaxies down to $M_r = -18$. If a red over-density (with $u-r \sim 3$ to 2.5) remains visible, the bimodality with an excess of blue galaxies is not as clear. Indeed, the right panel of Fig. 8 shows the color magnitude diagram in $u-r$, with the points color-coded according to their $NUV-r$ color and location within the Red Sequence (red), Green Plain (green), and Blue Cloud (blue), using the limits used in Sect. 4.1.2. One can see that in $u-r$, Green Plain galaxies have a comparable range of $u-r$ colors to Red Sequence galaxies, leaving no room in the $u-r$ versus r color-magnitude diagram for a transition region between the locus of quiescent and star-forming galaxies. This is due to the fact that the blue optical bands are only weakly sensitive to star formation, therefore the emission from old stars may dominate the $u-r$ color, in particular in the case of a significant bulge. Indeed the total $NUV-r$ range of the full color-magnitude diagram is ~ 5 magnitudes (Fig. 4) compared to ~ 1.5 magnitude in $u-r$ (Fig. 8). Moreover, the significant bulges in the Green Plain also weight the optical colors toward being redder (see Sect. 4.3.1). Therefore, we confirm that complementing optical data with a UV band is a requirement to study the Green Plain.

We then compare in Fig. 9 the $NUV-r$ (left panel) and $u-r$ histograms (right panel) of MorCat galaxies with aspect ratio ≥ 0.61as a function of absolute magnitude interval. Left panel of Fig. 9 shows two peaks in the $NUV-r$ distribution, one around $NUV-r \sim 6$ and another below $NUV-r = 3$, corresponding

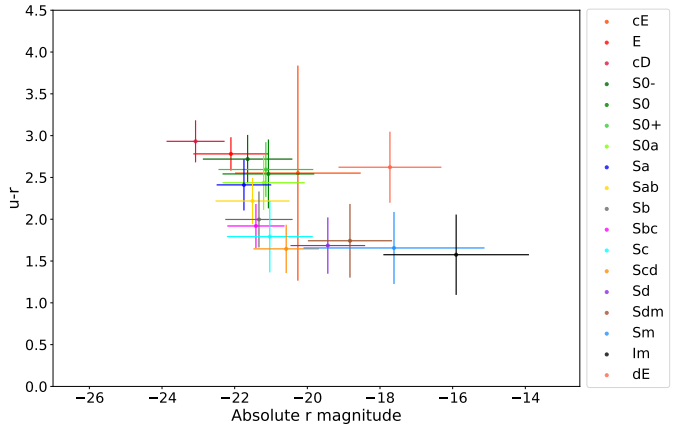

Fig. 10: Mean position of each Hubble Type in the color-magnitude diagram, using the absolute $u-r$ color for all EFIGI galaxies with `Incl-Elong` ≤ 2. One sees a similar "S" sequence as in $NUV-r$ color (see Fig. 5), but without the additional spacing of S0$^+$-S0a and Sa-Sab types that generates the Green Plain. The central point with very large error bars correspond to the rare cE types, whereas dE are located at $(-17.8, 2.6)$, away from the "S" sequence.

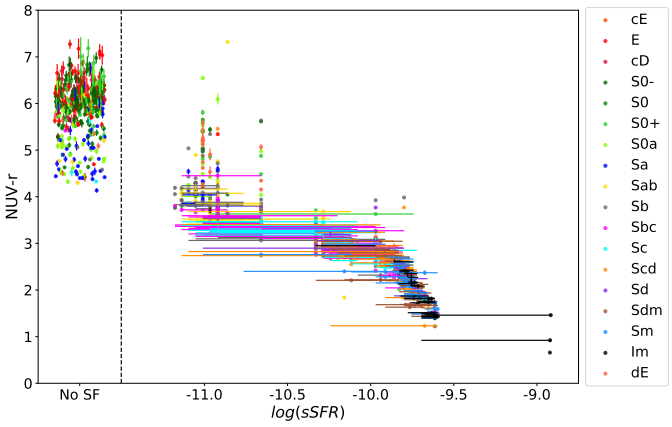

Fig. 11: Relation between the $NUV-r$ color and the sSFR inferred by SED model-fitting for EFIGI ∩ GALEX galaxies with `Incl-Elong` ≤ 2, showing the correlation between these two parameters, with the bluest galaxies being the most star forming, while red sequence galaxies mostly show no star formation. Intermediate colors are prone to larger uncertainties.

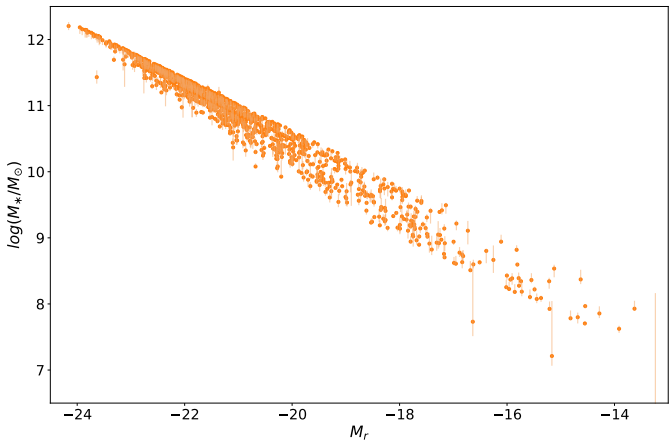

Fig. 12: Relation between the absolute magnitude in the r band M_r and the stellar mass M_* inferred by SED model-fitting for all EFIGI ∩ GALEX galaxies with `Incl-Elong` ≤ 2, showing a clear anticorrelation between these two parameters.

respectively to the Red Sequence and the Blue Cloud identified in Fig. 6. The $NUV-r$ "red" peak appears at all M_r magnitudes, whereas the "blue" peak appears at $M_r > -20$. The peaks of both features are shifted in M_r for different intervals of M_r because the two sequences are inclined in the $NUV-r$ versus r color-magnitude diagram (Fig. 6). In contrast, the right panel of Fig. 9 shows only one peak in the $u-r$ histograms, near $u-r=2.8$ for both bright magnitude intervals, and around $u-r=1.5$ for both fainter magnitude intervals (these peak values are in agreement with the results of Strateva et al. 2001 and Baldry et al. 2004).

The disappearance of the Green Plain in $u-r$ color is also illustrated in Fig. 10, which shows the mean position of Hubble types in the $u-r$ versus r absolute color-magnitude diagram. A similar S shape sequence as in $NUV-r$ is present (Fig. 4), spanning all morphological types. But the additional color spacings between morphological types S0$^+$-S0a and Sa-Sab in Fig. 5, that contribute to generate the Green Plain in $NUV-r$ are not present in $u-r$ (see also Sect. 4.1.2).

4.2. Specific star formation rates (sSFR) and stellar masses

The interest of the $NUV-r$ color is that it can be used as a proxy for the specific star formation rate (sSFR) of galaxies (Salim et al. 2007). Indeed we show in Fig. 11 the correlation between the sSFR inferred from SED model-fitting with ZPEG (see Sect. 3.2) and the $NUV-r$ color. Indeed, blue galaxies with $NUV-r<3$ are the most star-forming, with $\log(\mathrm{sSFR})>-10$, whereas most red galaxies with $NUV-r>5$ show no star formation ($\mathrm{sSFR}=0$), they are completely quiescent. Between these two extrema, there is a correlation between color and sSFR but it undergoes large uncertainties. This is partly due to the fact that there are only 10 ZPEG scenarios (see Fig. 3.2, which lead to a finite number of templates in terms of types and ages at each plausible redshift, therefore a limited number of values can be taken by the sSFR. The discreteness in the scenarios can be seen on the plot as vertical alignments of points. In the color range [3, 4] which corresponds to the reddest part of the Blue Cloud, the uncertainty in the sSFR is large because of the large step between the discrete values of sSFR for the subsequent Sab and Sb templates. Moreover, there is in the top-left of the plot an overwhelming majority of red galaxies that are completely quiescent while galaxies in the Green Plain ($NUV-r\in[3.75, 5.75]$) have either no star formation at all, or the lowest values available $\log(\mathrm{sSFR}[\mathrm{yr}^{-1}])\sim-11.0$; these values of sSFR also include some galaxies from both the bluest part of the Red Sequence and the reddest part of the Blue Cloud.

Another parameter inferred by the SED model-fitting which is useful to study galaxy evolution is the stellar mass. Fig. 12 shows that the stellar mass of EFIGI galaxies is strongly correlated to the absolute magnitude in the r band (we remind that in the ZPEG fits used in the present section, *gri* SourcExtractor++ photometry is used for all objects, complemented by the available NUV GALEX photometry for 1/2.4 of the objects, see Sects. 2.3 and 3.2.1.) Consequently, all the diagrams shown in the previous section have their equivalent in the sSFR vs M_*

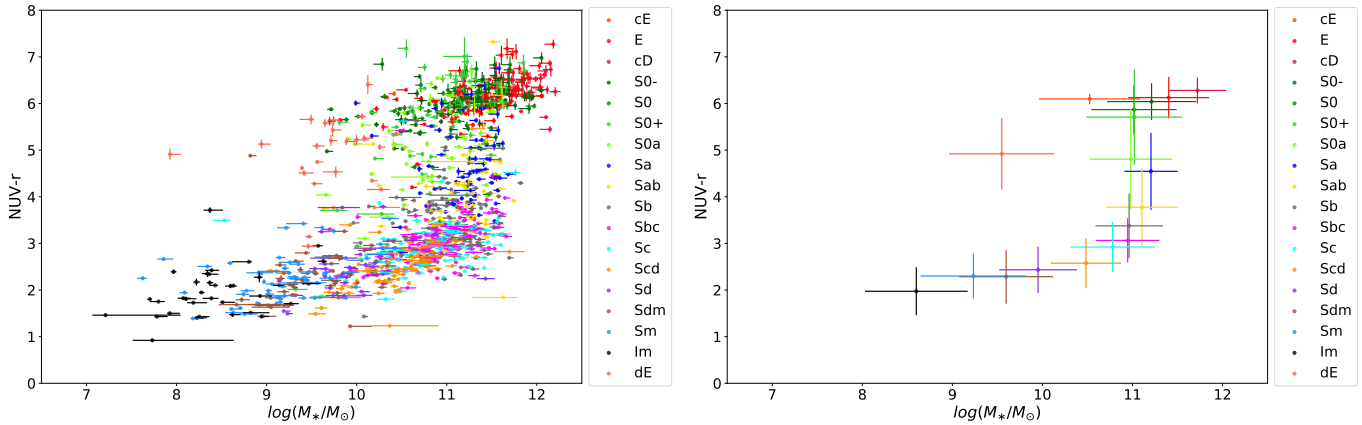

Fig. 13: Color-mass diagram. **Left:** Color-mass diagram for all EFIGI ∩ GALEX galaxies with `Incl-Elong` ≤ 2. The color of the points indicates their Hubble Type as classified in the EFIGI morphological catalog. The distribution of galaxies exhibits the bimodality between the ellipticals and lenticulars in the upper region (the Red Sequence), and spirals of type Sab and later in the lower region (the Blue Cloud). A lower density region (the Green Plain) connects both structures, with galaxies of types S0a and Sa. **Right:** Mean absolute $NUV - r$ color versus mean stellar mass for each Hubble type for EFIGI ∩ GALEX galaxies with `Incl-Elong` ≤ 2; the error bars represent the r.m.s. deviation within each type. The Hubble sequence draws an "S" shape that could be parameterized monotonously by the mean Hubble type, with the exception of dE at (9.6, 4.9).

plane. For clarity, and because our derived values of sSFR are discrete and related to the limited number of PEGASE.2 scenarios used in ZPEG, we continue to use $NUV - r$ color in the rest of the article. We however replace absolute r magnitude with the galaxy stellar mass M_*.

Fig. 13 shows in the left panel all EFIGI galaxies with `Incl-Elong` ≤ 2 in the color-mass diagram, whereas the right panel show the mean stellar mass and color per morphological type: both panels are almost mirror images of the right panel of Fig. 4 and of Fig. 5 respectively.

One noticeable difference is the larger error bars along the x-axis representing stellar mass (in the left panel), because masses inferred from the SED model-fitting are subject to larger uncertainties than those for the absolute magnitudes from which they were derived. The same observations that were made about the specific locations of each Hubble type, and how the Hubble sequence traces an S shape in Fig. 4 can be made from Fig. 13. There is also a correlation between the reddening of a galaxy and its mass growth in both the Blue Cloud and the Red Sequence, with an almost 4 orders of magnitude increase in stellar mass from the irregulars to the early spirals. In both sequences, mass growth along them translates into a morphological change between subsequent Hubble types, which is not the case in the Green Plain where mass growth at a fixed color happens at constant morphological type. In the Red Sequence, the stellar mass shift between lenticulars and ellipticals persists in their mass distributions, with mean masses located at $\log(M_*/M_\odot) \sim 11 - 11.2$ and $\log(M_*/M_\odot) \sim 11.4 - 11.7$ respectively (see also Fig. 14 below).

Moreover, Fig. 13 shows that the Green Plain is a low-density region of the color-mass diagram with a limited mass range of $\log(M_*/M_\odot) \in [10.5, 11.7]$ across the same wide color interval of $NUV - r \in [3.75, 5.75]$. Therefore, in order to study the quenching of galaxies from star-forming to quiescence, one must consider the full $NUV - r$ interval corresponding to the mass range $\log(M_*/M_\odot) \in [10.5, 11.7]$, that is $NUV - r = 6.8$ to 2.3: it represents as much as 83% of the full $NUV - r$ range (1.5 to 6.8) spanned by all galaxy types (see also Sect. 4.1.2).

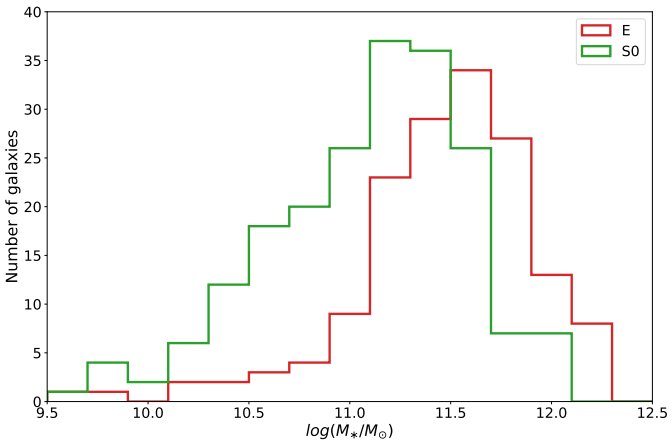

Fig. 14: Stellar mass distributions for EFIGI ellipticals (E and cD galaxies noted as E) and lenticulars (S0, S0$^+$ and S0$^-$ galaxies noted as S0) with `Incl-Elong` ≤ 2 in the Red Sequence. Ellipticals dominate the high-mass end of the Red Sequence, where $\log(M_*/M_\odot) > 11.5$, and lenticulars dominate the lower-mass part.

Lastly, Fig. 13 interestingly shows a common mass limit at $\log(M_*/M_\odot) = 11.7$ for all types from Sa to Sc, suggesting that there exists a critical mass limit over which spiral galaxies cannot exist. This limit is also visible in absolute r magnitude in Fig. 4. Therefore, if, through a major merger event a galaxy more massive than this limit is formed, it must end up in the Red Sequence and more often as an elliptical because the part of the Red Sequence with $\log(M_*/M_\odot) \geq 11.7$ contains 75% E and 25% S0, as shown in Fig. 14 presenting the distribution of stellar masses for both morphological types. This graph also shows that the $\log(M_*/M_\odot) = 11.7$ mass limit corresponds to the peak of the elliptical distribution, which also dominates the high-mass part of the Red Sequence. Using the magnitude-limited MorCat ∩ GALEX would probably yield different relative distributions of S0 and E types than with EFIGI ∩ GALEX, but the trend it-

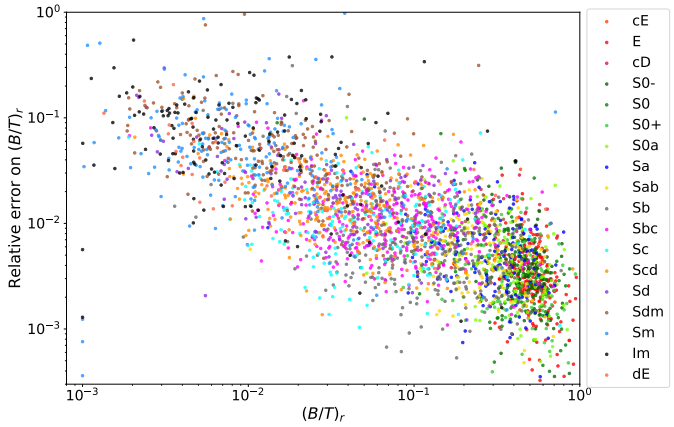

Fig. 15: Relative error on the bulge-to-total ratio in the r band $(B/T_{err})/(B/T)$ as a function of B/T for EFIGI galaxies with `Incl-Elong` ≤ 2, the color of the points indicating the galaxy Hubble type. There is a trend of lower B/T (that correspond to later-type galaxies) showing higher relative errors. All errors are small enough to not alter the results of the present analysis.

self cannot be a selection effect (see Quilley & de Lapparent, *in prep.*). This mass limit and the presence of mostly ellipticals beyond it, therefore supports a scenario in which mergers of massive spiral galaxies yields elliptical galaxies (see further discussion in Sect. 5.5).

4.3. Morphological changes around the Green Plain

4.3.1. Bulge growth

To further characterize the morphology of EFIGI galaxies using SourceXtractor++ parameters, we examine the derived bulge-to-total luminosity ratio B/T, as this parameter is key for determining of the morphological types. Indeed, early-type spirals are defined as having a larger B/T than their late-type counterparts, and ellipticals are pure bulge. Fig. 15 shows that the relative errors on B/T obtained through our SourceXtractor++ bulge and disk decomposition in the r band (see 3.1 describe a large range from $\sim 10^{-1}$ to $\sim 10^{-3}$, and depends strongly on the value of the B/T ratio itself. Obviously, higher B/T have smaller relative errors, with ellipticals and lenticulars having errors mostly on the order of 0.1%, while for late-type spirals with $B/T < 0.1$, it increases to around 10%. As we show below, the range of uncertainties in B/T plotted in Fig. 15 does not impair the subsequent analysis.

To examine B/T variation along the Hubble sequence, we show in the left panel of Fig. 16 the color-magnitude diagram in which the points are color-coded with the value of B/T in the r band. We find the highest values of B/T in the Red Sequence because it is populated by E galaxies that are almost pure-bulge, and lenticulars that have a dominant bulge. From early-type to late-type spirals, one can observe the expected decrease in the B/T, as this flux fraction is, with the pitch angle of the spiral arms, one of the criteria to classify spiral galaxies along the Hubble sequence (de Vaucouleurs 1959).

In our SourceXtractor++ bulge and disk decompositions (Sect. 3.1), the Sérsic component aims at adjusting a central concentration within the disk. For bulgeless galaxies (irregulars and very-late type spirals: Sd and later types), the sum of the Sérsic model and the exponential profile may be inappropriately used to model the whole galaxy in variable proportions, but with comparable effective radii. We identify these wrong fits by comparing the flux of the bulge component to the one from the zoom-in process described in Sect. 3.1, that is calculated as the excess flux in the center of the galaxy isophotal print (it may correspond to some star-forming regions in bulgeless galaxies). In the 3 bands g, r, and i, we discard these wrong fits and their erroneous B/T values by replacing them with the zoom-in estimate of B/T for all galaxies with $B/T > f(B/T_{zoom})$ and morphological types Sc and later (the f threshold function is empirically defined).

Through the bulge and disk SED model-fitting described in Sect. 3.2.2, one can convert fluxes to stellar masses for either the bulge or the disk of each galaxy. Right panel of Fig. 16 shows the distribution of the B/T stellar mass ratio in the color-mass diagram and consequently looks very similar to the left panel of Fig. 16, because of the strong anticorrelation between M_r and M_* (see Fig. 12): the fraction of mass in the bulge of a galaxy increases along the color-mass sequence from the Blue Cloud, through the Green Plain, and into the Red Sequence, hence from irregulars and late spirals to lenticulars and ellipticals.

To examine with more details the changes in the galaxy properties across the Green Plain, we zoom-in the region $\log(M_*/M_\odot) \in [10.5, 12.0]$, which also includes both the Red Sequence and the massive part of the Blue Cloud. In this series of graphs, we bin the bulge stellar mass values shown in Fig. 16 by intervals of 0.5 dex in $\log(M_*/M_\odot)$, and the $NUV - r$ color as [2.5, 4], [4, 5.5], and [5.5, 7] intervals, corresponding to the Blue Cloud, the Green Plain, and the Red Sequence, respectively. Within these cells defined by color and mass interval, we calculate the mean value of the B/T (left panel) and the bulge stellar mass (right panel). We also indicate the size of the sample N in each bin and estimate the associated error on the mean as the root-mean-square deviation within each cell divided by $\sqrt{N}$. We compared these errors with those derived from the quadratic mean of the errors on the individual points, and found that the latter range from similar to a factor of 10 lower than former, hence their use in the graphs.

One can see in the resulting graphs of Fig. 17 that the fraction of flux (left) and stellar mass (right) comprised in the bulge increases significantly through the Green Plain: it is doubled to tripled between the [2.5, 4.0] and the [5.5, 7.0] $NUV - r$ ranges (depending on the mass interval), and already almost doubled from [2.5, 4.0] to [4.0, 5.5], thus quantifying the fact that early-type spirals have a more prominent bulge than their late-type counterparts. We therefore confirm results by Bremer et al. (2018) that the bulge is already significant in the Green Plain, but contrary to their study, we show that bulge growth occurs all across this entire region (and does not precede the star formation decline). The use of dust corrected $u - r$ color rather than $NUV - r$, and the fact that the Galaxy And Mass Assembly (GAMA) survey is at more distant redshifts ($z < 0.2$), hence based on galaxies that are less resolved angularly than in EFIGI, might explain this discrepancy. One can further notice in both panels of Fig. 17 that there is no total mass effect on the fraction of luminosity and mass in the bulge in the Green Plain, similar to the morphological trend in and around the Green Plain, which is purely a trend in color (see Fig. 5 and Sect. 4.1). There is nevertheless a moderate increase in both panels of Fig. 17 with the total stellar mass across the massive end of the Blue Cloud, where mass growth is linked to morphological type change with a large dispersion (Sb to Scd), and across the Red Sequence due to the type transition from lenticulars to ellipticals. The fraction of light or mass in the bulge is therefore related to the morphology rather than to the galaxy stellar mass.

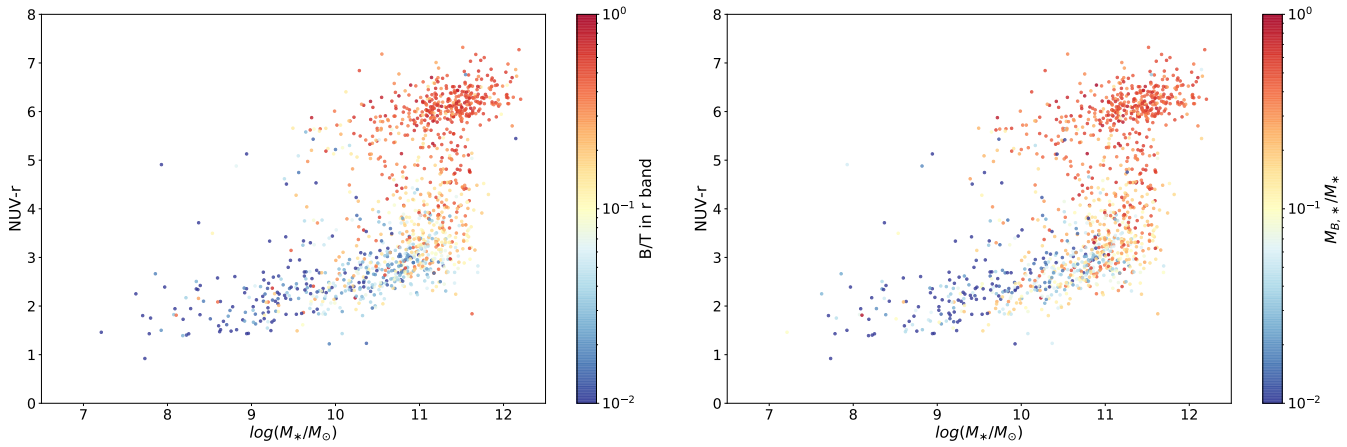

Fig. 16: Color-mass diagram for all EFIGI ∩ GALEX galaxies with `Incl-Elong` ≤ 2, in which the color of the points represents in the **left panel**, the bulge over total luminosity ratio (B/T) in the r band, and in the **right panel**, the bulge over total stellar mass ratio. Both graphs show the same trend of an increase from the tail of the Blue Cloud at the lowest stellar masses, to the Red Sequence.

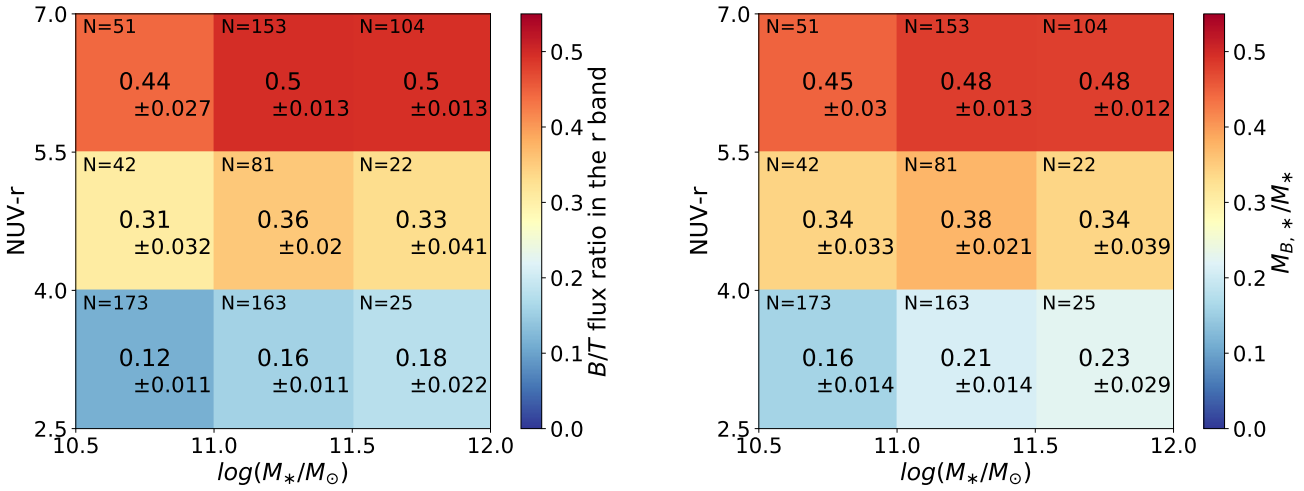

Fig. 17: Mean value of the bulge-to-total ratio for EFIGI ∩ GALEX galaxies with `Incl-Elong` ≤ 2 in color-mass cells of 0.5 dex in total stellar mass and 1.5 in $NUV - r$ color, and derived from Fig. 16. Only the bright part of the Blue Cloud, the Green Plain and the Red Sequence are shown. The associated error on the mean, and the number of galaxies in each cell are indicated. **Left:** Luminosity ratio in the r band, **Right:** Stellar mass ratio. There is a significant increase in the bulge-to-total ratio in both luminosity and mass with the $NUV - r$ color across the Green Plain, by a factor of $\sim 1.5-2.6$ and $\sim 2.1-3.6$ from the Blue Cloud to the Green Plain and the Red Sequence respectively. There is no effect with the galaxy stellar mass across the Green Plain, but a moderate one across the Red Sequence and sampled Blue Cloud.

To characterize the growth of the bulge mass $M_{B,*}$, the left panel of Fig. 18 shows its variation across the color-mass diagram: one can see a straightforward increase in the bulge stellar mass with the total galaxy stellar mass as an horizontal trend. As the bulge-to-total ratio of stellar mass also increases along the Hubble sequence, hence when going from the Blue Cloud through the Green Plain to the Red Sequence, and because there is on average a steady increase in total stellar mass from the irregulars to the ellipticals. One also expects an horizontal increase in the bulge mass across the massive part of the Blue Cloud, the Green Plain and the Red Sequence. The effect is indeed visible in the zoom-in graph of the right panel of Fig. 17; it is barely visible in the left panel of Fig. 18 due to the color-map encompassing several orders of magnitude to accommodate all of the galaxy populations. Indeed, the right panel of Fig. 18 confirms that in addition to the increase in bulge mass for more massive galaxies (horizontal gradient) there is an increase in bulge mass for redder galaxies, even at fixed total mass (vertical gradient).

4.3.2. Frequent bars in all disk galaxies

Bars are frequent and observed in all types of disk galaxies, that is both in spirals and lenticulars, as well as in Irregulars: a total of 52% of EFIGI galaxies from types S0$^-$ to Im have the `Bar Length` attribute > 0. They are an important dynamical feature to investigate when studying bulges, as they contribute to their formation by driving both stellar migration (Brunetti et al. 2011; Minchev et al. 2011; Di Matteo et al. 2013) and gas migration (Kormendy & Kennicutt 2004) toward the centers of galaxies. Fig. 19 shows the fraction of EFIGI barred galaxies in color-mass cells of the color-mass diagram after excluding E, cE, cD

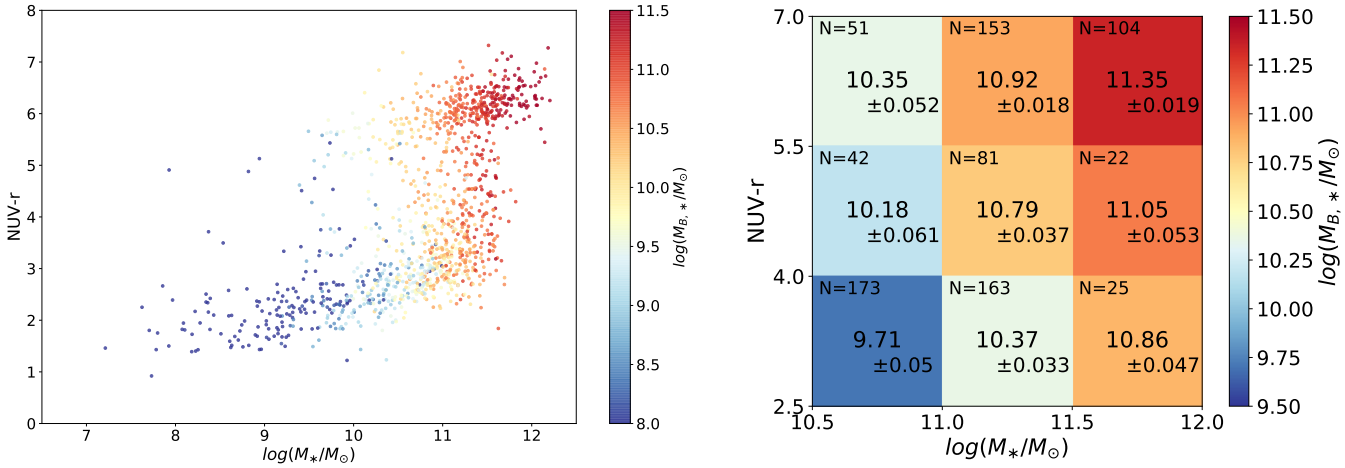

Fig. 18: Bulge stellar mass evolution in the galaxy color-mass diagram. **Left:** Color-mass diagram for all EFIGI ∩ GALEX galaxies with `Incl-Elong` ≤ 2, in which the color of the points represent the bulge stellar mass inferred from bulge and disk SED model-fitting. **Right:** Mean value of the bulge stellar mass in color-mass cells of 0.5 dex in total stellar mass and 1.5 in $NUV - r$ color. Only the bright part of the Blue Cloud, the Green Plain and the Red Sequence are shown. The associated error on the mean, and the number of galaxies in each cell are indicated. The bulge stellar mass increases with both the total stellar mass and the $NUV - r$ color of the galaxy.

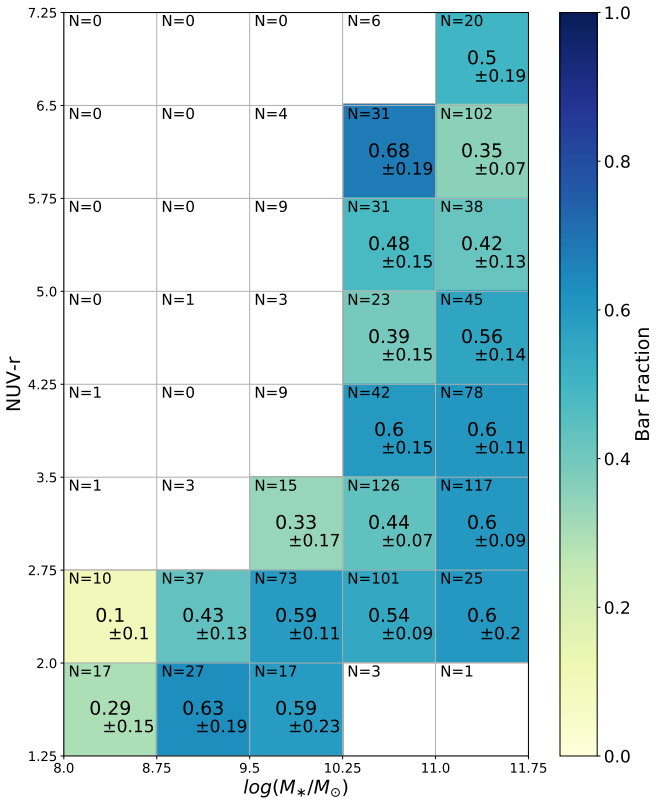

Fig. 19: Fraction of EFIGI ∩ GALEX galaxies with `Incl-Elong` ≤ 2 and types S0⁻ to Im having an attribute value `Bar Length` > 0, in color-mass cells of 0.75 dex in stellar mass and 0.75 in $NUV - r$ color, all the way from the Blue Cloud to the Red sequence. Apart from the low-mass irregulars having fractions below 30%, the fraction of EFIGI visually barred galaxies is large as it varies between 33% to 68% with a global mean of 52%, with no significant trend in either color or mass.

and dE types (as these types are not expected to host a bar due to the absence of a disk). The error in the plotted fractions is estimated as Poissonian, using $f_{err} = f * \sqrt{1/N_{barred} + 1/N_{total}}$ where $f = N_{barred}/N_{total}$.

In order to locate the dominant Hubble types within Fig. 19, Fig. 20 shows the three highest Hubble types fractions in cells of 0.75 dex in color and 0.75 dex in mass as well, the color of the bin corresponding to the dominant Hubble type. This graph illustrates the continuous spanning of the Hubble sequence seen in Fig. 5, and can help to further read the subsequent color-mass diagrams (using the same binning) to relate a variation in a parameter to the variation in morphological mix.

Comparison of Fig. 19 with Fig. 20 shows that except for the low-mass end of the Blue Cloud dominated by Irregulars, the junction pixel between the Green Plain and the Red sequence with a 0.35 ± 0.07 fraction of bars, in which lie many bar-less S0 or S0⁻, and the crook of the knee with a 0.33 ± 0.17 fraction of bars for only $N = 15$ objects, there is a high fraction of galaxies with a bar, from 0.39 ± 0.15 to 0.68 ± 0.19 (with no significant trend) across the entire Blue Cloud and Green Plain all the way to the lenticular galaxies of the Red Sequence. We therefore suggest that bars may play a role in the marked growth of B/T across the full color-mass diagram and in particular the Green Plain, as seen in Figs. 16 and 17. Additional mechanisms may nevertheless be needed to contribute to both the high bar fraction and the bulge growth. We suggest in Sect. 5.2 that mergers may play this role.

4.3.3. Disk reddening

By performing bulge and disk decomposition of galaxies from the GAMA survey, Bremer et al. (2018) highlight that the change in color from the Blue Cloud to the Red Sequence is driven by disk color. Examination of EFIGI disk parameters may also help us to understand the morphological transformations undergone by galaxies through the Green Plain. Fig. 21 shows the distribution of the absolute color $g - r$ of the SourceXtractor++ disk component in the color-mass diagram (individual points on the left, and values in cells on the right). Ideally, one should examine

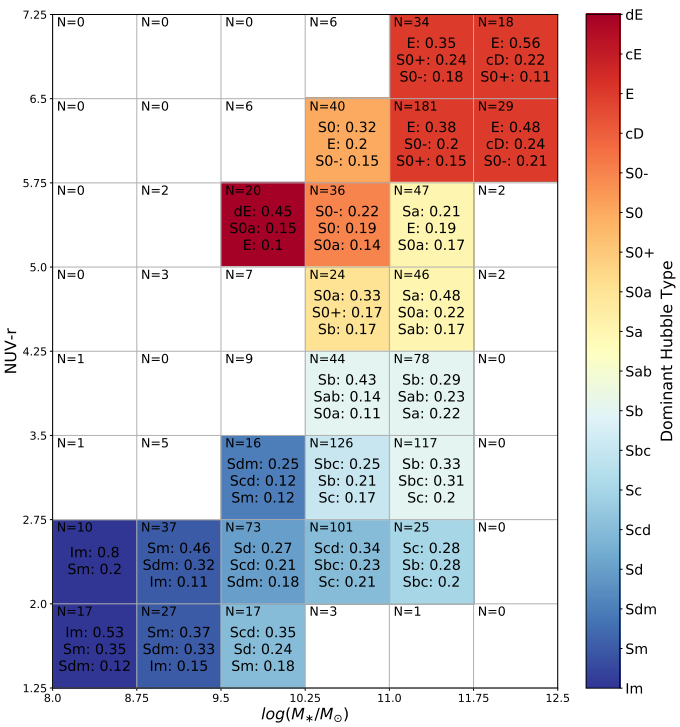

Fig. 20: Fractions of morphological types for EFIGI ∩ GALEX galaxies with `Incl-Elong` ≤ 2: the three most represented Hubble types are listed in color-mass cells of 0.75 dex in both color and mass. The associated error on the mean, and the number of galaxies in each cell are indicated. The color of the cells represents the most represented morphological type. Similarly to the effect seen in Fig. 13, the dominant Hubble type varies continuously along the color-mass diagram from the Im bluest and lowest mass galaxies to the blue and more massive spirals, through the massive and redder early-type spirals, and up to the red lenticulars and even more massive ellipticals.

the $NUV - r$ color of the disk in order to best trace star formation in the disk, but the GALEX NUV magnitude is only available for the whole galaxy. Left panel of Fig. 21 displays, similarly to Figs. 16 and 18, a trend related to the Hubble types: the disks of EFIGI galaxies are systematically redder for larger total $NUV-r$, and the continuous variation in Hubble types along the color-mass sequence implies that the reddening of the disk also takes place along the Hubble sequence, from late to early spirals, and all the way to lenticulars. Right panel of Fig. 21 also shows the mean values and associated r.m.s. deviation of the $g - r$ disk color in the Green Plain and around it, indicating a significant and $\sim$ 0.2 magnitude $g - r$ reddening of the disk as the total galaxy $NUV-r$ color increases (reddens). The frequent bars detected in all types of disk galaxies (see Fig. 19, Sect. 4.3.2) may play a role in the reddening of the disks of Blue Cloud and Green Plain galaxies.

The progressive disk reddening across the Blue Cloud can also be seen in right panel of Fig. 2: it shows that the *gri* photometry of EFIGI disks are on average best fitted by earlier and earlier PEGASE.2 templates from EFIGI galaxies with Hubble types from Im to Sa. In contrast, right panel of Fig. 2 shows that disks of lenticulars have red colors similar to those of ellipticals: indeed, the disks of S0$^-$, S0, S0$^+$ and E Hubble types are best fit by ZPEG with either the E or the Sab template, whereas the Sa and S0 templates rarely provide a good fit. While the necessity of a disk component in the bulge and disk profile modeling of a true morphological E galaxy may be due to the fact that a Sérsic profile is inadequate (and nevertheless yields nearly identical colors for both components), the fact that disks of lenticulars have colors preferentially described by the E and Sab templates as for the E galaxies indicates a remarkable color stability across the total stellar mass range covered by the Red Sequence, that is also seen in both panels of Fig. 21.

The right panel of Fig. 21 also shows a stable mean $g - r$ disk color for Green Plain galaxies, in the central $NUV - r$ row, whatever the total stellar mass is. A similar independence to total mass is seen in Fig. 17 showing the increasing fraction of luminosity or mass enclosed in the bulge from the tip of the Blue Cloud to the Red Sequence (except a weak increase with total mass in the massive end of the Blue Cloud). This independence of both the disk color and bulge ratio with total stellar mass, at constant $NUV - r$ color, results from the fact that the morphological type transitions in the Green Plain are characterized by strong color changes rather than stellar mass (see Fig. 5), to the contrary of the Blue Could and Red Sequence, in which type changes are dominated by total stellar mass variations.

Despite the major disk reddening detected for EFIGI galaxies across the color-magnitude sequence, left panel of Fig. 2 shows that it operates at a constant bulge color: all SourceXtractor++ bulges are best fit by PEGASE.2 E template (but see Quilley & de Lapparent, *in prep.*, for evidence of subtle variations in bulge colors with morphological type). There is also an exception for the latest types Sdm, Sm and Im; in these galaxies, the bulge is very faint or does not exist, and a bright HII region near the galaxy center may be fitted by the bulge component of the model (the resulting SEDs are then best fit by the Im or starburst template, see Sect. 3.2.2). The stability of bulge color, as long as the bulge is prominent enough to be fitted, confirms the results of Kim et al. (2016), also based on bulge and disk decompositions of SDSS images, who find a constant bulge color at all B/T (except for $B/T \leq 0.1$, where uncertainties dominate).

We now show that the $g-r$ disk reddening can be interpreted in terms of star formation fading of the disk. Because we do not have the disk NUV photometry, we cannot relate directly the $g-r$ disk optical reddening to a fading of the sSFR. However, Fig. 22 shows the relation between the absolute $NUV - r$ galaxy color and the absolute $g - r$ disk color. There is a tight correlation all across the Blue Cloud ($NUV - r \lesssim 3.75$), that is from types Im to Sb, with both the disk and the full galaxies undergoing reddening simultaneously. Because the Blue Cloud morphological types (Im to Sb) are disk dominated ($B/T \lesssim 0.1$, see Fig. 16), we can infer that the $NUV - r$ reddening of the entire galaxies must also be present in their disk component. As this $NUV - r$ reddening corresponds to a fading of star formation (and decrease in the sSFR; see Figs. 22 and 11), we can infer that the $g - r$ reddening of disk marks their star formation fading.

Fig. 22 also shows that the reddening of earlier type disks (Sab, Sa and S0a) from the knee and across the Green Plain occurs within a wide $g - r$ disk color interval ($\sim [0.6, 0.8]$ that is ~ 0.2 magnitude) while it also displays the stretching of $NUV-r$ due to the large range of sSFR across the Green Plain (discussed in Sect. 4.1.2). This graph illustrates the fact that the $NUV - r$ reddening and star formation fading across the Green Plain can also be detected in the optical via the disk $g-r$ fading. But as the early spiral types have significant bulge-to-total light and mass

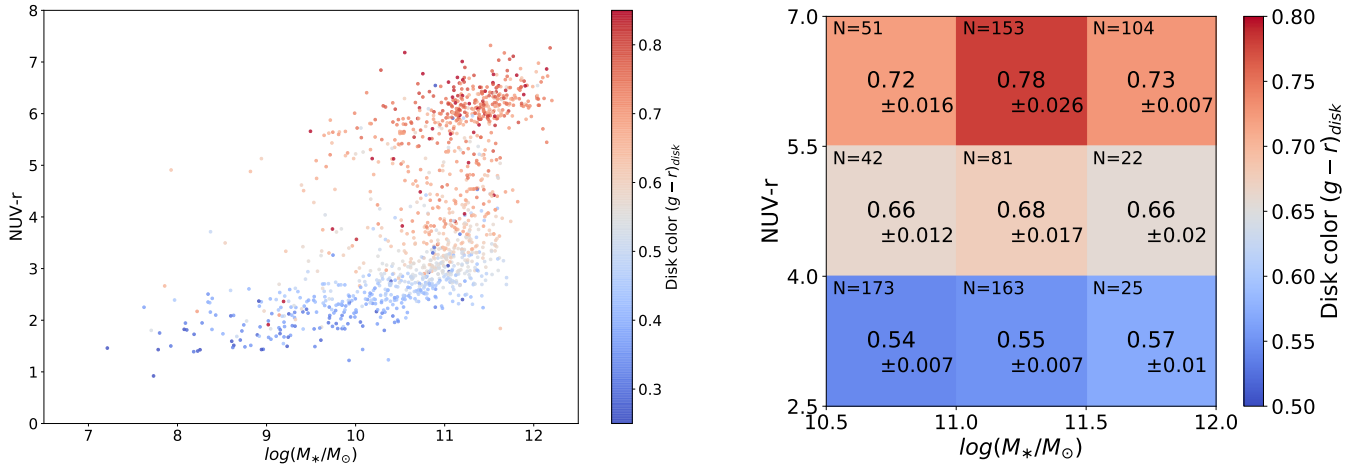

Fig. 21: Disk $g-r$ absolute color evolution in the galaxy color-mass diagram. **Left:** Color-mass diagram for all EFIGI ∩ GALEX galaxies with `Incl-Elong` ≤ 2, in which the color of the points represent the disk $g-r$ absolute color inferred from bulge and disk model-fitting. There is a systematic reddening of the disk along the Hubble sequence from irregulars to ellipticals. **Right:** Mean value of the disk color $(g-r)_{disk}$ for EFIGI ∩ GALEX galaxies in color-mass cells of 0.5 dex in total stellar mass and 1.5 in $NUV-r$ color. Only the bright part of the Blue Cloud, the Green Plain and the Red Sequence are shown. The associated error on the mean and the number of galaxies in each cell are indicated. There is a significant reddening of the disk for redder $NUV-r$ colors, as well as for earlier and earlier types along the color-mass sequence.

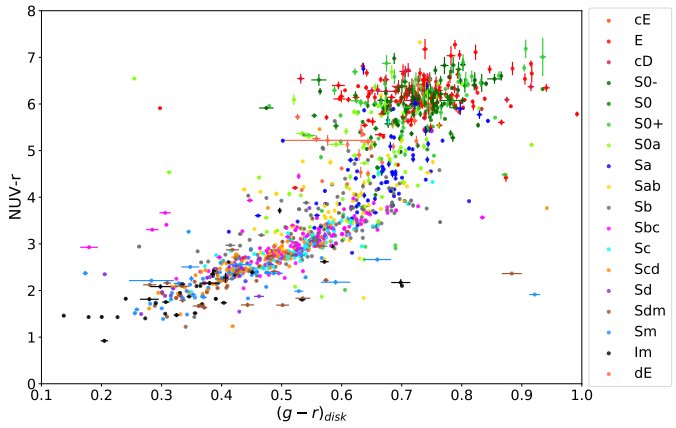

Fig. 22: Absolute $NUV-r$ color of the galaxy versus absolute $g-r$ color of the disk for EFIGI ∩ GALEX galaxies with `Incl-Elong` ≤ 2. The color of the points indicates the Hubble Type. The strong correlation between total galaxy $NUV-r$ color and disk $g-r$ color for types Im to Sb, having no bulge, or less than a 10% bulge-to-total ratio, suggests that their disk reddening translates into the fading of star formation.

ratio of ∼ 0.4 (see Fig. 17), the total optical colors fail in highlighting the Green Plain, as shown for total $u-r$ colors in Fig. 8 in Sect. 4.1.3). Note also that in the Red Sequence of Fig. 22, where galaxies gets redder in $NUV-r$, so does their disk in $g-r$ whether real (in S0), or only an artifact (in E, that could be due to either an inadequate profile fit for the bulge, or to a visual misclassification of an S0 into an E).

4.3.4. Spiral arms and flocculence as markers of star formation and gas supply

The fading of star formation in disks along the Blue Cloud and across the Green Plain (described in the previous subsection) leads us to further examine the morphological features within the disks of galaxies: spiral arms and flocculence. The RC3 classification (de Vaucouleurs et al. 1991) rests on how tightly wound are the spirals arms of spiral galaxies, whereas lenticulars have arm-less disks. A progressive decrease in spiral arms curvature is therefore expected for later and later spiral types, and is confirmed by the mean cell values of the `Arm Curvature` EFIGI attribute that is shown in the left panel of Fig. 23: `Arm Curvature` increases systematically from the Blue Cloud (late spirals) to the Green Plain (early spirals and lenticulars) (see also de Lapparent et al. 2011). We note that if one only considers bins with more than 50 galaxies, the abrupt step from 1.29 to 1.92 and higher to the left of the knee between the Blue Cloud and the Green Plain (in the second row) appears to correspond to the presence of Sc types and earlier, as shown in Fig. 20. Sc galaxies are called "grand design spirals" as their spiral arms are better defined (less broken by wide-scale flocculence) than those of the earlier and later types.

The central panel of Fig. 23 shows the EFIGI `Arm Strength` attribute, that estimates the light fraction in spiral arms compared to the total galaxy flux. There is a clear peak at the knee between the Blue Cloud and Green Plain, that can be defined by the 2 rightmost cells of the second row, and exhibits 2 dark blue pixels with `Arm Strength`= 2.15 ± 0.07 and `Arm Strength`= 2.08 ± 0.11, dominated by Sb, Sbc, Sc and Scd intermediate spiral types in comparable proportions (see Fig. 20). From these 2 pixels, `Arm Strength` decreases systematically across both the Blue Cloud and the Green Plain, at constant $NUV-r$ color when the stellar mass decreases, and at constant stellar mass across both the Blue Cloud and the Green Plain when $NUV-r$ increases (becomes redder), that is when the sSFR decreases. At $NUV-r > 5.75$, `Arm Strength` becomes negligible, as the low mass part of the Red Sequence is composed mostly of lenticulars, hence with no visible spiral arms.

The right panel of Fig. 23 shows the EFIGI `Flocculence` attribute, that measures the flocculent aspect of galaxies due to scattered HII regions relative to the galaxy disk profile. As for the `Arm Strength` attribute, `Flocculence` shows a systematic

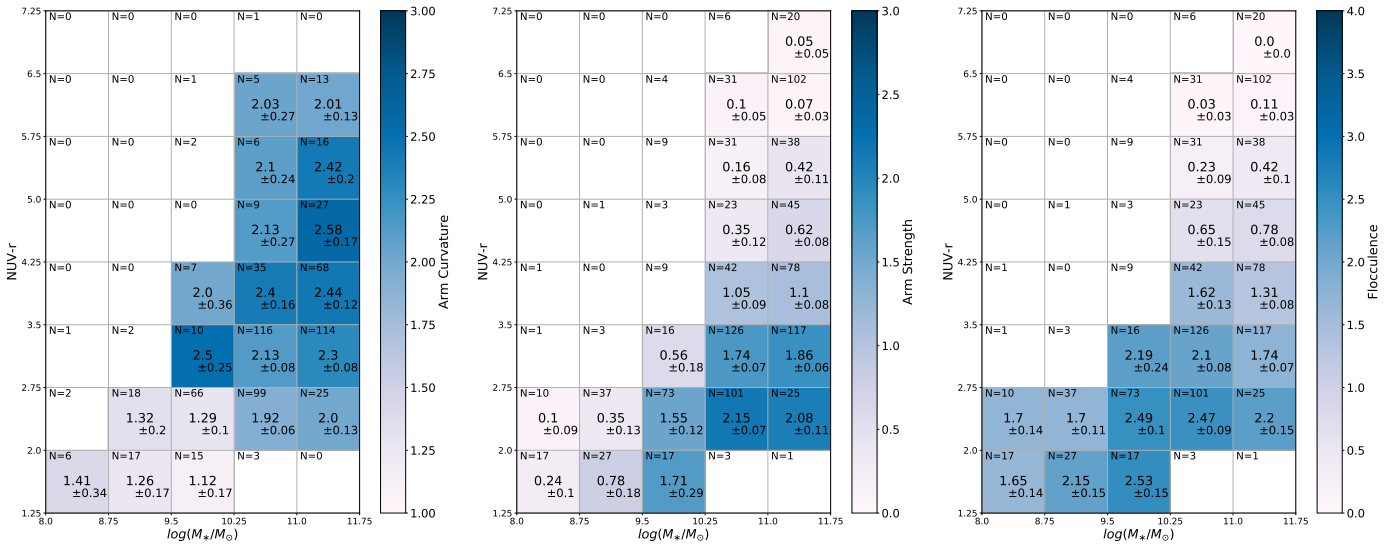

Fig. 23: Evolution of EFIGI attributes related to disk galaxies.**Left:** Mean values of the EFIGI `Arm Curvature` attribute for all EFIGI ∩ GALEX galaxies with `Incl-Elong` ≤ 2, in color-mass cells of 0.75 dex in stellar mass and 0.75 in $NUV - r$ color all the way from the Blue Cloud to the Red Sequence. `Arm Curvature` describes the intrinsic curvature of the spiral arms, when they are visible (hence the smaller samples compared to the central and right panels). It increases from late-type to earlier type spirals, in agreement with the definition of these types in the Hubble-de Vaucouleurs sequence. **Center:** Same as the left panel but for the mean values of the EFIGI `Arm Strength` attribute, which describes the strength of the spiral arms in terms of flux fraction relative to the whole galaxy. **Right:** Same as the left panel but for the mean values of the EFIGI `Flocculence` attribute, which measures the relative importance of flocculent features, due to scattered HII regions. The joint fading of `Flocculence` and `Arm Strength` across the Green Plain hints at a restriction in neutral gas supply.

decrease for redder $NUV - r$ color at all spiral stellar masses, except in the two lowest mass cells dominated by irregulars (see Fig. 20). The `Flocculence` attribute corresponds to inhomogeneities relative to the smooth profiles of all dynamical features: disk, bar, spirals arms, rings etc. Given that the Green Plain is the region where star formation fades upward, the concomitant decrease in both `Arm Strength` and `Flocculence` (see central and right panel of Fig. 23) suggests a decreasing gas content of early spirals along the Green Plain. In contrast, Blue Sequence galaxies maintain a significant `Flocculence` despite the vanishing `Arm Strength` in the latest spiral types (Sdm, Sm, Im). If spiral arms trigger star-formation by compressing the interstellar gas and dust on their edges, they are not indispensable for star formation to occur: Im galaxies have no spiral arms and strong sSFR (see Fig. 11). The EFIGI `Arm Strength` and `Flocculence` attributes therefore bring additional evidence that the reddening of Green Plain galaxy disks may be due to some restriction in the neutral gas supply available for stellar formation (called quenching, see Sect. 5.1).

5. Discussion

The present analysis of EFIGI data shows systematic and major morphological variations in the color-mass diagram (see Fig. 13), encompassing all galaxy types from the Main Sequence of star-forming galaxies (Blue Cloud) to quiescent ones (Red Sequence), through an intermediate region which we rename Green Plain (see Sects. 4.1.1 and 4.1.2). We characterize these changes not only in terms of Hubble type, but quantitatively in terms of bulge growth (see Fig. 16) and disk reddening (see Fig. 21), and show below that altogether, they strongly advocate for the Green Plain being a slow transition region between star-forming and quiescence.

We also discuss below the results of our analysis and show that these results obtained from low redshift galaxies confirm what was suggested from high redshift observations in the Hubble Deep Field (Abraham et al. 1996): that irregulars and the very late spiral types are the building blocks of the more massive early spiral type galaxies, and eventually of the lenticular and elliptical galaxies (see Sect. 5.2). Altogether, the mass distributions and limits for the bulges, disks, and more generally the various morphological types suggest that changes may take place on long timescales, as they may be triggered by flybys or mergers, and are tightly intertwined.

5.1. Quenching

Transition of galaxies from the Blue Cloud (star-forming) to the Red Sequence (quiescent) is obviously related to the gas cycle and resulting star formation in galaxies. Numerical simulations suggest that galaxies are gas fed from the cosmic streams (Dekel & Birnboim 2006), the circumgalactic medium (Maller & Bullock 2004, Dekel & Birnboim 2008, Kereš & Hernquist 2009), as well as during mergers. The decrease in star formation of galaxies with time (Madau & Dickinson 2014) has been attributed to quenching that would limit the cold gas supply. Quenching is theorized to either prevent gas from forming stars, or to prevent the building up of the gas reservoir, or even to expel gas from the galaxy. AGN feedback has been considered as playing a crucial role, by thermal feedback - causing gas heating (Croton et al. 2006), or mechanical feedback - expelling the gas (Silk & Rees 1998). There is however a significant scale ratio between the parsec scale of the central engine of an AGN, namely the supermassive black hole, and the more than kiloparsec scale of a galaxy disk and halo, questioning the ability of the AGN to affect the cold gas content of entire disks.

We emphasize that there is often confusion in articles between the decrease in star formation (the symptom) and the quenching (the cause), by invoking the latter when only observing the former. Here we make the distinction and, when appropriate, specifically refer to the symptom as **star formation fading**.

We note that the 4 order of magnitude range in stellar mass identified here for irregulars to spirals along the Blue Cloud (see Fig. 13) may have implications in terms of quenching. If the gas accretion from the cosmic streams (Dekel & Birnboim 2006) is independent of a galaxy mass but rather on its location in the cosmic web, this accretion may correspond to a smaller fraction of the gas reservoir in more massive galaxies. It may therefore not be sufficient to replenish the gas reservoir consumed by the on-going star formation above some mass threshold. This would lead to a quenching of star formation, hence redden the most massive spirals into the Green Plain. Combined with the mass limit described in Sect. 4.2, this could design the knee shape of the Green Plain.

5.2. Major mergers along the Blue Cloud

The 4 order of magnitude extent in M_* of the Blue Cloud (see Fig. 13) can be partly explained by galaxies consuming their large HI reservoir (van Driel et al. 2016) to form stars, which is made possible by their high sSFR values in the range of $10^{-9.7} yr^{-1}$ for irregulars to $10^{-10.5} yr^{-1}$ for Sc types (see Fig. 11). However, these galaxies would need several to almost 10 Gyr years to double their mass, so the scenario of an irregular or spiral galaxy evolving passively across the entire Blue Cloud can be ruled out. This indicates that mergers are also needed to explain the stellar mass increase for late-type spirals, and that these mergers should be major in order to allow the building-up of the massive spirals at the tip of the Blue Cloud.

Another piece of evidence for mergers along the Blue Cloud can be derived from the `Perturbation` attribute available in the EFIGI catalog, which measures the amplitude of distortions in the galaxy luminosity profile from rotational symmetry. Galaxies that went through a recent merger event, or only a flyby are expected to undergo strong to weak gravitational tidal field effects and consequently to have a non null value of the `Perturbation` attribute (see the study of peculiar galaxies to understand interactions, initiated by Arp 1966). Fig. 24 shows the fraction of galaxies having an EFIGI `Perturbation` attribute > 0. One can see that the Blue Cloud ($NUV - r \leq 3.5$) is the region of the graph where there is the highest fraction of perturbed galaxies, with only 34% showing no perturbation, against 62% for the bins roughly corresponding to the Green Plain ($NUV - r \in [3.5, 5.75]$) and 83% in the Red Sequence ($NUV - r > 5.75$). There is also a vertical trend over most of the Blue Cloud, in which the bluest galaxies are more frequently perturbed at a fixed mass (at the $\sim 2\sigma$ level). We interpret both trends as evidence that merger events increase star-formation in already star-forming irregular and spiral galaxies.

Another piece of evidence for mergers along the Blue Cloud is the presence of very bright regions, which are frequently visible along the spiral arms, but with no preferred location in Im galaxies, and they are characterized by the EFIGI `Hot Spots` attribute - on a scale of 0 to 4. It measures the strength of (a) region(s) with a very high surface brightness standing out in a galaxy and that correspond(s) to either a giant star-forming region, an active nuclei (very rarely), or a stellar nuclei (in the nucleated dE galaxies). The vast majority of the visually detected hot spots with low to intermediate values of the attribute (1-2) are strong HII regions, appearing as blue dots, contrary to the flocculence patches that are more diffuse and on larger spatial scales. In contrast, the highest values of the `Hot Spots` attribute (3,4) correspond to (often a single) huge star-bursting region, and are rarer by a factor of ~ 10.

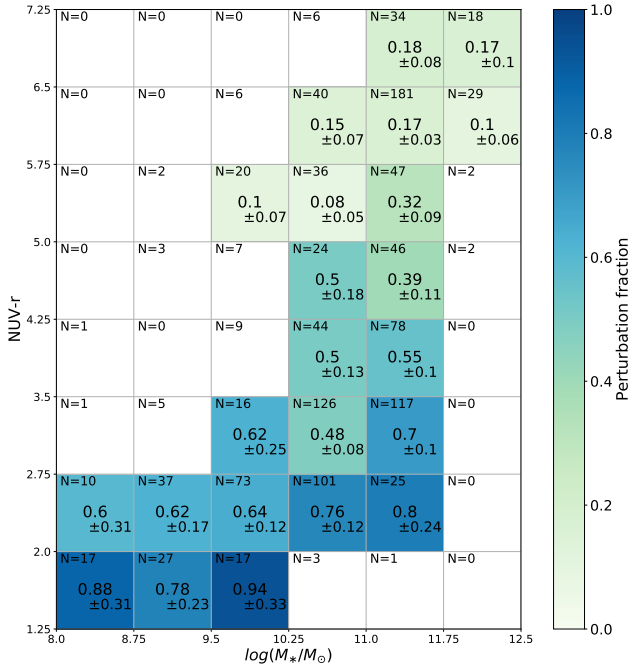

Fig. 24: Fraction of EFIGI ∩ GALEX galaxies with `Incl-Elong` ≤ 2 having an attribute value of `Perturbation` > 0, all the way from the Blue Could to the Red Sequence. This attribute measures the distortion of the galaxy profile from rotational symmetry, with a nonzero value thus indicating an asymmetry. Galaxies are binned in cells of 0.75 dex in stellar mass and 0.75 in $NUV - r$ color, and cells with less than 10 galaxies are discarded. The sample size as well as the error on the mean are indicated in each cell. Red Sequence galaxies are mostly unperturbed, while many of the Blue Cloud galaxies show various levels of `Perturbation`, with a trend of bluer galaxies being more frequently perturbed.

Fig. 25 shows the fraction of galaxies having some weak to strong evidence for hot spots within the Blue Cloud, in color-mass cells. There is, similarly to the `Perturbation` attribute a color trend with the bluest galaxies showing the highest frequencies of hot spot presence, at any given mass. Comparison with Fig. 20 shows that the vast majority of late-type spirals (Sd to Sm) and Im show evidence for some hot spot(s), as galaxies with $\log(M_*/M_\odot) \in [8.75, 10.25]$ and $NUV - r < 2.75$ show a fraction > 0.81 (the slight decrease in the Irregular dominated bin with a 0.5 ± 0.27 fraction seen in Fig. 20 is not significant given the quoted error). As for the `Perturbation` attribute, there is a vertical trend over most of the Blue Cloud, as well as the shown portion of the Green Plain, in which the bluest galaxies have more frequent visible hot spots in the form of bright HII regions. This attribute value distribution is also compatible with gravitational interactions and mergers driving the stellar mass build-up in the Blue Cloud: a minor encounter or a cosmic stream connecting to a specific region of a disk could lead to locally increased star formation; a tidal interaction on larger scales (due to a flyby) may lead to a general enhancement of the star formation in the disk and the rise of several bright HII regions.

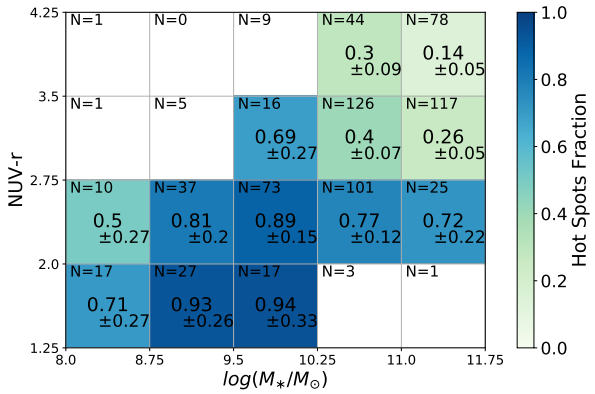

Fig. 25: Fraction of EFIGI ∩ GALEX galaxies with `Incl-Elong` ≤ 2 having an attribute value of `Hot Spots` > 0. The attribute measures the relative intensity of regions with a very high surface brightness. Galaxies are binned in cells of 0.75 dex in stellar mass and 0.75 in $NUV - r$ color. The sample size as well as the error on the mean are indicated in each cell. Cells with less than 10 galaxies are discarded, and the graph is limited to $NUV - r \leq 4.25$, as the fraction of `Hot Spots`> 0 is below 5% for redder galaxies.

In contrast, Fig. 24 shows that in the Red Sequence, there is a rather low fraction of galaxies showing perturbed isophotes (< 20%), at all masses, so it is valid for both lenticulars and ellipticals. There are two ways to interpret this lower fraction, either mergers are not as common for red galaxies, or the distortion of the light profile is often too weak or too short-lived to be visible. Mihos (1995) suggests that major mergers of spiral galaxies into ellipticals at $z \sim 0.4 - 1$ erase signs of distorted isophotes in only 0.2 Gyr, due to violent relaxation. This could explain the very low fraction of perturbed EFIGI galaxies in the massive part ($\log(M_*/M_\odot) \gtrsim 11.75$) of the Red Sequence, where ellipticals dominate. The similarly low frequency of perturbed galaxies in the low mass portion of the Red Sequence, in which S0 dominate, may indicate that the transformation from Green Plain spirals to relaxed lenticulars occurs on a comparable time-scale, despite the different nature and frequency of these mergers: minor and frequent mergers. We actually provide in Sect. and 5.4.1 and Sect. 5.5 arguments in favors of mergers forming galaxies in the Red Sequence, that are not contradicted by the `Perturbation` attribute distribution.

5.3. Main sequence of star-forming galaxies

The Blue Cloud is often referred to as the Main Sequence of star-forming galaxies, which was first discovered as a linear relation between the star formation rate and the stellar mass (in log-log), onto which an overwhelming majority of star-forming galaxies align (Brinchmann et al. 2004; Elbaz et al. 2007; Noeske et al. 2007). The rather small scatter of this relation, on the order of 0.3 dex, raises the question of the star-forming mechanisms that could explain this dispersion.

In the present analysis, we show that the variation along the Main Sequence can be described by the continuous change of morphological type from Im to Sbc (see Fig. 5). Moreover, the Main Sequence is curved at its massive end when reaching Sb and earlier types, corresponding to the knee of the Green Plain. As far as the scatter around the Main Sequence is concerned, we have brought to light several EFIGI morphological attributes that follow an increasing trend transverse to the Blue Cloud (hence the Main Sequence) when moving toward bluer $NUV - r$ colors: these attributes are spiral `Arm Strength` (Fig. 19), `Flocculence` (Fig. 23), `Perturbation` (Fig. 24) and `Hot Spots` (Fig. 25), which are all linked to the stellar formation processes in galaxies, either as a direct measure (flocculence, bright HII regions), or its triggering (strength of spiral arms, amplitude of distorted isophotes). We thus confirm that the scatter around the Main Sequence corresponds to variations in stellar formation, and identify dynamical processes that could cause them.

5.4. Transition through the Green Plain

In the following, we further examine and discuss the properties of the Green Plain, and suggest that it is a transitional region through which galaxies may pass when evolving from the Blue Cloud to the Red Sequence.

5.4.1. Bulge growth requires mergers

We propose here that the strong increase in bulge mass fraction across the Green Plain excludes a secular and passive reddening of galaxies from the Blue Cloud to the Red Sequence. Indeed, one can make the distinction between two kinds of bulges according to their formation processes: classical bulges, that were formed through violent events such as mergers, and pseudo-bulges, that were formed by secular evolution, with inward stellar migration from the disk to the bulge, over longer timescales (Kormendy & Kennicutt 2004). These different formation scenarios lead to different properties.

The Sérsic index of a bulge light profile (obtained through the bulge and disk modeling, see Sect. 3.1) has been proposed as a criterion to differentiate pseudo-bulges from classical bulges, with $n \leq 2$ and $n \geq 2$ respectively (Fisher & Drory 2008, Gadotti 2009). In order to further examine the pseudo-bulge and classical bulge distributions, we look in Fig. 26 at the variations of the bulge profile Sérsic index as measured in the r band, averaged in cells across the color-mass diagram. Compared to previous parameters, the quadratic mean of errors for the Sérsic index can be higher than the error on the mean we defined as $\sigma_{RMS} / \sqrt{(N)}$ (N being the number of galaxies in the bin) because of large error bars on this index. The plotted error in Fig. 26 is therefore the maximum of the two estimates. We precise that the value of 2.191 for the leftmost bin is caused by the large uncertainties for individual galaxies with very low bulge fluxes (most of these bulges are probably not real, and due to bright HII regions).

Fig. 26 shows that there is a systematic increase in the Sérsic index of the bulge profile when $NUV - r$ increases in the color-mass diagram, that is from late spiral types in the Blue Cloud to early types in the Red Sequence, meaning galaxies have more concentrated bulge light profiles when moving from the bottom-left to the top-right of the color-mass diagram. In the Blue Cloud and all the way to the knee of the Green Plain (for $NUV - r < 3.5$), galaxies have a mean Sérsic index of $n \sim 1.07 - 2.3$, thus indicating a mix of pseudo-bulges and classical bulges, or composite bulges which may have both a pseudo and a classical component. In contrast, the Green Plain galaxies have an average $n \sim 2.2 - 2.9$, and the Red Sequence an average $n \sim 2.6 - 3.1$, making all these galaxies dominated by classical bulges. Therefore, there is not only a growth of the bulge across the Green Plain (as seen in Sect. 4.3.1) but also a change in the nature of these bulges, from pseudo-bulges to classical ones, as

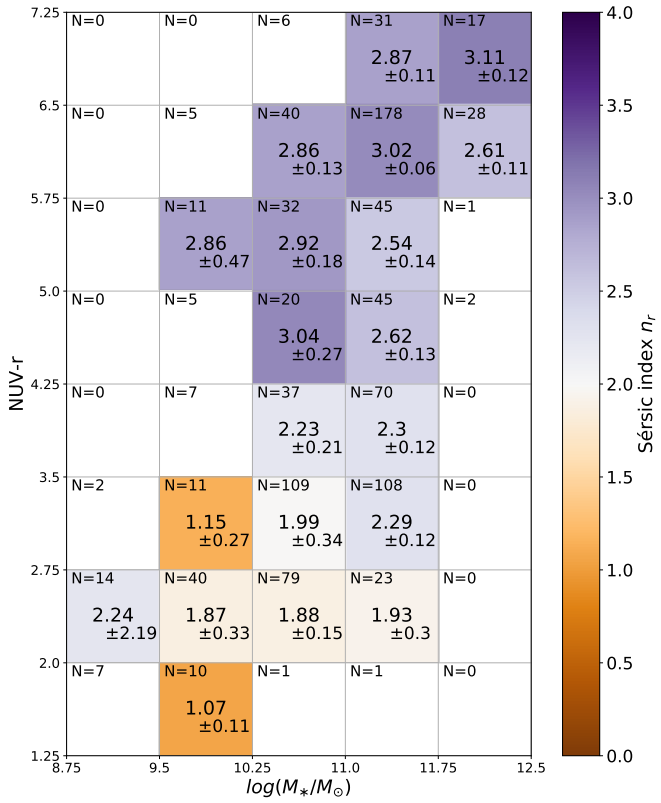

Fig. 26: Mean value of the Sérsic index of the bulge profile in the r band for galaxies in cells of 0.75 dex in stellar mass and 0.75 in $NUV - r$ color. Cells with less than ten galaxies are discarded, and the sample size as well as the maximum of the error on the mean and the quadratic mean of the errors on the individual points. Pseudo-bulges populate the Blue Cloud, whereas the Green Plain and the Red Sequence are dominated by classical bulges.

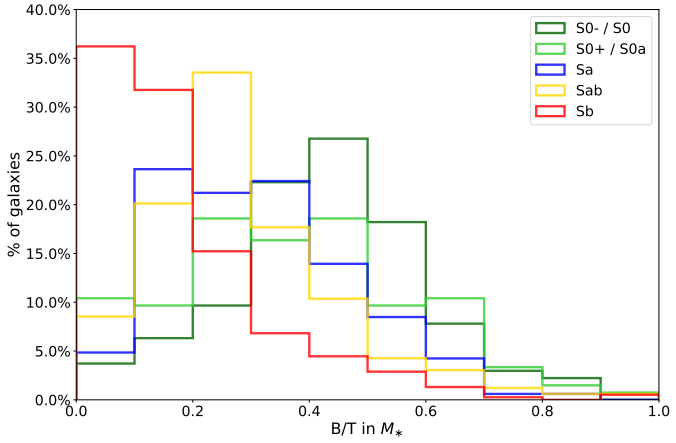

Fig. 27: Relative distributions of the bulge-over-total stellar mass ratio for early spirals and lenticulars. Each color represents a specific Hubble Type (or a combination of subsequent Hubble types). Despite a large dispersion, B/T systematically increases with morphological type. In particular, transformation of Sb types into S0$^-$-S0 or S0$^+$-S0a often requires bulge growth.

evidenced here by the sharpness of their light profile. These results are in agreement with Kim et al. (2016), who showed a positive correlation between B/T and bulge Sérsic index for SDSS galaxies in a similar redshift range as for EFIGI and MorCat ($0.005 < z < 0.05$).

In Fig. 27, we plot the relative distributions of the bulge-over-total stellar mass ratio for early spirals and groups of lenticular types, each histogram being normalized to 100%. Moving along the EFIGI Hubble sequence from Sb to S0, one can see that the peak of the distribution corresponds to increasing values of B/T, thus indicating a growth of the bulge prominence in galaxies of these types: B/T peaks at $\sim$ 0.45, $\sim$ 0.35, $\sim$ 0.25, $\sim$ 0.25 and $\sim$ 0.1 for S0$^-$-S0, S0$^+$-S0, Sa, Sab and Sb types respectively, and to lower values for later spiral types; and median values are 0.42, 0.37, 0.30, 0.26, 0.14 for S0$^-$-S0, S0$^+$-S0, Sa, Sab and Sb types respectively. Therefore, the dominant fractions of Sb types and later in the Blue Cloud (see Fig. 20) imply that pseudo-bulges correspond to the B/T values found in the Blue Cloud, whereas the B/T of bulges of S0$^-$, S0, S0$^+$ lenticulars located in the Red Sequence correspond to the values for classical bulges. Sachdeva et al. (2017) show from HST and SDSS data that, from $z = 1$ to $z = 0$, both pseudo-bulges and classical bulges grow significantly, with B/T in optical bands increasing from 21% to 52% for classical bulges, and pseudo-bulges from 10% to 26%. If we compare these values at $z = 0$ to the peak values of Fig. 27, we find that Sab and later types have pseudo-bulges, lenticulars have classical bulges, while the picture is a bit more mixed for Sa galaxies due to their wide distribution of B/T. This analysis of the B/T distributions per morphological type further confirms the shift from pseudo-bulges in the Blue Cloud to classical bulges in the Red Sequence. Sachdeva et al. (2017) also conclude that minor mergers are needed to obtain sufficient mass growth to produce classical bulges. This translates in our analysis into a need for minor mergers to explain the main trend of bulge growth seen across the Green Plain, and to reach the B/T observed for the lenticular galaxies.

Moreover, Fig. 27 shows that there is a wide distribution of B/T for each group of morphological types. We calculate that only 17.8% of Sb have a $B/T \geq 0.3$, and 19.7% of S0$^-$-S0 have a $B/T \leq 0.3$. More generally, there are no bins in B/T that include significant fractions of both S0 and Sb galaxies, suggesting that only a minority of Sb galaxies could evolve from spirals to lenticulars without seeing a significant change in their B/T. Therefore, secular evolution cannot be the main evolutionary pathway across the Green Plain, because processes that increase significantly the B/T are required for galaxies to transition across this region.

We emphasize that this picture of galaxy evolution in which the fading of star formation is linked to the growth of the bulge (through mergers), is compatible with the concept of "morphological quenching" proposed by Martig et al. (2009). The growth of a stellar bulge stabilizes the gas disk and quenches star formation, leading to a red quiescent galaxy without the need to deplete its gas supply.

5.4.2. Slow transition through the Green Plain

If there is a mass change in the color-mass diagram, the process that drives the mass growth is expected to impact the star forming state of the galaxy, hence its color. Gas-rich mergers initially create a burst of star formation which makes temporarily the galaxy bluer, before it proceeds with its secular fading.

The fact that the Green Plain is nearly vertical in the color-mass diagram, with a mass range of $\log(M_*/M_\odot) \sim 10.5 - 11.7$,

that is a factor of $\sim$ 10, leaves room for major mergers to play a role in the process of type transformation across this region. However, as the rate of major mergers decreases sharply from $z \sim 1$ to $z \sim 0$ (López-Sanjuan et al. 2009; Bluck et al. 2009; Bridge et al. 2010), they can only play a minor role in recent galaxy evolution. The building-up of the bulge across the Green Plain is expected to take several Gyr, if we consider the timescales quoted in Sachdeva et al. (2017), as a growth of B/T by a factor ~ 2.5 occurs between $z = 1$ and $z = 0$.

The coupling of star formation fading and morphological transformation detected across the Green Plain suggests that the timescales of these two phenomena may be of the same order. Indeed, Sampaio et al. (2022) derive from the analysis of 257 SDSS clusters that the morphological transition happens prior to the fading, or quenching, of star formation, with respective timescales of 1 Gyr and 3 Gyr. Note however that the authors define morphological transformations as when the galaxy converts from Sa to S0, hence the short timescale of 1 Gyr. Nevertheless, we observe in their Fig. 9 that the full morphological transformation from type Sbc (Blue Cloud) to S0, along with the decrease in sSFR, follows the same trend over the 5 Gyr that these changes take altogether. The dense environments of galaxy clusters analyzed by Sampaio et al. (2022), in which ram pressure effects are efficient at removing gas from disks differ from the EFIGI and MorCat catalogs analyzed here that sample the large-scale galaxy distribution, with some clusters and many groups (Baillard et al. 2011). Therefore even longer timescales than 1 and 5 Gyr may be needed to convert Sa and Sbc types to S0 respectively in the more representative environment of the general galaxy distribution provided by EFIGI and MorCat. Indeed, Phillipps et al. (2019) derived from SED fitting the star formation histories of galaxies in the GAMA survey (at redshifts $0.1 < z < 0.2$), assuming an exponential decay of the SFR: their conclusions are that Green Plain galaxies are experiencing a star formation decrease, due to the gradual shortage of their gas reservoir, over a timescale of 2 to 4 Gyrs.

5.5. Mass limits and formation of massive disks and ellipticals

Another interesting result seen in the color-mass diagram of Fig. 13, is that the Green Plain is nearly vertically aligned with the low-mass end of the Red Sequence and the high-mass end of the Blue Cloud ($\log(M_*/M_\odot) \in [10.5, 11.7]$; Fig. 13). Furthermore, there is a common mass limit of $\log(M_*) \sim 11.7 M_\odot$ for all early-type spirals from Sa to Sc. This probably corresponds to the exponential decrease in the galaxy luminosity function at bright luminosities (de Lapparent 2003), which is successfully reproduced in numerical simulations when introducing AGN feedback (Bower et al. 2006; Kaviraj et al. 2017). This mass limit also constitutes an almost upper mass limit for the lenticular galaxies within the Red Sequence, as shown in Fig. 14, whereas elliptical galaxies dominate the Red Sequence at high masses with $\log(M_*/M_\odot) \gtrsim 11.5$. This is consistent with kinematic studies which show that there exists a critical mass $\log(M_{crit}/M_\odot) \simeq 11.3$ separating slow and fast rotators (**?**).

We now examine how these mass limits and mass segregation with galaxy morphology can provide useful clues on the evolution of the various morphological types. Secular evolution from the low-mass lenticular part of the Red Sequence into its massive part dominated by ellipticals is not possible because the sSFR of both types of galaxies is too low to significantly increase their stellar mass by secular evolution ($\mathrm{sSFR} < 10^{-11} yr^{-1}$ or $10^{-2} Gyr^{-1}$; the sSFR can be seen as the inverse of the time needed to produce the stellar mass of a galaxy at its current SFR). Mergers (either major or many minor) are definitely needed to explain the existence of Red Sequence ellipticals with stellar masses larger than $log(M_*/M_\odot) \sim 11.5$.

This result is in good agreement with the results of Martin et al. (2018) who show from the cosmological hydrodynamical Horizon-AGN simulation, that mergers play a major part in driving morphological transformation, and especially disk-to-spheroid evolution, with this transformation being more drastic as the stellar mass of galaxies involved in the merger increases. Indeed, the difference in the dispersion of the stellar velocities between the most massive progenitor and the galaxy formed by the merger event is negative for a disk progenitor, indicating a shift toward a more dispersion-supported object, while the absolute value of the dispersion increases with stellar mass. The fact that the more massive spirals tend to form spheroids after a merger event is expected to deplete the color-mass diagram from early-spiral galaxies at the highest masses, as we obtain in Fig. 13.

In Martin et al. (2018), the highest mass bin where the morphological transformation is strongest at $z = 0$ is $\log(M_*/M_\odot) \in [11.5, 12.0]$, which corresponds to the mass limit of $\log(M_*/M_\odot) > 11.7$ detected in the present study. Moreover, the shift in morphology from disk to spheroid triggered by the merger event strongly depends on the mass ratio between the two merging galaxies, with an effect significantly higher for major mergers. Nevertheless, their low frequency rate, especially since $z \sim 1$ means that minor mergers are also needed to explain the formation of elliptical galaxies. The formation of either disk-dominated or bulge-dominated galaxies also cannot be solely explained by a difference in the merger history, and, still according to Martin et al. (2018), it is expected to mostly depend on the gas fraction of the progenitors, which is key to determine the remnant morphology.

Furthermore, our results are compatible with the samples analyzed in Jackson et al. (2020) and Jackson et al. (2022) that focus on the most massive spirals, with $\log(M_*/M_\odot) \geq 11.4$, with the goal to understand why, if the most massive galaxies have a rich merger history, these successive mergers do not systematically lead to an elliptical morphology. The authors answer to the issue of the existence of massive spiral galaxies by showing that gas-rich minor mergers allow for the persistence of a star-forming disk. Martin et al. (2018) also mention gas-rich interactions, as well as cosmological accretion, to explain that disk survival in mergers is driven by the accretion of cold gas.

At higher redshifts, De Propris et al. (2015, 2016); Mitsuda et al. (2017); Chan et al. (2021) observe in Red Sequence cluster galaxies a gradual disappearance of the disks, corresponding to the lenticular toward elliptical evolution reported here, and attribute it to disk fading and bar or bulge formation, without the need for mergers. So it seems that the morphological evolution around this mass limit could also happen through secular evolution, and mergers would then only be needed to explain the mass growth to form the most massive ellipticals.

5.6. Constraining evolutionary pathways

Numerical simulations propose scenarios of type transformations that we can confront with our observational results in order to check their compatibility.

5.6.1. Evolution pathways of lenticulars in numerical simulations

When discussing the growth of bulges and the transition across the Green Plain in Sect. 5.4, we extensively discussed the formation of lenticular galaxies. We here confront our observations with Deeley et al. (2021) who study the formation pathways of lenticular galaxies in the Illustris numerical simulation. This analysis puts an emphasis on mergers (both minor and major) in order to explain the formation of lenticulars from spirals in 57% of cases. Another major pathway to form 37% of lenticulars in this simulation is through tidal stripping of spiral disks. This process is however at play only in clusters, which are rare in surveys of the large-scale galaxy distribution that are more extended than the typical diameter of the voids in the cosmic web (de Lapparent et al. 1986), which the EFIGI and MorCat samples are; such surveys are therefore dominated by group galaxies in which stripping mechanisms are less efficient. A third and less dominant pathway to form 5% of lenticular galaxies identified by Deeley et al. (2021) is by passive evolution of spiral galaxies. We already discuss this scenario when describing the growth of bulges, and conclude that it is possible for only a minority of objects (see Sect. 5.4.1), hence in agreement with Deeley et al. (2021).

5.6.2. Evolution pathways of ellipticals in numerical simulations

Unfortunately, we do not find as much common ground as with Deeley et al. (2021) (discussed in the previous subsection), in other studies based on numerical simulations. For instance, Park et al. (2021) also used Illustris TNG50 cosmological hydrodynamical simulations of galaxy formation, and show that there are three main pathways leading to massive quiescent galaxies with $\log(M_*/M_\odot) \in [10.5, 11.5]$. Even though such galaxies are mainly lenticulars in the EFIGI sample (as we show in Figs. 12, 13 and 14), our observations are not in agreement with the evolutionary trajectories seen in Park et al. (2021). We emphasize that understanding their results in light of ours can be prejudiced by their choice in definition for the two splits describing galaxies : star-forming and quiescent as well as disk and elliptical. While the cut in sSFR shown in their Fig. 1 is coherent with our measured values presented in Fig. 11, their disk-to-total ratio D/T defined as the fractions of stars with circular orbits is different from the mass or luminosity ratios considered here, and a cut at 0.5 in stellar mass would not be adequate to split disks from ellipticals: Fig. 26 shows that 14%, 10% and 6% of early-spiral galaxies, of Sa, Sab and Sb morphological types respectively, have a $B/T > 0.5$ (hence $D/T < 0.5$), as well as up to a third of lenticulars.

Nevertheless, there are three evolutionary pathways to form massive quiescent ellipticals that are identified in the TNG50 numerical simulation, and that one can examine in light of the color-mass diagram for the EFIGI galaxies. The first scenario is a slow decrease in star formation turning star-forming disks into quiescent disks, which could be compatible with our observations, if we consider transition from early-type spiral to lenticulars that have similar values of B/T (see Fig. 27).

The second scenario is in two phases: a rapid star formation fading caused by strong AGN feedback (gas ejection) turns star-forming disks into quiescent disks; it is then followed by a disk dispersion mechanism turning the galaxy into a rather low-mass elliptical. The lenticulars and the less massive ellipticals overlap in the color-mass diagram (see Fig. 14), so this second phase morphological change between the two is possible; however, our EFIGI results strongly advocate against a rapid star formation fading or quenching due to the significant bulge growth across the Green Plain (see Sect. 4.3.1).

The third scenario involves (minor or major) mergers or misaligned gas accretion transforming a star-forming disk into a star-forming elliptical, that becomes quiescent through a delayed-then-rapid star formation fading or quenching process. This scenario seems incompatible with the EFIGI sample because it contains only 2 elliptical galaxies, out of the 158 in EFIGI ∩ GALEX with a non zero value of sSFR, and they are the lowest possible values (corresponding to the Sa SED template). These blue, hence star-forming, ellipticals seen in the simulation do not seem to exist in the nearby Universe: this class of object could be an artifact of the simulation. We therefore consider that the described pathway is at best a rare evolution pattern for the formation of massive quiescent galaxies.

At last, our analysis, by showing that Hubble types span the color-mass diagram at specific locations (see Figs. 13 and 5), and that many structural parameters follow the same trend, seems to indicate that the fading of star formation and the morphological transformations are intertwined. Therefore, we reach an opposite conclusion to Park et al. (2021) who finds that "quenching and morphological transformation are decoupled". We can temper our conclusion by mentioning the dispersion seen for each Hubble Type, that allows a galaxy to transform between subsequent types while maintaining its star formation constant, or to undergo a small decrease in its sSFR with no change in its morphology. Nevertheless, only minor changes are compatible with the values of the dispersion in both color and mass.

6. Conclusions

In this article, we examine the distribution of Hubble types for the EFIGI catalog of nearby galaxies with detailed visual classification in the $NUV - r$ versus r absolute color-magnitude and color-mass planes. The goal is to relate the morphology of galaxies to their evolution in terms of stellar mass and the star-forming state. We obtained precise apparent magnitudes and colors for all types of galaxies, as well as for their bulge and disk components by modeling the luminosity profiles of galaxy images from the SDSS using the Euclid SourceXtractor++ software, which allows one to perform simultaneous multiband model-fitting with priors. We then used ZPEG software to adjust SED based on templates from the PEGASE.2 scenarios of spectrophotometric galaxy evolution, to the apparent magnitudes of EFIGI galaxies in GALEX NUV and our SourceXtractor++ photometry in the gri bands from the SDSS images. From the ZPEG fits, we derived absolute magnitudes, stellar masses (M_*) and sSFRs for each galaxy. We repeated this process to bulge and disk apparent magnitudes in the gri bands to derive separate parameters for each component.

The distribution of $NUV - r$ absolute colors versus r absolute magnitudes for EFIGI galaxies recovers the well-known bimodality in the galaxy distribution between star-forming and quiescent galaxies (Figs. 4 and 6). We provide new information by showing that the different Hubble types occupy specific locations in the color-magnitude diagram (Fig. 5). The Hubble sequence draws an "S shape" in this plane, corresponding to three galaxy groupings: the **Red Sequence** composed of elliptical and lenticular galaxies, the **Green Plain** (formerly Green Valley, see below) populated by intermediate type S0a and early spirals Sa, and the **Blue Cloud** encompassing all spirals from the Sab types to the irregular galaxies.

We also confirm that the use of the optical $u-r$ photometry overlays the Green Plain and the Red Sequence and prevents one from studying these regions (Fig. 8). Complementing optical data with a UV band is pivotal to this study and we show that there is a strong correlation between sSFR and $NUV-r$ color (Fig. 11). There is also a tight correlation between the stellar mass M_* and absolute magnitude M_r (Fig. 12), which allowed us to convert the color-magnitude diagram into a color-mass diagram (Fig. 13), and interpret it in terms of sSFR.

The Blue Cloud and Red Sequence are confirmed to correspond to star-forming and quiescent galaxies respectively, while the Green Plain is a region of intermediate sSFR. Ellipticals dominate the massive part of the Red Sequence, while lenticulars do so in the lower mass part, and the full sequence spans 2 order of magnitudes in stellar mass (Fig. 14). In contrast, the Blue Cloud extends over 4 orders of magnitudes in stellar mass. $NUV-r$ varies only by $\lesssim 1$ and ~ 2 magnitudes across the Red Sequence and the Blue Cloud respectively, despite the large mass intervals they span. In contrast, the intermediate region encompassing the Green Plain is characterized by as wide a color range as the Blue Cloud (~ 2 magnitudes in $NUV-r$), but over a much smaller stellar mass interval of ~ 1 dex. From irregulars to ellipticals, the steps in $NUV-r$ color between types are small (~ 0.1) in the Red Sequence and the Blue Cloud, but much larger in the Green Plain (0.78 for the Sab-Sa, and 0.9 for the S0a-S0$^+$ types), thus indicating a wide stretching in $NUV-r$ in the intermediate region, which justifies it being renamed from "Green Valley".

We use the complete magnitude-limited MorCat catalog to show that the bimodality of the Red Sequence and Blue Cloud, as well as the under-dense Green Plain connecting them are not specific to the EFIGI catalog, nor caused by its selection effects aimed at densely populating all morphological types. We also argue, using MorCat, that the wider range of $NUV-r$ colors (hence sSFR) across the Green Plain, and for morphological types S0a and Sa, causes the lower galaxy density in this region of the color-magnitude and color-mass diagram, making it an under-density. In this picture, the Green Plain is neither due to an intrinsic lower frequency of the S0a and Sa galaxy types that populate it, nor to a shorter lifetime of these types compared to those in the Red Sequence and Blue Cloud: to our knowledge, there is no evidence that these types are more ephemeral than any other disk type (i.e., lenticular or spiral type) along the Hubble sequence.

Our analysis of the EFIGI sample allows us to quantify the morphological transformations that galaxies undergo when evolving from the Blue Cloud to the Red Sequence. To this end, we use their morphological types and detailed morphological features, their bulge-to-total flux ratios (B/T), their derived total and separate bulge and disk masses, as well as their total and separate bulge and disk colors, all based on our luminosity profiles and SED fittings. We quantify the morphological changes through the Green Plain as follows:

- **Bulge growth:** From intermediate spirals in the knee (in which the Blue Cloud breaks into the Green Plain) to S0 types in the Red Sequence, B/T varies from ~ 0.15 to ~ 0.5 (Fig. 17), and the bulge stellar masses more than double at all stellar masses (Fig. 18). There is also an increase in the Sérsic index of bulges across the Green Plain, with redder galaxies having more concentrated bulges (Fig. 26), marking a transition from pseudo-bulges to classical ones.
- **Disk reddening:** The bulge and disk decompositions of EFIGI galaxies show a systematic reddening in $g-r$ of all disks along the Blue Cloud (starting from the blue colors of irregular Magellanic types) through the Green Plain, which we demonstrate to indicate a fading of the disk sSFR (Figs. 21 and 22). In contrast, the bulges of all spiral types display a remarkable stability in color, which is identical to those of lenticulars and ellipticals (Fig. 2), as well as for pseudo-bulges. The decrease in the EFIGI spiral `Arm Strength` and `Flocculence` morphological attributes across the Green Plain (Fig. 23) suggest that the star formation fading of galaxy disks may be due to some restriction in the neutral gas supply available for stellar formation.

This analysis of the EFIGI bimodal color-mass diagram provides new clues on the evolution pathways of galaxies in the present and recent past of the Universe. In the Blue Cloud, the 4 orders of magnitude in stellar mass encompassed by late-type spirals, and the high fractions of galaxies with perturbed isophotes (60% to 90%, see Fig. 24) and bright HII regions (70% to 90%, see Fig. 25), advocate for a mass build-up through numerous mergers.

The fact that the bulge light and mass ratios of Green Plain galaxies are intermediate between those for the Blue Cloud and Red Sequence, together with the systematic and progressive bulge growth of galaxies from the former to the latter, provides evidence that the Green Plain is a **transition** region of galaxies in their evolution pathway from star-forming to quiescence. The characteristics of Green Plain galaxies moreover supports the idea that this transition operates through mergers, as stellar inward migration from the disk cannot transfer enough mass to grow a classical bulge. This is in agreement with the results from the numerical simulations that are reviewed in the discussion (Sect. 5.6), and that suggest the predominance of minor mergers in the formation of the massive spirals and lenticulars. In addition, the common mass limit of $\log(M_*)/log(M_\odot) = 11.7$ that we measured for all galaxies from Sc to S0 types in the Green Plain matches the mass at which ellipticals become dominant in the Red Sequence (Fig. 14). This suggests that some of the most massive ellipticals were formed by major mergers of the most massive early-type spirals (after the eventual fading of the starbursts that may be produced).

We emphasize that the known high frequency of flybys and mergers in the lifetime of a galaxy, as well as the fact that all parts of the color-mass diagram are populated with standard types from the full Hubble sequence are not compatible with the idea that the Green Plain is the locus of a rapid star formation fading (hence rapid quenching) that would happen while galaxies transit from the Blue Cloud to the Red Sequence. The high frequency of bars (Fig. 19) for all spirals as well as the stronger spiral arms and flocculence in the knee of the Green Plain (Fig. 23), suggest that internal dynamics, likely triggered by flybys or mergers, as well as the gas content and physics of star formation may be the key to the bulge growth, disk reddening and aging of galaxy disks from the Blue Cloud to the Red Sequence. Because EFIGI and MorCat are catalogs of nearby galaxies, our analysis is focused on the present and recent evolution of the Universe. Nevertheless, it provides useful insights into the transformations undergone by galaxies of similar morphological types at higher redshifts, whenever these types existed with similar masses.

Interestingly, our analysis suggests that the Hubble sequence can be considered as a reverse evolutionary sequence, with monotonous changes in the color-mass diagram characterized by bulge growth and disk reddening, and with the limitation that galaxies do not go linearly or systematically through all indi-

vidual types. Indeed, despite a systematic decrease in the B/T bulge-to-total ratio along the sequence (from E to Im), there is a significant dispersion in the measured values of B/T with morphological type (Fig. 27). However, a major mass build-up in the history of a galaxy requires many mergers that cause a significant B/T increase, and therefore a shift to earlier morphological types. Forward changes in morphology along the Hubble sequence can nevertheless occur as a result of individual mergers that are likely to temporarily boost the star formation rate, hence making the disk bluer. Nevertheless, as the Universe expands, the cosmic streams get thinner with time which may reduce the gas accretion from the cosmic web to galaxies, and the numerous mergers decrease the number density of galaxies, in particular of low mass, so galaxies will inexorably all age toward the Red Sequence.

Although we have reviewed some results from numerical simulations and assessed their compatibility with our observations (see Sect. 5.6), a direct comparison by deriving from cosmological volumes the color-mass diagram complemented by B/T and disk color would be a simple and critical test of the simulations. Ideally, use of the same approach based on producing projected image of the simulated galaxies and performing bulge and disk modeling with SourceXtractor++ would allow one to monitor the possible biases due to observational effects. To bring new insights into the characteristics of nearby galaxies as a function of their morphological types and location within the evolutive sequence displayed by the $NUV - r$ color-mass plane, we will report in Quilley & de Lapparent (*in prep.*) on other properties of the bulge and disks of EFIGI and MorCat galaxies, such as their distributions of bulge-to-total ratios, effective radii and Sérsic indexes, as well as the scaling relations.

7. Acknowledgements

We warmly thank Matthew Lehnert for enriching discussions, thorough reading, critical comments on this manuscript, and for suggesting the "Green Plain" renaming. We are very grateful to Emmanuel Bertin for initiating and leading the EFIGI project, and for maintaining the computer cluster on which all calculations were performed. We also thank Damien Le Borgne for his great help in using the ZPEG software. We are indebted to Aline Chu for her significant internship work that led to the selection of the MorCat catalog from HyperLeda galaxies, and for her making of the MorCat sky mask. We also thank the anonymous referee for their careful reading and important suggestions and comments.

This research made use of `SourceXtractor++`[2], an open source software package developed for the Euclid satellite project. This research made use of the VizieR catalog access tool, CDS, Strasbourg, France (DOI: 10.26093/cds/vizier). The original description of the VizieR service was published in A&AS 143, 23. This research also made use of NASA's Astrophysics Data System.

This work is based on observations made with the NASA Galaxy Evolution Explorer. GALEX is operated for NASA by the California Institute of Technology under NASA contract NAS5-98034. Funding for the SDSS and SDSS-II has been provided by the Alfred P. Sloan Foundation, the Participating Institutions, the National Science Foundation, the U.S. Department of Energy, the National Aeronautics and Space Administration, the Japanese Monbukagakusho, the Max Planck Society, and the Higher Education Funding Council for England. The SDSS Web Site is http://www.sdss.org/. The SDSS is managed by the Astrophysical Research Consortium for the Participating Institutions. The Participating Institutions are the American Museum of Natural History, Astrophysical Institute Potsdam, University of Basel, University of Cambridge, Case Western Reserve University, University of Chicago, Drexel University, Fermilab, the Institute for Advanced Study, the Japan Participation Group, Johns Hopkins University, the Joint Institute for Nuclear Astrophysics, the Kavli Institute for Particle Astrophysics and Cosmology, the Korean Scientist Group, the Chinese Academy of Sciences (LAMOST), Los Alamos National Laboratory, the Max-Planck-Institute for Astronomy (MPIA), the Max-Planck-Institute for Astrophysics (MPA), New Mexico State University, Ohio State University, University of Pittsburgh, University of Portsmouth, Princeton University, the United States Naval Observatory, and the University of Washington.

[2] https://github.com/astrorama/SourceXtractorPlusPlus

References

Abraham, R. G., Tanvir, N. R., Santiago, B. X., et al. 1996, MNRAS, 279, L47
Aihara, H., Allende Prieto, C., An, D., et al. 2011, ApJS, 193, 29
Allen, P. D., Driver, S. P., Graham, A. W., et al. 2006, MNRAS, 371, 2
Arp, H. 1966, ApJS, 14, 1
Baillard, A., Bertin, E., de Lapparent, V., et al. 2011, A&A, 532, A74
Bait, O., Barway, S., & Wadadekar, Y. 2017, MNRAS, 471, 2687
Baldry, I. K., Glazebrook, K., Brinkmann, J., et al. 2004, ApJ, 600, 681
Barway, S., Kembhavi, A., Wadadekar, Y., Ravikumar, C. D., & Mayya, Y. D. 2007, ApJ, 661, L37
Barway, S., Wadadekar, Y., Kembhavi, A. K., & Mayya, Y. D. 2009, MNRAS, 394, 1991
Barway, S., Wadadekar, Y., Vaghmare, K., & Kembhavi, A. K. 2013, MNRAS, 432, 430
Bertin, E. & Arnouts, S. 1996, A&AS, 117, 393
Bertin, E., Schefer, M., Apostolakos, N., et al. 2020, in Astronomical Society of the Pacific Conference Series, Vol. 527, Astronomical Data Analysis Software and Systems XXIX, ed. R. Pizzo, E. R. Deul, J. D. Mol, J. de Plaa, & H. Verkouter, 461
Bianchi, L., Rodriguez-Merino, L., Viton, M., et al. 2007, ApJS, 173, 659
Bianchi, L., Shiao, B., & Thilker, D. 2017, ApJS, 230, 24
Bluck, A. F. L., Conselice, C. J., Bouwens, R. J., et al. 2009, MNRAS, 394, L51
Bluck, A. F. L., Maiolino, R., Brownson, S., et al. 2022, A&A, 659, A160
Bluck, A. F. L., Mendel, J. T., Ellison, S. L., et al. 2014, MNRAS, 441, 599
Bower, R. G., Benson, A. J., Malbon, R., et al. 2006, MNRAS, 370, 645
Bremer, M. N., Phillipps, S., Kelvin, L. S., et al. 2018, MNRAS, 476, 12
Bridge, C. R., Carlberg, R. G., & Sullivan, M. 2010, ApJ, 709, 1067
Brinchmann, J., Charlot, S., White, S. D. M., et al. 2004, MNRAS, 351, 1151

Brunetti, M., Chiappini, C., & Pfenniger, D. 2011, A&A, 534, A75
Chan, J. C. C., Wilson, G., Balogh, M., et al. 2021, ApJ, 920, 32
Conselice, C. J. 2006, MNRAS, 373, 1389
Croton, D. J., Springel, V., White, S. D. M., et al. 2006, MNRAS, 365, 11
de Lapparent, V. 2003, A&A, 408, 845
de Lapparent, V., Baillard, A., & Bertin, E. 2011, A&A, 532, A75
de Lapparent, V., Geller, M. J., & Huchra, J. P. 1986, ApJ, 302, L1
De Propris, R., Bremer, M. N., & Phillipps, S. 2015, MNRAS, 450, 1268
—. 2016, MNRAS, 461, 4517
de Vaucouleurs, G. 1959, Handbuch der Physik, 53, 275
de Vaucouleurs, G., de Vaucouleurs, A., Corwin, Herold G., J., et al. 1991, Third Reference Catalogue of Bright Galaxies
Deeley, S., Drinkwater, M. J., Sweet, S. M., et al. 2021, MNRAS, 508, 895
Dekel, A. & Birnboim, Y. 2006, MNRAS, 368, 2
—. 2008, MNRAS, 383, 119
Di Matteo, P., Haywood, M., Combes, F., Semelin, B., & Snaith, O. N. 2013, A&A, 553, A102
Dimauro, P., Daddi, E., Shankar, F., et al. 2022, MNRAS, 513, 256
Driver, S. P., Popescu, C. C., Tuffs, R. J., et al. 2007, MNRAS, 379, 1022
Elbaz, D., Daddi, E., Le Borgne, D., et al. 2007, A&A, 468, 33
Fioc, M. & Rocca-Volmerange, B. 1999, arXiv e-prints, astro
Fisher, D. B. & Drory, N. 2008, AJ, 136, 773
Gadotti, D. A. 2009, MNRAS, 393, 1531
Gil de Paz, A., Boissier, S., Madore, B. F., et al. 2007, ApJS, 173, 185
Hubble, E. P. 1936, Realm of the Nebulae
Jackson, R. A., Kaviraj, S., Martin, G., et al. 2022, MNRAS, 511, 607
Jackson, R. A., Martin, G., Kaviraj, S., et al. 2020, MNRAS, 494, 5568
Kauffmann, G., Heckman, T. M., Budavári, T., et al. 2007, ApJS, 173, 357
Kaviraj, S., Laigle, C., Kimm, T., et al. 2017, MNRAS, 467, 4739
Kaviraj, S., Schawinski, K., Devriendt, J. E. G., et al. 2007, ApJS, 173, 619
Kennicutt, Robert C., J. 1998, ARA&A, 36, 189
Kereš, D. & Hernquist, L. 2009, ApJ, 700, L1
Kim, K., Oh, S., Jeong, H., et al. 2016, ApJS, 225, 6
Kormendy, J. & Kennicutt, Robert C., J. 2004, ARA&A, 42, 603
Lang, P., Wuyts, S., Somerville, R. S., et al. 2014, ApJ, 788, 11
Le Borgne, D. & Rocca-Volmerange, B. 2002, A&A, 386, 446
Lintott, C., Schawinski, K., Bamford, S., et al. 2011, MNRAS, 410, 166
López-Sanjuan, C., Balcells, M., Pérez-González, P. G., et al. 2009, A&A, 501, 505
Madau, P. & Dickinson, M. 2014, ARA&A, 52, 415
Makarov, D., Prugniel, P., Terekhova, N., Courtois, H., & Vauglin, I. 2014, A&A, 570, A13
Maller, A. H. & Bullock, J. S. 2004, MNRAS, 355, 694
Martig, M., Bournaud, F., Teyssier, R., & Dekel, A. 2009, ApJ, 707, 250
Martin, D. C., Wyder, T. K., Schiminovich, D., et al. 2007, ApJS, 173, 342
Martin, G., Kaviraj, S., Devriendt, J. E. G., Dubois, Y., & Pichon, C. 2018, MNRAS, 480, 2266
Mihos, J. C. 1995, ApJ, 438, L75
Minchev, I., Famaey, B., Combes, F., et al. 2011, A&A, 527, A147
Mitsuda, K., Doi, M., Morokuma, T., et al. 2017, ApJ, 834, 109
Nair, P. B. & Abraham, R. G. 2010, ApJS, 186, 427
Noeske, K. G., Weiner, B. J., Faber, S. M., et al. 2007, ApJ, 660, L43
Park, M., Tacchella, S., Nelson, E. J., et al. 2021, arXiv e-prints, arXiv:2112.07679
Phillipps, S., Bremer, M. N., Hopkins, A. M., et al. 2019, MNRAS, 485, 5559
Sachdeva, S., Saha, K., & Singh, H. P. 2017, ApJ, 840, 79
Salim, S. 2014, Serbian Astronomical Journal, 189, 1
Salim, S., Rich, R. M., Charlot, S., et al. 2007, ApJS, 173, 267
Sampaio, V. M., de Carvalho, R. R., Ferreras, I., Aragón-Salamanca, A., & Parker, L. C. 2022, MNRAS, 509, 567
Scaramella, R., Amiaux, J., Mellier, Y., et al. 2021, arXiv e-prints, arXiv:2108.01201
Schawinski, K., Urry, C. M., Simmons, B. D., et al. 2014, MNRAS, 440, 889
Silk, J. & Rees, M. J. 1998, A&A, 331, L1
Strateva, I., Ivezić, Ž., Knapp, G. R., et al. 2001, AJ, 122, 1861
van den Bergh, S. 1990, ApJ, 348, 57
—. 2007, AJ, 134, 1508
van Driel, W., Butcher, Z., Schneider, S., et al. 2016, A&A, 595, A118
Wyder, T. K., Martin, D. C., Schiminovich, D., et al. 2007, ApJS, 173, 293

4.5 Galactic rings within the Green Valley

We examine here the presence of EFIGI inner and outer rings along the color-mass diagram, which were not examined in the article. The EFIGI `Inner Ring` and `Outer Ring` attributes estimate, on a scale of 0 to 4, the contribution to the total galaxy light by a ring inside and outside the disk, respectively. They are indeed observed only in disk galaxies, that is lenticulars and spirals. These structures represent significant sub-areas of the galaxies, and are usually of low surface brightness, as confirmed by the distribution of the EFIGI attribute values with fractions of 55%, 29%, 11% and 5% for the 1 to 4 values respectively for inner ringed galaxies, and 63%, 24%, 9% and 4% for the outer-ringed ones. Similarly to what was done for other EFIGI attributes in the article, we compute in color-mass cells the fraction of objects showing each type of ring and then the average intensity of these rings within the sub-sample of ringed galaxies.

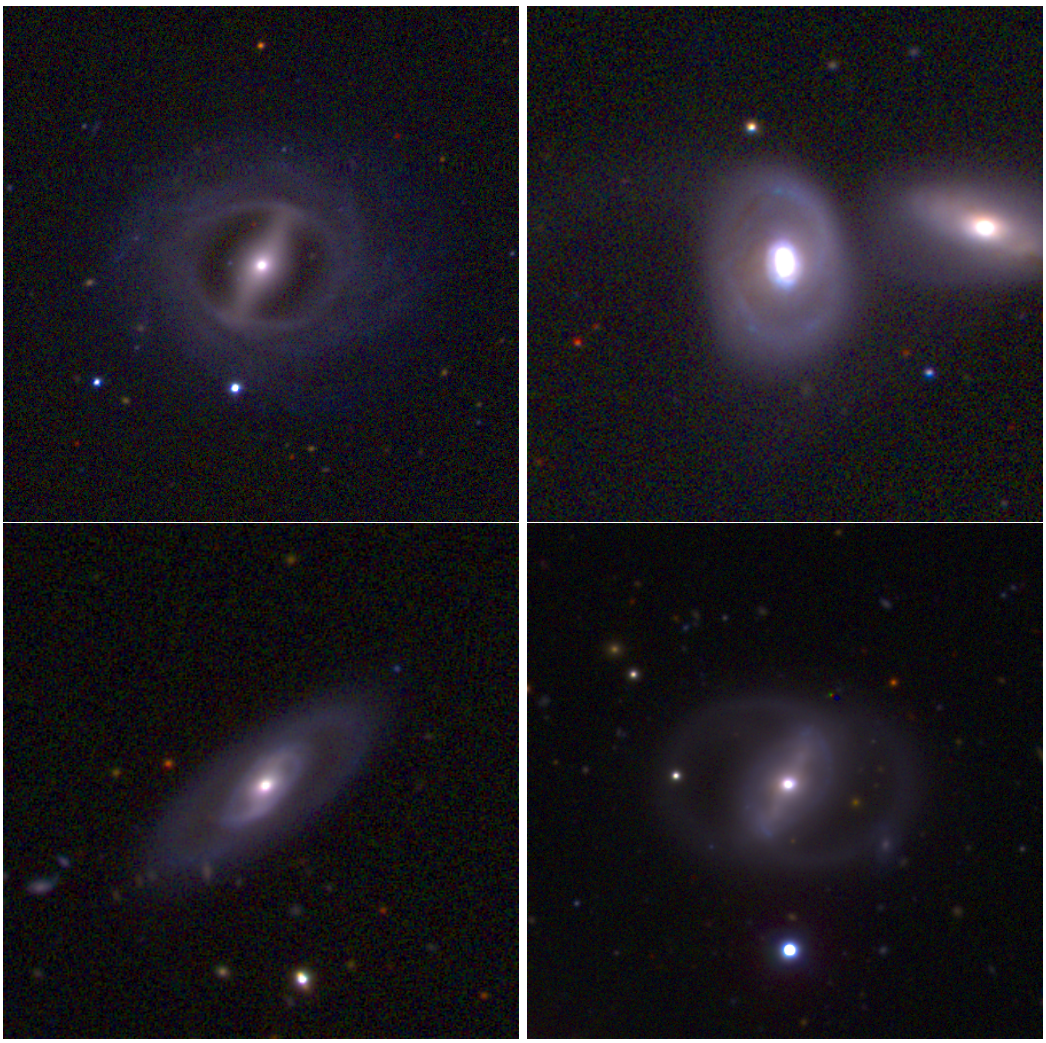

Figure 4.3: *gri* composite color images of the EFIGI galaxies PGC0049310 (top left), PGC0008228 (top right), that are examples of the `Inner Ring`(= 3) and `Outer Ring`(= 4) attributes respectively, as well as PGC0024710 (bottom left) exhibiting both rings (both at a 3 value), and PGC0010634 (bottom right) displaying a `Pseudo-Ring`(= 3), with also an `Inner Ring`(= 4). Both PGC0010634 and PGC0049310 have a bar that extends to the inner ring. Unlike most rings, PGC0008228 shows high surface brightness, as well as intense blue color in both its bulge and ring, indicating heavy star formation, likely triggered by the interaction with its neighboring galaxy.

Fig. 4.4 show the results for the inner and outer rings, in the top and bottom rows respectively. The approximate transition regions from the Green Valley to the Red Sequence and to the Blue Cloud are indicated by red and blue lines, respectively. In both cases, the fraction of ringed galaxies strongly peaks within the Green Valley, with a maximum value for $NUV - r \in [4.25; 5.0]$, and $\log(M_*/M_\odot) \in$

[11.0; 11.75] or [10.25; 11.0] for inner and outer rings respectively. The other largest values are reached in the neighboring color-mass cells. However, the inner and outer ring fractions are different from each other, with the former peaking at 80% for massive Green Valley galaxies, against 35% for the latter, as outer rings are generally rarer than inner rings. The fractions of both types of rings decrease for color-mass cells further away from the Green Valley, with fraction of inner and outer rings being around 30% and 20% respectively in the Red sequence respectively. A major difference is however that the fraction decrease for bluer galaxies is steeper for outer than inner rings, with outer ring fractions $\lesssim 7\%$ at the high-mass end of the Blue Cloud ($\log(M_*/M_\odot) > 10.25$ and $NUV - r < 3.5$), whereas the inner ring fractions in this region (34% to 57%) are similar or higher than those in the Red Sequence for the same mass interval. For low masses, the decrease continues until no more rings are present: not a single outer ring is observed below $\log(M_*/M_\odot) < 9.5$, as well as below $\log(M_*/M_\odot) < 8.75$ for inner rings.

Although the fractions of inner and outer rings are significantly different in the three regions of the color-mass diagram, the values of the mean attribute for the galaxies with either type of ring (shown in the right panels of Fig. 4.4) are comparable. This indicates that when inner rings or outer rings are present, they appear to include a similar fraction of the galaxy total light. Moreover, the inner rings are significantly more prominent within the Green Valley and Red Sequence than in the Blue Cloud, with respective mean attribute values of 1.88 ± 0.07 and 1.36 ± 0.04 above and below $NUV - r = 3.77$, which we defined as the color limit between the Blue Cloud and Green Valley, that is a 6.6σ difference. The statistics of outer rings are too low to examine this aspect. The rare outer `Pseudo-rings` (Buta & Combes 1996) measured in EFIGI that are very high winding spiral arms around the galaxy bar, also show a similar pattern of higher fraction in the Green Valley with $\sim 10\%$ of galaxies in the Green Valley, a few percents in one color step into either the Blue Cloud and Red Sequence, and only 1 pseudo-ring observed outside these regions.

As shown in (Quilley & de Lapparent 2022, see Sect. 4.4), the Hubble types span the color-mass plane, hence different types dominate specific regions, so we can also examine the impact of the morphological type to understand the prevalence of rings in and around the Green Valley. Fig. 4.5 shows the fractions of galaxies with an inner or outer ring as a function of Hubble type. In both cases, $S0^-$ types show very few rings (fractions of 3.9 % for inner and 3.1% for outer rings respectively). There is then a very steep increase of the fraction of rings towards later types within the lenticulars, that reaches a maximum at 51.7% of S0a types for outer rings, whereas it keeps increasing up to a peak fraction of 80.3% of the Sab early spiral types for inner rings. We see again that outer rings are rarer than inner rings, even for the morphological types for which they are frequent. In agreement with the slopes of the decreasing fractions towards bluer and less massive cells of the Blue Cloud exhibited in Fig. 4.4, the decrease towards later types is different for inner and outer rings: there is a steep decline of outer rings whose fraction per type is already at 6.6% for Sb and stays below 5% for all spiral types up to Sdm, while a more progressive decrease is observed for inner rings, with 59%, 44% and 23% of galaxies hosting an inner ring for the Sb, Sc, and Sd types respectively. The Green Valley being populated mainly by types Sa and S0a, whereas $S0^+$ and Sab types are at the junctions with the Red sequence and Blue Cloud respectively, the overall higher fractions measured for these Hubble types confirm the predominance of rings in and around the Green Valley, but also at the transition between spirals and lenticulars.

Previous studies had noted the prevalence of rings within the Green Valley. For instance, Smith et al. (2022) used the GAMA survey and the Galaxy Zoo classification to study the morphology of Green Valley galaxies and found that ring structures are more frequent in Green Valley galaxies than in their red and blue counterparts, in agreement with the results we derive here from EFIGI. Moreover, interesting results were obtained by Elagali et al. (2018) who developed a method to identify ring galaxies in the EAGLE simulation and examined the formation history of the objects obtained. These galaxies have intermediate $u - r$ colors at $z = 0.5$, with 5 out of 7 of them located in the Green Valley, while at $z = 0$, 4 are within the Blue Cloud and 3 others show slightly redder colors compatible with the Green Valley. The sample size is too small for a statistical analysis, and the use of $u - r$ color also limits the ability to properly identify Green Valley galaxies. However, these simulated galaxies seem to be in agreement with the observed ones as their intermediate colors and stellar masses around $10^{11} M_\odot$

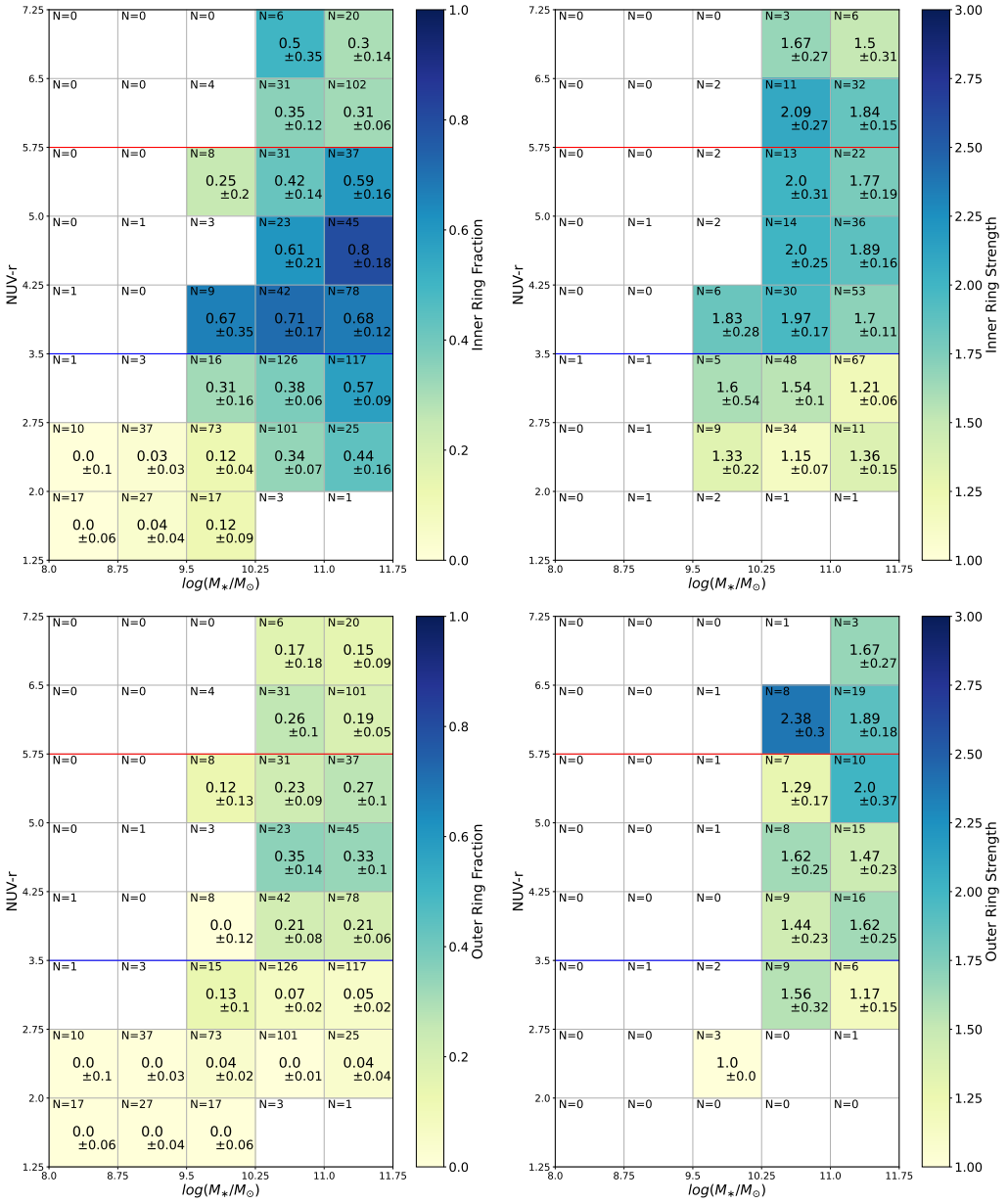

Figure 4.4: **Left:** Fraction of EFIGI ∩ GALEX galaxies with `Incl-Elong` ≤ 2 and types S0$^-$ to Im having an attribute value `Inner Ring` > 0 (top row) or `Outer Ring` > 0 (bottom row), in color-mass cells of 0.75 dex in stellar mass and 0.75 in $NUV - r$ color, all the way from the Blue Cloud to the Red sequence. The fraction of inner-ringed galaxies peaks above 60% within the Green Valley, and decreases towards the Blue Cloud or the Red Sequence, with more than a third of either red and blue galaxies still showing an inner ring in the same stellar mass range ($10.25 < \log(M_*/M_\odot) < 11.75$), and reaches 0 for low-mass galaxies. The fraction of outer-ringed galaxies peaks up to 35% within the Green Valley, decreases around 20% in the Red sequence, while only a few objects within the Blue Cloud show an external ring, at its intermediate and massive end. **Right:** Average value of the `Inner Ring` (top) or `Outer Ring` (bottom) attribute for the inner/outer-ringed galaxies in the same color-mass cells. Intermediate spirals located in the Blue Cloud have significantly less prominent inner rings than earlier galaxy types within the Green Valley.

correspond to the color-mass cells in which EFIGI galaxies are the most likely to exhibit rings. It is therefore insightful to look at their evolution with time in the EAGLE hydrodynamical simulation, that allows one to see how they formed. Among the total of 55 ringed galaxies identified at all redshifts, 46 (i.e. 84%) rings formed following an interaction, with one or more companion galaxies passing through their disk. The 9 remaining ring galaxies (i.e. 16%) have very long-lived ring morphologies (> 2 Gyr)

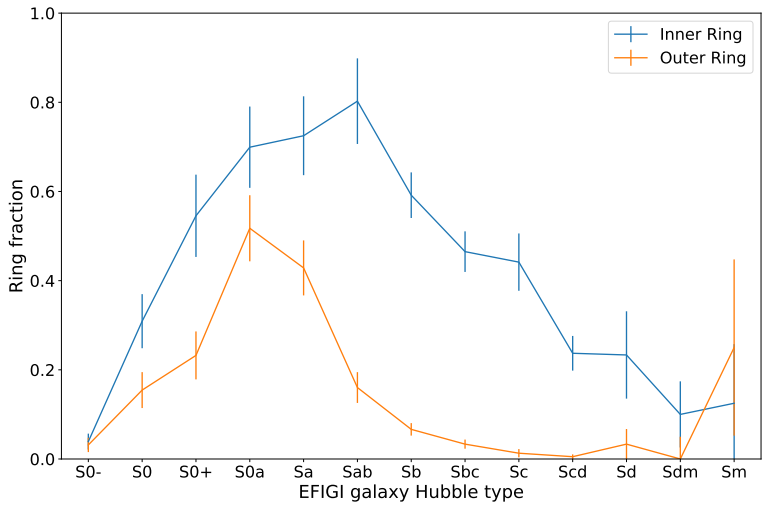

Figure 4.5: Fraction of EFIGI galaxies having an attribute value `Inner Ring` > 0 (blue line) or `Outer Ring` > 0 (orange line) as a function of Hubble Type, for all lenticulars and spirals. The outer ring fraction peaks for type S0a at 51.7% and then steeply decreases, whereas inner rings are overall more frequent, their fraction reaching a maximum for types Sab at 80.3 %. Sab and $S0^+$ types mark the limits of the Green Valley with the Blue Cloud and Red Sequence respectively, while Sa and S0a span the interior of the Green Valley. The fact that these 4 types show the highest ring fractions, considering both inner and outer rings further confirms that the onset of rings is related to the crossing of the Green Valley.

and host strong bars. Therefore , the higher fraction of ringed galaxies within the Green Valley, and the origin of these rings being linked to interaction in the EAGLE simulation constitute another element favoring the importance of minor mergers in driving the evolution through the Green Valley.

Regarding bars, we note that EFIGI inner rings are often observed to enclose a galactic bar whose extremities reach into the ring and sometimes an over-density is seen in the connecting region of the ring (see Fig. 4.3). The existence of a bar is systematic for the outer pseudo-rings that may be an intermediate or incomplete stage in the formation of an outer ring. Rings and bars actually appear to be related dynamical structures within the disks of galaxies, as shown in Fig. 4.6 : there is an increased fraction of inner ringed galaxies at an attribute value of 1, from 17% when no bar is visible (`Bar`$= 0$), compared to 21% to 27% for `Bar` attribute values 2, 3, and 4 (and a similar trend for `Inner ring` values of 2 and `Bar` values of 3 and 4). The effect is weaker but still present for `Outer ring` and `Pseudo ring` values of 1 and `Bar` values of 3 and 4. I also measure that $36.3 \pm 1.3\%$ of EFIGI spiral and lenticular galaxies exhibit inner rings, and this fraction increases to $46.4 \pm 2.2\%$ for EFIGI barred galaxies (for the same types), that is a 4σ increase. The increase remains of similar significance (3.4σ) for galaxies within the stellar mass range $10.25 < \log(M_*/M_\odot) < 11.75$, with inner-ring fractions of $48.9 \pm 2.0\%$ for all galaxies, and $61.3 \pm 3.1\%$ for barred galaxies respectively, so the increased fraction of inner-rings for barred galaxies is not a mass effect. The excess of rings measured for barred galaxies could be explained by either a bar origin of some rings, or a common origin of both types of structures, e.g. a merger or fly-by.

Our results are also qualitatively consistent with the theoretical predictions by Dekel et al. (2020) that massive bulges support long-lived rings (several Gyr) at high redshifts. These rings occur after the compaction events that have generated the massive bulges. These events, often caused by mergers, and driving gas inwards are considered to be "the early stages of quenching, namely in the Green Valley". The bulge growth we measured across the Green Valley, and which is related to quenching, also appears connected to the onset of galactic rings in the EFIGI sample. This is consistent with the higher ring fractions exhibited by early spirals Sa and Sab as well as S0a lenticulars (and especially S0a for outer rings, which is the dominant type of ring obtained in the simulations by Dekel et al. 2020). The mechanisms, e.g. mergers, that form these-bulge dominated galaxies tend to also create rings. However, we note that for earlier EFIGI types, namely lenticulars, that are located in the Red

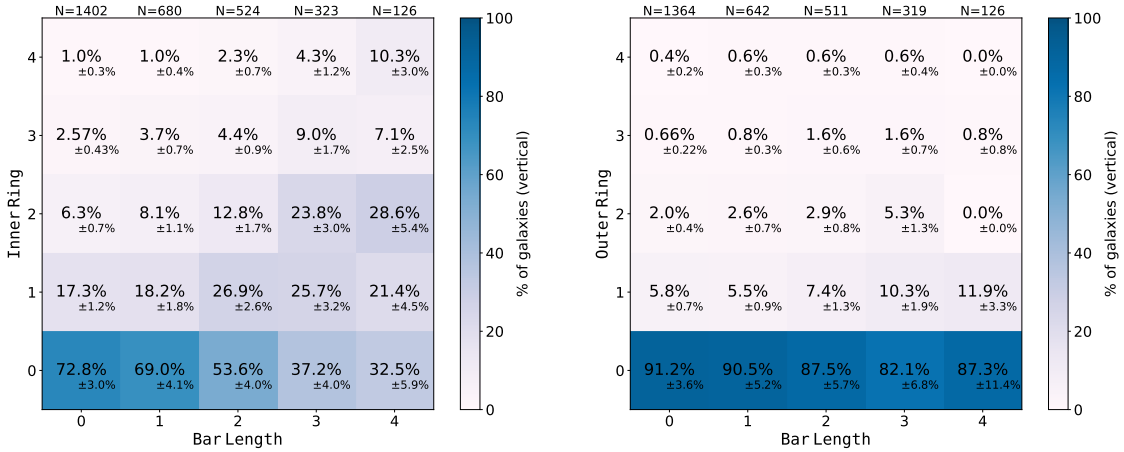

Figure 4.6: Percentages of galaxies with a given value of the `Inner Ring` (left) and `Outer Ring` (right) attributes among all galaxies having a certain value of the `Bar` attribute, which is classified as 0 when no bar is visible, and measures its length compared to the disk size for positive values. The number of galaxies per value of `Bar` is given at the top of each column. Barred galaxies exhibit larger fraction of both inner and outer rings. The inner ring fraction, as well as the inner ring strength, even increase with the bar length.

Sequence and with similar or greater B/T ratios than the early spirals, the fractions of rings plummet, so that the value of B/T does not determine the frequency of rings.

Regarding lenticulars, the red colors of the inner or outer rings of EFIGI galaxies examined using the *gri* color images suggest that they are made of old stars. However, the analysis by Salim et al. (2012) brought to light a link between residual star formation and the presence of rings. They examined 27 massive ETG in the Red Sequence that were chosen to be bulge-dominated (based on a concentration criterion) with quiescent SDSS spectra but strong UV excess, among an original sample of tens of thousands of galaxies. Their far-UV images obtained with HST revealed that 93% of them show low-level of ongoing star formation, which can occur in small patches, or extend to the whole galaxy for 3/4 of the objects. All galaxies that show galaxy-scale star formation are lenticulars according to their optical morphology, hence contain an old stellar disk, whereas their UV morphology exhibits a ring of star formation of varying size and morphology. Therefore, among the quenching galaxies, a ring may be the locus of star formation, in a similar way as a spiral arm. To further gain insight on the part played by rings in star formation, one would need to investigate their colors (see Sect. 6.2).

The results presented in this section bring insight into the formation and persistence of galactic rings. Buta & Combes (1996) state that "the standard mechanism to form rings [...] appears to require the presence of a bar", as the first simulated rings were triggered by bar forcing onto the gas of the galactic disk (Schwarz 1981). However, many non-barred ringed galaxies are observed, which raises the question of either another ring formation mechanism, or bar destruction while the ring remains. With an enhanced fraction of rings in barred galaxies, our study of EFIGI ringed galaxies is consistent with the bar contributing to the formation of rings. But we also find many non-barred galaxies and a strong predominance of rings within the Green Valley, whereas bars are present in similar proportions across the color-mass diagram. Therefore, a mechanism is needed to explain why rings appear more frequently in the Green Valley (or do not survive outside of it), without hosting also a bar. The EAGLE simulation brings evidence that mergers play this role (Elagali et al. 2018), but those are also expected in great numbers within the Blue Cloud. This difference can not be explained by stellar mass as Blue Cloud galaxies with similar masses as in the Green Valley still show lower fractions of rings. However, the fraction of rings appear to be strongly $NUV - r$ color-dependent (Fig. 4.4), which in this mass range also corresponds to a dependence on Hubble type (Fig. 4.5), hence B/T. In that regard, the simulations by Dekel et al. (2020) help us explain that for mergers to form long-lasting rings, a prominent bulge is also needed, which is the case for the early spirals of the Green Valley but not in the Blue Cloud. The exhaustion of gas in the Red Sequence is such that even if merger may

occur (note that large B/T bulges are present), rings can form only if residual gas remains, leading to the decreasing lower ring fractions in these red galaxies. This phenomenon might be similar to the decreasing fraction of strong bars in S0 galaxies that Buta et al. (2010) explain by a lack of gas accretion.

Chapter 5

Scaling relations of bulges and disks

We have thus far investigated the evolution of galaxies by relating their mass, star formation activity, probed with colors, and morphology (using their Hubble type and additional morphological parameters, most notably the bulge-to-total ratio B/T). To gain further insight into the evolution pathway of galaxies, we now present the analysis of the sizes of the bulges and disks for all morphological types. As we have built an evolution scenario based on successive mergers explaining the mass growth of galaxies, and in which significant bulge growth occurs concomitantly to the transition from star formation to quiescence, we expect that physical size variations of bulges, disks, and galaxies bring complementary information to this picture of galaxy formation. The bulge and disk decomposition and single-profile modeling of all EFIGI galaxies, which is described in Sect. 3.1 do provide us with all the needed information. The analysis described in this chapter is therefore complementary to that reported on in Chapter 4. As they are based on the same data set, we expect from them consistent conclusions on the evolution of the Hubble sequence.

5.1 Photometric scaling relations

The many scales, mediums (stars, gas, and dust) and interconnected physical processes required to model galaxies are too complex to be properly put into equations and solved analytically. To gain insight into the evolution of galaxies, astrophysicists therefore resort to simplified models that link only a few key parameters describing each galaxy and examining and interpreting possible correlations among them. One noteworthy example in that regard is the fundamental plane for normal E galaxies: they lie on a plane in the 3D space relating their effective radius, surface brightness and velocity dispersion, implying that any of these 3 quantities can be inferred from the other two (Djorgovski & Davis 1987). In our study, we only examine scaling relations between parameters derived only through the photometry of galaxies.

Scaling relations between the sizes of galaxies and other photometric parameters have been discovered and developed in previous landmark studies, and we recompute them with EFIGI galaxies. The Kormendy (1977a) relation links the effective radius of elliptical galaxies to their mean effective surface brightness. Due to similarities between bulges and E galaxies, the relation was reproduced by further studies on the bulges of galaxies (Allen et al. 2006; Kim et al. 2016). Most notably, Gadotti (2009) showed that some bulges were in the continuity of the relation for E galaxies, interpreting them as classical bulges, while those departing from the relation, towards smaller radii and fainter surface brightness, were inferred to be pseudo-bulges. Similar parameters were studied for the disks of galaxies by de Jong (1996), with larger sizes for dimmer objects. In addition, the size-luminosity relation, first highlighted by Binggeli et al. (1984) for elliptical galaxies, can be computed for whole galaxies (Trujillo et al. 2004; Brooks et al. 2011; Grazian et al. 2012; Kawamata et al. 2018; Yang et al. 2022a,b) as well as bulges and disks (Bruce et al. 2014; Dimauro et al. 2019). The size-luminosity relation is particularly important as it allows one to associate a physically meaningful size to a magnitude when creating synthetic, or "mock" galaxy images. When creating the corresponding mock catalog, it is common to draw a galaxy luminosity from a measured luminosity function, in order to ensure the agreement with it by design, and then the size-luminosity relation is essential to derive the associated size of each galaxy.

Due to the tight anti-correlation between magnitude and stellar mass (see Sect. 4.4), size-mass relations are also often computed, and yield similar information (Bruce et al. 2014; Dimauro et al. 2019; Mowla et al. 2019). The size-mass relation was investigated in terms of the morphology of galaxies by Lange et al. (2015) who computed this relation for two sub-samples of the GAMA survey corresponding to ETG and LTG, which were all fitted by a single Sérsic profile in 10 bands ($ugrizZYJHK_S$). The distinction was made between these populations using a Sérsic index cut and/or a color cut, as well as one based on visual morphological classification. All criteria used to separate between them led to a steeper size-mass relation for ETG than for LTG. By studying these various scaling relations for EFIGI galaxies, we test on the one hand their validity with improved morphological data and larger statistics, and on the other hand we may be able to relate these correlations to the evolution of galaxies along the Hubble sequence.

5.2 Synthesis

In this section, I summarize the article Quilley & de Lapparent (2023) presented in Sect. 5.3, and refer to its sections and figures.

In this analysis, I applied the Sérsic bulge and exponential disk decompositions using SourceXtractor++ to all galaxies, including those that do not have a bulge (E, dE, cD), in order to compare the scaling relations of the derived parameters across all morphological types. This is particularly justified for E types as it was shown that a fraction of them have a weak disk component that is detectable by its rotation (Krajnović et al. 2008, 2013). We therefore refer to the non-disk component of these types as their Seŕsic component, whereas it can be identified with the bulges for lenticular and spiral galaxies. For E, dE, cD as well as Im types, another type without a bulge, we also perform pure Sérsic profile fits.

We start by reproducing the Kormendy relation between effective radius R_e and mean effective surface brightness $\langle\mu_e\rangle$ for E, cD and dE EFIGI galaxies modeled as a single-Sérsic profile, and for the Sérsic components of E, cD, as well as the bulges of lenticular and spiral types, using their two-component decompositions (Fig. 3). We measure the relation for the single Sérsic profile fits to E galaxies with a slope of 2.87, compatible with the 3.02 value of Kormendy (1977a), and find a similar one for their Sérsic components with a less steep slope of 2.37. In both cases, this positive slope means that larger objects are dimmer in surface brightness $\langle\mu_e\rangle$, so that E galaxies get more diffuse as they grow. The bulges of types $S0^-$ to Sb appear to be in the continuity of this relation, with smaller R_e and brighter $\langle\mu_e\rangle$. The bulges of later spiral types gradually depart from the relation with even smaller R_e and fainter $\langle\mu_e\rangle$. This gradual departure from the relation is correlated with lower values of B/T as well as lower Sérsic indexes (Fig. 4), with less dispersion for the former parameter.

Similarly, we compute the size-luminosity relation between effective radius R_e and absolute magnitude M for E, cD and dE EFIGI galaxies modeled as a single-Sérsic profile, and for the Sérsic components of E, cD, lenticular and spiral types, from the bulge and disk decomposition (Fig. 6). There is once again a continuity between subsequent types with later types being shifted towards smaller R_e and fainter magnitudes. We compare the size-luminosity relation for E, cD and dE galaxies modeled as a single-Sérsic (Fig. 7) to the relation from Binggeli et al. (1984) and find steeper slopes of -0.37 against -0.30 for E galaxies at bright magnitudes ($M_g \lesssim -20$) and of -0.20 against -0.10 for dE galaxies at faint magnitudes ($M_g \gtrsim -19$). We find that a second-degree polynomial fit is more accurate to fit the size-luminosity of E galaxies, especially for both the brightest and faintest magnitudes. For the bulges, a second-degree polynomial fit is needed to allow for precise estimations of bulge sizes at all magnitudes, as the EFIGI size-luminosity relation a is convex, with a steeper size increase at brighter magnitudes.

We note that both previously analyzed relations are projections of the 3D parameter space relating effective radius R_e, absolute magnitude M and surface brightness $\langle\mu_e\rangle$ (Fig. 9), within which the position of bulges is driven by B/T, hence the morphological type (Fig. 14). The analysis of the bulge distribution in this 3D space lead us to argue that there is a continuous transition from faint and small bulges, both in terms of their sizes relative to other bulges (low R_e), and in comparison to the whole galaxy, through either the B/T or h_e/R_e values, embedded in late-type spirals, to larger, more

prominent and brighter bulges, with steeper light profiles embedded in early spirals and lenticulars. We interpret the two ends of this transition to correspond to pseudo-bulges and classical bulges respectively, in regard to the previous studies discussed in Sect. 5.2 (see also Sect. 2.1.1). This change of bulge type is identified as corresponding to a change of regime from increasing volume and surface density of the small bulges to more prominent bulges that are more diffuse as they grow in size. We also propose the bulge absolute magnitude range $[-19.1; -17.8]$ as a transition region, with classical bulges dominating at $M_g < -19.1$ and pseudo-bulges at $M_g > -17.8$ (Sect. 5.3.2), and a corresponding B/T range of $[0.08; 0.15]$. Furthermore, bulges with intermediate values of R_e, M_g, $n_{\text{Sérsic}}$ (most likely found within galaxies with intermediate B/T, h_e/R_e, or morphological type altogether) are proposed to be composite bulges formed of two stellar populations whose dynamics correspond to a pseudo or classical bulge respectively, and whose relative preponderance define where the bulge properties lie along this continuous transition.

For both the Kormendy and the size-luminosity relation, the choice between a single-Sérsic profile and the Sérsic component of the bulge and disk decomposition for Hubble types with no visible disk should be considered, as the derived magnitudes, effective radii, surface brightness and Sérsic indexes depend on the choice of the modeling profile. We emphasize that in our study the trends drawn by galaxies of these types within the parameter space are found in both cases, and their interpretation remains the same. However, one must remain careful when using the values, and especially comparing them to other types, or confronting them to results of other analyses with various modeling methods.

We then perform a similar analysis on the disks of EFIGI galaxies. An equivalent of the Kormendy relation can be computed, in which disks with larger effective radii h_e have fainter central surface brightness μ_0. There are small shifts in the distribution of of subsequent types of galaxies within the h_e-μ_0 plane with early spirals having slightly brighter and larger disks than lenticulars, whereas later spiral types have smaller and fainter disks, and exhibit a higher dispersion. The size-luminosity relation for disks is fitted using a 2nd degree polynomial function, as it is also a convex relation with a steeper effective radii increase at brighter magnitudes, similarly to the bulges. The tail of faint disks ($M_{\text{disk,g}} > -19$) is made of late spirals (Sd to Sm) disks and Im galaxies (modeled by single-Sérsic profiles whose Sérsic index distribution peaks around 1, leading us to examine them together with the disks of spirals). The disks of lenticular, early and intermediate spirals strongly overlap at brighter disk magnitudes ($M_{\text{disk,g}} < -19$), with effective radii $h_e \in [3; 30] kpc$.

We relate the size distributions measured in this study to the merger-driven evolution scenario proposed in Quilley & de Lapparent (2022, see Chap. 4) by noticing that the size of disks mostly increases from late spirals to intermediate spirals (Fig. 15), while for bulges the transition happens between intermediate and early spirals and lenticulars (Fig. 15), which corresponds to the crossing of the Green Valley. Due to the marked correlation between B/T and Hubble type (see Fig. 14), we also examine how the bulge and disk sizes vary with B/T and bring to light power-law relations between the effective radii of these components and the galaxy B/T, with steeper increases for lenticulars than for spirals (Fig. 16, and Tab. 2). Finally we compute the size ratio between disk and bulge h_e/R_e and show that it correlates with Hubble type and B/T as well (Fig. 17).

All the parameters of the fits of the various size-luminosity that we examined in this article are provided in Tab. 1 so they can be used to generate faithful synthetic images of the nearby galaxies. Specifically, the 2nd degree polynomial relations for the bulges and disks will provide better estimates of their sizes than what a linear relation would have provided. Given the importance of the B/T that was underlined throughout this thesis, we emphasize that mock catalogs of bulges and disks need to match the observed galaxy population properties but also to be consistent with each other within each synthetic galaxy. In that regard, we highlight in the article the discrepancy between the relative bulge and disk sizes produced by the Stuff software (Bertin 2009) and the results obtained for EFIGI galaxies. We also provide the parameters of the size-B/T power-laws and discuss their use to ensure that a correct association of bulge and disk is performed when generating a mock galaxy (see Sect. 5.4).

5.3 Article

"Tailoring galaxies: size-luminosity-surface brightness relations of bulges and disks along the morphological sequence"
Louis Quilley & Valérie de Lapparent
29 pages, 17 figures, 2 tables
Submitted 2 May 2023, to Astronomy & Astrophysics
In revision after a positive report
10.48550/arXiv.2305.02069
https://ui.adsabs.harvard.edu/abs/2023arXiv230502069Q/abstract

Astronomy & Astrophysics manuscript no. output
December 21, 2023
© ESO 2023

Tailoring galaxies: Size-luminosity-surface brightness relations of bulges and disks along the morphological sequence

Quilley, L.[⋆] de Lapparent, V.[⋆⋆]

Institut d'Astrophysique de Paris, CNRS, Sorbonne Université, 98 bis boulevard Arago, 75014 Paris, France

Received 28 April 2023 / Accepted 22 August 2023

ABSTRACT

Aims. We revisit the scaling relations between size, luminosity, and surface brightness as a function of morphology, for the bulge and disk components of the 3106 weakly inclined galaxies of the "Extraction de Formes Idéalisées de Galaxies en Imagerie" (EFIGI) sample, in the nearby Universe.
Methods. The luminosity profiles from the Sloan Digital Sky Survey (SDSS) *gri* images were modeled as the sum of a Sérsic (bulge) and an exponential (disk) component for cD, elliptical (E), lenticular, and spiral galaxies, or as a single Sérsic profile for cD, E, dE, and irregular (Im) galaxies, by controlled profile fitting with the SourceXtractor++ software.
Results. For the EFIGI sample, we remeasured the Kormendy (1977) relation between effective surface brightness $\langle\mu\rangle_e$ and effective radius R_e of elliptical galaxies, and show that it is also valid for the bulges (or Sérsic components) of galaxy types Sb and earlier. In contrast, there is a progressive departure toward fainter and smaller bulges for later Hubble types, as well as with decreasing bulge-to-total ratios (B/T) and Sérsic indices. This depicts a continuous transition from pseudo-bulges to classical ones, which we suggest to occur for absolute g magnitudes M_g between −17.8 and −19.1. We also obtain partial agreement with the Binggeli *et al.* (1984) relations between effective radius and M_g (known as "size-luminosity" relations, in log-log scale) for E and dE galaxies. There is a convex size-luminosity relation for the bulges of all EFIGI types. Both $\langle\mu\rangle_e - R_e$ and $R_e - M_g$ scaling relations are projections of a plane in which bulges are located according to their value of B/T, which partly determines the morphological type. Analogous scaling relations were derived for the disks of lenticular and spiral types, and the irregulars. The curvature of the size-luminosity relation for disks is such that while they grow, they first brighten and then stabilize in surface brightness. Moreover, we obtain the unprecedented result that the effective radii of both the bulges and disks of lenticular and spiral galaxies increase as power laws of B/T, with a steeper increase for the bulges. Both bulges and disks of lenticular galaxies have a similar and largely steeper increase with B/T than those for spirals. These relations propagate into a single scaling relation for the disk-to-bulge ratio of effective radii across ∼ 2 orders of magnitude in B/T, and for all types. We provide the parameters of all of these relations that can be used to build realistic mock images of nearby galaxies. The new convex size-luminosity relations are more reliable estimates of bulge, disk, and galaxy sizes at all magnitudes in the nearby Universe.
Conclusions. This analysis describes the joint size and luminosity variations of bulges and disks along the Hubble sequence. The characteristics of the successive phases of disk and bulge size growth strengthen a picture of morphological evolution in which irregulars and late spirals merge to form earlier spirals, lenticulars, and eventually ellipticals.

Key words. Galaxies: evolution – Galaxies: bulges – Galaxies : elliptical and lenticular, cD – Galaxies : spiral – Galaxies: structure

1. Introduction

In the Hubble sequence (Hubble 1926), spiral and lenticular galaxies are made of two components: a bulge and a disk, with the former being in the center of the latter. In order to better understand the formation and evolution of these galaxies, astronomers have naturally looked at the properties of each component, as well as the relations between the two. In order to do so, the bulge and disk decomposition have become a standard approach to model galaxy images (Simien & de Vaucouleurs 1986; de Jong 1996; Allen et al. 2006; Simard et al. 2011). Bulges are usually composed of old stellar populations, hence their redder colors, while disks are bluer because they are the major loci of star formation. Spiral and lenticular disks differ due to the presence or absence of spiral arms, respectively, as well as their significant or weak star formation, respectively. Another difference that partly characterizes galaxy types are the fractions of total light of the galaxy that bulges and disks enclose, with earlier Hubble types (from late spirals to lenticular) having more prominent bulges on average (Quilley & de Lapparent 2022).

Kinematics analyses have shown that early-type galaxies can be separated into two classes of objects between slow and fast rotators (Emsellem et al. 2007, 2011), depending on the overall level of rotation of their stellar orbits. Similarly, the bulges nested at the centers of lenticular and spiral galaxies can also be differentiated based on their kinematics. Classical bulges are nearly spherical in shape, dominantly pressure-supported, and built by violent relaxation events such as mergers, while pseudo-bulges are flatter in shape and mainly rotation-supported (Kormendy & Kennicutt 2004). Among the pseudo-bulges, one can further differentiate disky bulges that are within the disk and built through secular evolution, from boxy/peanut bulges that also show circular orbits but are vertically more extended than the disk, and thought to be built by the buckling of the bar (Athanassoula 2005, 2008, 2013; Debattista et al. 2006).

Classical bulges show similar properties to elliptical galaxies, which are also pressure-supported systems (Davies & Illingworth 1983), and tend to be oblate (Costantin et al. 2018).

⋆ email: louis.quilley@iap.fr
⋆⋆ email: valerie.de_lapparent@iap.fr

Elliptical galaxies can be characterized by a scaling relation between their effective surface brightness and effective radius across a large range in luminosities, as shown by the so-called Kormendy relation (Kormendy 1977): if the G absolute magnitude interval is limited to $\sim [-22.1; -19.75]$ (see Sect. 4.1 for details), and the interval of effective radius only spans ~ 1.2 dex, the surface brightness describes a very large interval of nearly 4 magnitudes per arcsec^2 ($\sim [19.5; 23.5]$). Across a much wider range in absolute B_T magnitude ($\sim [-23.5; -12.0]$[1]), and a similar interval of ~ 1.5 dex in effective radius, Binggeli et al. (1984) derived another relation between the absolute magnitude and radius of elliptical galaxies, hence its name, the size-luminosity relation[2]. The characteristic surface brightnesses of the disks of lenticular and spiral galaxies span a similar $\sim 3-4$ magnitude range, with indications of a scaling with effective radius (de Jong 1996; Simard et al. 2011).

In this article, we revisit these relations with larger statistics using the sample of nearby, well-resolved galaxies extracted from the Sloan Digital Sky Survey (SDSS) images to create the "Extraction de Formes Idéalisées de Galaxies en Imagerie" (EFIGI) catalog with visual morphological classification (Baillard et al. 2011). Our goal is to examine whether the scaling relations of Kormendy (1977) and Binggeli et al. (1984) also apply for bulges of lenticulars and spirals, and whether there are similar scaling relations for their disks. In Quilley & de Lapparent (2022), we performed bulge and disk decomposition of all EFIGI galaxies in order to obtain a reliable description of both galaxy components and to study the role of morphology in galaxy evolution. We suggest that the Hubble sequence is an inverse sequence of galaxy physical evolution driven by mergers and dominated by bulge growth and disk quenching, which can be characterized quantitatively using the bulge-to-total ratio and the disk color. We also show that as galaxies evolve along the Hubble sequence, they cross the Green Valley (the transition region between the Blue Cloud and the Red Sequence) which spreads between Sab up to S0$^+$ morphological types, in which the star formation of galaxies fades the fastest with respect to the change in morphological type, and the bulge profiles become steeper (Quilley & de Lapparent 2022).

The new analysis allows us to further examine how the bulges and disks of the various Hubble types change in their light profile as they grow in mass and progressively halt their star formation (commonly referred to as "quenching"). Drory & Fisher (2007) and Gadotti (2009) have proposed using the bulge light profiles to differentiate among the classical and pseudo-bulges (steeper for the former than for the latter) in lenticular and spiral galaxies. As these changes are symptomatic of the different processes driving the evolution of bulges and disks, they may shed further light on the evolution of the Hubble morphological sequence. Examining the evolution of the size-luminosity relation with cosmic time can provide insight into these issues by confronting the mass growth of galaxies with their size growth (Trujillo et al. 2004; Brooks et al. 2011; Grazian et al. 2012; Kawamata et al. 2018; Yang et al. 2022a,b). Time evolution of the size-luminosity relations are directly accessible from numerical simulations, and several studies have highlighted discrepancies between the sizes of observed and simulated galaxies (Joung et al. 2009; Bottrell et al. 2017).

[1] If one excludes dwarf spheroidal galaxies.

[2] Hereafter, although not mentioned, the size-luminosity relation is always considered in log-log scale, as it may be linear in this coordinate plane.

To fully describe the light profile of a galaxy, or its bulge or disk, one needs at least parameters characterizing the size of the profile, its level of flux, its steepness, and its ellipticity. We here focus on relations between parameters describing the light profiles of galaxies; however, for the sake of interpretation, it is important to note that this still carries information about the stellar mass distribution due to their strong correlation (Quilley & de Lapparent 2022). Replacing the absolute magnitude by the stellar mass or the surface brightness by the stellar mass density does indeed lead to similar scaling laws for elliptical galaxies and bulges (Gao et al. 2022).

The present article is structured as follows. In Sect. 2, we present the data used in this study. In Sect. 3, we detail the methodology used to perform disk and bulge decomposition (Sect. 3.1) with the SourceXtractor++ software (Bertin et al. 2020), as well as of the spectral energy distribution (SED) model-fitting (Sect. 3.3) using the ZPEG software (Le Borgne & Rocca-Volmerange 2002). We then present the analytical expressions for deriving the surface brightnesses and physical effective radii of the Sérsic and exponential profiles used to model the galaxy components (Sect. 3.4), and the technical approaches used to perform the fits (Sects. 3.5 and 3.6). In Sect. 4, we then analyze our results for the EFIGI scaling relations of surface brightness versus effective radii (Sect. 4.1), and effective radii versus magnitude (Sect. 4.2), and compare them with the original relations of Kormendy (1977) and Binggeli et al. (1984), respectively. We also show how these three quantities lie on a plane in the 3D parameter space (Sect. 4.4). We bring to light a size-luminosity relation for bulges of lenticular and spiral galaxies (Sect. 4.3), as well as for their disks (Sect. 4.5), and for the latter, we compare in Sect. 4.6 their bi-variate luminosity-radius distribution to the modeled function derived by de Jong & Lacey (2000). We show in Sect. 4.7 how bulge and disk radii vary along the Hubble sequence, and explain how we derived unprecedented power-law dependencies with the bulge-to-total ratio. Based on this analysis, we make the connection between the phases of mass and morphological evolution of galaxies along the Hubble sequence and the size variation of their bulges and disks (Sect. 5.1). Moreover, we discuss the distinction between pseudo- and classical bulges (Sect. 5.2), as well as the variations in the volume density of spheroids and in the surface density of disks (Sect. 5.3). Lastly, we provide the parameters to all fits in Sect. 5.4, so that they can be used to generate realistic galaxy mock catalogs of the full diversity of morphological types in the observed Universe at $z \sim 0$. In this article, we use the standard ΛCDM cosmology with parameters $H_0 = 70\,\mathrm{km\,s^{-1}\,Mpc^{-1}}$ (Freedman et al. 2001), $\Omega_m = 0.258 \pm 0.030$, $\Omega_\Lambda = 0.742 \pm 0.030$ (Dunkley et al. 2009).

2. Data

We use the EFIGI morphological catalog (Baillard et al. 2011) of 4458 galaxies which were visually classified based on g, r, i Sloan Digital Sky Survey (SDSS) images, by their Hubble type, as well as 16 morphological attributes (Baillard et al. 2011; de Lapparent et al. 2011) , taking integer values between 0 and 4. Here, we only use the `Incl-Elong` attribute, measuring the apparent elongation of objects, and the `VisibleDust` attribute, measuring the strength of the diverse features indicating the presence of dust in galaxies. Our profile fits are based on images extracted from the SDSS in the five optical bands u, g, r, i and z.

EFIGI is a subsample of the Morphological Catalog (MorCat ; see Quilley & de Lapparent, *in prep.*), which is complete in

apparent magnitude to $g \leq 15.5$. EFIGI is not magnitude-limited because it was designed with the goal of having, when possible, several hundreds of galaxies of each Hubble type. Therefore, it is not a representative sample of the Universe. Because it mostly includes galaxies with apparent diameter ≥ 1 arcmin, it is well suited for profile-fitting, and allows an in-depth study of the role of morphology on other galaxy properties.

In the current analysis, we limit the sample to the 3106 EFIGI galaxies with the EFIGI attribute `Incl-Elong` ≤ 2: this corresponds to face-on or moderate inclination of galaxies when they have a disk, that is $\leq 70°$, and elongation ≤ 0.7 for diskless galaxies; this removes highly inclined disks, but keeps all E galaxies as their values of `Incl-Elong` are between 0 and 2 (Baillard et al. 2011).

3. Methodology

3.1. Luminosity profile fitting using SourceXtractor++

3.1.1. Generalities

We use the new SourceXtractor++ software (Bertin et al. 2020) to decompose the 2D projected galaxy light profiles with the sum of two components, aimed at modeling the bulge and disk in lenticular and spiral galaxies, using a Sérsic (Sérsic 1963) and exponential profile, respectively. This model-fitting is performed simultaneously in the g, r, and i bands (further details on the SourceXtractor++ fits of the EFIGI galaxies can be found in Quilley & de Lapparent 2022). This model-fitting is preceded by multiple steps to measure bulge properties and use them as priors, thus leading to more reliable bulge and disk decompositions (suffering less degeneracies, see Quilley & de Lapparent, *in prep.*). We also model some Hubble types (E, cE, cD, dE, Im) with a single Sérsic profile, for reasons described in Sect. 3.1.2.

Although the SourceXtractor++ profiles have elliptical symmetry (as galaxies are frequently seen as elongated), in the following, we provide for simplicity the functional forms in the case of circular symmetry[3]. The Sérsic profile fitted to the galaxy bulges (and full galaxies for some types) is:

$$I(r) = I_e \exp\left\{-b_n\left[\left(\frac{r}{r_e}\right)^{1/n} - 1\right]\right\} \quad (1)$$

where r is the angular radius to the profile center, and r_e the effective radius that encloses half of the total light of the profile, that is

$$\int_0^{r_e} I(r)\, 2\pi r \mathrm{d}r = \frac{1}{2}\int_0^{+\infty} I(r)\, 2\pi r \mathrm{d}r \quad (2)$$

for a profile with circular symmetry (in the case of an elliptical profile, it is the ellipse of semi-major axis r_e and semi-minor axis $\frac{b}{a}r_e$ that encloses half of the total light). In Eq. 1, $I_e = I(r_e)$ is the intensity at r_e, n is the Sérsic index that defines the steepness of the profile, with higher n corresponding to steeper profiles, and b_n is a normalization parameter depending on n only.

The exponential profile used for galaxy disks can be written, in the case of circular symmetry, as

$$I(r) = I_0 \exp\frac{-r}{\mathfrak{h}} \quad (3)$$

where $\mathfrak{h}$ is the angular scale-length. The exponential profile is a Sérsic profile with $n = 1$, which can be written, using Eq. 1, as

$$I(r) = I_e \exp\left[-b_1\left(\frac{r}{\mathfrak{h}_e} - 1\right)\right] \quad (4)$$

where $\mathfrak{h}_e$ is the angular effective radius of the profile used for modeling the disks, which allows one to make the correspondence and perform comparisons with r_e, used in the bulge (Sérsic) profile (see Eq. 1). From Eqs. 3 and 4, we infer that the effective radius $\mathfrak{h}_e$ and scale-length $\mathfrak{h}$ only differ by a multiplicative factor:

$$\mathfrak{h}_e = b_1\mathfrak{h} = 1.678\mathfrak{h} \quad (5)$$

which remains unchanged when converting to physical distances h and h_e (see Sect. 3.4).

The model-fitting with SourceXtractor++ provides us with a set of parameters for the bulge (Sérsic) and disk (exponential) components fitted to each galaxy which are: the total integrated apparent magnitude m, the corresponding bulge and disk integrated apparent magnitudes m_{bulge} and m_{disk} resp., the n index of the Sérsic profile, the bulge and disk semi-major effective radii r_e and $\mathfrak{h}_e$ resp., the position angle of the major axis, and the elongation of the profile b/a (where a is r_e or $\mathfrak{h}_e$, and b is the semi-minor axis of the physical or angular profile, respectively).

3.1.2. Bulge and disk decomposition versus single-profile modeling

In the current analysis, the bulge and disk decomposition is applied to all types including E, cE, cD, and dE. Indeed, even though E galaxies do not show evidence for a disk in optical images, kinematic studies have shown that stellar disk components are present in many of them (Krajnović et al. 2008, 2011; Emsellem et al. 2011), leading to improved profile fits with a 2-component model (Krajnović et al. 2013). Fitting a bulge and disk profile to elliptical galaxies also allows us to compare their parameters to those of lenticular and spiral types via a common modeling method. Nevertheless, Bernardi et al. (2014) showed that the choice between a single Sérsic profile and a bulge and disk decomposition conditions the resulting ranges and properties of the derived parameters. A single Sérsic profile is therefore fitted to E, cE, cD and dE galaxies in order to compare our results with the historical relations that were derived using a single Sérsic or de Vaucouleurs profile (see Sects. 4.1 and 4.2). In the following, we mention the "Sérsic component" and the "exponential component" when referring to corresponding components of the bulge and disk decomposition applied to E and cD types, to be differentiated from the "single Sérsic" profile.

In the bulge and disk decomposition, if the Sérsic component aims at adjusting a central concentration within the disk, it sometimes fails, and such objects need to be identified in order to minimize biases in the measured bulge radii. Indeed, because of the very faint bulges of the latest Sd and Sm spiral types (and even more so in the bulgeless Im types), the Sérsic bulge component might be inappropriately used to model either the whole galaxy in addition to the exponential profile intended for the disk, or any other kind of excess light, such as an HII region. To identify these erroneous fits, we compare the flux of their bulge component to the one from the zoom-in process mentioned in Sect. 3.1, estimated as the excess flux in the center of the galaxy isophotal print above an approximate 2D background calculated from the inner disk, and providing an estimated B/T_{zoom} when compared to the galaxy isophotal flux. We discard the fits for Sc and later morphological types for which the B/T value from the bulge

[3] See Graham & Driver (2005) for an exhaustive description of the circular Sérsic profile

and disk decomposition in any of the g, r or i bands verifies $B/T > f(B/T_{zoom})$, with the f threshold function empirically defined as a second degree polynomial: 32% Sc, 41% Scd, 59% Sd, 80% Sdm, and 83% Sm fits are removed.

We tested this bulge validating procedure on the extreme case of Im galaxies, that do not host a bulge. Among the 179 Im with `Inclination`≤ 2 in EFIGI, only 31 have a bulge modeling that verifies the previously described criterion, and among them, only 6 have a $B/T > 1\%$ (caused by an HII region or a contaminating star), confirming that these types do not host a bulge. We therefore only use the results of the single-Sérsic profile fits for Im galaxies. As their Sérsic index distribution peaks near 1, in the following, we examine the scaling relations for Im galaxies with those for the disks of the lenticulars and spirals.

3.2. Correcting extinction effects

We correct all magnitudes obtained from the luminosity profile-fitting for both atmospheric and galactic extinction. For the atmospheric correction, we use the kk coefficients multiplied by the air masses provided for the SDSS[4]. We base the galactic correction on the dust reddening galactic maps from Schlegel et al. (1998) from which we obtain $E(B-V)$ values for each galaxy with its sky coordinates, as well as on the conversions to extinction in the g, r, i bands listed in Table 6 of Schlafly & Finkbeiner (2011) using a Milky Way reddening law with an extinction to reddening ratio $A_V/E(B-V) = 3.1$.

3.3. SED fitting with ZPEG

We use the ZPEG software (Le Borgne & Rocca-Volmerange 2002) to fit Spectral Energy Distributions (SED) to the apparent magnitudes of the EFIGI galaxies, in order to derive their absolute (rest-frame) magnitudes and colors. This software receives as inputs the apparent magnitudes in the g, r, i for EFIGI galaxies measured by SourceXtractor++ (Sect. 3.1) and corrected for extinction (Sect. 3.2), as well as the HyperLeda redshifts corrected for Virgocentric infall (see Sect. 2.2 of de Lapparent et al. 2011). ZPEG adjusts to these apparent magnitudes the SEDs of families of templates from the PEGASE.2 library, that were determined from the major galaxy types (E, S0, Sa, Sab, Sb, Sbc, Sc, Sd, Im, starburt), and are characterized by specific functions for the evolution of the star formation rate with time (Fioc & Rocca-Volmerange 1999). We also obtain from this SED model-fitting the age of the scenario corresponding to the best-fit template, as well as several galaxy parameters including most notably the stellar mass M_* and the star formation rate (SFR). This analysis is then repeated separately for the magnitudes of both bulges and disks, in order to also obtain the absolute magnitudes (hence colors), as well as the stellar masses of these components. Further details, robustness checks and results regarding these fits are given in Quilley & de Lapparent (2022).

3.4. Computing the mean effective surface brightness

The (major axis) effective radii r_e or $\mathfrak{h}_e$ provided by the model-fitting with SourceXtractor++ for the bulge and disk components resp., are angular distances. To deduct from them the physical effective radii R_e and h_e resp., we multiply by the angular diameter distance D_{ang} derived from the HyperLeda redshifts (see Sect. 3.3). This yields

$$R_e = \frac{\pi}{180}\, r_e\, D_{ang} \tag{6}$$

where the distances R_e and D_{ang} are in parsec, and r_e in degree. The equation relating h_e and $\mathfrak{h}_e$ is identical to Eq. 6. In the rest of this section, we only refer to the bulge parameters r_e and R_e for simplicity (but equations also apply for the disk component with parameters $\mathfrak{h}_e$ and h_e).

The mean effective surface brightness $\langle\mu\rangle_e$ is defined as the mean surface brightness in the central region of an object above the isophote containing half of the object total flux. For a circular object, it is the mean surface brigthness in a disk of radius r_e: $\langle\mu\rangle_e = \langle\mu(r \leq r_e)\rangle$. The mean surface brightness of a galaxy in a photometric band and within a projected area $\mathcal{A}$ on the sky measured in square arcseconds, is derived from its apparent magnitude $m(r \in \mathcal{A})$ in this area using

$$\langle\mu(r \in \mathcal{A})\rangle = m(r \in \mathcal{A}) + 2.5\log(\mathcal{A}). \tag{7}$$

In the case of the bulge and disk elliptical profiles defined here, the mean effective surface brightness $\langle\mu\rangle_e$ is computed over the area of the ellipse with major axis the angular effective radius r_e and of elongation b/a. It corresponds to half the total flux, hence to a magnitude $m + 2.5\log(2)$ if m is an estimate of the total apparent magnitude, so for $\mathcal{A}$ the area of the effective ellipse, one can write $\langle\mu\rangle_e$ as

$$\langle\mu\rangle_e = m + 2.5\log\left(2\pi r_e^2 \frac{b}{a}\right), \tag{8}$$

which is the equation we use to compute the mean effective surface brightness from the SourceXtractor++ parameters m, r_e and b/a.

As far as disks are concerned, one often considers the central surface brightness $\mu_0 = -2.5\log I_0$, with I_0 the central intensity of the exponential disk profile defined in Eq. 3. Graham & Driver (2005) indicate in their Eqs. 7 and 9 that the difference between μ_0 and μ_e and between μ_e and $\langle\mu\rangle_e$ respectively, are only dependent on n. In particular, for the $n = 1$ Sérsic index of an exponential profile, one can write

$$\mu_0 = \langle\mu\rangle_e - 1.123. \tag{9}$$

These considerations show that the choices between h_e or h (see Eqs. 3 and 4) and between $\langle\mu\rangle_e$ and μ_0 (see Eq. 9) do not affect the measured correlations between disk radii in logarithmic scale and surface brigthness as it merely shifts all data points by a constant value. Here, we then use Eq. 9 to derive the central surface brightness μ_0 of the disks of EFIGI galaxies from the mean effective surface brightness $\langle\mu\rangle_e$, in turn computed using Eq. 8, and which takes into account the moderate inclinations of disks in the considered EFIGI subsample (see Sect. 2).

To rewrite the mean effective surface brightness in terms of the physical effective radius R_e and the absolute magnitude M, hence to estimate how these 3 quantities characterizing galaxy fluxes and profiles scale with each other, we use

$$M = m - 5\log D_{\rm lum}(z) + 5 - K_{\rm cor}(z), \tag{10}$$

where m and M are in the same band, $D_{\rm lum}(z)$ is the luminosity distance at redshift z, and $K_{\rm cor}$ the k-correction in the considered band at that redshift. Using $D_{\rm lum}(z) = (1+z)^2 D_A(z)$ and Eqs. 6

[4] https://classic.sdss.org/dr5/algorithms/fluxcal.html

and 10, we then rewrite the mean effective surface brightness in Eq. 8 as

$$\langle\mu\rangle_e = M + 5\log R_e + 2.5\log(1+z)^4 + K_{\rm cor}(z) - 5 + 5\log\frac{648000}{\pi} + 2.5\log\left(2\pi\frac{b}{a}\right) \quad (11)$$

with $\langle\mu\rangle_e$ in mag arcsec^{-2}, and R_e in parsec. The term $2.5\log(1+z)^4$ corresponds to the surface brightness dimming with redshift.

Because most galaxies in the EFIGI sample have $z \lesssim 0.05$, the surface brightness dimming term is $\lesssim 0.2$, and the k-correction term is $\lesssim 0.2$ in the g band and 0.1 in r and i bands. As we have limited our sample to low values of the `Incl-Elong` attribute (see Sect. 2), the elongation term $2.5\log\frac{b}{a}$ is $\lesssim 0.4$. Added in quadrature, all three terms would add a total dispersion of $\lesssim 0.5$, which is negligible compared to the $\sim$ 9-magnitude interval for bulges and disks magnitudes, and the $\sim$ 15 and $\sim$ 7 dex intervals for $5\log R_e$ and $5\log h_e$ respectively (see Figs. 7 and 11). These considerations therefore justify the following approximate scaling relation between absolute magnitude M, R_e and $\langle\mu\rangle_e$ for nearby galaxies:

$$\langle\mu\rangle_e \simeq M + 5\log R_e + \kappa, \quad (12)$$

where κ is a constant only for galaxies of equal redshift, k-correction and elongation. Otherwise, when considering the whole EFIGI sample, and more generally a sample of galaxies of different Hubble types, distances and elongations, κ undergoes a limited dispersion of 0.5 at maximum (as indicated above).

3.5. Uncertainties in effective radii

EFIGI is an incomplete sample (it is not volume limited). First, it is not limited in apparent magnitude as is usually the case for observed galaxy samples. It displays a fast decreasing incompleteness below an isophotal diameter of $D_{25} = 1$ arcminute, but it is not either complete above this value (de Lapparent et al. 2011). Moreover, the cone-shape of the sampled volume (resulting from the sky projected area selection) combined with the shape of the luminosity function of galaxies in which brighter galaxies are much rarer result in a cone-like volume, with small and faint galaxies detected in large numbers in the nearby tip of the cone, and large and bright galaxies detected predominantly at larger distances. Moreover, the depth of the EFIGI survey does not encompass a large number of walls and voids of the cosmic web, hence its redshift distribution is affected by these large-scale inhomogeneities (Baillard et al. 2011). In particular, the survey has a nearby over-density at $z \sim 0.005$ due to the Virgo cluster, in which reside most of the Im, cE and dE morphological types which add up to the previously mentioned over-selection of small and faint galaxies in the nearest part of the survey.

Combination of all the above mentioned selection effects yields the strong correlation of the physical effective radii of EFIGI galaxies with their distance from us. This can be seen in the left panel of Fig. 1, showing the physical effective radii h_e of disk galaxies (lenticular and spiral types, shown as dots), and the physical effective radii R_e of E, cD, cE, dE and Im adjusted by a single Sérsic profile (shown as crosses), which can all be considered as estimates of the various galaxy sizes (in the g band), as a function of the angular diameter distance D_{ang} of each object. One can see that the effective physical radii of the various plotted types of galaxies systematically increase when they are more distant (the color-map in absolute magnitude M_g shows that more distant galaxies are also brighter). Ideally, one should have a sample in which galaxies of all physical sizes are equally sampled at all distances so that there is no such bias.

As a result, if one considers first EFIGI disk (lenticulars, spirals) galaxies, as well as Im galaxies, galaxies with large physical effective disk radii h_e have smaller angular sizes, estimated by their angular disk effective radii $\mathfrak{h}_e$, as shown in the right panel of Fig. 1. Therefore, the physically larger EFIGI disk galaxies are spread over a systematically smaller number of fixed size pixels of the SDSS imaging survey (0.385 arcsec) than smaller objects, causing a systematically larger relative uncertainty $\sigma(\mathfrak{h}_e)/\mathfrak{h}_e$ estimated by SourceXtractor++ for large h_e. This relative error is equal to the relative uncertainty in the physical disk effective radius $\sigma(h_e)/h_e$ (see Eq. 6), therefore the latter is larger for larger h_e. This is indeed what we obtain for EFIGI disk and Im galaxies, as seen on Fig. 2: despite a large dispersion, there is a systematic increase in $\sigma(h_e)/h_e$ with h_e (by $\sim$ 1 dex over the $\sim$ 1 dex interval of measured h_e), with slopes in the interval $[-0.2; 0.2]$ (in log-log) across 12 absolute g band magnitude intervals of width ΔM_g in the $0.2 - 0.5$ range - except for extremal bins, adapted to contain a weakly varying number of galaxies (between 194 and 272).

Because we use the total least square estimation in all fits that are performed in the present article (see Sect. 3.6), which takes into account the errors on both axes, any systematic trend in the errors as a function of any axis would bias the corresponding fit. Therefore the biased distribution of relative errors on h_e illustrated in Fig. 2 would tend to give systematically more weight to intrinsically smaller galaxies, hence biasing the size-magnitude relations toward small radii. We therefore choose to eliminate this overall systematic increase in $\sigma(h_e)/h_e$ with h_e by a linear regression, while keeping unchanged the dispersion around the linear fits. As seen in Fig. 2, the slopes are positive, and should be flattened. Nevertheless, using the factor that flattens the slope of the fit to galaxies of all M_g together (shown in blue in Fig. 2, labeled as "Global corr.") is insufficient to correct for the bias. We therefore iteratively find the common factor to apply to the slopes of the fits per M_g interval in order to minimize the sum of the squares of the slopes over the 12 defined M_g intervals. This sum of squares behaves as a parabola without noise, and the minimum yields a factor 3.18 that is applied to $\sigma(h_e)/h_e$ to correct for its systematic and biased increase with h_e. These corrected slopes are shown in green in Fig. 2 (labeled as "Mag. corr.").

When considering the effective angular and physical radii, r_e and R_e respectively, of the single-Sérsic profile fits to E, cD, cE and dE galaxies, the gradients in R_e and r_e with D_{ang} in both panels of Fig. 1 are less visible than for disk and Im galaxies, as these spheroid types populate different and narrow ranges of R_e (see left panel of Fig. 7): E and cD are among the largest galaxies with 80% of objects having their R_e in the interval $4 - 42$ kpc, whereas cE and dE are among the smallest with 80% of both types of objects having their R_e in the interval $0.9 - 5$ kpc. There is however also an overall systematic increase in $\sigma(R_e)/R_e$ with R_e as in Fig. 2 (although smaller, $\sim$ 0.5 dex for $\sim$ 1 dex in R_e), that we correct in the same iterative approach as for disks and Im galaxies, using the three [-23.7;-22.0], [-22.0;-21.0] and [-21.0;-13.3] M_g magnitude intervals containing 102, 115, and 112 galaxies respectively.

We emphasize that these corrections leave intact the fact that 2 galaxies with identical values of h_e (or R_e) may have their $\sigma(h_e)/h_e$ (or $\sigma(R_e)/R_e$) differ by a factor as large as 10. We also checked that this flattening correction preserves the decreasing trends of $\sigma(\mathfrak{h}_e)/\mathfrak{h}_e = \sigma(h_e)/h_e$ versus the angular effective radius $\mathfrak{h}_e$, and $\sigma(r_e)/r_e = \sigma(R_e)/R_e$ versus r_e.

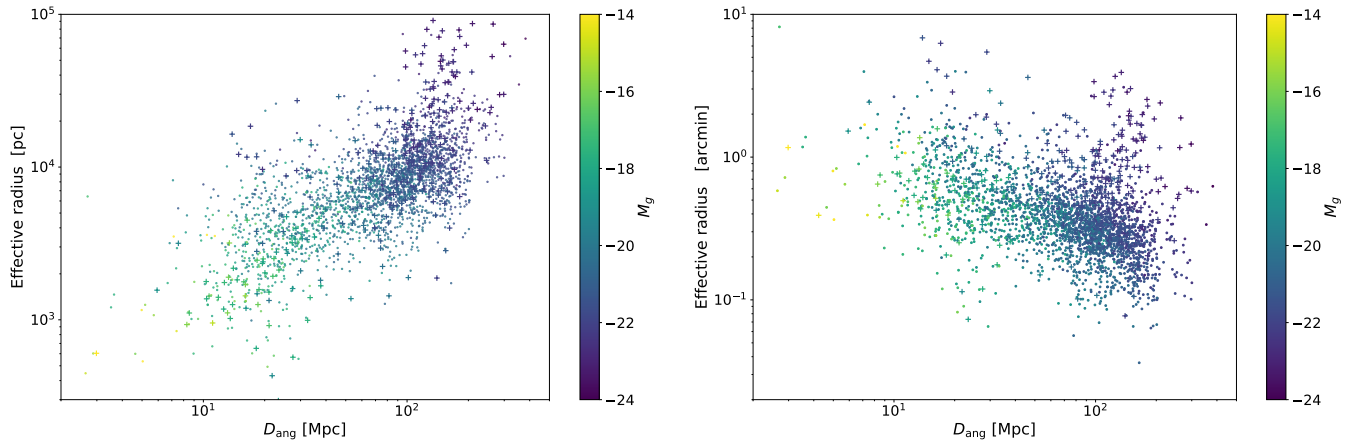

Fig. 1: Distribution of the effective radii of E, cD, dE, cE and Im galaxies modeled as a single Sérsic profile (crosses), and the disk effective radii for spiral and lenticular EFIGI galaxies (dots), as a function of the angular diameter distance D_{ang}. Depending on the Hubble type, either radius can be considered as an estimate of the galaxy size. Left panel shows the physical radii, while the right panel shows the angular radii. The points are also color-coded with the absolute magnitude in the g band. This graph shows that selection effects affecting the EFIGI sample leads to larger/brighter galaxies of a given type being preferentially located at large distances, and having preferentially small angular radii.

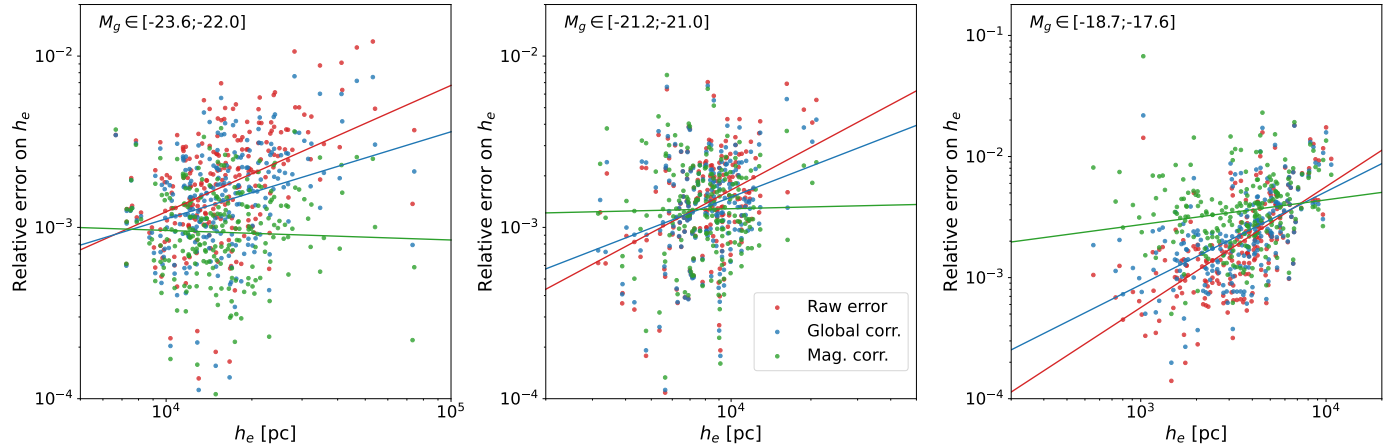

Fig. 2: Distribution of the relative error on the physical disk effective radii $\sigma(h_e)/h_e$ as a function of h_e in bins of total galaxy absolute magnitude in the g band. Only 3 bins are shown as examples of the general behavior. The color of the points represent the type of plotted error (see text for details) and the lines are the corresponding linear regression. There is a trend of relative errors increasing with h_e for the raw errors (in red). The correction derived globally over all absolute magnitudes (in blue) reduces the bias, whereas the correction by minimization over 12 magnitude intervals (in green), actually erases it.

We also performed tests on synthetic images of galaxies generated with Stuff and SkyMaker (Bertin 2009) in order to check the uncertainties provided by SourceXtractor++. We measured that the relative errors on bulge and disk effective radii are underestimated by a varying factor increasing from 1 to $\sim$ 10 at the smallest relative uncertainties. We initially tried to correct for this effect, but the correction is insufficient to eliminate the biases in $\sigma(h_e)/h_e$ versus h_e and $\sigma(R_e)/R_e$ versus R_e, which the minimization procedure per magnitude interval described here succeeds in doing.

At last, we measure a similar $\sim$ 1 dex dispersion in $\sigma(R_e)/R_e$ versus R_e for the effective radii of the bulges of lenticular and spiral galaxies as in Fig. 2, but we do not detect any systematic trend with R_e. We suspect this is due to the fact that the bulges are internal smaller regions of lenticular and disk galaxies, and are less affected by the biases in the total galaxy size distribution with distance. Therefore we do not apply any correction to $\sigma(R_e)/R_e$ versus R_e for the bulges in the bulge and disk decomposition of lenticular and spiral galaxies.

3.6. Orthogonal distance regression

In this article, we derive multiple relations between the parameters of the bulge and disk components for the galaxies in the EFIGI catalog. Because all parameters estimated by the SourceXtractor++ modeling undergo uncertainties, we use the ODRPACK Version 2.01 Software for Weighted Orthogonal Distance Regression (ODR hereafter, Boggs et al. 1992) of the *scipy Python* library (Virtanen et al. 2020), which allows one to fit any functional form. Although this is not stated, we suppose that this method corresponds to the total least squares estimation, which is the generalization of the Deming regression[5] for

[5] https://en.wikipedia.org/wiki/Deming_regression

the linear case, which is itself a generalization of the orthogonal distance regression for identical variance along both axes. The advantage of these various estimates is that they take into account the errors on both axes when performing the fit (including the covariances, which we neglect here), contrarily to the linear regression approach, which considers the x-axis values as the truth. The minimization of the ODR package is done on the distances between the data points and the fit along both axis, which simplifies to the distance orthogonal to the fit when both axis have the same weight, and not only along the y-axis as this is done in a linear regression. For this reason, the ODR package leads to different functions than the regression along the y-axis when fitting a linear model, but we checked that these differences do not alter the qualitative conclusions of the current analysis.

Moreover, we have discarded points with anomalously low errors compared to the rest of the distribution (at least one order of magnitude below the median value) when performing the ODR fits. This is mandatory to avoid that the resulting model does not only go through these data points while ignoring the rest of the sample. The minimum error threshold value was found empirically for all parameters involved in such fits, and such filtering only reduces the sample size by a few percents. Finally, the adjustment made on the errors on h_e described in the previous section (Sect. 3.5) is pivotal to obtain a realistic fit of the size-luminosity relation for disks (see Sect. 4.5 hereafter) but would still be needed if we had opted for a linear regression, as the systematic trends in the errors occur along the y-axis.

4. Results

4.1. Revisiting the Kormendy relation for E and bulges

Kormendy (1977) was the first to show that elliptical galaxies showed a correlation between $\langle\mu\rangle_e$ and R_e, measured in a 4600-5400 Å band denoted "G", that corresponds to the red wavelength part of the SDSS g band. One-dimensional surface brigthness profiles were obtained by processing photographic plate images of the galaxies with a microdensitometer, and "to minimize effects of the three-dimensionality of spheroids, the profile at 45° to the major axis was used" (Kormendy 1977). In contrast, the EFIGI effective radii derived by SourceXtractor++ are provided along the major axis. However, we calculated the effective radius at 45° for our models on all EFIGI E galaxies and the ratio between the former and the latter has a median value of 0.89 and is below 0.8 (but higher than 0.67) for only 11.5% of objects. More importantly, this limited difference between the two sets of values leads to a 10^{-3} difference in the slope of the $\langle\mu\rangle_e$ versus R_e relation, so we directly compare below the Kormendy relation with our results based on the semi-major axes of the fitted profiles. We also investigated the effect of elongation for elliptical galaxies, and detected no effect on the $\langle\mu\rangle_e$ versus R_e distribution for the three subsamples with `Incl-Elong` attribute equal to 0, 1 and 2.

The upper left panel of Fig. 3 shows the relation between $\langle\mu\rangle_e$ obtained using Eq. 8, and R_e obtained using Eq. 6, with m and r_e provided by the single-Sérsic profile fits with SourceXtractor++ to all 226 EFIGI elliptical galaxies (in purple). The points are color-coded as a function of B/T_g, the bulge-to-total flux ratio in the g band. An ODR linear fit (see Sect. 3.6) of $\langle\mu\rangle_e$ as a function of R_e (in blue) yields

$$\langle\mu\rangle_e = 2.87^{\pm0.14} \log R_e + 19.00^{\pm0.53} \quad (13)$$

with R_e in kiloparsecs. The derived slope is compatible with the 3.02 value measured by Kormendy (1977), also plotted in green, but with a 0.74 magnitude per arcsec^2 brighter $\langle\mu\rangle_e$ for EFIGI E galaxies in g, which could be due to the different (G) photometric band used in the original measurement. No uncertainty on the slope is provided by the author for the original relation, but by performing a linear regression on the tabulated values in his article, we derived a 0.28 uncertainty in the slope, so the difference between the slope in Eq. 13 and that measured by Kormendy (1977) is at the 0.5σ level. We also obtain a nearly identical result to Eq. 13 if we use a linear regression, with a slope of 2.86 ± 0.15 and an intercept of 19.08 ± 0.58 for EFIGI ellipticals.

In the upper left panel, the relation obtained for the Sérsic components of elliptical galaxies is different from that obtained from the single-Sérsic fits, with R_e smaller by ~ 0.7 dex and $\langle\mu\rangle_e$ brighter by ~ 3 magnitudes, which highlights the strong impact of the modeling method. Indeed, the ODR linear fit for E Sérsic components (in black in the graph) yields:

$$\langle\mu\rangle_e = 2.37^{\pm0.11} \log R_e + 18.49^{\pm0.35} \quad (14)$$

with R_e in kpc. There is a 2.8σ difference with the slope of the relation fitted to the E single Sérsic profiles given in Eq. 13, and a 0.8σ difference between the intercepts (these differences are not of concern as different modeling methods have been used). In the other panels of Fig. 3 showing the bulge components of the fits from cD to Sm types, the linear fit to the E Sérsic components from the upper left panel (Eq. 14) is also indicated as a reference, and the dashed lines above and below correspond to the value of the intercept offset by $\pm3\sigma$, where σ is the r.m.s. dispersion in $\langle\mu\rangle_e$ around the fit.

The upper central panel of Fig. 3 shows that the Sérsic components of cD galaxies follow the Kormendy relation for the Sérsic components (in black), but only populate the larger values of effective radius for E elliptical galaxies. A similar effect is seen for the single Sérsic profiles of cD versus E galaxies (purple circles). In contrast, the single-Sérsic fits to the dE types shown in the same panel (purple crosses), are shifted to smaller R_e than the single-Sérsic fits to both cD and E types. Nevertheless, dE and E types exhibit a similar interval of μ_e between 20 and 25 g magnitude, despite the intuitive expectation that the effective surface brightness of the centrally very dense elliptical galaxies should be significantly brighter than that of dE galaxies, as they are fitted by Sérsic profiles with indices in the intervals $n = 3.5-7$ and $n = 1-3$ respectively (see Sect. 4.2). This is due to the fact that the Sérsic profile has a significant flux out to very large distances (in particular when $n > 3$), and the effective radii of both E and dE type are therefore much larger than the central parts of the galaxies, which have markedly different appearances for these types and are used in particular to determine the visual morphological type. However, the flux accounted for in the calculation of the effective surface brightness, makes μ_e an average quantity dominated by the low level wings of the profiles.

Fig. 3 also shows separately and for each EFIGI morphological type $\langle\mu\rangle_e$ versus R_e derived from a bulge and disk modeling, also color-coded with B/T_g, and compared to the fit to the Sérsic component of E types shown in the upper left panel (Eq. 15), as a reference. For all lenticular and spiral types, EFIGI galaxies display a systematically decreasing interval of R_e. Also, for a given surface brightness, bulges of later Hubble types have, on average, smaller R_e than earlier types, or equivalently that they are fainter at a given R_e. For instance, the bulges of Sbc are ~ 6 times smaller or 2.4 mag arcsec^{-2} fainter than what is predicted by the fit for E galaxies, from their surface brightness or effective radius respectively. Size variations are further explored in Sect. 4.7 and Fig. 15. Moreover, for a given Hubble type, the variations in R_e and $\langle\mu\rangle_e$ are linked to the value of the B/T ratio.

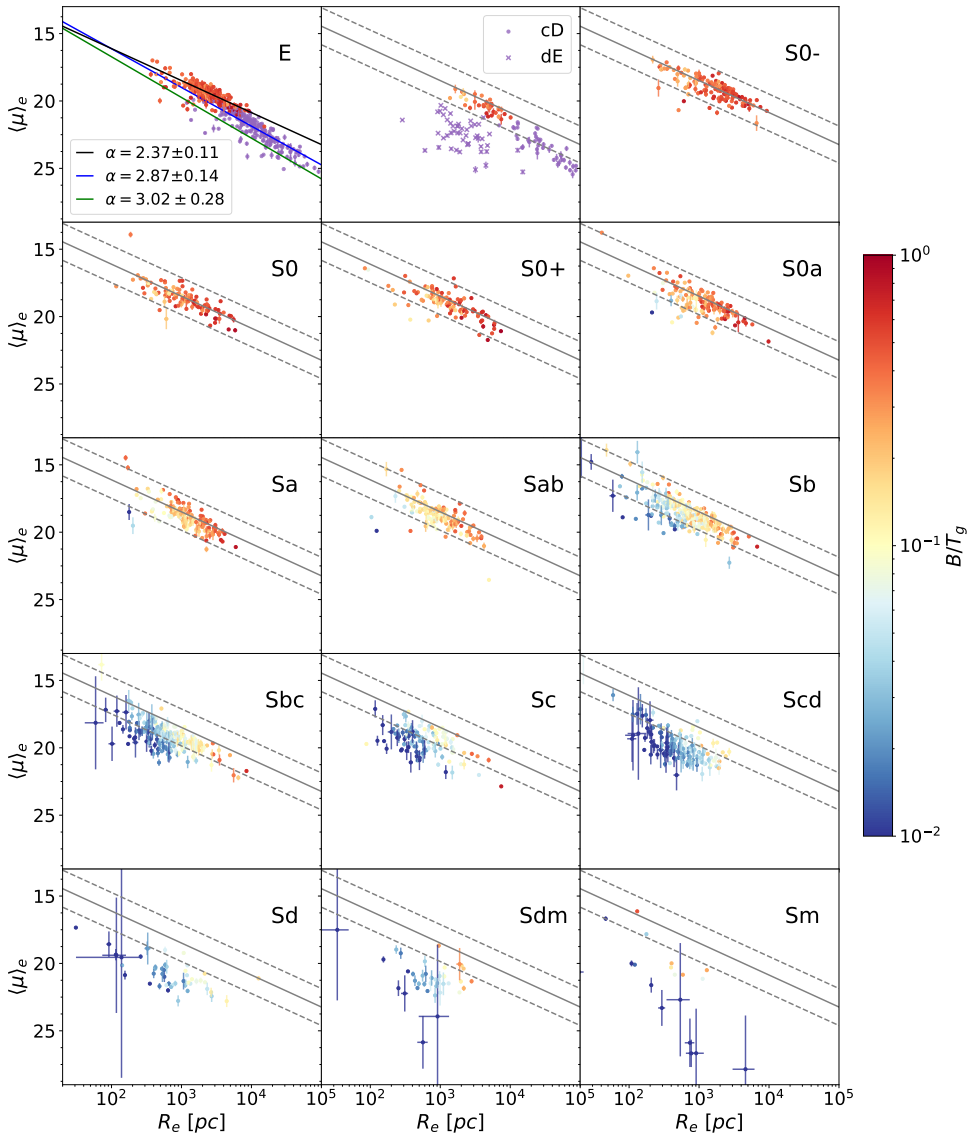

Fig. 3: Mean effective surface brightness $\langle\mu\rangle_e$ versus effective radius R_e for the Sérsic components of EFIGI E and cD galaxies, and for the bulges of lenticular and spiral types with `Inclination` ≤ 2, all derived from the Sérsic bulge and exponential disk decompositions, in the g band. The purple points in the 2 upper left panels represent the same relation for the E, cD and dE galaxies modeled as a single Sérsic profile. In the upper-left panel are shown the linear fits of $\langle\mu\rangle_e$ as a function of R_e for the Sérsic components and single-Sérsic fits to elliptical galaxies in black and blue respectively, as well as the Kormendy (1977) relation, in green. The fit to the E Sérsic component (in black) is repeated in solid gray in the other panels, with the dashed lines showing the same line offset by ±3 times the r.m.s. dispersion in $\langle\mu\rangle_e$ around the fit for the E types. The color of the points represent the bulge-to-total luminosity ratio in the g band B/T_g. Almost all bulges of types S0$^-$ to Sb are within 3σ of the linear fit to the E Sérsic components. Later types progressively shift to smaller effective radii and lower values of B/T_g, as well as dimmer effective surface brigthnesses than what would be expected from the Kormendy relation at these radii.

Fig. 3 also shows that the Kormendy relation remains valid for the bulges of lenticulars and early-type spirals up to Sab type. However, for Sb and later types, the relation between $\langle\mu\rangle_e$ and R_e departs from the Kormendy relation, as B/T_g decreases: these bulges have lower values of mean effective surface brightness $\langle\mu\rangle_e$ than what would be predicted from their effective radius R_e using the Kormendy relation. To evaluate this difference in surface brightness, we compute linear fits for each type and note that the main change is that the intercept of the fit shifts toward fainter magnitudes, but the slope of the relation remains rather stable. For instance, Scd galaxies are fitted by a slope which differs by less than 1σ from that for E galaxies, but the intercept is 2 magnitudes below that for the fit to E galaxies. There is also a systematic decrease of R_e for later types, by 1 to 2 orders of magnitude between E and Scd types.

In Quilley & de Lapparent (2022), we showed that bulges of EFIGI late-type spirals not only have smaller B/T values but also smaller Sérsic indices than bulges of early-type spirals and lenticulars. In Fig. 4, we therefore plot $\langle\mu\rangle_e$ versus R_e for the Sérsic component of E types, and the bulges of lenticular and spiral galaxies, color-coded by B/T_g (left panel), and by the bulge Sérsic index (right panel). The three black lines are again

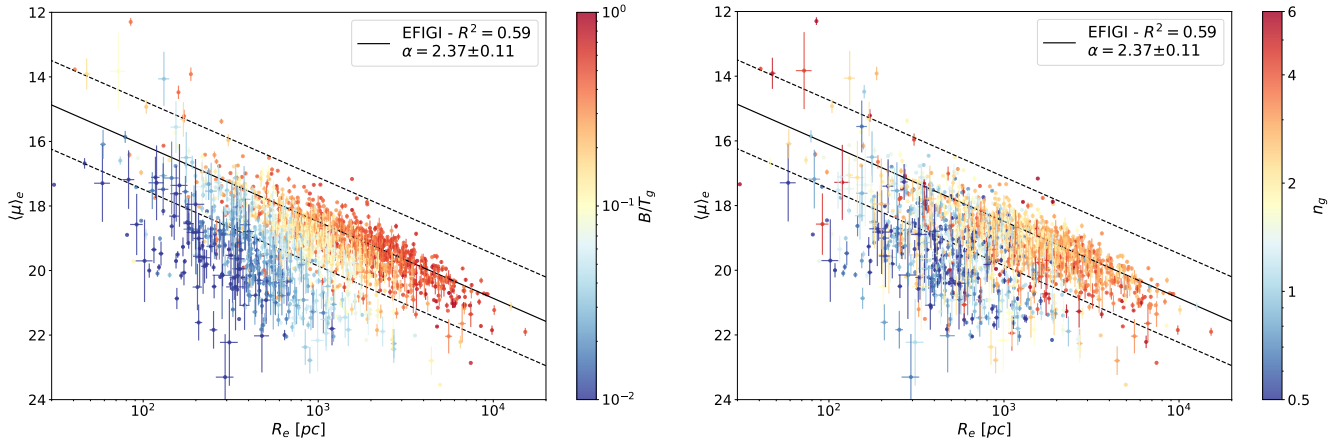

Fig. 4: Mean effective surface brightness $\langle\mu\rangle_e$ versus effective radius R_e for the Sérsic components of E types and the bulges of all Hubble types from S0$^-$ to Sm with `Inclination` ≤ 2, all in the g band (dE types are excluded from this graph). The panels are color-coded by the bulge-to-total ratio B/T_g (left) and the Sérsic index n_g (right) respectively. The black solid line in both panels is the linear fit for EFIGI E Sérsic components, while the dashed lines have the same slope and are offset by ±3 times the r.m.s. dispersion in $\langle\mu\rangle_e$ around that fit. The departure from the Kormendy relation occurs as both B/T_g and n_g decrease to the lowest possible values, while the highest ones are found for the highest radii along the Kormendy relation.

the linear fit (solid line) of $\langle\mu\rangle_e$ as a function of R_e for E galaxies (see upper left panel of Fig. 3 and Eq. 14), and ±3 times the r.m.s. dispersion in $\langle\mu\rangle_e$ around that fit (dashed lines).

One can see that the departure at $R_e \lesssim 2$ kpc from the Kormendy relation followed by Sérsic components of E types occurs for bulges with smaller radii and fainter effective surface brightness, as well as with decreasing values of both B/T_g and the Sérsic index, but with more dispersion in the latter which is affected by larger relative uncertainties, likely due to the stronger degeneracies in this parameter when performing the luminosity profile fitting. This effect corresponds to the progressive shift below the Kormendy relation for later Hubble types, seen in Fig. 4. We also note that the left panel of Fig. 4 is in agreement with Fig. 8 of Kim et al. (2016), who also showed a larger deviation from the Kormendy relation for bulges with lower B/T, also using disk and bulge decomposition on SDSS data.

We agree with the proposition of Gadotti (2009) that galaxies whose bulge deviate from the Kormendy relation are likely to be such bulges, and Fig. 4 also shows that they have smaller B/T_g and Sérsic indexes. In contrast, classical bulges are probably those that fall along the Kormendy relation: these bulges have $B/T_g \gtrsim 0.1$ and $n \gtrsim 2$. This is also consistent with the Sérsic index limit of 2 inferred by Fisher & Drory (2008). We further discuss these interdependent trends in terms of bulge structure along the Hubble sequence, as well as the lack of kinematics to identify pseudo-bulges (as rotationally supported components), in Sect. 5.2.

Another feature regarding the departure from the Kormendy relation is suggested by Allen et al. (2006) based on the Millenium Galaxy Catalogue: from their bulge and disk decompositions, the authors claim that bluer bulges tend to be below the relation compared to redder ones. However their Fig. 18 depicting this effect shows a very small deviation between the two clouds of points corresponding to bluer and redder bulges in $u-r$ color, whose overlap is moreover not quantified. An agreement with Allen et al. (2006) would require that EFIGI bulges of later types be bluer. We do measure systematic variations of the $g-r$ bulge color along the Hubble sequence, but there is no clear color shift of bulges across the surface brightness versus effective radius plane. Fig. 5 shows that intermediate spirals host

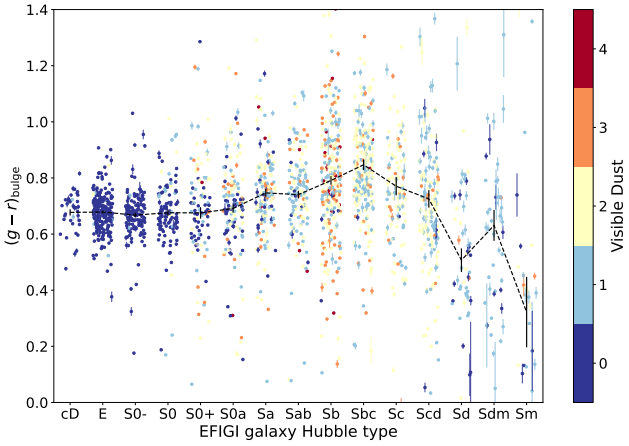

Fig. 5: Distribution of the $g-r$ absolute color of the EFIGI bulges (or Sérsic component) for each Hubble type (with `Inclination` ≤ 2). The black dashed line represents the mean color by type and its associated error. Bulge color is overall stable with most bulges in the 0.5-0.9 range. There is a 0.17 mag reddening between lenticulars and intermediate spirals (Sbc), which could be due to dust reddening, as it is more frequently present in large amounts in these galaxies. This effect decreases for Scd types, with some bluing possibly being present for the bulges of Sd and later types, compared to the lenticular and early spirals.

redder bulges than lenticulars in $g-r$, then the trend inverts itself. Indeed, there is a reddening of bulges between the lenticular types with a mean $g-r$ color of 0.67 – 0.69 up to Sbc types with a 0.85 mean (8σ difference between the S0 and Sbc types). This reddening could result from the presence of larger amounts of dust in intermediate spirals, as shown by the color-coding of the points with the value of the `VisibleDust` attribute. The offset between the largest amounts of `VisibleDust` in Sb types and the peak of the mean reddening trend in $g-r$ bulge color for Sbc types could result from the fact that this attribute estimates the presence of dust in the whole galaxy which is often dominated by disk dust, and does not necessarily represent well the dust im-

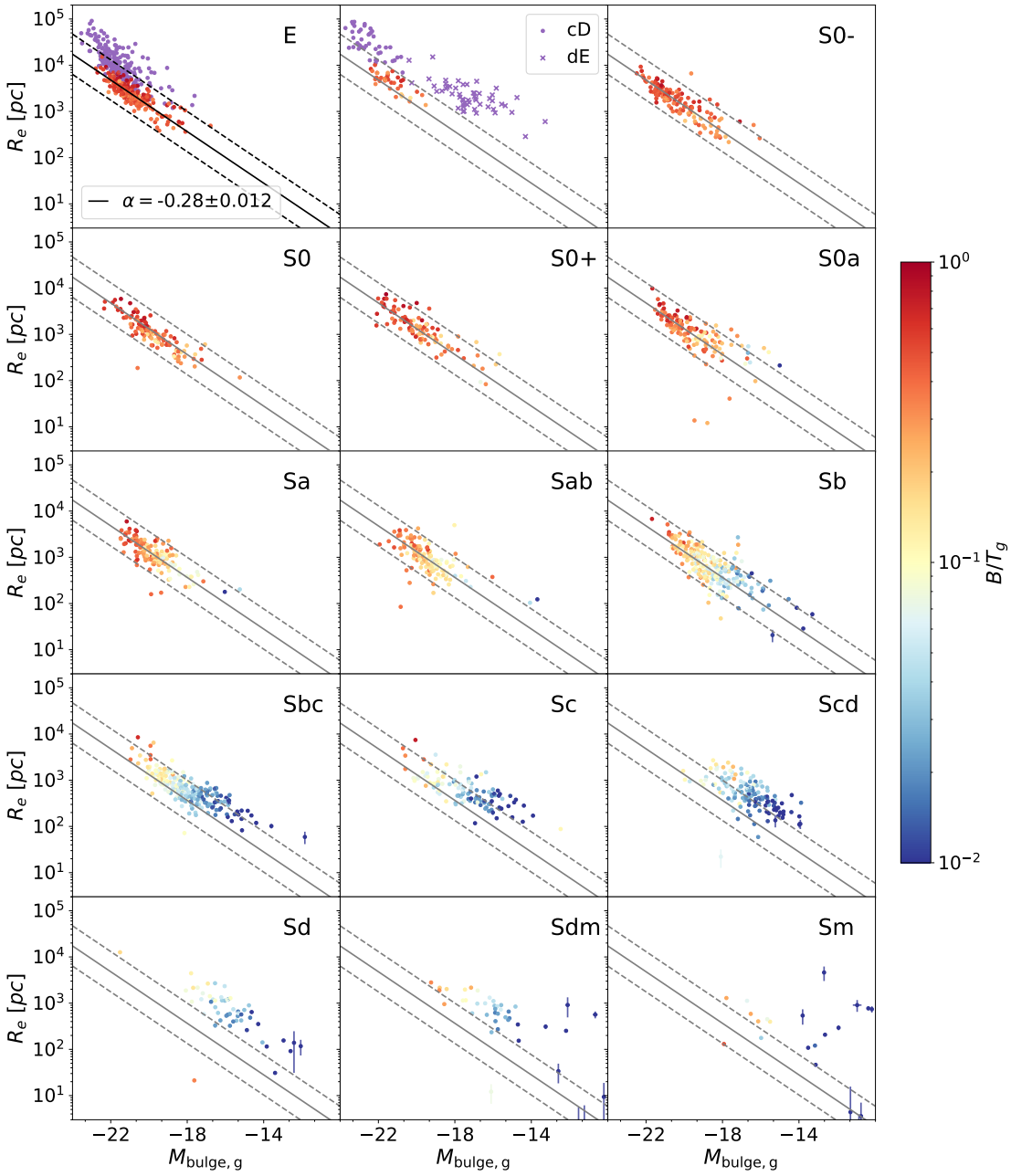

Fig. 6: Size-luminosity relation for the Sérsic components of EFIGI E and cD galaxies, and for the bulges of lenticular and spiral types with `Inclination` ≤ 2, all in the g band. The purple points in the 2 upper left panels represent the same relation for the E, cD and dE galaxies modeled as a single Sérsic profile. The solid line in the upper-left panel shows the linear fit of $\log(R_e)$ as a function of M_g for all EFIGI E Sérsic components, and the dashed lines are offset by ±3 times the r.m.s. dispersion in $\log(R_e)$ around the fit. These solid and dashed lines are repeated in gray in all other panels. The color of the points represents the bulge-to-total luminosity ratio in the g band, B/T_g. Both effective radii and luminosities of bulges get smaller while spanning the Hubble sequence.

pacting the bulge light. For later Hubble types, $g-r$ decreases down to 0.73 for Scd types (with a 3.3σ difference between the Sbc and Scd types), similar to the 0.74 mean color for both Sa and Sab types. The bulges embedded in later types of spirals (Sd to Sm) exhibit even bluer colors, but the low statistics and the larger individual uncertainties, due to the difficulty to measure their faint bulges, do not allow for conclusive results. We note that this bulge reddening in $g-r$ is also detected in $g-i$. However, $NUV-r$ would be a better choice than optical colors to differentiate stellar populations (Quilley & de Lapparent 2022), but bulge and disk decomposition in the near ultraviolet has not yet been performed.

4.2. Revisiting the size-luminosity relation for pure spheroids

In complement to the Kormendy relation between $\langle\mu\rangle_e$ and R_e, Binggeli et al. (1984) brought to light a correlation between R_e and M for a sample of nearby E and dE galaxies (which is further described below), and is called the "size-luminosity" relation. The upper left panel of Fig. 6 shows the relation be-

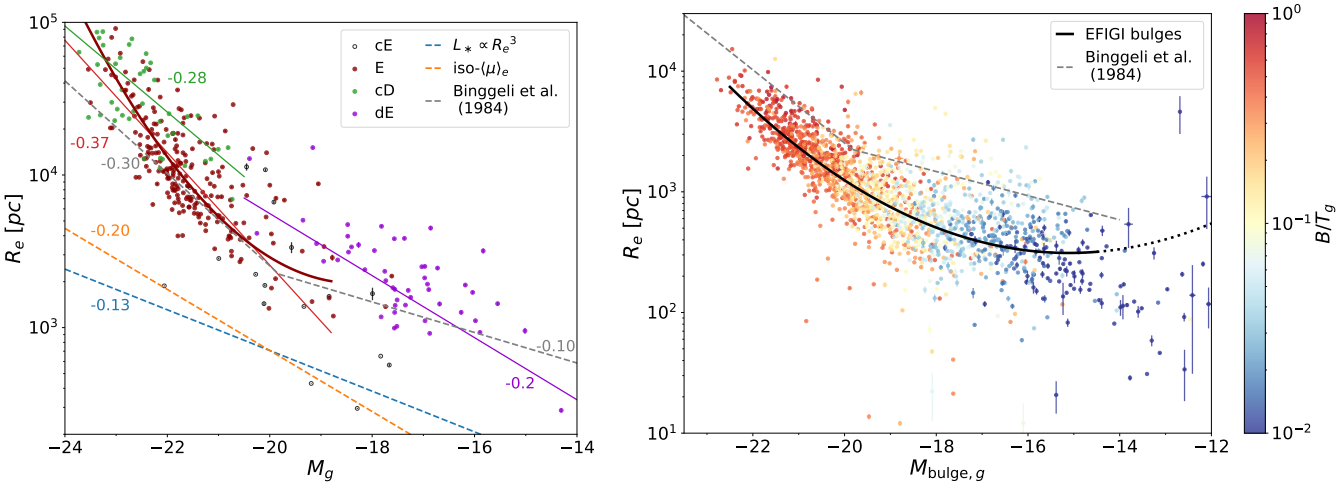

Fig. 7: Size-luminosity relations for elliptical, cD, cE and dE galaxies, and bulges of lenticulars and spirals. *Left:* Size-luminosity relation for the single-Sérsic fits to the E, cD, cE and dE galaxies color-coded by type (with effective radius and absolute magnitude as measures of the size and luminosity respectively), and their corresponding linear fits. A second order fit for E galaxies (thick dark red line) is also plotted. *Right:* Size-luminosity relation for the Sérsic components of E and cD types and the bulges of lenticular and spiral types with `Inclination` ≤ 2. The color of the points represent B/T_g, the bulge-to-total luminosity ratio in the g band. The solid black line is the second degree polynomial fit to all points. In both panels, the dashed gray lines are the historical fits from Binggeli et al. (1984), using the intercepts defined in the text.

tween the effective radii R_e in logarithmic scale and the g-band absolute magnitude M_g for the Sérsic components fitted with SourceXtractor++ to EFIGI E galaxies. The points are again color-coded as a function of B/T_g, the bulge-to-total flux ratio in the g band. A linear fit to these E components using the ODR package yields

$$\log R_e = -0.279^{\pm 0.012} M_g - 2.457^{\pm 0.242} \quad (15)$$

also shown in the graph (solid line), along with the ±3 times the r.m.s. dispersion in $\log R_e$ around that fit (dashed lines). In this first panel, we also show the distribution of R_e versus M for E galaxies modeled with a single Sérsic profile (in purple). The upper central panel of Fig. 6 similarly shows the distribution of R_e and M for the Sérsic components and the single Sérsic profiles of both the cD and dE types (in purple).

In the other panels of Fig. 6, we show the relation between R_e and $M_{\mathrm{bulge},g}$ both derived from the bulge and disk SourceXtractor++ profile modeling, separately for each morphological type from S0$^-$ to Sm (also color-coded with B/T_g), compared to the fit of the Sérsic components for E types (upper left panel and Eq. 15). One can see that there are similar size-luminosity relations for the bulges of disk galaxies (that is lenticulars and spirals). As morphological types advance along the Hubble sequence, bulges have smaller R_e Moreover, while bulges of types until Sb follow the E relation, there is a progressive departure toward fainter magnitudes at a given R_e for later types, similarly to what is observed for the Kormendy relation (see Sect. 4.1). The color-coding of the points in Fig. 6 by the bulge-to-total flux ratio in the g band B/T_g shows that for each lenticular and spiral type, there is a B/T_g positive gradient for larger and brighter bulges. This is further explored in Sect. 4.7 and Fig. 15.

In the left panel of Fig. 7, we gather on the same graph the variation of R_e versus M_g for EFIGI E (in dark red), cD (in green), dE (in purple) and cE types (as black open circles), derived from the single-Sérsic profile fits to these types. We also include the ODR linear fits for E galaxies (in red)

$$\log R_e = -0.368^{\pm 0.017} M_g - 3.955^{\pm 0.368} \quad (16)$$

for cD galaxies (in green)

$$\log R_e = -0.282^{\pm 0.046} M_g - 1.791^{\pm 1.032} \quad (17)$$

and dE galaxies (in purple)

$$\log R_e = -0.203^{\pm 0.027} M_g + -0.319^{\pm 0.488} \quad (18)$$

No size-magnitude relation is fitted to the cE galaxies as they are too few and too dispersed for a fit to be meaningful. We note that the slope of the fit to cD types (Eq. 17) is flatter than that of the linear fit to E galaxies (Eq. 16), but not at a significant level (1.8σ). cD galaxies are located among the brightest and largest E galaxies, but are limited by the poor statistics of this rare type, hence are not further discussed in this study.

It is interesting to compare our derived size-magnitude relations to those obtained by linear regression by Binggeli et al. (1984) for a sample of E and dE from the Virgo Cluster, E and dE from the local group, and dwarf spheroidal satellites of the Milky Way. Binggeli et al. (1984) measured slopes of -0.3 and -0.1 by fitting $\log R_e$ as a function of absolute magnitude in the B band for their sample galaxies brighter and fainter than ~ -20 respectively (with $H_0 = 50\,\mathrm{km\,s^{-1}\,Mpc^{-1}}$), with no distinction of type, leading to $M_g = -19.82$ (with $H_0 = 70\,\mathrm{km\,s^{-1}\,Mpc^{-1}}$ and using the B to g color correction from Fukugita et al. 1995). The dashed gray lines in Fig. 7 show both fits from Binggeli et al. (1984), while the intercept values (not provided in the article) were chosen to match the default parameters of the Stuff software for generating synthetic galaxies (Bertin 2009), with an R_e break value between the 2 regimes scaled to 3.35 kpc using $H_0 = 70\,\mathrm{km\,s^{-1}\,Mpc^{-1}}$, as used in the present article (see Sect. 1).

Given the various linear size-magnitude relations plotted in the left panel of Fig. 7, we first note a steeper slope $\alpha = -0.368$ for the size-magnitude relation of EFIGI E galaxies (Eq. 16)

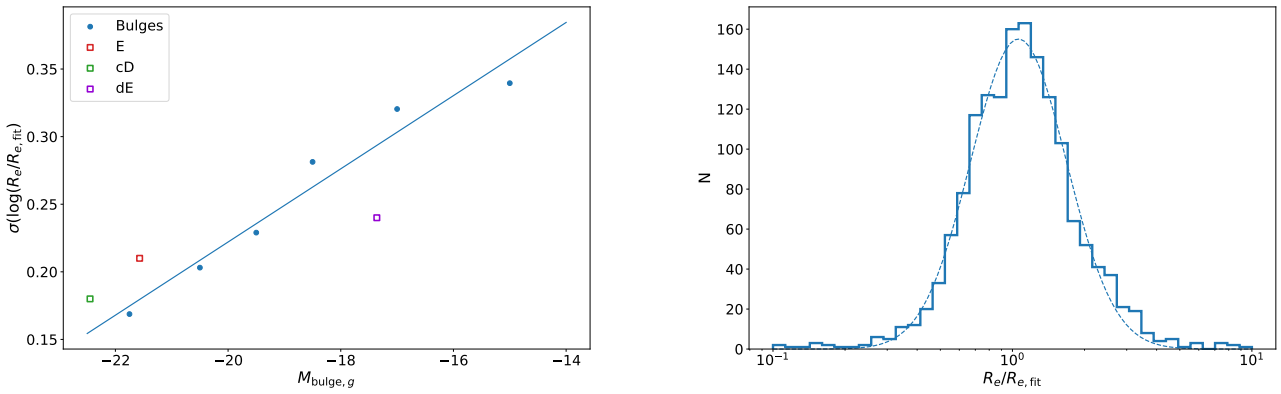

Fig. 8: Dispersion around the size-luminosity relations for the EFIGI Sérsic and bulge components from Fig. 7. *Left*: Variation of the r.m.s. dispersion in the logarithm of the ratio between the actual bulge effective radius R_e and the fitted value $R_{e,\mathrm{fit}}$ as a function of bulge magnitude $M_{\mathrm{bulge},g}$ around the size-luminosity relation (Eq. 19) for the Sérsic components and bulges of all types of EFIGI galaxies plotted in the right panel of Fig. 7. The estimated r.m.s. dispersion in $R_e/R_{e,\mathrm{fit}}$ increases for fainter bulges, and can be approximated by a linear regression. For comparison, the dispersion around the second-degree fit for the single-Sérsic profile of E galaxies (Eq. 15), and the linear fits to cD and dE galaxies (Eqs. 17 and 18) at the mean magnitude of galaxies of each type are shown with different symbols and colors. *Right*: Histogram of $R_e/R_{e,\mathrm{fit}}$ for the Sérsic components and bulges of all types of EFIGI galaxies. In order to account for the increasing dispersion around the fit seen in the left panel, the values of $\log(R_e/R_{e,\mathrm{fit}})$ are divided by the dispersion in the magnitude bin in which they lie, then renormalized to the average over the values for all magnitude intervals.

compared to the −0.3 value measured by Binggeli et al. (1984) for galaxies brighter than −20 in the B band, which we estimate as a 2.8σ difference. Here again, as the authors do not provide errors on the derived slope, which may be larger than the one in Eq. 16 (0.017) due to the smaller statistics of their sample compared to EFIGI, we use this latter underestimated error for this fit by Binggeli et al. (1984), and we proceed similarly below for all comparisons with their results. For the dE galaxies, which dominate below $M_g > -19$, we compare the EFIGI dE slope in Eq. 18 to the one obtained by Binggeli et al. (1984) for E and mostly dE galaxies fainter than $M_B = -20$, that is −0.10, which is half the slope we measure, and differs from it by 3.4σ. It is likely that the slope differences for E and dE types between EFIGI and Binggeli et al. (1984) are due to the non-linearity of the photographic plates that they used, as well as their profile extraction based on growth curve calculated from the two-dimensional galaxy surface brightnesses, and extracted from photographic plates using a microphotometer. The difference in photometric bands with EFIGI, and their limited sample of 109 E and dE in total, compared to 171 E and 48 dE used for the EFIGI fits, may also play a role in the discrepancies.

We also compare the size-luminosity relation fitted to the Sérsic components of EFIGI E galaxies in Fig. 7 (Eq. 15) to both the size-luminosity relations for EFIGI E galaxies modeled by a single Sérsic profile (Eq. 16), and that of Binggeli et al. (1984), with the limitation of a varying fraction of the galaxy light taken into account. The slope obtained for the Sérsic components is compatible with Binggeli et al. (1984) results with a 1.75σ difference, but differs more strongly from the slope obtained for EFIGI single-Sérsic fits to E galaxies, with a 4.3σ difference.

Nevertheless, we obtain for EFIGI galaxies the same qualitative result as Binggeli et al. (1984), namely that the slope for the size-magnitude relation of dE galaxies (Eq. 18) is flatter than for E galaxies (Eq. 16), with a 5.7σ difference. We also note that EFIGI E and dE types dominate at M_g magnitudes fainter than −19 and brighter than −20, respectively, which is not discordant with the interpretation by Binggeli et al. (1984) that the slope break near absolute magnitude -20 is due to a change in surface brightness of elliptical galaxies. Indeed, the break in the size-magnitude relations of E and dE types may result from the markedly different profiles of the E and dE galaxies : for EFIGI E galaxies we measure a single-Sérsic profile index in the interval n = 3.5-7 with a peak at $n \simeq 5.5$, whereas it is in the interval n = 1-3 for dE galaxies with a peak at $n \simeq 1.5$.

The dashed orange line in the left panel of Fig. 7 with a slope of -0.2 corresponds to a fixed surface brightness (see Eq. 12), which is nearly identical to the slope for dE (Eq. 18). It is not the case for the E types with a steeper -0.37 ± 0.04 slope (Eq. 16), which indicates a varying mean μ_e within the population, as expected from the Kormendy relation (see Sect. 4.1, Figs. 3 and 4). The dashed blue line with a slope of $-1/7.5 = -0.13$ in the left panel of Fig. 7 corresponds to the case of a scale-invariant spheroid for which the total luminosity grows as the cube of the radius. All slopes for the E, cD, dE types in the left panel of Fig. 7 are steeper than this ideal case of a scale-invariant spheroid. The implications are further discussed in Sects. 5.3.1 and 5.3.2.

At last, and because the linear fit to the E galaxies of Eq. 16, shown as a red line in the left panel of Fig. 7, would underestimate the effective radius of galaxies with $M_g < -22.7$, we also add in this graph an ODR second degree fit to the single-Sérsic fit of EFIGI E galaxies

$$\log R_e = 0.062^{\pm 0.010} M_g^{-2} + 2.268^{\pm 0.420} M_g - 24.093^{\pm 4.463} \quad (19)$$

which is steeper and better matches the E types at the bright ($M_g \lesssim -22.5$) and faint ends ($M_g \gtrsim 20.$) than the linear fit in Eq. 16. We quantify this improved fit by calculating the residuals of the $R_e/R_{e,\mathrm{fit}}$ ratios for $R_{e,\mathrm{fit}}$ given by either Eq. 16 or Eq. 19, for the M_g values of the considered sample. In both cases, the distribution of $\log(R_e/R_{e,\mathrm{fit}})$ in bins of 0.1 dex can be fitted by Gaussian distributions centered at -0.045 and -0.032, with standard deviations 0.207 and 0.186, and reduced χ_2 of 3.3 and 1.9 for the linear and second degree fits, respectively (with some skewness beyond ±0.3 dex for both).

4.3. The size-luminosity relation for bulges

In the right panel of Fig. 7, we plot the effective radii versus the magnitudes of the bulges from the bulge and disk decomposition for all galaxies. The bulge data points are again color-coded by B/T_g, the bulge-to-total luminosity ratio of each galaxy in the g band. As already seen in Fig. 6, B/T_g determines the position of bulges in this 2D plane. The right panel of Fig. 7 shows that both the luminosity and radii of the bulges continuously decrease as B/T_g decreases from $\lesssim 1$ to 10^{-2}, down to $M_{\mathrm{bulge},g} > -17$. At lower luminosities, R_e decreases less steeply as the luminosity decreases. This bending of the trend justifies the use of a second degree polynomial fit rather than a linear model for the size-luminosity relation of EFIGI bulges. The result of this fit appears as a black solid line and has the following equation:

$$\log R_e = 0.025^{\pm 0.0014}\ M^2_{\mathrm{bulge},g} + 0.762^{\pm 0.053}\ M_{\mathrm{bulge},g} + 8.253^{\pm 0.498} \quad (20)$$

We now examine the dispersion around the size-luminosity relation of the EFIGI bulges presented in the right panel of Fig. 7. We first compute for all bulges the ratio of R_e to the value $R_{e,\mathrm{fit}}$ given by Eq. 20 for the $M_{\mathrm{bulge},g}$ bulge magnitude of each EFIGI galaxy. We then calculate the r.m.s. dispersion around the value of 1 in log-scale, which is the quadratic mean of $\log(R_e/R_{e,\mathrm{fit}})$, in the six following intervals of $M_{\mathrm{bulge},g}$: $[-22.5,-21]$, $[-21,-20]$, $[-20,-19]$, $[-19,-18]$, $[-18,-16]$ and $[-16,-14]$. Left panel of Fig. 8 shows the variation in these dispersions as a function of the mean $M_{\mathrm{bulge},g}$ for each interval. For bright bulges, the dispersion is the lowest and is also similar to those measured around the single-Sérsic size-luminosity relations for cD, E and dE galaxies, also plotted in the graph. There is a systematic increase in the dispersion for fainter $M_{\mathrm{bulge},g}$, which we fit using a linear regression (as a blue line in the graph), whose coefficients are given in Table 1. In the right panel of Fig. 8, we show the histogram of the values of the log-ratios $\log(R_e/R_{e,\mathrm{fit}})$ for all EFIGI galaxies in the sample, divided by the dispersion in the bulge magnitude interval in which they lie, and renormalized by the mean dispersion (0.27) over the six $M_{\mathrm{bulge},g}$ intervals. This histogram can be fitted by a Gaussian with a central offset of only 0.025 dex in $R_e/R_{e,\mathrm{fit}}$, an r.m.s. dispersion of 0.20 dex, and a reduced $\chi^2 = 1.508$, hence validating the Gaussian shape of the residual distribution.

4.4. Understanding the surface brightness, effective radius and absolute magnitude relationships for E galaxies

Both the Kormendy and Binggeli relation are actually 2D projections of a 3D relation in the parameter space $\langle\mu\rangle_e$, R_e, M, where galaxies are distributed along a plane. This is illustrated by the approximate relation Eq. 12, which is the equation of a plane. Fig. 9 shows this plane from two different angles: face-on (left panel) and edge-on (right panel). There is a small dispersion perpendicular to the plane which is due to the redshift surface brightness dimming, the K-correction and the profile elongation, that we all neglect when deriving Eq. 12 from Eq. 11 (see Sect. 3.4). This plane is not homogeneously populated: most E galaxies (in dark red) have M_g in the range $[-23;-20]$, they span 2 dex in R_e but are mostly within $\log R_e \in [3.3;4.3]$ while the range of surface brightness $\langle\mu\rangle_e$ is large and encompass ~ 6 magnitude. The cD galaxies are among the most massive and largest E galaxies. On the other side, prominent bulges, mostly found in lenticulars, are mixed with the smallest and faintest E galaxies (here we consider the parameters from the single-Sérsic fits to E, cD, dE et cD types, and from the bulge and disk decomposition for lenticulars and spirals). As the B/T_g ratio decreases, bulges get smaller and fainter (in magnitude), but their effective surface brightness $\langle\mu\rangle_e$ has a more complex behavior as seen with the Kormendy relation in Fig. 4: it brightens for decreasing B/T_g with $B/T_g \gtrsim 0.1$, then dims for $B/T_g \lesssim 0.1$.

4.5. Novelty of disk scaling relations

Freeman (1970) modeled the luminosity profile of galactic disks using an exponential profile and found an approximately constant central surface brightness μ_0 of 21.65 ± 0.3 mag arcsec^{-2} for 28 of the 36 disks considered, even though they cover 5 magnitudes and span the Hubble sequence from S0 to Im types. Such a nearly constant surface brightness for very different disks would strongly constrain their formation scenario based on angular momentum considerations. However, de Jong (1996) disproved this result by examining, for nearly face-on disks, the distributions of their μ_0 and scale-lengths h, that fully parameterizes the variation of the mean surface brightness in an exponential disk (see Eq. 3). The low statistics of de Jong (1996) did not allow him to perform any fit but both panels of his Fig. 5 showing μ_0 versus h in the B and K bands respectively, seem to show that disks with a larger h are dimmer.

Using the EFIGI large statistical samples of all morphological types with improved profile modeling, we show in Fig. 10 the relations between μ_0 and h in the g band for the exponential profile of all EFIGI elliptical, spiral and lenticular galaxies decomposed into the sum of a Sérsic bulge and an exponential disk. We perform a linear fit using the ODR package (see Sect. 3.6) for E and cD types taken together and obtain the relation

$$\mu_0 = 2.33^{\pm 0.11} \log h + 18.60^{\pm 0.42} \quad (21)$$

with h in kpc, shown as a black solid line in the top left panel of Fig. 10. The fit is repeated in gray in the other panels, showing the variations of μ_0 versus h for the disks of all lenticular and spiral types, in order to guide the eye for comparisons between Hubble types. The joint E and cD fit (shown in the upper left panel) could match the S0$^-$, S0, S0$^+$, S0a and Scd types, whereas the disk of all other types have a different behavior: early and intermediate spirals (Sa to Sc) follow a similar slope but with a brighter zero-point than for E-cD (and S0$^-$-S0), while disks of types Sd and later have a weaker correlation between μ_0 and h, and a fainter zero-point than for E-cD (and S0$^-$-S0).

We have examined the μ_0 versus $\log h$ relations in the r and i filter and note that these shifts are filter-dependent for spiral types: the Scd fall mostly below the joint S0$^-$-S0 fit in the r and i bands, whereas the Sc types match this fit in both bands, and Sbc match it in i only. There is nevertheless no visual change in zero-point for the S0$^+$ -S0a compared to the joint E and cD fit in the r and i bands. This is due to the fact that the elliptical and lenticular types (including S0a) have similar colors, as shown by the color coding of the points by $g-r$ disk color in Fig. 10, whereas the disks of spiral types become bluer and bluer for later and later types along the Hubble sequence.

We also measure the size-luminosity relation of the disks of EFIGI galaxies by examining in Fig. 11 the distribution of their disk effective radii h_e versus absolute magnitude $M_{\mathrm{disk},g}$. Despite the large range of central disk surface brightness from 17.5 to 23.5 encompassed by these disks and illustrated with gray dashed lines of constant surface brightness (with a slope of -0.2, see Eq. 12), EFIGI disks exhibit a correlation between the disk effective radii and their absolute magnitudes.

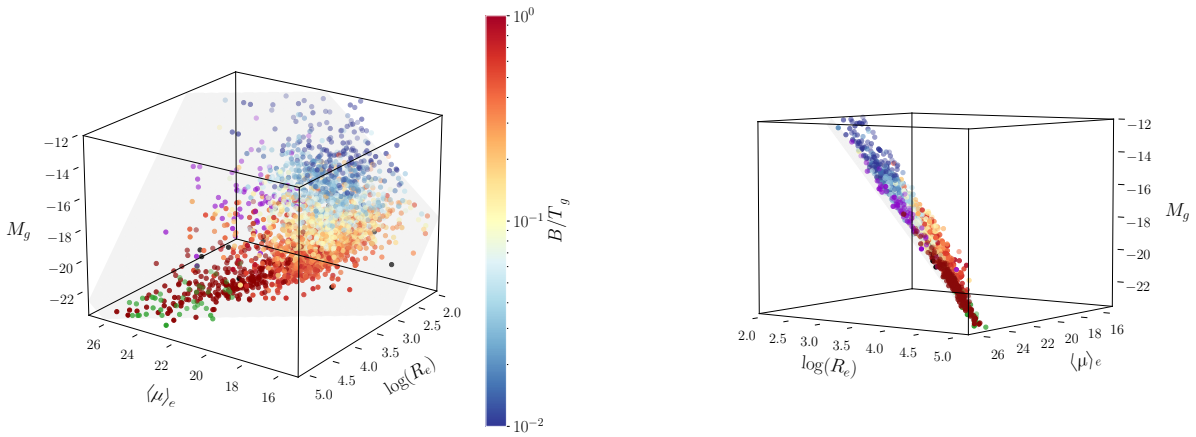

Fig. 9: Distribution in the $\langle\mu\rangle_e$, R_e, M_g tridimensional space of E (dark red), cD (purple), dE (green), cE (black) galaxies using their single-Sérsic fits, and of the bulges of all lenticular and spiral types from bulge and disk decompositions color-coded by B/T_g, the bulge-to-total luminosity ratio in the g band. Two different views are shown on the left and right, in order to highlight the fact that galaxies are distributed along a plane, as predicted from Eq. 12, with a small dispersion around it due to redshift: the gray plane is drawn for $z = 0$ and is best seen in the left panel. The Kormendy and size-luminosity relations are projections against the corresponding faces of the cube.

On one hand, a linear fit (using the ODR package) to the size-magnitude relation of disks of lenticulars and spirals of Scd type and earlier yields

$$\log h_e = -0.208^{\pm 0.004} M_{\mathrm{disk},g} - 0.434^{\pm 0.084} \quad (22)$$

shown in red in Fig. 11. This fit is close to the iso-surface brightness trend characterized by a slope of -0.2, thus indicating that the luminosities of these disks scale as h^2: $M_{\mathrm{disk}} \sim 5 \log h_e$ (see Eq. 12 and Sect. 5.3). The dispersion around this fit can be parameterized by a large range of μ_0 values (2.8 magnitude/arcsec^2 for 90% of the galaxies).

On the other hand, disks of Sd and later spiral types, that are fainter and bluer (see Fig. 10, deviate at $M_{\mathrm{disk},g} > -19$ from the extrapolation of the relation for earlier types (Eq. 22), with systematically larger disk radii and fainter surface brightness. We also include the Im galaxies (in black) modeled as a single Sérsic in Fig. 11, as they appear to extend the size-magnitude relation of late-type disks. The ODR linear fit to Sd, Sdm, Sm and Im types altogether is

$$\log h_e = -0.140^{\pm 0.007} M_{\mathrm{disk},g} + 0.983^{\pm 0.145} \quad (23)$$

shown in blue in Fig. 11. The dispersion around this fit can be parameterized by an even larger range of μ_0 than for earlier type spirals (4.4 magnitude/arcsec^2 for 90% of the galaxies). Moreover, there is a 7.3σ difference between the slopes in Eqs. 22 and 23, validating the two different trends.

We also show in Fig. 11 the measured effective radii versus absolute g-band magnitude for the exponential component of the E and cD types (in purple). A linear fit (also shown in purple) to these data points using the ODR package yields

$$\log h_e = -0.249^{\pm 0.012} M_{\mathrm{disk},g} - 1.123^{\pm 0.266} \quad (24)$$

The E and cD components exhibit larger sizes than the disks of lenticulars and early spirals at the bright-end of their size-luminosity relation. Therefore, its slope is steeper than in the fits for the early disks (Eq. 22). These components consequently have fainter surface brightnesses than lenticulars and early spirals, with values in the [19; 23] mag arcsec^{-2} interval, similarly to the disks of the latest spiral types, but with a much smaller contribution to the total galaxy light.

The decreasing slopes of the size-magnitude relations with morphological types in 22, 23 and Eq. 24 justify that we perform a second degree polynomial fit of $\log h_e$ as a function of magnitude for the exponential or disk or single Sérsic component of all types altogether (E, cD, all lenticulars, all spirals, Im[6]), which yields the following relation:

$$\begin{aligned} \log h_e =& 0.020^{\pm 0.0019}\ M^2_{\mathrm{disk},g} \\ &+ 0.623^{\pm 0.078}\ M_{\mathrm{disk},g} + 8.25^{\pm 0.808} \end{aligned} \quad (25)$$

The dispersion around this fit can be parameterized by an even larger range of μ_0 values than for earlier type spirals ($\sim$ 3 magnitude/arcsec^2).

To quantify the increasing spread in surface brightness of EFIGI disks at fainter magnitudes seen in Fig. 11, we examine the dispersion in h_e with disk magnitude (as in Sect. 4.3). As in Eq. 25, we include in this calculation the Im single-Sérsic profile magnitudes. We first compute for all disks as well as the E and cD exponential component, the ratio of h_e to the value $h_{e,\mathrm{fit}}$ given by Eq. 25. We then calculate the r.m.s. dispersion around the value of 1 in log-scale, which is the quadratic mean of $\log(h_e/h_{e,\mathrm{fit}})$, in the six following intervals of $M_{\mathrm{disk},g}$ (or magnitude of the E-cD exponential component, or Im single-Sérsic total magnitude): $[-23.5, -22]$, $[-22, -20.5]$, $[-20.5, -19]$, $[-19, -17.5]$, $[-17.5, -16]$ and $[-16, -13]$. Left panel of Fig. 12 shows the variation in these dispersions as a function of the mean magnitude for each interval. There is a systematic increase in the dispersion for fainter disks, which we

[6] Because Im types are fitted with single Sérsic profile, it is their total absolute magnitude that is plotted along the x-axis of Fig. 11, despite its labeling as $M_{\mathrm{disk},g}$.

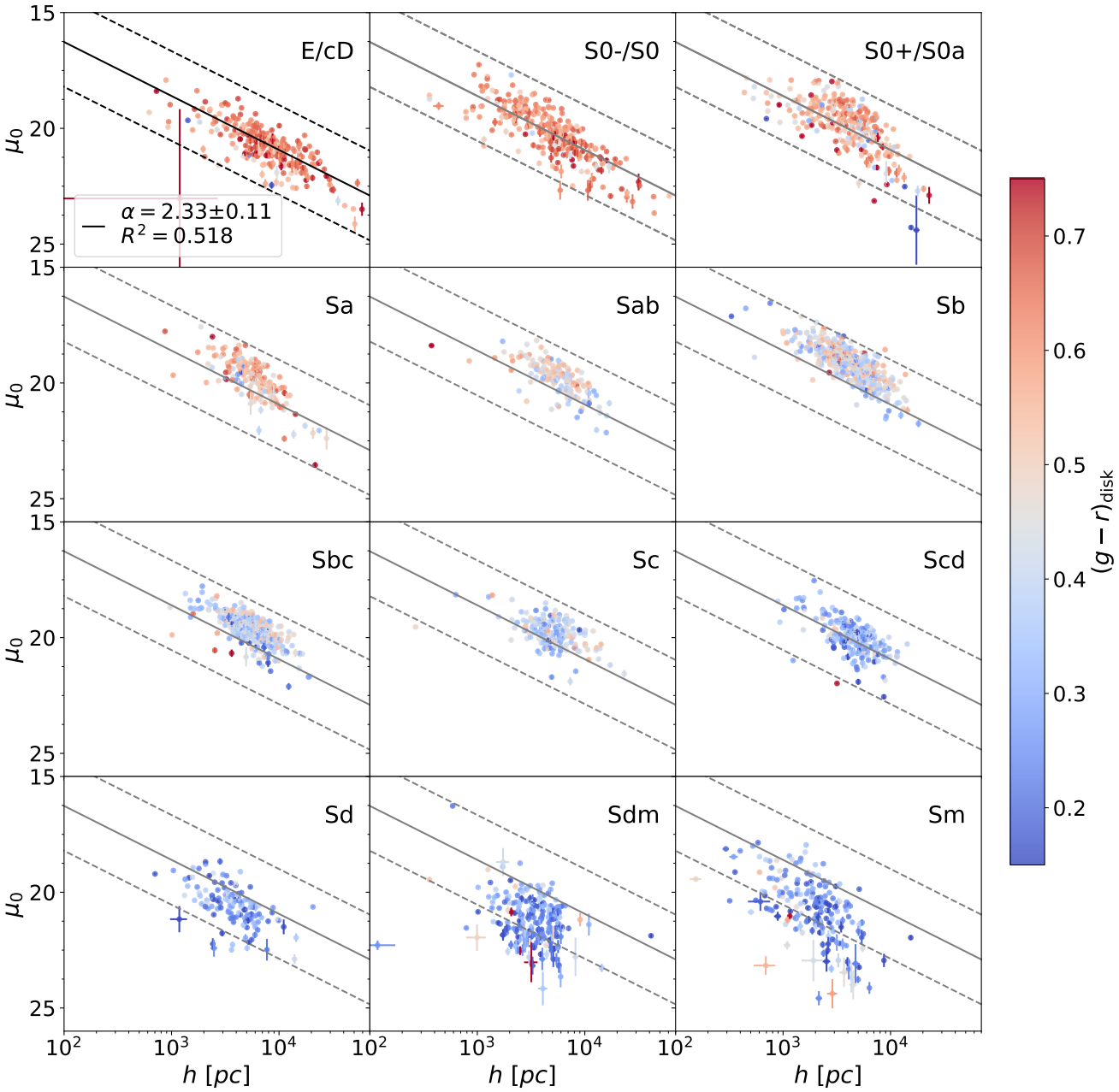

Fig. 10: Central surface brightness μ_0 versus scale-length h for the disk (or exponential) component of the different Hubble Types. The linear fit obtained for E and cD types (upper left panel) is shown in all panels as solid lines, along with the parallel dashed lines at ±3 times the r.m.s. dispersion in μ_0 around the fit. Points are color-coded with the $g-r$ color of the disk (or exponential) component. For all lenticular types as well as early and intermediate spirals up to Scd, h is correlated with μ_0 with different intercept values, but a common slope would be an acceptable approximation to each distribution. For Sdm and Sm late-type spirals, the distribution is more dispersed.

fit using a second degree regression (shown in the graph as the black solid line), and whose coefficients are given in Table 1.

We also calculate similarly the dispersion around the linear fit of Eq. 23 restricted to the disks of Sd, Sdm, Sm types and the Im single Sérsic profiles that dominate the faint-end of the size-luminosity relation in Fig. 11. A linear model to the dispersion in $\log(h_e/h_{e,\rm fit})$ around the fit in Eq. 23 computed in the four faintest magnitude intervals, and plotted in blue, appears sufficient at magnitudes fainter than −20.5 for these late types, as shown in Fig. 12. The dispersion around this linear fit does not increase as steeply as for the second degree polynomial fitted to the dispersion for all disk types. In the right panel of Fig. 12, we show the histogram of the $h_e/h_{e,\rm fit}$ ratios around the second degree size-luminosity relation of Eq. 25, for all EFIGI galaxies in the sample. The $\log(h_e/h_{e,\rm fit})$ are divided by the dispersion in the disk magnitude bin they lie in, and renormalized by the mean dispersion (0.211) over the six $M_{\rm disk,g}$ intervals. This histogram can be fitted by a Gaussian with a central offset of only 0.015 dex in $h_e/h_{e,\rm fit}$, an r.m.s. dispersion of 0.20 dex, and a reduced $\chi^2 = 1.864$, hence validating the Gaussian shape of the residual distribution.

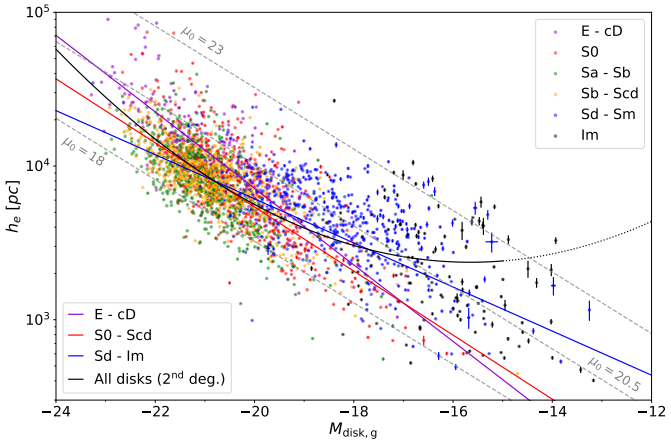

Fig. 11: Effective disk radius versus absolute g magnitude for the EFIGI disk (or exponential) components. The color of the points correspond to groups of Hubble type. Dashed gray lines are iso-μ_0 lines, of slope -0.2, which for an exponential profile corresponds to a disk luminosity scaling as $h_e{}^2$. They allow to see that disks span $\sim$ 6 dex in central surface brightness at all magnitudes. The solid lines are ODR fits: three linear models for disks of types E-cD, S0-Scd and Sd-Im, in purple, red and blue respectively, whereas the black line is the second degree polynomial fit of $\log h_e$ as a function of $M_{\mathrm{disk},g}$ for all disks. The size-luminosity relation is close to an iso-surface brightness growth for lenticulars as well as early and intermediate spirals, but there is a tail of faint disks for (dimmer) late-type spirals and irregulars with a larger size than earlier spirals at these faint magnitudes, for $M > -19$.

4.6. Bi-variate luminosity-radii distribution function for disks

We now compare the EFIGI disk sizes with those obtained by de Jong & Lacey (2000) for a sample of 1007 Sb-Sdm spirals with $z < 0.025$ (widely distributed on the sky). We display in Fig. 13 the distribution of EFIGI galaxies as a function of h_e, per interval of disk absolute magnitude $M_{\mathrm{disk},i}$, and per group of morphological types. Here we use EFIGI magnitudes in the i band, in order to compare with the de Jong & Lacey (2000) analysis performed in the Cousins I_C band. All galaxies fainter than $m_i = 15.5$ are excluded, and those remaining are weighted by w/V_{max}, where w is the incompleteness correction, calculated as the ratio of galaxies, per bin of 0.5 apparent i magnitude, between a power law fitted in the $8.5 \leq i \leq 14$ interval on the number counts of the complete magnitude limited MorCat sample (see Sect. 2) and EFIGI number counts. The volume correction $V_{\mathrm{max}} = \Omega \frac{4\pi}{3} D^3_{\mathrm{lum,max}}$ is obtained using $\Omega = 6670$ deg^2, the solid angle of sky covered by EFIGI (Baillard et al. 2011), and $D_{\mathrm{lum,max}}$ the luminosity distance to a galaxy with absolute magnitude M_i if its apparent i magnitude was equal to the survey magnitude limit $m_{i,\mathrm{lim}} = 15.5$, chosen for the present calculation (we thus use Eq. 10 and the k-correction of each object). The V_{max} weighting allows one to correct for the fact that galaxies of fainter absolute magnitudes (hence later types among the star-forming galaxies) are visible out to shorter distances (hence a smaller volume) than brighter galaxies, therefore providing a fair comparison of volume densities of the different galaxy types. Fig. 13 shows the resulting density distributions of h_e measured in the SDSS i band for EFIGI S0$^-$ to Sab types (in red), Sb to Sbm types (in green) and Sm to Im types (in blue): the Sb-Sdm grouping corresponds to the types studied by de Jong & Lacey (2000), while the S0$^-$-Sab and Sm-Im types group the earlier and later lenticular and spiral types, respectively, along the Hubble sequence in the EFIGI sample (the Im are fitted as single Sérsic profiles). We also chose the SDSS i magnitude intervals derived from those of Fig. 5 of de Jong & Lacey (2000) using a 0.51 color correction between the i_C band that they use, and the SDSS i band for EFIGI (Fukugita et al. 1995).

For comparison with the results of de Jong & Lacey (2000), we show as black curves in Fig. 13 the density distributions per absolute i magnitude interval of the bi-variate function that they propose to model the distribution of disk effective radii for their Sb-Sdm sample. Given the error bars, one can see marked differences with the EFIGI distribution of disk effective radii of the corresponding type group, in the magnitude intervals of all disks (or single-Sérsic for Im). First, in the brightest intervals $[-23.5; -22.0[$ and $[-22.0; -20.5[$, the curve over predicts the density of small disk radii compared to the data but there is agreement on the decreasing trends at large h_e in both panels. Then, in the three magnitude intervals $[-20.5; -19.0[$, $[-19.0; -17.5[$ and $[-17.5; -16.0[$ the under prediction of galaxies by the curves shifts to large h_e. The quasi absence of EFIGI Sb-Sdm galaxies in the faintest $[-16.0; -13.0]$ interval, in which de Jong & Lacey (2000) predict a significant volume density of objects, whereas the EFIGI density of Sm-Im galaxies is above the curve, may result from classification errors of the latest spirals in the Sb-Sdm sample of de Jong & Lacey (2000). As this magnitude interval does not appear in their Fig. 5 (probably due to an absence of data), it could be beyond the range of validity of their proposed function.

Moreover, we do not show in Fig. 13 the $[-25.0; -23.5[$ M_i interval of de Jong & Lacey (2000) (corresponding to their brightest magnitude interval), because it only contains 10 EFIGI galaxies (4 S0, and 6 Sb-Sdm spirals) that are all located near the faint edge of the interval (with $M_{\mathrm{disk},i} \geq -23.83$). These bright disks all have $h_e > 10^4$ pc and no h_e bin contains more than 2 galaxies. Altogether, this prevents any meaningful analysis. One may wonder whether the sample of de Jong & Lacey (2000) contains disks which are clustered near the faint edge of the interval, and in that case the bi-variate functional form cannot be validated for $M_i \lesssim -24$, or it does include a significant number of disks brigther than $M_i = -24$. In the latter case, we suspect that a bulge and disk decomposition that underestimates the bulge contribution, hence overestimates the disk component could explain why the EFIGI sample does not contain such bright disks.

Another bias that could affect the comparison of EFIGI disk sizes with the model of de Jong & Lacey (2000), shown in Fig. 13, could be a higher threshold in surface brightness detection in their data, as these observations are based on photographic plates: at a fixed radius h_e, a faint absolute magnitude implies a fainter central surface brightness μ_0 (see Fig. 11), and such objects could fail to be detected. The joint bias resulting from the fact that at a fixed absolute magnitude, a larger h_e radius implies a fainter central surface brightness μ_0 (see Fig. 11) could also explain the large h_e under prediction of the galaxy densities by the curves derived from de Jong & Lacey (2000) compared to EFIGI for magnitudes intervals $[-20.5; -19.0[$, $[-19.0; -17.5[$, and $[-17.5; -16.0[$.

At last, the distribution of the other EFIGI type groupings, namely S0-Sab types and Sm-Im types show different density distributions from the Sb-Sdm types, with smaller h_e for S0-Sab for $M_{\mathrm{disk},i} \geq -20.5$, and a similar interval of h_e for the Sm-Im, except for the two brightest magnitude intervals in which there are no or very few EFIGI galaxies of Sm-Im types. In the 2 faintest magnitude intervals, the Sm-Im types have a similar den-

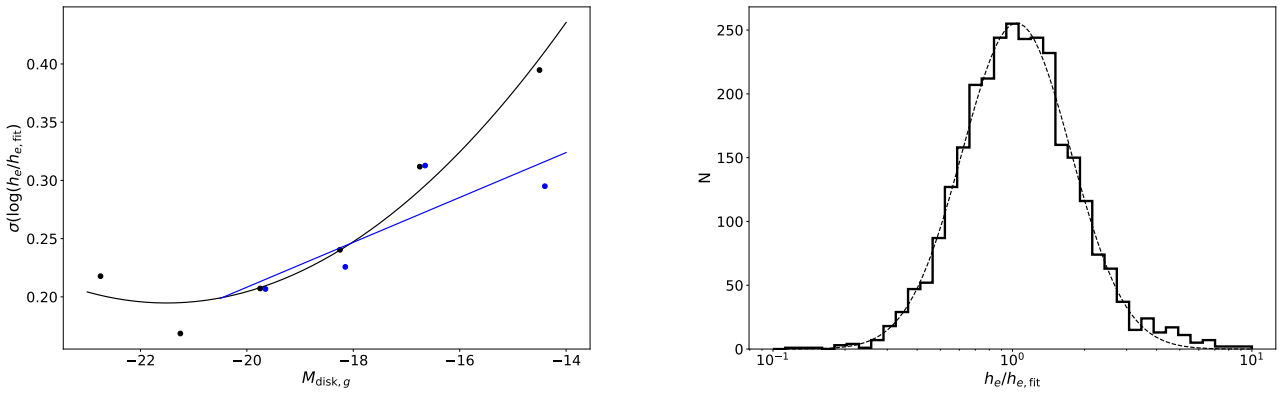

Fig. 12: Dispersion around the size-luminosity relations for the EFIGI exponential and disk components from Fig. 11. *Left*: Variation of the r.m.s. dispersion in the logarithm of the ratio between the actual disk effective radius h_e and the fitted value $h_{e,\rm fit}$ as a function of disk magnitude $M_{\rm disk,g}$ around the size-luminosity relations plotted in Fig. 11 for EFIGI galaxies, as a function of the mean disk magnitude in 1.5 or 3 mag. intervals. The dispersion around the second degree fit is shown as black points, and that around the linear fit to Sd-Im types only as blue points (and calculated only for $M_{\rm disk,g} > -20.5$). The resulting dispersion values are fitted with a second degree polynomial (black), and a linear regression (blue) respectively. In both cases, the estimated dispersion increases for fainter disks. *Right*: Histogram of $h_e/h_{e,\rm fit}$ for the size-luminosity relation for all disks of EFIGI lenticulars and spirals as well as irregulars. In order to account for the increasing dispersion around the fit seen in the left panel, the values of $\log(h_e/h_{e,\rm fit})$ are divided by the dispersion in the magnitude bin in which they lie, then renormalized to the average over the values for all magnitude intervals.

sity distribution to that of the model, but with a 1 dex higher density. The model function proposed by de Jong & Lacey (2000) therefore does not appear appropriate to describe any of the broad groups of Hubble types considered in the EFIGI sample. We intend to derive an updated functional form in the g band based on the magnitude limited MorCat catalog to $g \leq 15.5$, hence with higher statistics and smaller type groupings. The large incompleteness corrections performed near the 15.5 apparent i magnitude limit used for producing here Fig. 13 will then be circumvented.

4.7. How bulge and disk bulge prominence and size vary among Hubble types

In Quilley & de Lapparent (2022), we showed that the Hubble sequence is an inverse evolutionary sequence, characterized by disk reddening and an increase in the bulge-to-total mass and light ratio (denoted B/T). Here we examine the changes in effective radii of bulge and disk that accompany these changes in color and luminosity. In all of this subsection, even though the Hubble types in all graphs are ordered from left to right along the historical sequence, we present and discuss all variations of EFIGI galaxies from right to left, that is across types from late to earlier types, as this is the main direction of galaxy evolution.

4.7.1. Bulge-to-total ratio growth with Hubble type

The strong increase in B/T toward earlier Hubble types that we highlighted in Quilley & de Lapparent (2022) can be seen in Fig. 14, showing the distribution of the bulge-to-total luminosity ratio in the g band as a function of Hubble type. There is moreover a significant dispersion in B/T_g within each type. The black dashed line shows the geometric mean[7] value per type and the associated error, which is estimated as the r.m.s. deviation in $\log B/T_g$ divided by $\sqrt{N}$ with N the number of galaxies in the type bin (we verified that it is larger than the error derived from the quadratic mean of errors on individual points).

The frequently failed bulge fits for types Sd, Sdm and Sm, as these are very faint, are discarded (see Sect. 4.1), leading to very low statistics and a large dispersion in B/T_g (describing nearly the whole plotted interval $10^{-3} - 1$ in Fig. 14) for these late spiral types. The graph then shows that for earlier types, that is from Scd to Sb galaxies, each Hubble type displays an interval of ~ 1.5 dex in B/T_g, and a strong systematic increase of the mean B/T_g per type from the Scd late-type spirals to earlier spiral types and lenticulars. Indeed Scd, Sc and Sbc types have geometric mean values of $B/T_g \sim 0.025 - 0.045$, while the mean reaches 0.09 for Sb galaxies. The increase persists but not as steeply for earlier types, with a geometrical mean B/T_g of 0.18 for Sab galaxies, and reaches 0.37, 0.40 and 0.43 for $S0^+$, S0 and $S0^-$ lenticular types, respectively. At last, E galaxies exhibit the highest average B/T_g value at 0.50.

The increase in B/T_g for earlier types along the Hubble sequence seen in Fig. 14 is a direct consequence of the Hubble sequence classification system which includes the visually perceived B/T_g as one of the criteria to differentiate among the spiral types. It is also physically meaningful because the bulge growth in both B/T_g and absolute bulge luminosity is a key factor in the evolution of galaxies, and is related to the fading of their star formation (Bluck et al. 2014; Lang et al. 2014; Bremer et al. 2018; Dimauro et al. 2022; Quilley & de Lapparent 2022). Fig. 14 also shows that the dispersion in B/T_g abruptly decreases from an r.m.s. dispersion in $\log B/T_g$ included in the 0.4-0.5 interval for types Scd to Sb, to the 0.2-0.3 interval for types Sab to S0a, and to the 0.1-0.2 interval for types $S0^+$ to E. At last, each point representing a galaxy in Fig. 14 is color-coded according to the effective radius R_e of the bulge (or Sérsic component for E and cD types), and this shows a systematic trend that within a

[7] We use the geometric mean as it is less sensitive to outliers in logarithmic scale.

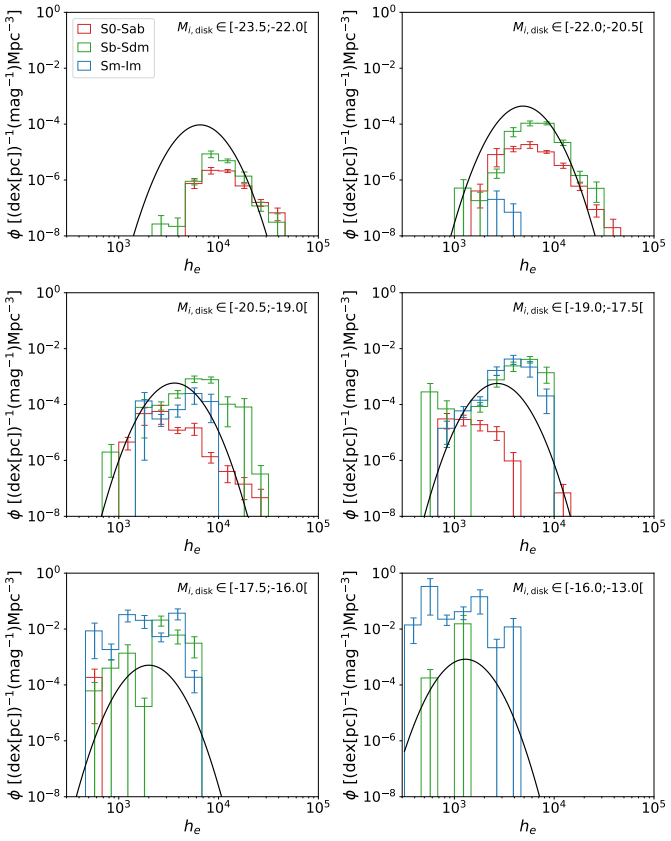

Fig. 13: Spatial density of disk effective radius for EFIGI morphological types grouped as S0$^-$-Sab, Sb-Sdm, Sm-Im (the effective radii of single-Sérsic fits are used for the Im), compared to the expected density from the bi-variate luminosity-disk radius function proposed by de Jong & Lacey (2000) for a sample of $\sim$ 1007 Sb-Sdm galaxies. For each magnitude interval, its mean magnitude is used to derive the plotted analytical curve.

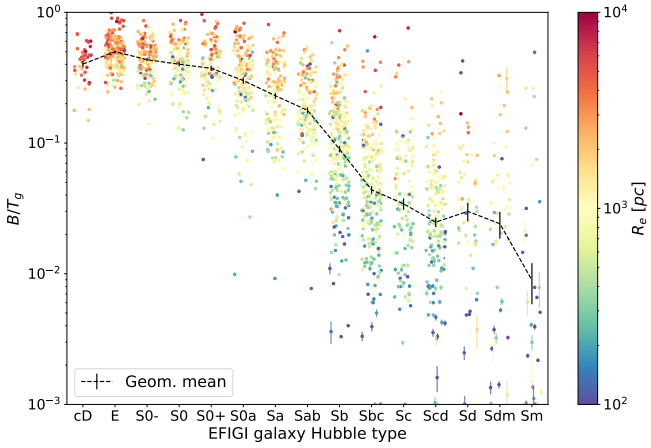

Fig. 14: Bulge-to-total luminosity ratio in the g band B/T_g from the bulge and disk decomposition of all EFIGI galaxies with `Inclination` $\leq$ 2 as a function of Hubble Type. The color of the points represent the effective radius R_e of the bulge (or Sérsic component for E and cD types). The black dashed line shows the geometric mean value per type, and the vertical bars the estimated uncertainties in this mean (see text for details). There is a correlation between Hubble type and B/T_g with the latter increasing sharply along the sequence toward earlier types. However, there is also a significant dispersion of B/T_g within each type, ranging from $\sim$ 0.25 dex for lenticulars to almost 1 dex for late-type spirals, with the other trend that larger B/T_g correspond to larger bulge R_e overall, as well as within each type.

given Hubble type, as well as across types, galaxies with larger B/T_g also have larger bulge R_e. These large dispersions in B/T_g and bulge R_e for each Hubble type means that any given set of values of these parameters cannot solely define a galaxy morphological type, at least the disk characteristics also need to be defined.

4.7.2. Variation of bulge and disk radius with Hubble type

Here we further examine the implications of the observed trends in bulge predominance between morphological types in terms of the effective radii of both the bulge and disk components. The scaling relations per Hubble type of the left panel of Fig. 4 and the right panel of Fig. 7 show that in addition to a systematically decreasing interval of R_e for later Hubble types, R_e also varies within each type with effective surface brightness and absolute magnitude respectively, and that this variation is linked to the variations in the B/T ratio. The left panel of Fig. 15, directly shows the distribution of the effective radius R_e of the bulge (or Sérsic component for E and cD types) as a function of Hubble type, color-coded with B/T for EFIGI galaxies, as well as the geometric means and the estimated errors per type (calculated as in Fig. 14, see Sect. 4.7.1). Again, the very faint bulges of EFIGI galaxy types Sm, Sdm and Sd (see Sect. 4.1) lead to low statistics for these spiral types, but the range of effective radii for the few successfully modeled bulges (with an uncertainty in $\log R_e \lesssim 0.2$ dex) nevertheless lies within the same interval as the earlier spiral types (Sb to Scd types). For the earlier Scd to Sb types, there is a "plateau" in effective radius with a mean value of $R_e = 0.60, 0.62, 0.61$ kpc for Sc, Sbc, Sb respectively.

The mean R_e then increases between late and early spirals, with 0.9 kpc for Sab galaxies to 1.2 kpc for Sa galaxies. The rms dispersion in $\log R_e$ for any given type of lenticulars and spirals from Scd to S0$^-$ in the left panel of Fig. 15 is between 0.31 and 0.43 dex. When weighted by the square root of the number of galaxies and adopted as an estimate of the uncertainty in the geometric mean, the doubling of the mean R_e from Sb to Sa types corresponds to a 7.5σ increase. This significant step in mean B/T is obtained thanks to the large statistical size of the EFIGI sample per Hubble type.

There is then another "plateau" in bulge effective radii for types between Sa up to S0. We note that the Sb to Sa increase in mean R_e corresponds to the entry of galaxies into the Green Valley, which we characterized in Quilley & de Lapparent (2022) by a stronger bulge-to-total ratio in both luminosity and mass. What the left panel of Fig. 15 provides here is the additional information that this stronger bulge prominence is also detected by larger effective radii by a factor of 2 on average.

For the lenticulars and ellipticals, the significant increase in R_e from a geometric mean of 1.0 kpc for S0 types to a mean of 1.6 kpc for S0$^-$ types could be the result of misclassifications of E galaxies into S0$^-$, driving the mean value for S0$^-$ types higher than it should be. Indeed, the bulge and disk decompositions applied to E galaxies (with high B/T, hence mostly red colored points) lead to larger values of R_e with a geometric mean at 2.3 kpc, and a dispersion of 0.27 dex.

The left panel of Fig. 15 also shows the effective radii derived from the single-Sérsic profile modeling of E and cD galaxies as

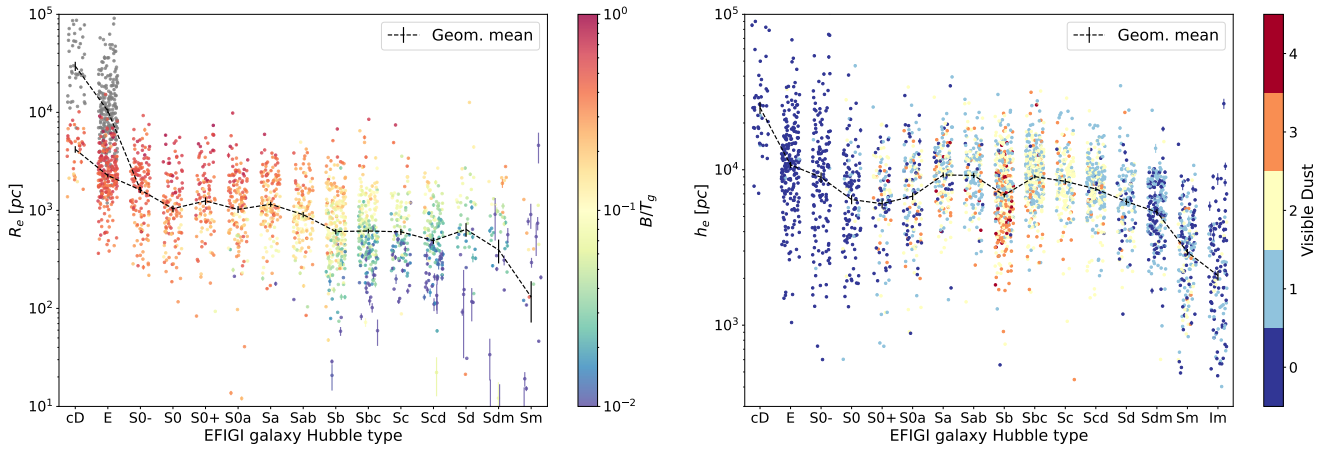

Fig. 15: Distributions of the effective radius R_e of the bulge (or Sérsic) component (left) and h_e of the disk (or exponential) component (right) from the bulge and disk decomposition of all EFIGI galaxies with `Inclination`≤ 2, as a function of Hubble Type. The black dashed lines represent the geometric mean value for each Hubble type, and the vertical bars the estimated uncertainties on this mean (see Sect. 4.7.1 for details). In the left panel points are color-coded with the bulge-to-total ratio in the g band B/T_g, except for the gray dots, corresponding to the single-Sérsic profile modeling. In the right panel, Im sizes are derived from their single-Sérsic profile modeling, and the points are color-coded with the EFIGI `Visible Dust` attribute, which suggests that the lower radii measured for Sb galaxies compared to adjacent types are likely due to strong dust extinction.

gray dots (see Sect. 3.1), and indicates a shift in R_e from 1.1 kpc for the mean over S0 to S0a types (if one excludes S0$^-$ as they may be contaminated by E galaxies), to a mean of 10.4 kpc and 29.6 kpc for E and cD types respectively.

We now examine the corresponding effective radii h_e of the disk (or exponential component for E and cD types) for EFIGI galaxies in the right panel of Fig. 15, which shows the variations of h_e for each Hubble Type, as well as the geometric means and the estimated errors per type (determined as for Fig. 14, see Sect. 4.7.1). One can see that there is a marked increase in the geometric mean of h_e from 2.1 kpc to 5.3 kpc for Im and Sdm types respectively, that is by a factor of $\sim$ 2.6 and a 11.3σ increase. The increase in the mean h_e is less abrupt between Sdm and Sbc types with a factor of $\sim$ 1.7 and a 10.5σ increase between these two types.

Between Sbc and Sa types, the mean effective radii of the disks presents a "plateau" at 9.0 – 9.3 kpc, with a systematic shift toward lower values for Sb types, at a geometric mean radius of 6.9 kpc. As the distribution of h_e as a function of Hubble type does not display any systematic trend with B/T, we color-code the points in the right panel of Fig. 15 with the EFIGI `VisibleDust` attribute. Interestingly, the more frequent presence of large amounts of dust in disks of Sb types compared to the other spiral types may cause the lower tail and lower mean h_e for the Sb types: the high dust content of these galaxies would obscure their disks and make them apparently smaller (there is a similar effect with the isophotal diameter D_{25}, see de Lapparent et al. 2011).

Moreover, in the right panel of Fig. 15, S0a and lenticulars display smaller mean disk radii than early-type spirals except for the S0$^-$ type, whose large 9.0 kpc radii could be due to a contamination by misclassified E galaxies, as already discussed for the bulge radii (left panel of Fig. 15). Taken together, S0a, S0$^+$ and S0 types have a mean h_e = 6.4 kpc, which is $\sim$ 42% lower (and 4.9σ) than the 9.1 kpc "plateau" value for Sbc, Sab and Sa spirals. At last, the exponential components (of the bulge and disk decompositions) of E and cD galaxies have mean h_e of 10.7 and 25.1 kpc respectively, confirming again that these types are the largest of the Hubble sequence. We can note that these values are nearly identical to and consistent with the single profile effective radii of 10.4 kpc and 29.6 kpc for E and cD types respectively (plotted in gray in the left panel of Fig. 15). This confirms the larger overall size of E compared to lenticular and spiral disks (hence the full galaxy sizes), and the fact the cD galaxies are giant galaxies built by the merger of galaxies in dense regions such as clusters of galaxies (Edwards et al. 2020; Chu et al. 2022).

4.7.3. Variation of bulge and disk radius with B/T

Another major feature seen in the left panel of Fig. 15 is that there is a strong B/T gradient with R_e within each Hubble type, as well as from type to type, suggesting that B/T may actually be a useful quantity to parameterize the variations in R_e among galaxies. This can be seen directly in the left panel of Fig. 16, which shows the distribution of the effective radius R_e of the bulge (or Sérsic component for E and cD types) as a function of B/T in the g band for EFIGI galaxies separated into spirals (left subpanel) and early Hubble types from E to S0a (right subpanel). Despite a large dispersion, there is a continuous linear increase in the mean $\log R_e$ with $\log B/T_g$, independently of the galaxy type, with earlier Hubble types having on average larger B/T_g and R_e in both subpanels.

More specifically, one can see in the left panel of Fig. 16 an increase in R_e with B/T_g for all spiral types from Sa to Sm in the $B/T \sim 0.002 - 0.6$ interval (left subpanel). For the E to S0a types, there is a steeper increase in the $B/T \sim 0.2 - 0.7$ interval. We therefore linearly model the $\log R_e$ variations with $\log B/T_g$ for both samples using the ODR package (see Sect. 3.6), and obtain

$$\log R_e = 0.612^{\pm 0.018} \log B/T + 3.571^{\pm 0.021} \quad (26)$$

for Sa to Sm spiral types, and

$$\log R_e = 3.174^{\pm 0.166} \log B/T + 4.341^{\pm 0.063} \quad (27)$$

for E to S0a lenticular types. Indeed, Eq. 27 indicates a steeper increase of R_e with B/T_g for E to S0a types compared to spirals.

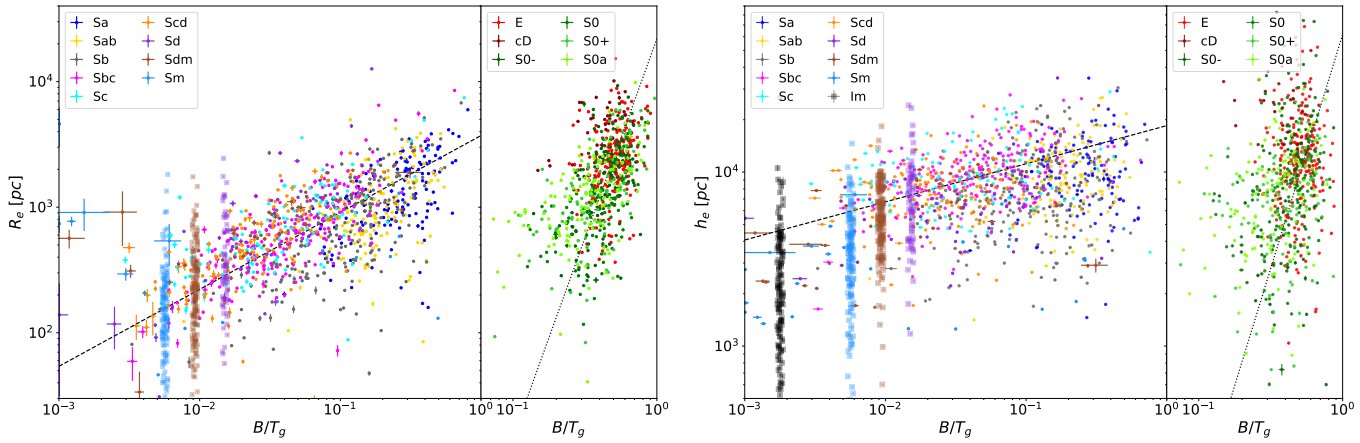

Fig. 16: Distributions of the effective radius R_e of the bulge (or Sérsic) component (left), and h_e of the disk (or exponential) component (right) of all types of EFIGI galaxies with `Inclination`$\leq$ 2, as a function of the bulge-to-total ratio B/T_g in the g band, identified in Quilley & de Lapparent (2022) as a tracer of Hubble type. Both panels are color-coded with the Hubble type of the galaxy, with subplots corresponding late (spiral and Im) types on the left, and to early (E and S0) types on the right. The corresponding ODR fits are plotted in each panel. The indicative positions in B/T_g, R_e and h_e for the Sd, Sdm, and Sm types are added in both panels (see text for details). For the Im types (added in the right panel), the effective radii from the single-Sérsic modeling are added at an arbitrary small B/T_g value (see text). These graphs show that for spiral types, R_e increase strongly with B/T_g, whereas there is only a weak increase in h_e with B/T_g. S0 and E galaxies have the highest B/T_g values, but only some of them actually have the highest R_e or h_e, with a tail of S0 toward lower values encompassing $\sim$ 1 dex for both their R_e and h_e. The smallest S0 R_e correspond to the smallest R_e of early spirals (left panel), and the smallest S0 h_e correspond to the intermediate h_e between those of the smallest disks (Sm types) and of the Im galaxies (right panel).

The r.m.s. dispersion in $\log R_e$ around both fits is higher for E to S0a types, with 0.55 dex compared to 0.31 dex for spirals. We also calculate the residuals of the $R_e/R_{e,\rm fit}$ ratios for $R_{e,\rm fit}$ given by Eq. 26, for the B/T_g values of the considered sample. The distribution of $\log(R_e/R_{e,\rm fit})$ in bins of 0.1 dex can be fitted by a Gaussian distribution centered at 0.021, and with reduced χ_2 of 3.3 (with some skewness beyond $\pm$0.4 dex). All parameters, including the r.m.s. dispersion, about both fits are listed in Table 2 in Sect. 5.4.

We now examine in the right panel of Fig. 16 the distributions of the effective radii h_e of the disk (or exponential component for E and cD type) as a function of B/T_g. E to S0a types show again a steeper variation than for spiral types. We therefore perform ODR linear fits to the separate early and late type subsamples, and obtain

$$\log h_e = 0.219^{\pm 0.013} \log B/T + 4.267^{\pm 0.019} \quad (28)$$

for Sa to Sm spiral types, and

$$\log h_e = 2.691^{\pm 0.133} \log B/T + 4.790^{\pm 0.042} \quad (29)$$

for E to S0a types. As for R_e, the r.m.s. dispersion in $\log h_e$ around both fits is higher for E to S0a types, with 0.59 dex compared to 0.22 dex for spirals (all parameters are also listed in Table 2 in Sect. 5.4). There is therefore a similar and steep increase in the effective radii of the disk (or exponential component) of E to S0a types with B/T_g as for their bulges (see Eqs. 27 and 29), whereas the disk radii increase with B/T_g for spiral types is lower by a factor of $\sim$ 3 in log-log compared to the bulge radii variations of these types (see Eqs. 26 and 28).

We see in both panels of Fig. 16 that the Sa types show a larger dispersion in B/T_g, as well as in R_e and h_e, compared to the other types, encompassing both the spiral and lenticular sequences. Excluding them from the spiral ODR fits increases the slopes by small amounts (0.025 and 0.024 for Eq. 26 and 28 respectively), and would lead to the same conclusions. We also calculate the residuals of the $h_e/h_{e,\rm fit}$ ratios for $h_{e,\rm fit}$ given by Eq. 28, for the B/T_g values of the considered sample. The distribution of $\log(h_e/h_{e,\rm fit})$ in bins of 0.1 dex can be fitted by a Gaussian distribution centered at -0.064, and with reduced χ_2 of 3.3 (with some skewness beyond $\pm$0.4 dex).

We position, in the right panel of Fig. 16, the effective radii measured for the single-profile Sérsic modeling of Im galaxies near the lower left limit of the graph of $B/T_g \simeq 10^{-3}$, namely at $B/T_g = 1.7\ 10^{-3}$ (in black). We also display the missing late spiral galaxies in both panels of Fig. 16. As shown in the left panel of Fig. 15, only 52, 43 and 24 galaxies of Sd, Sdm, and Sm types respectively have their bulge successfully modeled by the bulge and disk decomposition (see Sect. 4.1). These galaxies nevertheless do have small or very small bulges. In order to show indicative positions for the bulge and disk effective radii of these types in Fig. 16, we first estimate their mean B/T_g by linearly interpolating (in logarithmic scale) in Fig. 14: we use the geometric mean values of B/T_g for Sab and Scd types and extend the line between these points to later types, leading to extrapolated values of $B/T_g = 0.015, 0.009, 0.006$ for Sd, Sdm and Sm types, respectively. We also linearly interpolate (in logarithmic scale) in the left panel of Fig. 15 between the geometric mean value of R_e for Scd types (0.49 kpc), and that for Sm types (0.13 kpc), and obtain mean estimates of 0.32 kpc and 0.20 kpc respectively for Sd and Sdm types. We then introduce a dispersion in these R_e values using a normal distribution in logarithmic scale with an r.m.s. dispersion equal to that measured for Scd types (the most populated of the late types) in Fig. 15, and plot the resulting points in the left panel of Fig. 16 as dodger blue, brown and purple squares for Sm, Sdm and Sd types respectively, in order to differentiate them from the data points from the successful fits (shown as dots). To position these galaxies in the right panel of Fig. 16, we use the actual geometric mean h_e of the disk component provided by the bulge and disk decomposition (if the

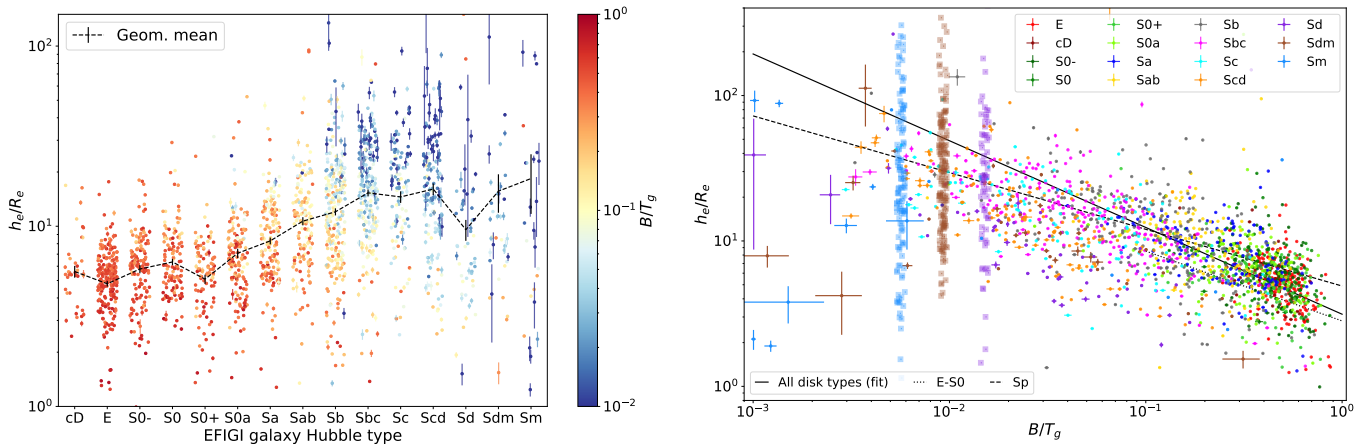

Fig. 17: Ratio between h_e the effective radius of the disk (or exponential) component and R_e the effective radius of the bulge (or Sérsic) component as a function of Hubble type (left) and B/T_g (right). The black dashed line in the left panel is the geometric mean value of this h_e/R_e ratio, and the vertical bars the estimated uncertainties on this mean (see Sect. 4.7.1 for details). Disk radii are on average 6 times larger than their bulge radii for lenticular galaxies. The size ratio increases along the Hubble sequence toward later and later spiral types, reaching ∼ 15 for Sbc, Sc and Scd types. This ratio is linked to the B/T_g luminosity bulge-to-total ratio, with higher values corresponding to relatively larger bulges, as highlighted by the linear fit (solid line, right panel). The dashed and dotted lines are the linear relations (in log-log scale) of h_e/R_e versus B/T_g derived from the two separate relations for h_e or R_e versus B/T_g obtained in Fig. 16 for Sa to Sm, and E to S0a types, respectively.

bulge fit fails for these small bulges, the disk fits are robust and the parameters can be used). For all the added Sd-Sdm-Sm and Im types in both panels of Fig. 16, an arbitrary uniform spread of ±5% in $\log B/T_g$ is used in order to visualize the density of added galaxies for each Hubble type.

We emphasize that if the E to S0a types and spiral samples in Fig. 16 are fitted based on a visual split according to their observed distribution, this choice is comforted by the fact that they are located in the Blue Cloud and the Red Sequence, respectively, and we showed in Quilley & de Lapparent (2022) that they exhibit marked differences in their combination of B/T_g and disk color. The intermediate location of the Sa galaxies in both panels of Fig. 16 is consistent with the fact that they populate the core of the Green Valley (the transition region between the Blue Cloud and the Red Sequence).

Moreover, in Quilley & de Lapparent (2022), we suggested that spiral galaxies increase in mass (under the effects of mergers and gas accretion) while becoming of earlier and earlier type, and that this can be quantified by the growth of their light and mass bulge-to-total ratio B/T_g, and the quenching of their disks. In this article, Fig. 16, and Eqs. 26, 27, 28, and 29 provide more information on the changes in the bulge and disk parameters in this scenario. Figs. 14 and 16 shows that the measurable range in B/T_g from the EFIGI spiral galaxies using our bulge and disk decompositions (see Sect. 3.1) is from $B/T \sim 0.002$, but with low statistics (see Sect. 4.1),[8] to $B/T \sim 0.2$, that is a factor ∼ 100. Over this B/T_g interval, the mean increase in the galaxy bulge radii R_e is a factor of $\sim 100^{0.64} = 19 \pm 6$ (derived using Eq. 26 and the dispersion around this fit), and the mean increase in their disk radii h_e is a factor of $\sim 7 \pm 2$ (calculated from the mean h_e of ∼ 2.1 kpc for Im in the right panel of Fig. 15, to 13 kpc for h_e at $B/T = 0.2$ using Eq. 28, and the dispersion around the fit in Eq. 28).

When comparing the left and right panels of Fig. 16, lenticular galaxies display different behaviors for their disks and bulges compared to spirals. The range of disk radii spanned by the S0⁻ to S0a types reaches smaller values than for early spirals, and as low as the lowest values for the latest Sm spirals (dodger blue squares). Only the irregulars (black squares) have even smaller values of h_e using single-Sérsic profiles. These small disk radii of lenticulars coincide with the low luminosity and low mass end of the Red Sequence shown to be dominated by lenticulars in Quilley & de Lapparent (2022). In contrast, the S0⁻ to S0a types span a narrower range of bulge effective radius R_e from the values for the smallest bulges of the intermediate Sc types of radii ∼ 200 pc, up to ∼ 6 kpc, which is beyond the values for the largest spiral bulges by a factor of ∼ 3. This suggests the possible existence of a direct evolutive channel from small spirals (with small bulge radii and light fraction ($B/T \sim 0.0025 - 0.05$) to small lenticulars with more prominent bulges (with $B/T_g \sim 0.25 - 0.5$). It however remains to be explained how the bulge could grow by a factor of 10 to 100. We also note that the effective radii of the Sérsic and exponential components of the E and cD galaxies populate the high radii and high B/T_g part of the full range encompassed by the lenticulars (in the right subpanels of both panels of Fig. 16), and appear in the continuity of the spiral relations for both bulges and disks.

4.7.4. Ratio of disk-to-bulge radius variation with B/T

We now examine in the left panel of Fig. 17 the ratio of the effective radii of the disk (or exponential component of E and cD types) and the bulge (or Sérsic component of the E and cD types) as a function of Hubble morphological type (with color-coding of each point according to the B/T_g luminosity ratio). Starting from the latest type, one can see again the low statistics for Sm to Sd types, because they rarely host a measurable bulge (see Sect. 4.1). For Scd to Sbc types, the geometric mean of the radii ratio and its dispersion have stable values of $< h_e/R_e > \simeq 15$ and σ_{h_e/R_e} of 0.29, 0.35 and 0.40 dex for types Sbc, Sc, and Scd respectively. The mean radii ratio steadily decreases from Sbc types all the way to S0⁺ types where it reaches $< h_e/R_e > \simeq$

[8] There are some galaxies with $B/T \sim 0.001 - 0.002$ in both panel of Fig. 16, but larger statistics are necessary to confirm them.

5, and remains at this value for all S0, E and cD galaxies. We measure an r.m.s. dispersion of σ_{h_e/R_e} between 0.19 and 0.32 dex for all types between Sbc and S0$^-$, with no noticeable trend, and a slight increase in dispersion for later-types with Sc, Scd having σ_{h_e/R_e} of 0.35 and 0.40 dex respectively. The decrease is therefore significant at a 3.7−4.0σ level between most individual subsequent types across the Sbc to S0$^+$ interval, except for the Sbc to Sb and Sab to Sa transitions at 1.7σ and 2.2σ respectively. The full shift between Sbc and S0$^+$ is significant at the 15σ level.

Comparison of the left panel of Fig. 17 with both panels of Fig. 15 shows that the decrease of h_e/R_e from Sb to S0$^+$ types results from 2 different regimes: the distribution of disk h_e is stable from types Sc to Sa (except for the already mentioned low h_e tail of Sb galaxies, likely due to dust extinction, see Sect. 4.7.2), whereas the bulge R_e increases for earlier types across this interval, and this is concomitant with the marked increase in the mean B/T_g per $NUV-r$ color-mass bin from ∼ 0.15 up to ∼ 0.45 that we detected through the Green Valley (Quilley & de Lapparent 2022). The continuing decrease in h_e/R_e into the lenticular types, namely for S0a and S0$^+$ types, is explained by the fact that the mean h_e shifts to lower values, whereas the distribution of R_e is stable (see Fig. 15). We emphasize that these marked variations of h_e/R_e for EFIGI galaxies disprove the claim by Courteau et al. (1996) that the radii ratio is independent of Hubble type. This is probably due to the low statistics of their study, combined with the large dispersion among each Hubble type that the EFIGI sample reveals.

There is moreover a strong B/T_g gradient with h_e/R_e and with Hubble type in the left panel of Fig. 17 (as seen for R_e in the left panel of Fig. 15). For any Hubble type, the larger h_e/R_e values correspond to smaller B/T_g. However, similar values of h_e/R_e can also correspond to very different values of B/T_g. Indeed, in Fig. 17, galaxies with a radius ratio of ∼ 10 may span more than a dex in B/T_g between the lenticulars and the intermediate to late spirals. This is due to the strong difference in the surface brightness between the bulges of these different morphological types, that we quantified in Sect. 4.1.

The right panel of Fig. 17 directly shows the variation of h_e/R_e with B/T_g. In log-log scale, there is a linear increase in h_e/R_e with decreasing B/T_g by ∼ 0.7 dex from B/T ∼ 0.5 to ∼ 0.01. In contrast with the variations of R_e and h_e with B/T_g separately shown in both panels of Fig. 16, the E, cD and lenticulars do not show a distinct behavior from the spiral types, and h_e/R_e shows a smoothly decreasing trend with B/T_g over ∼ 2.5 orders of magnitude and all morphological types. Therefore, despite the steeper variations of h_e and R_e with B/T_g for lenticular galaxies, their ratio h_e/R_e follows the same scaling law as the spiral galaxies, meaning that both tails of lower radii seen in the right subpanels of both panels of Fig. 16 correspond to the same objects.

Overall, the monotonous variation of the mean h_e/R_e with B/T_g indicates that the increase of the radii ratio occurs jointly with the increase in the luminosity ratio between the bulge and the disk. In other words, moving toward earlier types of the Hubble sequence, the share of flux within the bulge increases on average as its relative size compared to that of the disk (similar to the size of the whole galaxy) also increases. This testifies that on average, mass is transferred from the disk into the bulge as galaxies evolve backward along the Hubble sequence, therefore increasing the bulge radius, even when the disk radius remains constant, as it is the case for early type spirals (see left and right panel of Fig. 15). Of course, this average scenario does not exclude more complex paths of individual galaxies as they evolve from star-forming to quiescent.

We show in the right panel of Fig. 17 as a black solid line the ODR linear fit of h_e/R_e versus B/T_g for all types from E to Sm:

$$\log \frac{h_e}{R_e} = -0.597^{\pm 0.013} \log B/T + 0.496^{\pm 0.010} \quad (30)$$

We add in this graph the indicative position of the late spirals types Sd-Sdm-Sm (plotted in Fig. 16), by using for h_e/R_e the mere ratio of the true h_e values by the indicative R_e values, as a function of the interpolated values of B/T_g for these types (see Sect. 4.7.3). These added late spirals, as well as earlier spirals of Sbc-Sc-Scd types suggest a possible curving down of h_e/R_e below the linear fit at low B/T_g, but more statistics are required to clarify this issue.

We also show as dashed and dotted lines in the right panel of Fig. 17 the relation of h_e/R_e versus B/T_g calculated as the ratio of the linear relations of h_e versus B/T_g (Eqs. 28 and 29), and R_e versus B/T_g (Eqs. 26 and 27) for spirals and for S0 and E galaxies respectively. This allows us to test whether the disk-to-bulge size ratios deducted from the size versus B/T_g relation for each component are consistent with the observed ones. It appears that for, on one hand the E, cD and S0 types, and on the other hand the spiral types, both ratios of the linear relations (dotted and dashed lines) would yield an acceptable variation with B/T_g, the picture is more complex for E, cD and S0 : despite the large dispersion in both h_e and R_e and a strong covariance between R_e and h_e, there is a much smaller dispersion in h_e/R_e compared to those in the individual radii for these types. As a result, when assigning a bulge and disk effective radii to lenticular galaxies for a given B/T_g value, small bulges should be matched with small disks and large bulges with large disks. We therefore advise to use only one among the bulge and disk versus B/T_g relations (Eqs. 27 and 29) and complement it with the h_e/R_e vs B/T_g relation, rather than using both size versus B/T_g relations separately, in order to generate physically meaningful bulge and disk sizes for the lenticular galaxies.

5. Discussion

5.1. Galaxies evolve both in mass and size

In Quilley & de Lapparent (2022), we showed that the Hubble sequence was an inverse evolutionary sequence, with all its types spanning continuously the color-mass diagram. Three consecutive phases of evolution were identified: (i) 3 orders of magnitude in luminosity and mass growth through mergers and consumption of the gas reservoir from irregulars to Sb spirals forming the Blue Cloud; (ii) star formation fading between Sab early spirals and lenticulars along with a marked growth by a factor of 2 in bulge-to-total ratio (B/T), with Sa and S0a types populating the Green Valley; (iii) another mass growth by 1 order of magnitude between the faintest lenticulars and the most massive ellipticals (a factor of ∼ 4 above the upper mass limit of spirals).

In the current analysis, we show that these three evolution phases along the Hubble sequence not only determine the luminosity and stellar mass growth of galaxies along the Hubble sequence, but also their growth in size. This is a consequence of the size-luminosity scaling relations for bulges and disks measured in the present analysis. Fig. 15 in Sect. 4.7 indicates that the above three evolution phases can be matched to the three following regimes of bulge and disk size variations: (i) a 0.45 dex increase in the mean effective radius of the disks h_e from late-type (Sm) to intermediate-type (Sc) spirals; (ii) a stable mean disk h_e of ∼ 8 kpc from intermediate (Sc) to early (Sa) spirals, whereas the mean bulge effective radius R_e doubles from

$\sim$ 0.6 kpc for Sb types to $\sim$ 1.2 kpc for Sa types, which corresponds to the entry into the Green Valley; (iii) a smaller mean disk h_e of lenticular galaxies (S0a to S0$^+$) in the interval $6-7$ kpc, whereas the mean bulge R_e remain stable in the $1-1.5$ kpc range, and ultimately, reaches 2.3 kpc and 4.2 kpc for the Sérsic components of E and cD types, respectively. The mean effective radii for the E and cD galaxies fitted as single Sérsic profiles (or equivalently the h_e of the exponential component) reach 10 and 30 kpc respectively (see Fig. 15), making these two types the largest among the Hubble sequence, in the same way that they are the most luminous and massive. This is consistent with them being built in part by major mergers of the lenticular and spiral galaxies.

5.2. Different types of bulges: Pseudo and classical

Pseudo-bulges are central concentration of stars built through secular evolution processes within the disk plane, whereas classical bulges are spheroids built by violent relaxation in mergers (Kormendy & Kennicutt 2004). In order to properly distinguish between these two classes, one would need to know for each bulge its formation scenario, which could be deciphered observationally from the bulge stellar kinematics. In an attempt to have available a quantitative criterion for differentiating among bulge types based on their photometric properties, two criteria have been widely used, which are improperly identified with the physical definition of pseudo and classical bulges. Kormendy & Kennicutt (2004) and Fisher & Drory (2008) first proposed to use the Sérsic index $n_{\rm Sérsic}$ of the bulge as a criterion, with a transition value of $n_{\rm Sérsic} = 2$, pseudo-bulges and classical bulges having lower and higher indexes respectively. However, the Sérsic index is the parameter of the model-fitting showing the largest uncertainties, which can hinder the reliability of this criterion. In addition, we emphasize that Fisher & Drory (2008) use HST-ACS high-resolution imaging to label bulges as either pseudo or classical based on the presence or absence of morphological features within the images (nuclear ring, spiral or bar) respectively, and then show that the value of the Sérsic index correlates with this labeling. There is however no evidence in their analysis that bulges labeled as classical or pseudo went through the related formation processes, or have the corresponding dynamical signatures. Later on, Gadotti (2009) suggested that bulges following the Kormendy relation for ellipticals are likely to have a similar structure, hence to be classical bulges. The author therefore proposed to use the Kormendy relation as a criterion to differentiate classical bulges from pseudo-bulges, the latter being outliers of this relation, with larger values of $\langle\mu\rangle_e$, that is fainter surface brightnesses, than what the relation predicts based on their R_e. Some of these effects are also detected in EFIGI galaxies and are presented below.

In Quilley & de Lapparent (2022), we identified the bulge growth through the Green Valley and demonstrated that it was concomitant to a change toward steeper light profiles of the bulges, which could correspond to the transition from pseudo to classical bulges. Indeed, Figs. 20 and 26 of Quilley & de Lapparent (2022) show that the EFIGI color-mass bins with $n_{\rm Sérsic} \gtrsim 2$ are mainly populated by Sb types, compared to Sbc and Sc types for the bins with $n_{\rm Sérsic} \lesssim 2$. That analysis also revealed how EFIGI galaxies display a continuous variation in their bulge Sérsic index along the Hubble morphological sequence within the $NUV - r$ color versus stellar mass diagram. This is in agreement with the present result that the $n_{\rm Sérsic} \gtrsim 2$ bulges follow the Kormendy relation for ellipticals, whereas the $n_{\rm Sérsic} \lesssim 2$ bulges deviate from it, and this departure from the Kormendy relation for elliptical galaxies starts between Sb and Sbc types (see Sect. 4.1 and Figs. 3 and 4). As the latter morphological types deviate more from the relation, we conclude that they are the types more likely to be dominated by pseudo-bulges. Therefore, we confirm that both criteria of Fisher & Drory (2008) and Gadotti (2009) agree between each other for characterizing bulges when applied to the EFIGI sample. As both the departure from the Kormendy relation, and the $n_{\rm Sérsic} = 2$ transition occur at $B/T \sim 0.1$, our analysis highlights the additional morphological information that the small B/T bulges of late spiral type galaxies are predominantly pseudo-bulges, whereas the larger B/T bulges of early spirals and lenticulars tend to be classical bulges.

We have therefore identified three parameters that can be used to characterize the nature of bulges: Sérsic index, distance from the Kormendy relation for ellipticals, and the bulge-to-total ratio B/T (characterizing the whole galaxy). As the three parameters vary simultaneously in a plane within the 3D $\langle\mu_e\rangle$-M-R_e space (see Figs. 4, 7 and 9), they could a priori be used in isolation. Using them jointly could be a way to check the reliability of the bulge modeling, by allowing to spot cases in which one of these parameters has an inconsistent value with the others.

Taken altogether, these elements paint a picture of continuous bulge evolution from small, faint and low contrast central disk concentrations toward prominent spheroids with steeper profiles, rather than a dichotomy between two separate classes of objects (pseudo-bulges and classical bulges). By analyzing spatially resolved star formation histories (based on population spectral synthesis models) of the bulges and disks of 135 late-type spirals from the CALIFA survey, Breda & Papaderos (2022) reach the same conclusion that the two types of bulges are extremities of a continuous sequence rather than clearly distinguishable classes. This is further confirmed by kinematical studies such as those by Méndez-Abreu et al. (2014) and Erwin et al. (2015). The two teams investigated the stellar dynamics inside the bulges of 10 face-on barred galaxies (5 spirals and 5 lenticulars) and 9 S0-Sb galaxies, respectively. For 7 out of 10 galaxies studied by Méndez-Abreu et al. (2014), and for all 9 objects from Erwin et al. (2015), the authors found that a disky pseudo-bulge and a classical one were actually coexisting, with one galaxy in each sample showing evidence for an additional boxy-peanut component to its bulge. These studies therefore indicate that bulges are often composite systems, so that the continuous transition in Sérsic index and deviation from the Kormendy relation that we detect for EFIGI galaxies can be interpreted as a predominance of either one of the possible central components: a rotation-supported accumulation of stars from the thick and old disk at its center (Di Matteo et al. 2019), a steep profile and dispersion-supported spheroid build by mergers.

In the next subsection (Sect. 5.3.2), we propose an empirical magnitude interval, as well as a corresponding B/T interval, in which the bulges may transition between pseudo to classical structure.

5.3. Spatial density of bulges and disks

5.3.1. Larger ellipticals are more diffuse

The Kormendy and size-luminosity relations of Eq. 13 and 16, based on the single Sérsic modeling of elliptical galaxies, can be interpreted in terms of their stellar density. If elliptical galaxies were spatially scale-invariant (that is all had the same 3D

density profile, only scaled by their spatial effective radius[9], denoted $\mathcal{R}_e$), their flux would grow as ${\mathcal{R}_e}^3$. Young (1976) showed that an angular $r^{1/4}$ profile in projection on the sky (i.e. , a Sérsic profile with $n = 4$) can be deprojected into a function that is indistinguishable from a 3D $r^{1/4}$ profile (except in the very central region), and he measured $\mathcal{R}_e = 1.350 R_e$ (see their Eq. 17). As a result, the variation of the absolute flux with ${\mathcal{R}_e}^3$ can be written as a variation in ${R_e}^3$ (the physical effective radius derived from the sky projected profile, used in the present analysis), which yields, in terms of the absolute magnitude:

$$M \simeq -2.5 \log {R_e}^3 + \kappa' \tag{31}$$

with κ' a constant. This equation can be applied to elliptical galaxies as they can be well fitted by a Sérsic profile with an index $n_{\rm Sérsic}$ index varying from 3.5 to 7, with a peak at $n_{\rm Sérsic} \simeq 5.5$. Although ellipticals tend to be oblate (Costantin et al. 2018), and this should also be taken into account when deprojecting their profile, we assume in the following that Eq. 31 remains valid in the case of scale-invariant elliptical galaxies.

The size-luminosity relation for EFIGI ellipticals obtained in Eq. 16 (see Sect. 4.2 and left panel of Fig. 6) can be rewritten as

$$M \simeq -2.5 \log {R_e}^{1.09} + \kappa'' \tag{32}$$

with κ'' a constant. We interpret the difference between Eqs. 31 and 32 as an indication that E galaxies get more diffuse as they grow in size, with a dilution factor of ${R_e}^{-1.91}$. This remains valid using the scaling relations for the Sérsic component of E galaxies (Eq. 15): the R_e exponent in Eq. 32 becomes 1.43 and the dilution factor decreases to ${R_e}^{-1.57}$. Given that that their magnitude is tightly anticorrelated to the stellar mass (see Quilley & de Lapparent 2022), we further suggest that these estimated dilution factors may also be valid for the stellar mass.

5.3.2. Spatial densities of pseudo and classical bulges

We perform for bulges of lenticular and spiral galaxies a derivation similar to that for ellipticals (in Sect. 5.3.1). Let us denote α the slope of a linear approximation of the size-luminosity relation

$$\log R_e = \alpha M + \lambda \tag{33}$$

where λ is a constant. It can be rewritten as

$$M \simeq -2.5 \log {R_e}^{\beta} + \kappa''' \quad \text{with} \, \beta = -\frac{1}{2.5\alpha} \tag{34}$$

and κ''' a constant, so that β measures the scaling of the luminosity L with the effective radius.

$$L \propto {R_e}^{\beta} \tag{35}$$

If we define the volume density ρ of the bulges, and their surface density Σ, depending on whether they can be considered as spheroidal or disky (as can be the case for pseudo-bulges Athanassoula 2005, 2008), we can write

$$\begin{aligned} L \propto \rho\, {R_e}^3 \Rightarrow \rho \propto {R_e}^{\beta-3} \\ L \propto \Sigma\, {R_e}^2 \Rightarrow \Sigma \propto {R_e}^{\beta-2} \end{aligned} \tag{36}$$

[9] Or more generally semi-major axis of the isophote enclosing half of the total light.

We emphasize again that, because luminosity is tightly correlated with stellar mass (Quilley & de Lapparent 2022), the following remarks remain valid for the stellar mass and stellar mass density within galaxies. Within the low redshift approximation used to derive Eq. 12, the surface brightness (defined in Eq. 8) also provides directly the physical surface density of the considered galaxy perpendicular to the line-of-sight, which is, in the case of a weakly inclined disk, close to its surface density Σ. We note that the values of $\beta = 2$ and $\beta = 3$ are critical as they correspond to fixed surface density and fixed volume density respectively.

The second degree polynomial size-luminosity relation of Eq. 20 (see Fig. 7) lies mostly between both linear relations of Binggeli et al. (1984), with α varying from −0.1 to −0.3 from late to early Hubble types (and from small to large B/T values). We therefore compute the tangents to this polynomial curve at key values of β and α, and derive the corresponding values of $M_{{\rm bulge},g}$:

$$\begin{aligned} &\beta = 4.0 \text{ for } \alpha = -0.10 \text{ at } M_{{\rm bulge},g} = -17.1 \\ &\beta = 3.0 \text{ for } \alpha = -0.13 \text{ at } M_{{\rm bulge},g} = -17.8 \\ &\beta = 2.0 \text{ for } \alpha = -0.20 \text{ at } M_{{\rm bulge},g} = -19.1 \\ &\beta = 1.3 \text{ for } \alpha = -0.30 \text{ at } M_{{\rm bulge},g} = -21.2 \end{aligned} \tag{37}$$

In the following, we make the correspondence between each of the above magnitudes and a B/T value (justified by the fact that B/T varies continuously along the size-luminosity relation shown in Fig. 7): we compute the geometric mean of B/T for galaxies whose bulge magnitude $M_{{\rm bulge},g}$ is within 0.05 mag of the values listed in Eq. 37.

Along our proposed evolutionary path of the joint B/T, R_e and h_e growth, as galaxies move backwards the Hubble sequence, the value of β in Eq. 37 allows one to track how the densities of the bulges of spirals and lenticulars scale with effective radius R_e. Bulges with $M_{{\rm bulge},g} > -17.8$ (hence $B/T \lesssim 0.08$), have the highest values $\beta > 3$, so spheroids would have their volume density still growing with the radius, and disky systems would see their surface density increase faster than R_e. Brighter bulges in the range $-19.1 < M_{{\rm bulge},g} < -17.8$ (and $0.08 \lesssim B/T \lesssim 0.15$) become more diffuse in volume density as they grow in R_e, with a dilution factor $\leq R_e$, as β decreases from 3 to 2. In contrast, a disky bulge in that magnitude interval would still have an increasing surface density as it grows in radius, but with an exponent lower than 1 in R_e. As galaxies continue to evolve by growing their bulges to $B/T \gtrsim 0.15$ and $M_{{\rm bulge},g} \lesssim -19.1$, they reach $\beta < 2$, meaning that both spheroidal and disky systems would see their volume density and surface density, respectively, decrease as they grow in radius. The brightest of these bulges, with $M_{{\rm bulge},g} \lesssim -19.1$, hence $\beta \leq 1.3$, become diffuse faster for larger R_e, nearly reaching the strong dilution factor of the ellipticals (Eq. 32).

We can relate these trends in the variations of the density of bulges to the distinction between classical and pseudo bulges, which, as discussed in Sect. 5.2, has not yet been defined unequivocally from galaxy photometric properties. Given that the EFIGI disk galaxies analyzed here are weakly inclined, Eq. 36 indicates that a disk-like system such as a pseudo-bulge (discarding the more complex boxy-peanut bulges), would have a surface density Σ that would increase with radius, as it would scale as ${h_e}^{\beta-2}$ with $\beta \geq 3$ for $M_{{\rm bulge},g} > -17.8$. This would imply that the central accumulation of stars that they harbor within the disk would not only extend in radius, but strongly increase its surface brightness, and equivalently its surface density.

In contrast, classical bulges, with the brightest $M_{\mathrm{bulge},g}$ and highest B/T, would correspond to the $M_{\mathrm{bulge},g} \lesssim -19.1$ interval, for which both the volume and surface density decrease with radius. As classical bulges are thought to be spheroidal systems, only the volume density decrease is relevant here. Classical bulges are therefore expected to show a similar behavior as ellipticals, becoming more diffuse as they grow in size. Violent relaxation in these massive systems may be responsible for their puffing up with increasing size.

In the intermediate interval $-19.1 < M_{\mathrm{bulge},g} < -17.8$ (and also $0.08 \lesssim B/T \lesssim 0.15$), in which the surface density still increases but the volume density decreases as bulges grow, both behaviors could be accounted for, whether the bulge is disky or spheroidal: the surface density would be nearly constant up to an increase as R_e, or the volume density would be nearly constant up to a decrease as $1/R_e$. We therefore propose that the $-19.1 < M_{\mathrm{bulge},g} < -17.8$ magnitude range corresponds to the transition region between classical and pseudo-bulges. The associated $0.08 < B/T < 0.15$ interval is in agreement with the transition near $B/T \sim 0.1$ discussed in Sect. 5.2 (see also Fig. 4).

5.3.3. Surface density of disks of lenticulars and spirals

We also interpret the size-luminosity relation for disks in terms of density using the formalism introduced in Sect. 5.3.2. Fig. 11 shows that the small disks of the late-type spirals grow on average as $\log h_e \simeq -0.140 M_{\mathrm{disk},g}$ (see Eq. 23), which corresponds to $\beta = 2.9$ (see Eq. 34). Therefore, for a weakly inclined disk, Eq. 36 implies that the surface density Σ (and the surface brightness μ_0) increases as ${h_e}^{0.9}$. This behavior is analogous to that for the pseudo-bulges (in Sect. 5.3.2), that are also disky structures. For early disks, we fit in Fig. 11 $\log h_e \simeq -0.208 M_{\mathrm{disk},g}$ (see Eq. 22), yielding $\beta = 1.92$. This means that the total disk flux almost grows with disk effective radius as ${h_e}^2$, that is at a nearly constant disk luminosity surface density (Eq. 36), as well as a nearly constant central (or effective) surface brightness μ_0 (or μ_e), as already mentioned in Sect. 4.5.

Consequently, as disk galaxies merge, their disks first grow both in size and surface density: light and matter are redistributed across the disk during the mergers of either irregular or very late spirals, as expected for major mergers. Then, for the larger disks of early spirals and lenticulars resulting from mergers of the late spirals, the size growth occurs at nearly constant surface density, maybe under the effects of flybys or minor mergers. As mentioned in Quilley & de Lapparent (2022), the spiral arms and bars may play a role in this evolution.

5.4. Multiband scaling relations for mock images

In Figs. 7 and 11, we have shown linear and polynomial fits for the size-luminosity relations of galaxy bulges and disks. These fits may play a key role in building realistic mock images as they allow one to deduct a size from a luminosity. Current softwares creating galaxy images such as Stuff (Bertin 2009) use size-luminosity relations from Binggeli et al. (1984) for spheroids and de Jong & Lacey (2000) for disks. These previous works have been very useful but remain limited by their sample size or the quality of the available data at that time. For instance, Binggeli et al. (1984) uses data collected with photometric plates that suffer from nonlinear effects. Updating the size-luminosity relation thus appears as a key lever of action to improve the generation of mock images.

We provide in Table 1 the parameters of the size-luminosity relations obtained for the bulges and disks of various morphological types or type groupings of the EFIGI sample, in the g and i bands, for cD, E, dE and Im galaxies modeled as a single Sérsic profile (see Sect. 3.1), and for the bulges (or Sérsic components) and the disks (or exponential components) of all types from E to Sm modeled as the sum of a Sérsic profile and an exponential one (see Sect. 3). The relations in the g band are those obtained and commented throughout the article, those in the i band are presented here for the first time. All these fits are polynomial, either linear or of second degree, and were obtained using the ODR package (Sect. 3.6), after correcting for the systematic trend in the relative error in the disk effective radii (Sect. 3.5). All values are given along with their associated uncertainty.

We also calculated and provide in Table 1 for each fit its residuals defined as the difference between the actual $\log R_e$ or $\log h_e$ values and the ones predicted from the polynomial fit using the absolute magnitude values $M_{\mathrm{bulge},g}$ or $M_{\mathrm{disk},g}$ for the considered subsample. If, when binning the residuals in magnitude intervals (see for example Fig. 8 in Sect. 4.2, and Fig. 12 in Sect. 4.5), we noticed a systematic variation in the r.m.s. deviation of these residuals, we fitted it with a polynomial of degree 1 or 2, and list the corresponding coefficients in the columns labeled "1st order" and when appropriate "2nd order" of Table 1 under "Dispersion in residual". Otherwise, we list in column labeled "0th order" the r.m.s. deviation over the entire absolute magnitude interval of the size-magnitude relation. The residual from the scaling relations that were fitted by a Gaussian are labeled in Table 1, and the parameters can be retrieved in the text in the mentioned sections.

Table 1 shows that the size-luminosity relations in the g and i band have similar slopes within the error bars (for linear relations), as well as similar second degree coefficients, except for the second degree fit for the disks (or exponential components) of all Hubble types. In contrast, the zero-points of linear relations show expected shifts between the two bands, on the order of a few σ, similarly to the shifts of the μ_0 versus $\log h$ relation among the g, r, and i filters (see Sect. 4.5). The various coefficients of the dispersion in the residuals listed in Table 1 are also mostly within 1σ between the two bands.

As far a generating mock distributions of nearby galaxies is concerned, the ideal way to proceed would be to know the quadri-variate luminosity functions (in the observing band) of galaxies as a function of absolute luminosity and physical effective radii for both the bulges (or Sérsic component) and the disks (or exponential component). These would then implicitly include the size-magnitude relations of both components, as well as the luminosity functions of the bulges and disks (or both components) of the various morphological types. In the following, we only mention bulge and disk, but every statement also applies for the Sérsic or exponential components of E and Im types.

In the absence of this quadri-variate luminosity function, one should use the luminosity function of galaxies of the various morphological types to draw the total luminosity distributions of these galaxies. Then using a probability distribution function (PDF) of B/T (or an average value and a dispersion around it) for each morphological type would provide pairs of bulge and disk luminosities for each generated galaxy, and then yield effective radii using the respective size-magnitude relations for bulge and disks (and the dispersion in their residuals). Because the luminosity functions per morphological types are not yet known even for nearby galaxies, one could instead use the luminosity function of galaxies over all galaxy types. In that case it would be crucial to use a realistic PDF of B/T over the whole magnitude

Type	Component	Band	Size-magnitude relation Polynomial fit[(a)]			Dispersion in residual Polynomial fit[(b)]		
			2nd order	1st order	0th order	2nd order	1st order	0th order
cD	Single-Sérsic	g	-	$-0.28^{\pm0.05}$	$-1.79^{\pm1.03}$	-	-	$0.18^{\pm0.03}$
		i	-	$-0.28^{\pm0.04}$	$-2.06^{\pm0.93}$	-	-	$0.18^{\pm0.03}$
dE	Single-Sérsic	g	-	$-0.20^{\pm0.03}$	$-0.32^{\pm0.49}$	-	-	$0.24^{\pm0.03}$
		i	-	$-0.19^{\pm0.03}$	$-0.15^{\pm0.48}$	-	-	$0.23^{\pm0.03}$
E	Single-Sérsic	g	-	$-0.37^{\pm0.04}$	$-3.95^{\pm0.37}$	-	-	[(c)]$0.24^{\pm0.02}$
			$0.062^{\pm0.010}$	$2.27^{\pm0.42}$	$24.09^{\pm4.46}$	-	-	$0.21^{\pm0.02}$
		i	-	$-0.32^{\pm0.02}$	$-3.16^{\pm0.46}$	-	-	$0.23^{\pm0.02}$
			$0.053^{\pm0.012}$	$2.04^{\pm0.53}$	$23.02^{\pm5.85}$	-	-	$0.22^{\pm0.02}$
E	Sérsic	g	-	$-0.28^{\pm0.01}$	$-2.46^{\pm0.24}$	-	-	$0.15^{\pm0.01}$
		i	-	$-0.24^{\pm0.02}$	$-1.91^{\pm0.34}$	-	-	$0.14^{\pm0.01}$
E to Sm	Sérsic or bulge	g	$0.025^{\pm0.001}$	$0.76^{\pm0.05}$	$8.25^{\pm0.50}$	-	[(d)]$0.027^{\pm0.003}$	[(d)]$0.76^{\pm0.06}$
		i	$0.026^{\pm0.001}$	$0.83^{\pm0.05}$	$9.35^{\pm0.52}$	-	[(d)]$0.039^{\pm0.002}$	[(d)]$1.03^{\pm0.05}$
E and cD	Exponential	g	-	$-0.249^{\pm0.012}$	$-1.12^{\pm0.27}$	-	-	$0.18^{\pm0.01}$
		i	-	$-0.243^{\pm0.011}$	$-1.26^{\pm0.26}$	-	-	$0.18^{\pm0.01}$
S0$^-$ to Scd	Disk	g	-	$-0.208^{\pm0.004}$	$-0.43^{\pm0.08}$	-	-	$0.175^{\pm0.004}$
		i	-	$-0.214^{\pm0.004}$	$-0.73^{\pm0.09}$	-	-	$0.170^{\pm0.004}$
Sd to Im	Disk	g	-	$-0.140^{\pm0.007}$	$0.98^{\pm0.14}$	-	$0.019^{\pm0.009}$	$0.59^{\pm0.16}$
		i	-	$-0.151^{\pm0.007}$	$0.71^{\pm0.15}$	-	$0.018^{\pm0.010}$	$0.58^{\pm0.18}$
E to Im	Exponential, disk or single-Sérsic	g	$0.020^{\pm0.002}$	$0.63^{\pm0.08}$	$8.29^{\pm0.81}$	[(d)]$0.0043^{\pm0.0013}$	[(d)]$0.18^{\pm0.05}$	[(d)]$2.17^{\pm0.45}$
		i	$0.032^{\pm0.002}$	$1.17^{\pm0.09}$	$14.34^{\pm0.91}$	[(d)]$0.013^{\pm0.001}$	[(d)]$0.55^{\pm0.06}$	[(d)]$6.04^{\pm0.57}$

Table 1: Coefficients and associated uncertainties of the polynomial fits to the size-magnitude relations for the various components of the single profile fits or bulge and disk decompositions for different EFIGI morphological subsamples, and dispersion in the residuals from these fits.

Notes:
(a) Coefficients of the polynomials obtained by ODR fitting of the profile effective radius (in log) versus magnitude, for a sample of EFIGI galaxies defined by their morphological types, in the listed band. Bulge (or Sérsic) and disk (or exponential) refer to the corresponding component in the bulge and disk decomposition. When indicated, E, cD, dE and Im galaxies are modeled as single Sérsic profiles (see Sect. 3.1).
(b) Coefficients of the polynomials providing the r.m.s. dispersion (in dex) around the size-magnitude relation fit.
(c) The center and χ^2 of the Gaussian fit to the residuals of the elliptical size-luminosity relation appear in the descriptive text in Sect. 4.2.
(d) The Gaussian fits to the residuals of the bulge and disk 2nd degree polynomial size-luminosity relations are shown in the right panels of Figs. 8 and 12, respectively, and their centers and χ^2 values appear in the descriptive texts in Sect. 4.3 and 4.5, respectively.

range, as this will carry the information about the fractions of galaxies in the various morphological types. The B/T PDF cannot be derived from the EFIGI sample as this sample with visual morphology was designed to have several hundreds of galaxies of each Hubble type, being therefore non representative of a complete magnitude limited sample of the nearby Universe. We intend to measure this B/T PDF using the MorCat magnitude-limited survey of nearby galaxies, of which EFIGI is a subsample (in Quilley & de Lapparent, *in prep.*). On the contrary, the fact that all morphological types are nearly equally densely populated in EFIGI implies that the size-magnitude scaling relations can be considered as reliable for generating mock catalogs (if one excludes systematic deviations caused by some subpopulations of objects within some Hubble type). The larger MorCat sample that contains about ~ 4 times more galaxies than EFIGI may however improve the statistics of the size-magnitude relations.

We also provide in Table 2 the relations between the B/T of EFIGI galaxies and the effective radii of their bulges and disks, as well as their ratio, as derived in Sect. 4.7, for the lenticular and spiral types in the g and i bands. The relations in the g band are those obtained and commented throughout the article, those in the i band are presented here for the first time. All these fits are polynomial, either linear or of second degree, and were obtained with the ODR package (Sect. 3.6), after correcting for the systematic trend in the relative error in the disk effective radii with radii (Sect. 3.5). We list in column labeled "Dispersion in residual" of Table 2 the r.m.s. deviation of the residuals from the corresponding size-B/T relation. All values are given along with their associated uncertainty. For Sa to Sm disks, these residuals were fitted by a Gaussian (labeled as *(b)*) and the parameters can be retrieved in the text in the mentioned sections.

These derived relations between the B/T of galaxies and h_e, R_e, or their ratio h_e/R_e, could also be used to generate mock distributions. Using the galaxy total luminosity function of galaxies as well as a realistic distribution function of B/T would here be necessary. As we pointed out in Sect. 4.7.4, the behavior of the size versus B/T relation for lenticular galaxies is such that generating separately a bulge and a disk can easily lead to nonphysical radii ratio, as ~ 1 dex of both h_e and R_e is spanned across the same B/T interval, but small bulge radii actually match small disk radii, and vice versa. For all galaxy types, we therefore advise to generate one of the two radii R_e or h_e using the scaling relations and their dispersion listed in Table 2, and then to generate a ratio using the corresponding scaling relation and its dispersion in order to derive the other radius, so as to circumvent the issue of unrealistic combinations of bulges and disks. It should however be checked by deriving bulge and disk absolute magnitudes from each value of B/T, that the R_e and h_e yield size-magnitude relations that are consistent with those in Eqs. 20 and 25 for bulges and disks, respectively, of lenticular and spiral galaxies (and for Sérsic or exponential components of E and Im types).

Type	Component	Band	Effective radius versus B/T Linear fit[(a)] Slope	Intercept	Dispersion in residual
E to S0a	Sérsic or bulge	g	$3.17^{\pm0.17}$	$4.34^{\pm0.06}$	$0.55^{\pm0.02}$
		i	$3.58^{\pm0.20}$	$4.48^{\pm0.07}$	$0.58^{\pm0.02}$
	Exponential or disk	g	$2.69^{\pm0.13}$	$4.79^{\pm0.04}$	$0.59^{\pm0.02}$
		i	$2.41^{\pm0.11}$	$4.70^{\pm0.03}$	$0.48^{\pm0.02}$
Sa to Sm[(b)]	Bulge	g	$0.61^{\pm0.02}$	$3.57^{\pm0.02}$	$0.31^{\pm0.01}$
		i	$0.67^{\pm0.02}$	$3.57^{\pm0.02}$	$0.30^{\pm0.01}$
	Disk	g	$0.22^{\pm0.01}$	$4.27^{\pm0.02}$	$0.220^{\pm0.007}$
		i	$0.26^{\pm0.01}$	$4.25^{\pm0.02}$	$0.218^{\pm0.007}$
E to Sm	Exponential-to-Sérsic or disk-to-bulge ratio[(c)]	g	$-0.60^{\pm0.01}$	$0.50^{\pm0.01}$	$0.291^{\pm0.008}$
		i	$-0.62^{\pm0.02}$	$0.47^{\pm0.01}$	$0.338^{\pm0.008}$

Table 2: Coefficients and associated uncertainties of the polynomial fits to the effective radii of both components of the profile decompositions in the g and i bands for different EFIGI morphological subsamples, versus the bulge-to-total light ratio B/T in the corresponding band, and dispersion in the residuals from these fits.

Notes:
(a) Coefficients of the linear polynomials obtained by ODR fitting of the profile effective radius (in log) versus B/T (in log), for a sample of EFIGI galaxies defined by their morphological type, in the listed band. Bulge (or Sérsic) and disk (or exponential) refer to the corresponding component in the bulge and disk decomposition.
(b) The center and χ^2 of the Gaussian fits to the residuals of the bulge and disk effective radius versus B/T relations appear in the descriptive text in Sect. 4.7.3.
(c) Coefficients of the linear fits to the effective radii ratio of the exponential to Sérsic components for E types, and the disk to bulge components for all lenticular and spiral types.

At last, we make a comparison of h_e/R_e with the values obtained from Stuff (Bertin 2009) using the default configuration file, which uses the size-luminosity relations from Binggeli et al. (1984) not only for ellipticals, but also for bulges of lenticulars and spirals. Stuff therefore applies for bright bulges the size-luminosity relation for E galaxies, and that for dE galaxies for intermediate and faint bulges, which are shown in the right panel of Fig. 7 (Sect. 4.3) to overestimate the bulge radii by factors of $\sim 2-3$. Stuff also uses for all bulge and disk galaxy types the bivariate luminosity function derived for disks of Sb to Sdm types by de Jong & Lacey (2000), which we showed in Fig. 13 and Sect. 4.5 to underestimate the frequency of large disk radii for Sb-Sdm and Sm-Im types at disk magnitudes $M_{i,\rm disk} \geq -20.5$, whereas this function overestimates the frequency of large disks for S0 to Sab types. Among the generated lists of synthetic Stuff galaxies, those with $0.05 \leq B/T_g \leq 0.6$ have $h_e/R_e \simeq 0.5-6$, whereas we measure $h_e/R_e \simeq 5-50$ in the right panel of Fig. 17 for EFIGI galaxies within this B/T_g interval. Also, synthetic Stuff galaxies with $0.6 \leq B/T_g \leq 1$ have $h_e/R_e \simeq 0.2-2.5$, compared to $h_e/R_e \simeq 2-8$ (Fig. 17). EFIGI galaxies therefore appear ~ 1 order of magnitude larger in their disk-to-bulge effective radius ratio than those generated by Stuff. Moreover, the bivariate luminosity function of disks is modeled in the i_C Cousins band by de Jong & Lacey (2000), whereas the reference passband in the default Stuff configuration is Couch B_J, which may contribute to the unrealistic values of h_e/R_e in the default Stuff setup (see Fig. 13 and Sect. 4.5 for a comparison with EFIGI).

We emphasize that using for the bulge and disk scaling relations that originate from different studies based on different data and methodologies is likely to lead to discrepancies. To generate realistic galaxies as the sum of a disk and a bulge, consistent relations between these two components are needed, which require that bulges and disks of the same sample of galaxies are actually measured and consistently matched together. This is what we perform here with the EFIGI sample.

6. Conclusions

In this article, we examine the relations between size, luminosity, and surface brightness for the bulges and disks of the 3106 weakly inclined nearby galaxies from the EFIGI morphological catalog. By controlled profile modeling with the SourceXtractor++ software, we performed bulge and disk decomposition of SDSS images simultaneously in the g, r, and i bands to obtain the aforementioned parameters, using a Sérsic and an exponential profile for the bulge and disk, respectively, for all types from E and cD to Sm. We also modeled E, cD, dE, and irregular (Im) galaxies as single Sérsic profiles, with the Im being best fitted by nearly exponential profiles (see Sect. 3.1).

All linear or higher order polynomial fits to the derived relations take uncertainties on both axes into account, using the total least square method available in the Orthogonal Distance Regression *Python* package (see Sect. 3.6). The quality of the fits also benefits from eliminating the overall systematic decrease in the relative uncertainties of the disk radii, caused by the survey selection effects in angular diameter versus distance for the sample galaxies.

We first remeasured the relation between the mean effective surface brightness and the effective radius of E galaxies that was found by Kormendy (1977), as well as those between the effective radius and the absolute magnitude established by Binggeli et al. (1984) for E and dE galaxies, by modeling both types as single Sérsic profiles. With the improved statistics and profile modeling provided by the EFIGI sample, we obtained the linear fits of Eqs. 13, 16 and 18. In the present analysis, we also adopted the nonconventional approach of applying the bulge and disk decompositions to E and cD types, as kinematic studies of ellipticals have shown evidence for stellar disk components, and a two-component profile allows one to model both the steep central light concentrations and large envelopes of cD galaxies. The Sérsic and exponential components of E types can then be considered together with the bulges and disks, respectively, in both scaling relations.

Regarding the relation between the surface brightness and the logarithm of the effective radius, we show that the slope of the linear Kormendy (1977) relation for E types is also valid for the Sérsic components of E types as well as for bulges of $S0^-$ to Sb types. In contrast, there is a gradual departure from the relation toward the fainter and smaller bulges of later spiral types, which also have smaller bulge-to-total ratios (B/T) and Sérsic indices (Fig. 3).

Regarding the relation between the logarithm of the effective radius and magnitude, the so-called size-luminosity relation (always considered in a log-log plane), we measured a steeper relation than that obtained by Binggeli et al. (1984) for E galaxies when using single-Sérsic profiles, and show that a second degree polynomial provides a better size estimation for both the faint and bright ends of the elliptical population. Flatter size-luminosity relations than for EFIGI E types were also derived for the EFIGI cD and dE types, also using single-Sérsic profiles (left panel of Fig. 7), with the latter types nevertheless yielding a steeper relation than that measured by Binggeli et al. (1984).

It is remarkable that the Sérsic components of E galaxies as well as bulges of lenticular and spiral galaxies can be considered altogether rather than for each morphological type separately, as they form a continuous size-luminosity relation, along which the B/T ratio varies from measured values of $\lesssim 1$ to 0.01 (see right

panel of Fig. 7). Moreover, the bulge size-luminosity relation is convex, with a curvature leading to ∼ 2 dex larger radii than interpolated from the E galaxies modeled as a single-Sérsic profile (and ∼ 1 dex larger radii than interpolated from the E Sérsic components) at the faintest bulge magnitudes (∼ −15 in g band). Bulges have a surprising Gaussian distribution of the logarithm of their effective radii around this relation (see Fig. 8), whose rms deviation increases from 0.17 dex to 0.33 dex from bright to faint bulges (compared to 0.21 dex for E types at the bright end).

We highlight that both scaling relations are projections of the planar relation (at null redshifts) between the surface brightnesses, radii, and absolute magnitudes in 3D space (Fig. 9). We also show that the position of bulges within this plane is driven by the bulge-to-total ratio B/T, and by the Sérsic index $n_{\rm Sérsic}$ to a lesser extent.

We interpret these changes in the bulge characteristics across the Hubble sequence as a progressive and continuous transition from "pseudo-bulges" to "classical bulges." This gradual shift is observed in terms of B/T, $n_{\rm Sérsic}$ and the position within the $\langle\mu\rangle_e - M - R_e$ 3D space, and equivalently in the location along both of its projections that are studied. At one end of this transition lie the small and faint bulges with rather smooth profiles that account for a very small fraction of the total luminosity, which we interpret as pseudo-bulges, and they are found in late-type spirals. At the other end, there are larger and brighter bulges with steeper profiles that account for around half the total galaxy light, which we interpret as classical bulges, and they are found in lenticulars as well as early spirals.

A similar study was then performed on the disks of the EFIGI galaxies and we derived analogous scaling relations for the surface brightness versus effective radius, and the size-luminosity relation (Figs. 10 and 11). The latter relation for EFIGI lenticular and spiral disks (as well as the exponential components of E galaxies) is also convex, with 0.5 dex larger radii of giant disks at ∼ −16 absolute magnitude in the g band than interpolated from the bright lenticular disks, and with again a Gaussian dispersion that increases from 0.18 dex at the bright end to 0.32 dex at the faint end. The curvature of the size-luminosity relation for disks is such that disks become larger and denser as they grow in luminosity from Im galaxies and very late spirals to Scd types. Then for types earlier than Scd, the average variation in effective radius with magnitude occurs at a constant mean central surface brightness.

The second degree polynomial fits to the size-luminosity relations (in log-log) that we derived for the Sérsic components of elliptical galaxies and the bulges of all types of lenticulars and spirals, as well as for the exponential components of the elliptical, the single Sérsic profiles of irregulars, and the disks of all types of lenticulars and spirals all appear critical in deriving a physically meaningful size for all of these components of galaxies. Indeed, single linear fits would lead to a systematic underestimation of effective radius in some intervals of absolute magnitude, when generating simulated galaxy parameters.

We further discuss the changes in bulge and disk structure as galaxies merge and evolve along the Hubble sequence in terms of bulge and disk volume and surface density, respectively (Sect. 5.3). The size-magnitude relations derived for this study did indeed allow us to estimate the absolute magnitudes and B/T critical values at which a bulge or disk luminosity scale as either R^2 or R^3. From our derived size-magnitude relations, we detected a change of regime from increasing volume and surface density of the small bulges to more prominent bulges that are more diffuse as they grow in size, which we interpret as related to the change of dynamics from pseudo to classical. We propose that the change from pseudo- to classical bulges occurs in the interval $-19.1 < M_{{\rm bulge},g} < -17.8$ (corresponding to $0.08 \lesssim B/T \lesssim 0.15$), in which the surface density of disky bulges increases with increasing radius, but the volume density of spheroidal bulges decreases. We show that at the extreme end of this bulge decreasing volume density trend lie elliptical galaxies, which become more and more diffuse as they grow in size; they are therefore not scale invariant. Regarding the disks, we show that they grow with luminosity both in size and surface density in late-type spirals, whereas they grow at a constant surface brightness on average in earlier spiral types and lenticulars.

We also obtained the unprecedented result that the bulge and disk effective radii vary as power laws of the galaxy B/T, which is a key parameter characterizing galaxies along the Hubble sequence (Quilley & de Lapparent 2022). The B/T ratio grows along the reverse Hubble sequence (Sect. 4.7.1), together with the bulge effective radius, whereas if the disk effective radius grows as the irregulars and late spirals merge to form earlier spirals, it stagnates or even decreases for lenticulars (Sect. 4.7.2). We provide the linear scaling relations between the logarithm of the effective radii of both the bulges and the disks, as well as their ratio, as a function of B/T, with 0.31 dex and 0.22 dex dispersion for the bulge and disk, respectively. In particular, we show that there is a significant increase in bulge radii for increasing B/T across all spiral types (from Sm to Sa types), as well as an even steeper increase in the bulge radii for lenticular galaxies. For the spiral types, the increase in the disk radii is flatter than for the bulges; however, for lenticulars, both components have a much steeper and similar rate of growth. It is noticeable that the Sa types, which mark the transition between the scaling of spirals and lenticular radii with B/T, correspond to the core of the Green Valley (Quilley & de Lapparent 2022).

These scaling relations propagate into a single scaling relation for the ratio of disk-to-bulge effective radii, h_e/R_e, across two orders of magnitude in B/T for all types. The mean ratio of radii ranges from ∼ 4 to 6 for lenticulars and ellipticals to ∼ 14 to 16 for Sbc to Scd types. A larger statistical sample, as well as higher angular resolution images (in order to resolve their small bulges) are needed for measuring the bulge radii of Sd to Sm types. There is a remarkably small dispersion in both B/T (between 0.1 and 0.2 dex) and h_e/R_e (between 0.2 and 0.3 dex) for the lenticular galaxies, indicating that lenticulars with small bulges also have a small disk and vice versa.

We emphasize that in the present article we confirm and complement the galaxy evolution scenario inferred from the color-mass diagram of EFIGI galaxies in Quilley & de Lapparent (2022), in which irregulars and late-type spirals merge to form more massive and earlier-type spirals, which then become passive as they merge into lenticulars and ellipticals. These mergers, along with the consumption of the gas reservoir of galaxies, explain the growth in stellar mass across the full reversed Hubble sequence, from the small irregulars to the giant elliptical galaxies, with a three order of magnitude increase in stellar mass or absolute luminosity across EFIGI spiral galaxies, and the corresponding three order of magnitude increase in their disk luminosity and mass – at the bright end of the Blue Cloud, where $B/T \lesssim 0.2$ (Quilley & de Lapparent 2022). Our proposed scenario of galaxy evolution in the previous analysis is complemented by the present results that galaxy growth occurs with a moderate increase in disk and total galaxy size by a factor of ∼ 7, but with a massive increase in B/T by a factor of ∼ 100 and of the bulge radius by a factor of ∼ 20 along the Blue Cloud.

Therefore, as galaxies merge along the spiral sequence, there are three parallel processes occurring: (1) an ∼ 1 order of magni-

tude increase in the disk effective radius (right panels of Fig. 15 or Fig. 16 in Sect. 4.7); (2) a redistribution of matter over the disks that boosts their projected central surface brightness by ∼ 4 magnitudes (Fig. 11 in Sect. 4.5); (3) a factor of ∼ 3 increase in the bulge effective radius (left panels of Fig. 15 or Fig. 16 in Sect. 4.7), along with an ∼ 2 order of magnitude growth in B/T, and an ∼ 5 order of magnitude growth in bulge absolute luminosity (Fig. 7 in Fig. 4.2). The various phases of bulge and disk growth occurring at different rates across morphological types are likely to be intertwined and to result from the different dynamics between both components.

Finally, all the relations derived here are useful to build more realistic mock catalogs. By providing the relations between size and luminosity, and further relating them to Hubble type and B/T, it is possible to derive – from a given luminosity of a bulge or a disk – a set of parameters describing its light profile, and thus leading to improved simulated images. We provide in Table 1 the parameters of the power-law fits to the size-luminosity relations performed for the Sérsic or bulge components, as well as the exponential or disk components of E, cD, dE, lenticular, and spiral galaxies. In Table 2, the parameters of the power-law fits to the bulge and disk effective radii as a function of B/T are also listed. In both Tables, the dispersion in the residuals from the fits are also provided, whether constant or variable along the relations.

As we have shown in Quilley & de Lapparent (2022) and in the present analysis via the coherent variations of the sizes and luminosities of bulges and disks of galaxies along the Hubble classification scheme, we intend to explore in a forthcoming analysis a physical and quantitative characterization of the morphological sequence in terms of these various bulge and disk parameters, using a complete magnitude-limited sample of the nearby Universe (Quilley & de Lapparent, *in prep.*), the MorCat completion of the EFIGI sample to $g \leq 15.5$. We also plan to use MorCat to calculate the quadri-variate luminosity functions of the bulges and the disks of galaxies as a function of absolute luminosities and physical effective radii of both types of components, as these are essential for generating realistic mock images and catalogs of galaxies in the nearby Universe. Generating mock catalogs at larger distances will require one to measure the evolution of the sizes of bulges and disks with redshift for all morphological types that may exist.

7. Acknowledgments

We are very grateful to Emmanuel Bertin for initiating and leading the EFIGI project, and for maintaining the computer cluster on which all calculations were performed. We also thank the anonymous referee for their insightful comments and suggestions.

This research made use of `SourceXtractor++`[10], an open source software package developed for the Euclid satellite project. This research made use of the VizieR catalog access tool, CDS, Strasbourg, France (DOI: 10.26093/cds/vizier). The original description of the VizieR service was published in A&AS 143, 23. This research also made use of NASA's Astrophysics Data System.

This work is based on observations made with the NASA Galaxy Evolution Explorer. GALEX is operated for NASA by the California Institute of Technology under NASA contract NAS5-98034. Funding for the SDSS and SDSS-II has been provided by the Alfred P. Sloan Foundation, the Participating Institutions, the National Science Foundation, the U.S. Department of Energy, the National Aeronautics and Space Administration, the Japanese Monbukagakusho, the Max Planck Society, and the Higher Education Funding Council for England. The SDSS Web Site is http://www.sdss.org/. The SDSS is managed by the Astrophysical Research Consortium for the Participating Institutions. The Participating Institutions are the American Museum of Natural History, Astrophysical Institute Potsdam, University of Basel, University of Cambridge, Case Western Reserve University, University of Chicago, Drexel University, Fermilab, the Institute for Advanced Study, the Japan Participation Group, Johns Hopkins University, the Joint Institute for Nuclear Astrophysics, the Kavli Institute for Particle Astrophysics and Cosmology, the Korean Scientist Group, the Chinese Academy of Sciences (LAMOST), Los Alamos National Laboratory, the Max-Planck-Institute for Astronomy (MPIA), the Max-Planck-Institute for Astrophysics (MPA), New Mexico State University, Ohio State University, University of Pittsburgh, University of Portsmouth, Princeton University, the United States Naval Observatory, and the University of Washington.

[10] https://github.com/astrorama/SourceXtractorPlusPlus

References

Allen, P. D., Driver, S. P., Graham, A. W., et al. 2006, MNRAS, 371, 2
Athanassoula, E. 2005, MNRAS, 358, 1477
Athanassoula, E. 2008, in Formation and Evolution of Galaxy Bulges, ed. M. Bureau, E. Athanassoula, & B. Barbuy, Vol. 245, 93–102
—. 2013, in Secular Evolution of Galaxies, ed. J. Falcón-Barroso & J. H. Knapen, 305
Baillard, A., Bertin, E., de Lapparent, V., et al. 2011, A&A, 532, A74
Bernardi, M., Meert, A., Vikram, V., et al. 2014, MNRAS, 443, 874
Bertin, E. 2009, Mem. Soc. Astron. Italiana, 80, 422
Bertin, E., Schefer, M., Apostolakos, N., et al. 2020, in Astronomical Society of the Pacific Conference Series, Vol. 527, Astronomical Data Analysis Software and Systems XXIX, ed. R. Pizzo, E. R. Deul, J. D. Mol, J. de Plaa, & H. Verkouter, 461
Binggeli, B., Sandage, A., & Tarenghi, M. 1984, AJ, 89, 64
Bluck, A. F. L., Mendel, J. T., Ellison, S. L., et al. 2014, MNRAS, 441, 599
Boggs, P. T., Byrd, R. H., Rogers, J. E., & Schnabel, R. B. 1992, National Institute of Standards and Technology, 1
Bottrell, C., Torrey, P., Simard, L., & Ellison, S. L. 2017, MNRAS, 467, 2879
Breda, I. & Papaderos, P. 2022, arXiv e-prints, arXiv:2210.10038
Bremer, M. N., Phillipps, S., Kelvin, L. S., et al. 2018, MNRAS, 476, 12
Brooks, A. M., Solomon, A. R., Governato, F., et al. 2011, ApJ, 728, 51
Chu, A., Sarron, F., Durret, F., & Márquez, I. 2022, A&A, 666, A54
Costantin, L., Méndez-Abreu, J., Corsini, E. M., et al. 2018, A&A, 609, A132
Courteau, S., de Jong, R. S., & Broeils, A. H. 1996, ApJ, 457, L73
Davies, R. L. & Illingworth, G. 1983, ApJ, 266, 516
de Jong, R. S. 1996, A&A, 313, 45

de Jong, R. S. & Lacey, C. 2000, ApJ, 545, 781
de Lapparent, V., Baillard, A., & Bertin, E. 2011, A&A, 532, A75
Debattista, V. P., Mayer, L., Carollo, C. M., et al. 2006, ApJ, 645, 209
Di Matteo, P., Fragkoudi, F., Khoperskov, S., et al. 2019, A&A, 628, A11
Dimauro, P., Daddi, E., Shankar, F., et al. 2022, MNRAS, 513, 256
Drory, N. & Fisher, D. B. 2007, ApJ, 664, 640
Dunkley, J., Komatsu, E., Nolta, M. R., et al. 2009, ApJS, 180, 306
Edwards, L. O. V., Salinas, M., Stanley, S., et al. 2020, MNRAS, 491, 2617
Emsellem, E., Cappellari, M., Krajnović, D., et al. 2011, MNRAS, 414, 888
—. 2007, MNRAS, 379, 401
Erwin, P., Saglia, R. P., Fabricius, M., et al. 2015, MNRAS, 446, 4039
Fioc, M. & Rocca-Volmerange, B. 1999, arXiv e-prints, astro
Fisher, D. B. & Drory, N. 2008, AJ, 136, 773
Freedman, W. L., Madore, B. F., Gibson, B. K., et al. 2001, ApJ, 553, 47
Freeman, K. C. 1970, ApJ, 160, 811
Fukugita, M., Shimasaku, K., & Ichikawa, T. 1995, PASP, 107, 945
Gadotti, D. A. 2009, MNRAS, 393, 1531
Gao, H., Ho, L. C., & Li, Z.-Y. 2022, ApJS, 262, 54
Graham, A. W. & Driver, S. P. 2005, PASA, 22, 118
Grazian, A., Castellano, M., Fontana, A., et al. 2012, A&A, 547, A51
Hubble, E. P. 1926, ApJ, 64, 321
Joung, M. R., Cen, R., & Bryan, G. L. 2009, ApJ, 692, L1
Kawamata, R., Ishigaki, M., Shimasaku, K., et al. 2018, ApJ, 855, 4
Kim, K., Oh, S., Jeong, H., et al. 2016, ApJS, 225, 6
Kormendy, J. 1977, ApJ, 218, 333
Kormendy, J. & Kennicutt, Robert C., J. 2004, ARA&A, 42, 603
Krajnović, D., Alatalo, K., Blitz, L., et al. 2013, MNRAS, 432, 1768
Krajnović, D., Bacon, R., Cappellari, M., et al. 2008, MNRAS, 390, 93
Krajnović, D., Emsellem, E., Cappellari, M., et al. 2011, MNRAS, 414, 2923
Lang, P., Wuyts, S., Somerville, R. S., et al. 2014, ApJ, 788, 11
Le Borgne, D. & Rocca-Volmerange, B. 2002, A&A, 386, 446
Méndez-Abreu, J., Debattista, V. P., Corsini, E. M., & Aguerri, J. A. L. 2014, A&A, 572, A25
Quilley, L. & de Lapparent, V. 2022, A&A, 666, A170
Schlafly, E. F. & Finkbeiner, D. P. 2011, ApJ, 737, 103
Schlegel, D. J., Finkbeiner, D. P., & Davis, M. 1998, ApJ, 500, 525
Sérsic, J. L. 1963, Boletin de la Asociacion Argentina de Astronomia La Plata Argentina, 6, 41
Simard, L., Mendel, J. T., Patton, D. R., Ellison, S. L., & McConnachie, A. W. 2011, ApJS, 196, 11
Simien, F. & de Vaucouleurs, G. 1986, ApJ, 302, 564
Trujillo, I., Rudnick, G., Rix, H.-W., et al. 2004, ApJ, 604, 521
Virtanen, P., Gommers, R., Oliphant, T. E., et al. 2020, Nature Methods, 17, 261
Yang, L., Leethochawalit, N., Treu, T., et al. 2022a, MNRAS, 514, 1148
Yang, L., Morishita, T., Leethochawalit, N., et al. 2022b, ApJ, 938, L17
Young, P. J. 1976, AJ, 81, 807

Chapter 6

Bulge and disk color bimodality and color gradients

This section presents ongoing work that will be included in an article to be submitted to Astronomy & Astrophysics by Quilley, de Lapparent & Lehnert.

Our use of nearly face-on galaxies and a large statistical sample for all Hubble types, as well as simultaneous bulge and disk profile fitting allows us to measure physically plausible colors for these components, in agreement with those seen by eye when examining the EFIGI *gri* color images.

As explained previously (Sect. 1.4.4), different stellar populations emit in different wavelength ranges, with older stars having a redder emission than younger stars. Therefore, by comparing the results of our model-fitting process between the three available bands g, r, and i, we can gain insight into the way the different generations of stars are distributed within a galaxy. This has been done to a certain extent by analyzing the color of galaxies in Quilley & de Lapparent (2022) (see Chap. 4). Here, we examine in more details the colors and color profiles of both bulges and disks.

6.1 Bulge and disks colors along the Hubble sequence

In Quilley & de Lapparent (2023) (see Sect. 5.3) we have shown in Fig. 5 the $g-r$ bulge color as a function of Hubble type to discuss the claim by Allen et al. (2006) that it had an impact on the Kormendy relation followed by bulges, while in Quilley & de Lapparent (2022) we examined the distribution of the $g-r$ disk color in the color-mass plane, and identified disk reddening as a key variation along the Hubble sequence.

In Fig. 6.1, we show the $g-r$ colors of bulges (left, same plot as Fig. 5 in Quilley & de Lapparent 2023) and disks (right) as a function of Hubble type. The left panel shows an overall stable bulge color, with a small reddening for intermediate spirals. The dust within these spirals could cause a reddening of the bulge light. The right panel confirms that the disk color is a marker of the Hubble type as it evolves monotonously all along the Hubble sequence.

The color bimodality presented and discussed in Chap. 4 can therefore be understood as a transition between spirals with blue disks and red bulges, with the light of the former component dominating (low B/T values) the overall galaxy light, while earlier types have redder disks, whose colors progressively resemble those of their bulges. So both the growing prevalence of the bulge (B/T increase) and the disk reddening ($(g-r)_{disk}$ increase) will play a part in going from blue to red galaxies.

Fig. 6.2 allows us to characterize the joint color evolution for the bulges and disks all along the Hubble sequence by showing the $g-r$ color distribution of bulges and disks against each other, with a color code and mean value (square symbols) for each Hubble type. The evolution from late to early types is mainly vertical with a disk reddening of 0.35 mag between the mean values of E-cD (0.62) and Sd-Sdm-Sm (0.27) types respectively, while all mean bulge colors remain in an interval of width 0.16 mag ($[0.67; 0.83]$) for all types until Scd, i.e. for which mean bulge colors can be properly computed, and that would surely be even narrower if we could correct for dust reddening. Almost all galaxies are positioned right of the grey-dashed line representing identical $g-r$ bulge and disk color, as they have

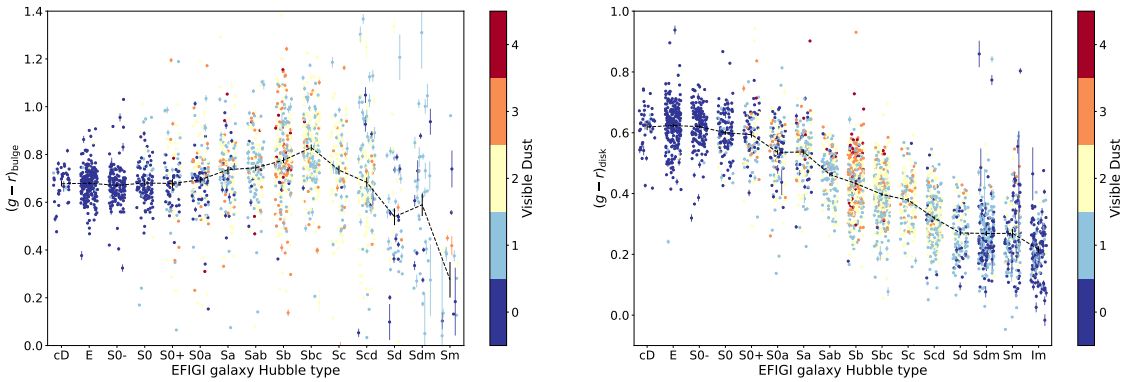

Figure 6.1: The distribution of the $g-r$ colors of the bulge (left) and disk (right) components of the bulge-disk decompositions of all EFIGI morphological types with `Inclination`≤ 2. The points are color-coded with the EFIGI attribute `Visible Dust`, as dust is known to redden the colors of galaxies. The results for the single-Sérsic modeling of Im galaxies are added with the disks.

Hubble Type		E	cD	S0$^+$	S0	S0$^-$	S0a	Sa	Sab	Sb	Sbc	Sc	Scd	Sd	Sdm	Sm	Im$^{(b)}$
Galaxy	Mean	0.64	0.65	0.64	0.63	0.62	0.59	0.59	0.53	0.49	0.45	0.41	0.34	0.28	0.29	0.29	0.22
	$\sigma^{(a)}$	0.03	0.04	0.05	0.05	0.07	0.07	0.06	0.07	0.07	0.07	0.08	0.09	0.08	0.08	0.1	0.08
Bulge	Mean	0.68	0.68	0.67	0.68	0.68	0.69	0.74	0.74	0.78	0.83	0.73	0.68	0.54	0.59	0.28	-
	$\sigma^{(a)}$	0.07	0.07	0.08	0.11	0.19	0.17	0.15	0.15	0.18	0.19	0.2	0.24	0.25	0.27	0.3	-
Disk	Mean	0.62	0.62	0.62	0.6	0.59	0.54	0.54	0.46	0.43	0.4	0.38	0.32	0.27	0.27	0.27	0.22
	$\sigma^{(a)}$	0.07	0.08	0.07	0.07	0.1	0.1	0.1	0.08	0.1	0.09	0.09	0.08	0.08	0.11	0.11	0.08
Bulge - Disk	Mean	0.06	0.05	0.05	0.08	0.09	0.17	0.2	0.28	0.33	0.41	0.35	0.36	0.27	0.3	-0.03	-
	$\sigma^{(a)}$	0.11	0.12	0.11	0.14	0.22	0.18	0.19	0.18	0.19	0.2	0.21	0.22	0.23	0.25	0.3	-

Table 6.1: $(g-r)$ colors of the bulges, disks and whole galaxies for all EFIGI morphological types.

Notes:

(a) We compute the r.m.s. dispersion of the $(g-r)$ colors. Note that the standard error on the mean value is defined as $\sigma/\sqrt{N}$

(b) We list the single-profile modeling of Im as disks because they do not host a bulge and the resulting Sérsic index distribution peaks around 1. Therefore, the color mean and associated dispersion of all Im single-profile are repeated in both the whole galaxy and disk category.

a bulge redder than their disk, but earlier and earlier galaxies get progressively closer to it with E and S0s having almost identical bulge and disk colors: $\overline{(g-r)_{bulge}} - \overline{(g-r)_{disk}} = 0.06, 0.05, 0.08$ for types E, S0$^-$ and S0 respectively.

The results we derived here from EFIGI divert from the conclusion of Peletier & Balcells (1996) that color variations from galaxy to galaxy are much larger than color differences between disk and bulge in each galaxy. They measure optical and NIR $UBRKJ$ bulge and disk colors by using wedge-shape apertures on inclined galaxies, and averaging over a certain radius interval, hence not computing the color of the whole component. Their study is focused on early spirals, for which they find $\overline{(U-R)_{bulge}} - \overline{(U-R)_{disk}} = 0.126 \pm 0.165$ and $\overline{(R-K)_{bulge}} - \overline{(R-K)_{disk}} = 0.078 \pm 0.165$. In our case, EFIGI Sa spiral galaxies show an average color difference $\overline{(g-r)_{bulge}} - \overline{(g-r)_{disk}} = 0.20$, with a dispersion $\sigma(g-r_{galaxy}) = 0.06$ so we find a greater difference between bulge and disk color than from galaxy to galaxy. For types E to S0$^+$, the color difference is roughly the same as the dispersion value, so we would reach the same conclusion as Peletier & Balcells (1996), but for later type, even if the dispersion slightly increases, the difference between the bulge and disk colors overtakes it, with types Sb, Sbc and Sc having $\overline{(g-r)_{bulge}} - \overline{(g-r)_{disk}} = 0.33, 0.41, 0.35$ whereas their color dispersions are $\sigma = 0.07, 0.07, 0.08$. Therefore the color differences between bulge and disk are only of the order of the color differences from galaxy to galaxy for ETG, but become much stronger for later types for later

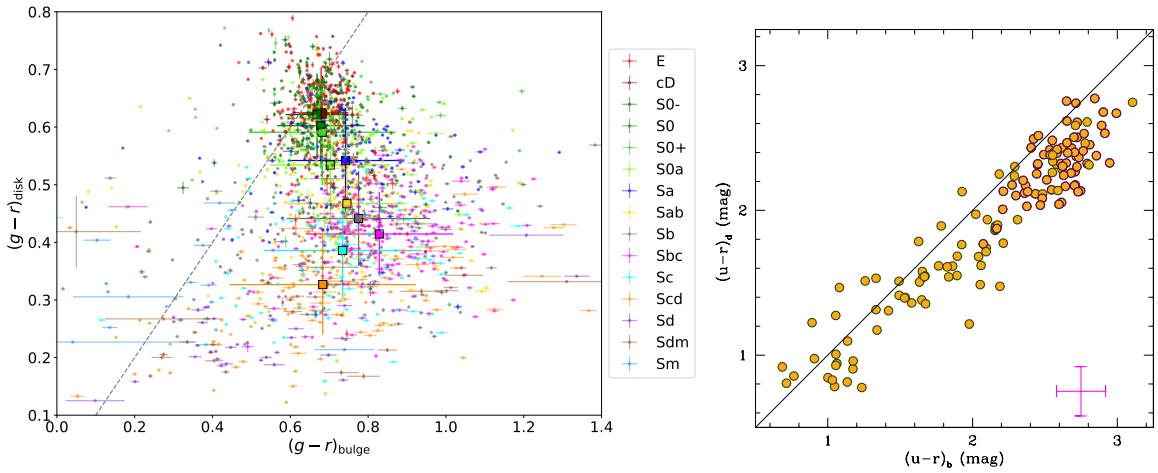

Figure 6.2: **Left:** Disk versus bulge $g-r$ color for all EFIGI galaxies with `Inclination`≤ 2, and color-coded by their Hubble type. The square represent the mean colors for each Hubble type. **Right:** Fig. 5 from Cameron et al. (2009) showing the relationship between the bulge and disk $(u-r)$ colors of two-component galaxies in the Millenium Galaxy Catalogue (MGC). The estimated uncertainties are indicated by the magenta error bar. EFIGI galaxies show rather stable bulge color and a marked disk reddening from late to early morphological types, with bulges redder than disks, whereas similar bulge and disk colors were measured for MGC galaxies over several magnitudes.

types.

We also emphasize that our Fig. 6.2 disproves the tight correlation between the bulge and disk $u-r$ colors found by Cameron et al. (2009) through the bulge and disk decomposition performed with GIM2D of the Millenium Galaxy Catalog. Simply from examining galaxy images, it is crystal clear that bulge and disk color differ strongly from each other for spiral galaxies. Therefore, we argue that to obtain such a trend as in their Fig. 5, their bulge and disk decomposition likely fails in disentangling both components, both profiles of their model seemingly measuring a similar color which maybe the total galaxy color.

6.2 Color gradients

The top right panel of Fig. 6.3 shows the ratio between the effective radii of the EFIGI disk components in the g and i bands, so the bluest and reddest bands available, for all EFIGI galaxies with `Inclination`≤ 2, as a function of their visually classified Hubble type. The dispersion of these color gradients by type are all in the interval $[0.03; 0.05]$ dex (see Tab. 6.2), allowing us to detect small effects, but the high individual uncertainties measured for types Sdm and later (~ 0.1 dex) prevent us being as conclusive for these types. For lenticulars ($S0^-$ to $S0^+$) the mean ratio between the two effective radii equals $1.024, 1.003, 1.006$ respectively, indicating no significant difference between the two bands. Whereas for spiral types, the mean effective radii of the g disk exponential profile becomes larger than for the i disk profile as we go toward later types, by factors of $1.044, 1.056, 1.097$ for Sa, Sb and Sc types respectively, thus reaching a peak value of $\sim 10\%$ difference for late spirals (Sbc to Scd). A more extended disk at bluer wavelengths mean that younger generations of stars are more spatially extended than their older counterparts, so they represent a higher share of the surface brightness (hence stellar mass density) at the outskirts of the disks than in its innermost parts.

On the contrary, the color gradients measured for the Sérsic profiles of the bulge components present the opposite trend, as seen in the top left panel of Fig. 6.3. Similarly to the top right panel, it shows the ratio between the effective radii of the bulge in the g and i bands for all EFIGI galaxies with `Inclination`≤ 2, as a function of their visually classified Hubble type, with the added condition presented in Sect. 4.3.1 of Quilley & de Lapparent (2022) (which is included in Sect. 4.4 of this thesis), ensuring that the bulge radii can be trusted. The type dispersion in the effective radii ratio increases with Hubble type from 0.05 dex for S0 galaxies to ~ 0.1 for all spiral types (Sa to Scd all have dispersion

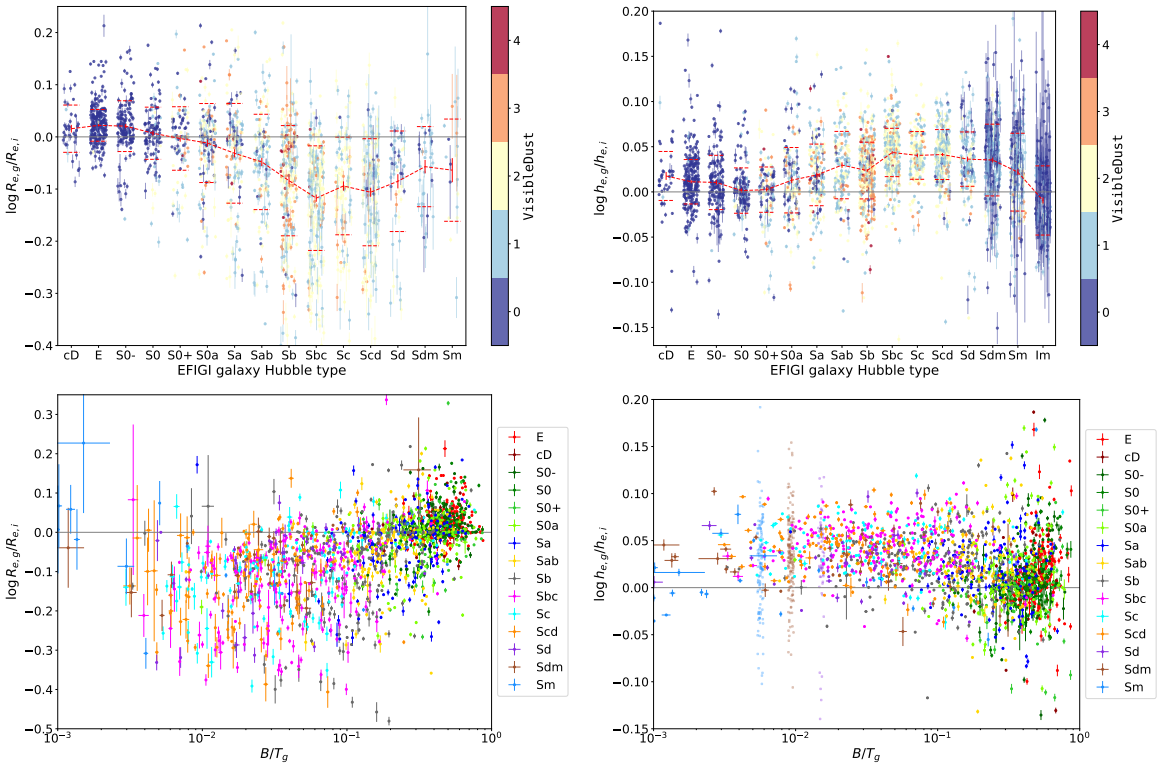

Figure 6.3: The distribution of effective radii of the bulge (left) and disk (right) components of the bulge-disk decompositions of all EFIGI morphological types with `Inclination`≤ 2 as a function of Hubble type (top) and as a function of B/T (bottom). The red dashed lines correspond to the mean value per type, and the dashed horizontal lines to $\pm 1\sigma$, with σ the root mean square dispersion. Intermediate spirals with $B/T \leq 0.1$ exhibit color gradients in both their bulges and disk, but of opposite directions, and of stronger amplitude for bulges. Disks are bluer in their outskirts, whereas bulges are redder outwards.

within the $[0.09, 0.11]$ dex interval), due to smaller values of B/T, hence larger uncertainties in the R_e for later types. For the lenticulars, the color gradients have a mean value of $R_{eg}/R_{ei} \sim 1$ with a small dispersion of 0.05 dex, whereas the bulge effective radius for the g band becomes smaller than the one for the i band as we go towards intermediate spirals, with mean ratio of 0.930, 0.824 and 0.805 for types Sa, Sb and Sc respectively. The strongest gradient is exhibited for the types Sbc, with a g band bulge effective radius measuring only 76.5% of the i radius.

Because B/T can be used to parameterize the Hubble type (Quilley & de Lapparent 2022), we also examine both the bulge and the disk color gradients as a function of B/T in the bottom left and right panels of Fig. 6.3, respectively, with the Hubble type indicated as the color of the points. As expected from the variations with Hubble type, on the one hand, for high values of B/T, i.e. $[0.2; 0.8]$ interval, the disk color gradients of S0s and early spirals are distributed around 0, with a mean value of $\log(h_{e,g}/h_{e,i}) = 0.014$, and a dispersion of $\sigma = 0.040$. They increase for lower values of B/T and are almost systematically positive for $B/T < 0.1$, which corresponds to intermediate to late spirals, with log-values in the interval $[0.; 0.1]$, a mean gradient of $\log(h_{e,g}/h_{e,i}) = 0.038 \pm 0.001$, corresponding to a disk on average 9% larger in g than in i. On the other hand, the mean bulge gradients are also close to 0 with $\log(R_{e,g}/R_{e,i}) = 0.013 \pm 0.003$ in the B/T interval $[0.3; 0.8]$. Bulge color gradients decrease towards lower B/T and are systematically negative for $B/T < 0.1$, with a mean of $\log(R_{e,g}/R_{e,i}) = -0.108 \pm 0.004$. Therefore, the discrepancy between the g and i effective radii is stronger for the bulge than for the disk profiles, as the mean gradient over the same B/T interval is almost 3 times stronger (and opposite). The log-values of the bulge color gradients are spread over the $[0.; -0.4]$ interval for $B/T < 0.1$, so for bulges, the red profile can be up to 2.5 times larger than the bluer one.

Because both the bulge and disk models are interdependent in the bulge and disk SourceXtrac-

Type	Bulge						Disk						
	$R_{e,g}$ [kpc]	$\sigma^{(a)}$ [dex]	$\frac{R_{e,g}}{R_{e,i}}$	$\log(\frac{R_{e,g}}{R_{e,i}})$ [dex]	σ [dex]	$N^{(b)}$	$h_{e,g}$ [kpc]	$\sigma^{(a,b)}$ [dex]	$\frac{h_{e,g}}{h_{e,i}}$	$\log(\frac{h_{e,g}}{h_{e,i}})$ [dex]	σ [dex]	$N^{(b)}$	r^2
cD	4.2	0.21	1.037	0.016	0.045	38	24.39	0.25	1.041	0.018	0.027	42	0.19
E	2.27	0.27	1.052	0.022	0.03	217	10.74	0.29	1.026	0.011	0.025	217	0.27
S0-	1.62	0.35	1.048	0.021	0.049	139	8.94	0.39	1.024	0.01	0.03	142	0.26
S0	1.04	0.35	1.016	0.007	0.05	114	6.43	0.32	1.003	0.001	0.025	121	0.27
S0+	1.25	0.38	0.993	-0.003	0.061	100	6.05	0.31	1.006	0.002	0.025	109	0.22
S0a	1.02	0.41	0.973	-0.012	0.076	140	6.76	0.29	1.03	0.013	0.036	145	0.27
Sa	1.16	0.31	0.93	-0.031	0.096	147	9.26	0.21	1.044	0.019	0.034	159	0.20
Sab	0.9	0.32	0.895	-0.048	0.091	136	9.22	0.21	1.071	0.03	0.037	157	0.30
Sb	0.61	0.43	0.824	-0.084	0.106	246	6.87	0.29	1.056	0.024	0.031	376	0.03
Sbc	0.62	0.34	0.765	-0.116	0.101	215	9.03	0.2	1.106	0.044	0.027	333	0.04
Sc	0.6	0.34	0.805	-0.094	0.094	113	8.42	0.24	1.097	0.04	0.026	170	0.07
Scd	0.49	0.38	0.785	-0.105	0.102	143	7.52	0.19	1.1	0.041	0.028	250	0.0002
Sd	0.64	0.5	0.828	-0.082	0.097	52	6.23	0.23	1.087	0.036	0.03	129	0.10
Sdm	0.4	0.78	0.889	-0.051	0.08	43	5.35	0.28	1.083	0.035	0.039	223	0.01
Sm	0.13	0.96	0.918	-0.037	0.108	24	2.95	0.27	1.052	0.022	0.043	178	0.0002
Im$^{(c)}$	-	-	-	-	-	-	2.12	0.36	0.978	-0.009	0.038	142	-

Table 6.2: Geometric mean of the effective radii (in kpc) and mean of the color gradients, as well as their associated r.m.s. dispersions (in log-scale), and sample size, for the bulges and disks of EFIGI morphological types, with `Inclination` ≤ 2. The last column is the squared Pearson correlation coefficient r^2 between the bulge and disk gradients.

Notes:

(a) We compute here the r.m.s. dispersion of the logarithms of the effective radii, which is therefore given in dex

(b) The standard error on the mean value is defined as $\sigma/\sqrt{N}$

(c) We list the single-profile modeling of Im as disks because they do not host a bulge and the resulting Sérsic index distribution peaks around 1.

tor++, we had concerns about the symmetry in these trends actually arising from the model-fitting step, rather than representing a physical effect. We therefore examine whether the bulge color gradient could simply be a consequence of the disk gradient, with the red profile being more extended only to balance the slower exponential decrease of the blue surface brightness. We show in Fig. 6.4 that the relation between both gradients are not correlated for individual galaxies. Instead we see that E ans S0s are spread around the origin, while spirals, mainly intermediate spirals that show the highest values of color gradients are spread out over the interval $\log(h_{e,g}/h_{e,i}) \in [0; 0.1]$ at all values of the bulge gradients. The dashed line represents the linear relation interpolated from the mean bulge and disk gradients of the Sbc type (which shows the highest values for both gradients), data points should align along this line if the bulge gradient was a consequence of the disk one, but it is not the case here. This is quantitatively confirmed by computing the Pearson correlation factor between both gradients for all Hubble types, as they all verify $r^2 < 0.3$, indicating an absence of correlation.

Unlike the exponential disk, the shape of the bulge surface brightness profile is modeled by a Sérsic function, so the interpretation of different effective radii between bands is not as straightforward, and one must also takes into account the impact of varying Sérsic indexes between bands. Fig. 6.5 presents the difference between the g and i Sérsic indexes obtained through the multi-band light-profile fitting. Once again, for lenticulars, the values do not vary between bands, but a gradient appear towards later types with the Sérsic index in the i band having higher values, with an average difference of 0.31, 0.29 and 0.27 for types Sab, Sb and Sbc repectively, which means that the red profile is not only more extended, but also steeper than the blue one.

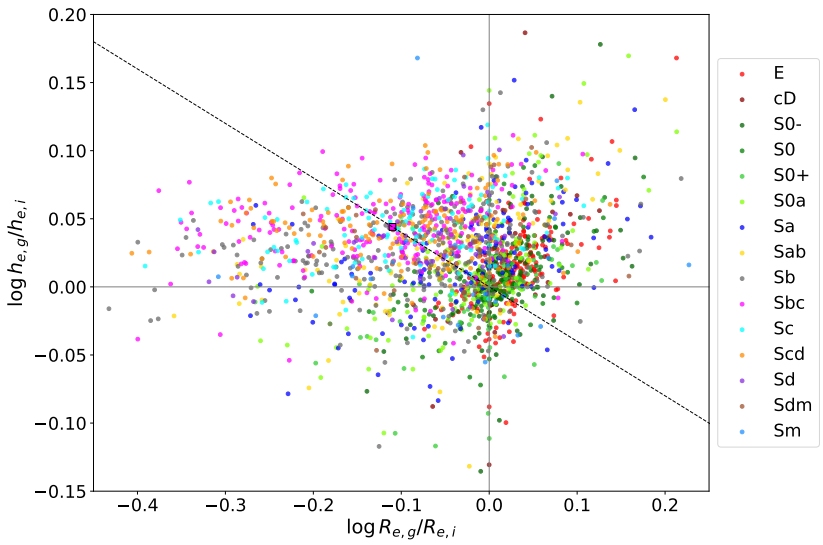

Figure 6.4: Disk color gradient versus bulge color gradient for all EFIGI Hubble types, indicated by the color of the points. The pink square show the average gradients for Sbc types, and the dashed line correspond to the linear relation going through this mean. Bulge and disk gradients appear uncorrelated with each other, as confirmed by their low Pearson correlation coefficients (see Tab. 6.2).

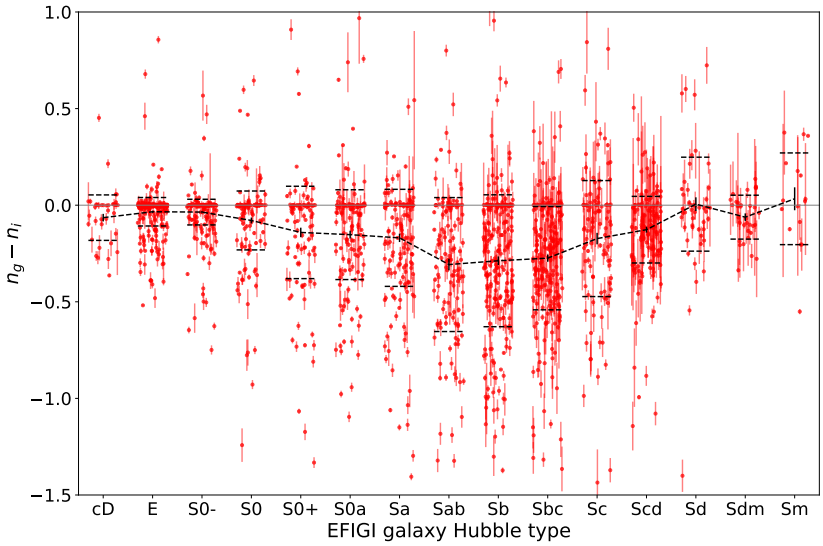

Figure 6.5: Distribution of the difference between the bulge Sérsic indexes fitted in the g and i band as a function of Hubble Type. A similar trend as for the radii appear here, with a Sérsic index color gradient for intermediate spirals, mainly Sab, Sb and Sbc types, for which the i bulge profile is steeper than the g bulge profile.

The results derived here for the bulges of EFIGI galaxies are in contradiction with the analysis by Balcells & Peletier (1994) who examined 18 bulges of non-barred S0, Sa, Sab, Sb and Sbc types, with disk inclinations larger than 50 deg, and unaffected by dust (based on visual examination of the bulge, using total $U - R$ and $B - R$ colors, and considering the disk dust content by comparing its scale lengths in U and R). The surface brightness profiles were measured in wedge-shape regions of the bulge an disk (and away from the disk dust lane). They derived $U-R$ and $B-R$ color gradients within bulges that are predominantly bluer outwards, and found that the strength of the gradient increases toward later types, as for EFIGI galaxies, but with an opposite gradient. Despite the claim by these authors that the magnitude of the measured gradients scales with luminosity for bright bulges, their

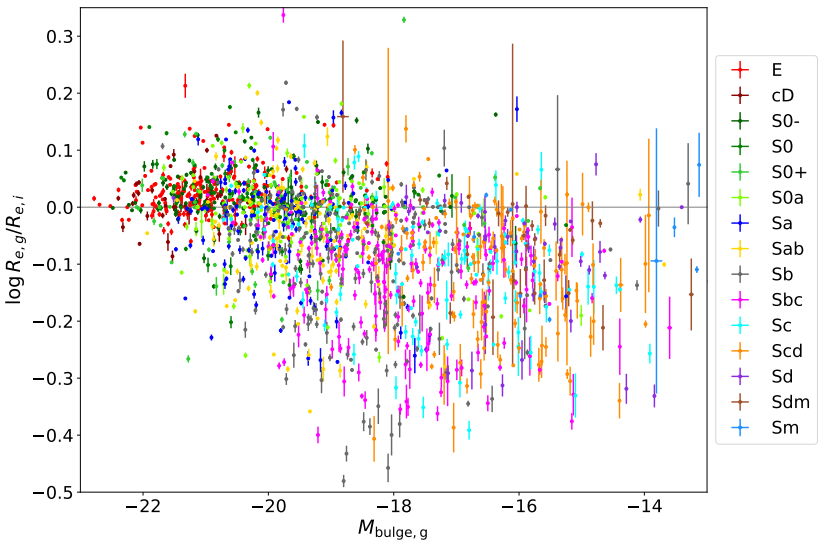

Figure 6.6: Distribution of the ratio of the effective radii in the g and i bands of the bulge components of all EFIGI morphological types with `Inclination`≤ 2 as a function of bulge absolute magnitude in the g band. Bright bulges $M_g \leq -20$ do not show significant color gradients, whereas fainter bulges $M_g \geq -19$ exhibit redder-outwards color gradients, with a strong dispersion in their values.

Fig. 9 shows no clear trend in the -24 to -20 interval in the R band, which we confirm with EFIGI in the -22.5 to -19 interval in the g band for the bulge component of ellipticals and lenticulars, as shown in Fig. 6.6. For fainter EFIGI bulges (of Hubble types Sa and later), there is a large scatter in the blue-to-red color gradient from -20 to -17 in bulge g, in agreement with the results of Balcells & Peletier (1994), but with very low statistics.

We also note in Fig. 6.6 that redder outwards color gradients dominate the magnitude interval $-19 \leq M_g \leq -14$, with a mean color gradient of $\log(R_{e,g}/R_{e,i}) = -0.091 \pm 0.004$, whereas brighter bulges $M_g \leq -20$ do not exhibit this gradient, with a mean $\log(R_{e,g}/R_{e,i}) = 0.009 \pm 0.003$. In Quilley & de Lapparent (2023), we proposed the $-19.1 \leq M_g \leq -17.8$ as a transition magnitude interval between pseudo and classical bulges. Therefore classical bulges do not seem to show these color gradients, but pseudo-bulges and "mixed" bulges do (we recall that bulges with intermediate properties could actually be decomposed as the sum of a pseudo and a classical bulge, see Quilley & de Lapparent 2023).

The disagreement between our analysis of EFIGI and the results of Balcells & Peletier (1994) demonstrate the importance of performing reliable bulge and disk decomposition such as designed here using SourceXtrator++ (see Sect. 3.1).

The two most significant results of this work has been to show that the bulges appear on average systematically more compact in the g-band than in the i-band as one moves from early (cD through S0a) to late type galaxies (Sa through Sm) and that the galaxy disks have the opposite trend with lenticular galaxies having the same effective radii in the g and i bands, while disks of later spiral types galaxies up to Sbc have systematically smaller half-light radii in the i-band compared to the g-band.

Furthermore, the decrease in intensity of the disk color gradient from late to early spirals is concomitant to a progressive reddening of the disks. So it seems that star formation is suppressed first in the inner disks, with late spirals exhibiting intense star formation in their disks, but relatively less in its inner part, and then as quenching extends itself, the difference in star formation between inner and outer disks fades away and the global disk color reddens.

Nuclear spirals are ubiquitous in spiral galaxies (e.g. Schinnerer et al. 2002; Martini et al. 2003a,b) and especially in galaxies with bars. These nuclear spirals can efficiently drive material (gas, dust, stars) to the bulge centers. Because of the high stellar density in the cores of bulges, the pressure is high (cosmic rays etc.) and in a couple of million years a globular cluster can form from molecular gas and dust that has fallen into the bulge (Kruijssen et al. 2015). This causes very low level star formation in the core of the bulge, which could result in an apparent smaller effective radius in the g compared to i bands, as is obtained here in EFIGI. Moreover, bulge gradients are observed in late type

spirals, usually hosting small bulges that can be considered as pseudo-bulges or a mix of pseudo and classical bulges (Quilley & de Lapparent 2023, see Sect. 5.3). Therefore, their color gradients could also result from a bar-like pseudo-bulge, whose shear would prevent star formation at its outskirts, so the star forming regions would only be central within the bulge.

Regarding the disks, the color gradients measured in EFIGI are opposite to those measured in bulges, with bluer color at the outskirts, indicating either enhanced star formation in these regions, or suppressed star formation in the inner disk. Interestingly, the formation of a bar through tidal interaction, mergers, and the basic fact that galaxies with relatively low central mass concentration are unstable to bar formation, can also lead to the suppression of star formation in the inner disk, by the same mechanism that leads to gas falling into the central potential: the gas is being swept up by the bar and dynamically stirred. Both of these would tend to suppress star formation in the bar region where its pattern speed is different from that of the underlying disk (Khoperskov et al. 2018). Such an effect would lead to the reddening of the inner disk with time, so inner disks, that is the region generally unstable to bar formation, would systematically host redder stellar populations than their outer disks. The disk color gradients we observe in EFIGI are not typical of barred galaxies, so for bars to explain them, it would require that they actually are a transient feature that would suppress star formation without being present all the time. If we assume that the observed fraction of barred galaxies roughly corresponds to the fraction of time over which spiral galaxies host a bar, then it would mean that a bar duty cycle of $\sim 40\%$ is enough to explain the suppression of star formation in the inner disk.

This preliminary analysis therefore shows that secular processes within spiral galaxies resulting from internal instabilities that form bars and spiral arms may condition how star formation locally evolves within bulges and disks, hence explaining their quenching from the Blue Cloud to the Red Sequence.

Conclusion

Throughout this thesis, I have performed an in-depth analysis of the morphology of the 4458 nearby galaxies of the EFIGI catalog in order to quantify their structural properties, and ultimately to gain insight into their formation.

I started by developing a methodology to reliably characterize the morphological parameters of their bulges and disks, which is presented in Chap. 3. I use SourceXtractor++ to perform multi-band luminosity profile-fitting of the *gri* images obtained from the SDSS, using the new functionality of priors. Bulge priors derived by an automatic zoom-in procedure and Gaussian band-to-band priors allow me to reduce degeneracies in the bulge and disk decomposition, and to precisely measure the color profiles of these components. Photometric data in the ultraviolet wavelength range are added through a cross-match with a GALEX catalog, and all these obtained apparent magnitudes are corrected for both atmospheric and galactic extinction. The corrected magnitudes and redshifts of EFIGI galaxies serve as inputs in a spectral energy distribution fit performed with the ZPEG software, which allows me to compare the spectral types of the best-fit templates to the morphological types classified in EFIGI. This step provides absolute magnitudes in all bands, as well as estimates of the stellar masses and star formation rates of all EFIGI galaxies. The exhaustive data set obtained through this process provides a broad and quantitative description of the morphology of nearby galaxies, which can be used together with the 16 visual attributes of EFIGI to better understand their morphological evolution.

The first idea I pursued during my thesis was to relate the morphological types constituting the Hubble sequence to the bimodality of galaxies by locating them in the $NUV - r$ absolute color versus stellar mass diagram (see Chap. 4 describing the results of Quilley & de Lapparent 2022). I show that the Hubble sequence describes monotonously an "S" shape across this plane, with specific types corresponding to either the Blue Cloud (Sab to Im), Red Sequence (E and S0s) and Green Valley (S0a and Sa). Importantly, the continuous trend in Hubble type across the color-mass diagram can be characterized by a continuous increase in the bulge-over-total luminosity and stellar mass ratios (B/T) from 10^{-2} to $\lesssim 1$, and a reddening of disk colors by 0.6 magnitude in $g - r$. Inside both the Blue Cloud and the Red Sequence, the evolution towards earlier morphological types corresponds to a growth of stellar mass over ~ 5 dex. In contrast, the Green Valley carries most of the color change within only a ~ 1 dex stellar mass interval, which is common to all types from Sb to S0. However, the observed gradual increase of B/T and reddening of disk color seen along the Hubble sequence is significant across the Green Valley, with a doubling of B/T and a 0.4 magnitude disk reddening in $g - r$. The Green Valley is also characterized as the locus of ringed galaxies, which are most common for S0a and Sa types, and are also more often observed in barred galaxies. We propose that the onset of rings is caused by minor mergers or bar formation, but for rings to persist, the galaxy must host a significant bulge and contain gas, both conditions being only met in the Green Valley.

My study also highlights the role of mergers at all steps of galaxy evolution. Indeed, the 4 orders of magnitude in the stellar mass across the Blue Cloud cannot be solely explained by the replenishment and consumption of their gas reservoir. Moreover, the bulge growth described previously is concomitant to a profile change to more concentrated bulges (with a steeper Sérsic index), and is likely caused by minor mergers. At last, the existence of very massive ellipticals beyond the $M_{\rm lim} = 10^{11.7} M_\odot$ mass limit for spirals, can only be explained by dry mergers, as E galaxies form few or no stars, hence cannot increase their stellar mass by converting gas into stars.

Then, I revisit the scaling relations of bulges and disks at present times, that allow one to relate their effective radii with their apparent surface brightnesses and absolute magnitudes (see Chap. 5 describing the results of Quilley & de Lapparent 2023). I show that the Kormendy (1977a) relation

between effective surface brightness and effective radius of E galaxies extends to the bulges of S0 and Sb types, whereas fainter and smaller bulges of later Hubble types depart from it, with decreasing B/T and Sérsic indices. I provide evidence that there is a continuous transition from pseudo-bulges to classical ones, rather than a strict dichotomy between these two classes, and propose bulge magnitude and B/T intervals within which this transition occurs. I recompute size-luminosity relations for E and dE types that are steeper and similar to those from Binggeli et al. (1984), resp., below which EFIGI lenticular and spiral bulges display a curved relation. The disks and irregulars also follow a curved size-luminosity relation such that while they grow, they first brighten and then stabilize in surface brightness. Moreover, I obtain the unprecedented result that the effective radii of both the bulges and disks of spirals increase as power-laws of B/T, with a steeper increase for the bulges. The increase with B/T is much steeper and similar for the bulges and disks of lenticulars. The ratio of disk-to-bulge effective radii varies accordingly across 2 orders of magnitude in B/T for all lenticular and spiral types, with a mean disk-to-bulge ratio decreasing from ~ 15 for Sbc to Scd types, to ~ 6 for S0. The new curved size-luminosity relations that I derived in my analysis present the advantage to avoid over or under estimates of bulge, disk and galaxy sizes at all magnitudes. Because these scaling relations allow one to derive from the absolute magnitude of a bulge/disk a distribution of effective radii and surface brightness, they are moreover crucial for generating realistic mock catalogs with all existing galaxy types, which are necessary to control the systematic effects in the forthcoming very large surveys (Euclid, LSST).

Finally, I examine the color and color gradients of bulges and disks as a function of morphological type. Bulge colors are overall stable while disk redden along the Hubble sequence, from late to early types. Spiral disks are bluer than the bulges embedded at their center but this difference fades for early type spiral and lenticular galaxies. The reddening of whole galaxies along the Hubble sequence, as they transition from the Blue Cloud to the Red Sequence, can therefore be explained as a combination of two effects: the growth of the bulge implies that the redder component of a galaxy participates to an increasingly higher fraction of its flux, whereas the reddening of the disk, which is related to star formation fading, means that mostly older stars emitting redder light remain in the galaxy. We measure color gradients of opposite directions in the bulges and disk of spirals, whose amplitude is maximal for Sbc to Scd types, with a mean difference between the effective radii of the g and i bands of $\sim -20\%$ and $\sim +10$ for bulges and disks respectively. Bulges appear redder outwards as the residual star formation occurring in them is centrally concentrated, maybe due to the shear of bar-like pseudo-bulges preventing star formation at the edge of the bulge. In contrast, disks appear bluer outwards, so their star formation is relatively suppressed in its innermost regions, which we interpret as a bar quenching effect.

Overall, the Hubble sequence therefore appears to be an inverse sequence of galaxy physical evolution: morphology changes continuously from Irregulars, through spirals, up to lenticulars and elliptical types, while galaxies grow in stellar mass, and their star formation fades to quiescence. The growth of the bulge characterizes this evolution, with a transition from pseudo to classical bulges, as well as a reddening of the disk. All presented evidence is consistent with galaxy interactions such as mergers, and internal instabilities such as bars and rings, to drive this morphological evolution. A hierarchical formation scenario is therefore proposed for the establishment of the present-day Hubble sequence.

Perspectives

MorCat a magnitude-limited sample of the nearby Universe

As explained in Sect. 2.2.3, the EFIGI catalog of 4458 galaxies is a sub-sample of a larger magnitude-limited ($g \leq 15.5$) catalog called MorCat. It was extracted from HyperLeda (Makarov et al. 2014) assuming that all galaxies to that g limit are included to $B_T \leq 18.0$. After restricting this HyperLeda sample to a sky mask corresponding to the SDSS northern galactic cap, extracting the images of each galaxy from the SDSS image database, measuring their photometry by bulge and disk modeling using SExtractor (Bertin & Arnouts 1996), and discarding spurious sources (unresolved objects and image artifacts), a total of 20126 MorCat galaxies with $g \leq 15.5$ are obtained. I will apply my bulge and disk decomposition methodology to the full sample, in order to characterize its 20126 galaxies. This will allow me to obtain the distribution of all bulge and disk structural parameters for a galaxy population representative of the nearby Universe, which can be named a "morphometric" characterization. MorCat is not affected by the type selection effects of EFIGI (see Sect. 2.2.3). A magnitude-limited sample is not a volume-limited representation of the nearby galaxy population either, but it is possible to evaluate the biases it introduces against faint galaxies by by making some homogeneity assumptions (see the volume correction performed in Sect. 4.5 of Quilley & de Lapparent 2023).

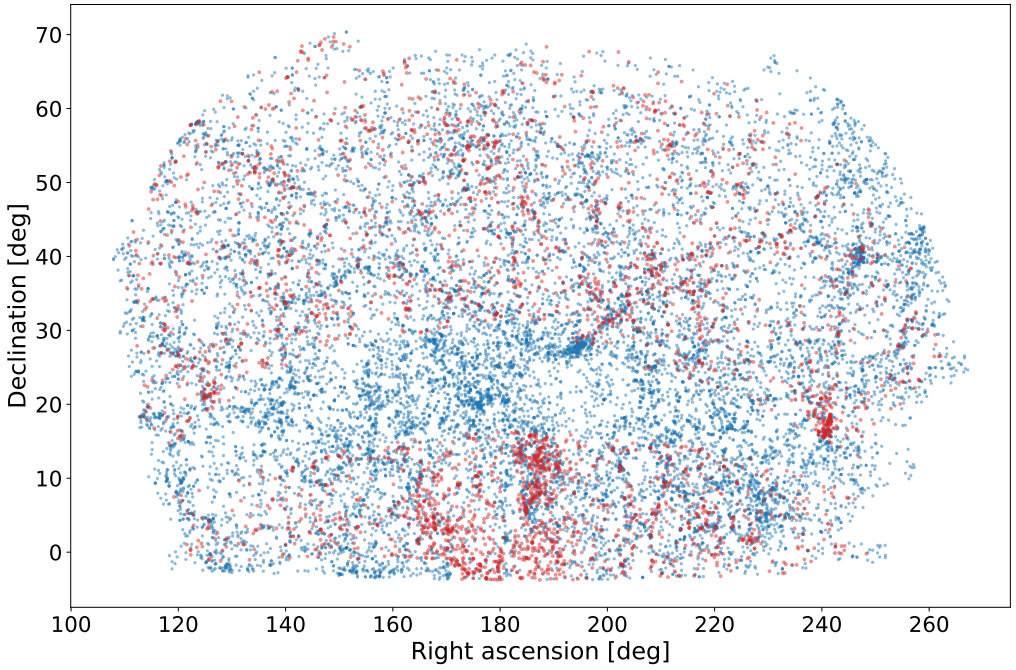

Figure P.1: Sky coordinates of the 20126 MorCat galaxies with $g \leq 15.5$ (in blue), as well as the 3801 EFIGI galaxies restricted to the northern galactic cap (in red).

A morphometric sequence of galaxy types

For MorCat galaxies not included in the EFIGI catalog, no visual classification has been performed, so we do not have access to the same richness of information about their morphology: the 16 shape attributes on a 5-level scale designed for EFIGI are undefined, and are replaced with the binary information provided by the HyperLeda database (Makarov et al. 2014) about bars, rings, and central nucleus, as well as the RC3 morphological type. Therefore, we intend to use our in-depth study of EFIGI to infer a morphological type by leveraging the knowledge we have acquired about correlations between Hubble type and the flux and structural parameters: B/T, disk color, bulge and disk effective radii and absolute magnitudes... Using different sets of the aforementioned parameters, of various sizes and content, I plan to use dimensionality reduction algorithms to summarize this information into a single parameter that would represent a quantitative morphological type. In this approach, EFIGI will constitute a precious validation sample within MorCat. I could also use EFIGI as a training sample in a supervised learning method applied to the bulge and disk parameters in order to retrieve an approximate Hubble type for all MorCat galaxies. Because we have identified many correlations between Hubble type and the flux and structural parameters, it will be interesting to compare their relevance, and methods such as the principal component analysis can bring insight into this question, by deciphering the main predictors, from other correlated quantities. Still regarding the use of machine learning to classify galaxies (Sect. 2.3.3), unsupervised methods could also be used so as to obtain a morphological classification independent of the visual one, and then compare both results, to examine how the new classes are physically motivated.

Luminosity, mass and size functions

Once all MorCat galaxies are characterized, I will be able to compute the distributions of their key parameters, with the novelty that I will be able to do so for not only the whole galaxies, but also their bulges and disks separately, and as a function of the galaxy type(s) that will have been derived (see previous section). Most notably, we would like to obtain the luminosity, mass and size functions of MorCat bulges and disks. These functions would allow us to test the results of hydrodynamical simulations at $z = 0$ from a morphology standpoint, to see if the physics encoded can reproduce the more detailed properties of observed galaxy populations, beyond the global galaxy luminosity functions, which are now well reproduced (see Sect. 1.3.5).

Preliminary measurements based on EFIGI (corrected for incompleteness in apparent magnitude) indicate that the luminosity functions of whole galaxies vary along the morphological sequence with a fainter characteristic magnitude and a steeper faint-end slope for later Hubble types. This effect converts into a similar variation for smaller B/T, as we obtained evidence of the importance of this ratio in Quilley & de Lapparent (2022) and its relation with morphological changes. In contrast, these preliminary measurements of the bulge and disk luminosity functions show markedly different behaviors with B/T, with a systematic dimming of the characteristic luminosity by 4 magnitudes from $B/T \sim 0.6$ to $B/T \sim 0.03$ for bulges, but a constant characteristic magnitude across the same B/T range and down to $B/T \sim 0.006$ for disks (de Lapparent & Lheureux 2023, private communication). These results are related to the new power-laws of the bulges and disk effective radii with B/T that we brought to light in Quilley & de Lapparent (2023). These power-laws also indicate that the radii distribution are systematically shifted to smaller sizes for smaller B/T, with a smaller exponent for disks compared to bulges. Altogether, this suggests that it would be insightful to compute bi-variate distribution functions of luminosity, mass or size with B/T. This would hold the strong advantage to provide implicitly the B/T probability distributions for the full Hubble sequence of nearby galaxies. Moreover, in Quilley & de Lapparent (2023), we obtained convex size-luminosity relations for bulges and disks, with a Gaussian dispersion in effective radii around them. Therefore, rather than obtaining distinct luminosity and size distributions, it would be more appropriate to compute the joint probability distributions through bi-variate functions, for bulges and disks.

Mock galaxy fields and catalogs

The size-luminosity distribution of bulges and disks derived from the EFIGI galaxies in Quilley & de Lapparent (2023), as well as the probability distributions of the bulge and disk sizes and luminosities that are in preparation would be very useful for generating synthetic images of galaxy fields. To prepare the astrophysical analysis of a survey, mock catalogs and images are produced and studied with a forward modeling pipeline reproducing the future observations by the telescope. The systematic effects and biases of the survey are then evaluated by comparing the input data to the measurements extracted from the images. The process of creating mock galaxies that reproduce as faithfully as possible our Universe is therefore a challenge for any observational mission.

A key and topical example is the Euclid mission whose core science objective is derive constraints on the dark energy responsible for the acceleration of the expansion of the Universe. To measure the imprints of dark energy over the last 10 billion years, two cosmological probes will be used by the Euclid space telescope: weak gravitational lensing and galaxy clustering. The former probe consists in measuring the gravitational lensing with large scale-structures, referred to as "cosmic shear", which elongates background galaxies in a coherent way and produces an alignment of these sources. To measure such effects, Euclid will observe 10 billion galaxies, among which 1 billion will serve for the weak lensing measurements, and most of the signal will come from sources that are located in the redshift interval $0.7 < z < 2.0$ (Laureijs et al. 2011). Because the shear measurements will be derived from the distorted shapes of distant galaxies, knowing their intrinsic morphologies, sizes and luminosities across the $0.7-2.0$ redshift range is pivotal in exploiting Euclid data at its fullest, in order to reach the best precision in the constraints on the cosmological parameters given the characteristics of the telescope and planned surveys. Indeed, galaxies with different properties will be affected by different systematics, which might in the end impair the shear measurement.

The mock galaxy catalog used by Euclid is the Flagship catalog, based on a large volume dark matter particle simulation, and that uses the 'halo occupation distribution' (HOD) formalism to assign galaxies inside the dark mater halos. The morphological properties of galaxies within the flagship catalog are provided by a study of the CANDELS survey (Dimauro et al. 2018) of 17,600 galaxies in the redshift interval $0 < z < 2$, with a limited number of spectroscopic redshifts available (< 3000, as CANDELS is a fraction of the GOODS North and South surveys, see Dahlen et al. 2013). While this catalog has been very useful to prepare the data processing pipelines before launch, extensive modeling of all realistic morphological types at the various redshifts of interest is needed to exploit Euclid exquisite data set at its fullest.

In order to include in the Euclid mocks the evolution of the bulges and disks of the various galaxy types, one essentially needs to know how the $z \sim 0$ scaling relations that we derived in Quilley & de Lapparent (2023) evolve with redshift. There are few such analyses using HST data, and significant discrepancies exist between their results. For instance, Bruce et al. (2014) and Dimauro et al. (2019) measure the evolution of the size-mass relation of bulges and disks for galaxies in the CANDELS field, and while both studies find comparable results for the bulge sizes, the disk sizes differ by 70% for $1 < z < 2$. Regarding the COSMOS survey, the recent results of Mowla et al. (2019) provide a size-mass relation for whole galaxies, but objects are modeled as single profiles, so their results can not be compared to those aforementioned. Apart from the study of Huertas-Company et al. (2007) for a sample of 79 galaxies only, there is no published study on the size evolution of galaxies using bulge and disk decompositions with larger statistics in the COSMOS field.

In addition to the size evolution of the bulges and disks of galaxies of all types and absolute magnitudes, one needs to know what is the proportion of the various morphological types with redshift. We suggest in Quilley & de Lapparent (2022) that the bulge-to-total light ratio (B/T) of a galaxy and the color of its disk can parameterize the full Hubble sequence (this is further developed in Sect. 6.2). Ideally one could use about ten types to represent the diversity across the whole Hubble sequence and about ten redshift intervals of 0.2 to track evolution over the full interval $0 < z < 2$, which would divide any observed or simulated sample into about 100 type times redshift sub-samples. To have a reliable description of the evolution of galaxies in this context, sub-samples with sufficient statistics would be desired. For example, the results of Mowla et al. (2019) and Dimauro et al. (2019) use large redshift intervals of 0.5 in order to limit the uncertainties in the effective radii and to be able to detect

variations with redshift.

Unfortunately, for the 17,600 galaxies characterized by Dimauro et al. (2018) that are actually used for the Euclid mocks, this would on average yield 176 galaxies per type and redshift sub-sample. However, as elliptical and lenticulars are much rarer than spirals in the present Universe, and even more so in the past, there would be a large variance in the number of galaxies per type interval, and some systematic shifts per redshift interval as well. I therefore caution that the morphological sample used by the Euclid Flagship mock catalog may have insufficient statistics for deriving a realistic picture of the Hubble sequence and its evolution over the last 10 billion years ($z < 2$).

One solution would be to use exquisite image quality deep ground based surveys such as the Canada-France-Hawaï Telescope Legacy Survey (CFHTLS) *ugriz* (Hudelot et al. 2012) and the WIRCam Deep Survey (WIRDS) *JHK* (Bielby et al. 2012) of the four 1 deg^2 deep fields, as well as the Hyper SuprimeCam (HSC) Subaru Strategic Program (SSP) survey providing *grizy* (and 3 narrow IR bands) photometry in 4 deep fields covering 26 deg^2 (Aihara et al. 2018). For example, the bulge and disk decomposition of the CFHTLS Deep fields using SourceXtractor++ would lead to the creation of an unprecedented morphological sample of 250,000 galaxies to $z < 1.5$. These data have a combination of deep flux limit and superb seeing (0.6 arcsec seeing in the g and K bands), allowing such a morphological analysis. The 250,000 galaxies to $z < 2.0$ contained in these images with photometric redshifts from Coupon et al. (2009) will increase the sample size by a factor of ~ 15 compared to Dimauro et al. (2018). Moreover, thanks to the already measured spectroscopic redshifts of $\sim 30,000$ and $\sim 12,000$ galaxies by zCOSMOS (Lilly et al. 2007) and the VIMOS VLT Deep Survey (Le Fèvre et al. 2005) respectively, within the CFHTLS fields, one would be able check the reliability of the evolution derived from the photometric redshifts. Such an analysis would provide useful measurements of the evolution in luminosity, size and frequency of the various bulges and disks that constitute the different types of the Hubble sequence, with statistics and the potential to reduce the systematics in the Euclid shear measurements.

Besides, as the overwhelming amount of data that will be obtained by forthcoming surveys, such as Euclid telescope and Vera Rubin Observatory, calls for data processing based on machine learning. Providing a large data set of bulge and disk parameters will also be of great value for supervised machine learning algorithms.

History of the Hubble sequence

As already mentioned, studies of the evolution of galaxy sizes at intermediate to high redshifts ($z < 3$) from Hubble Space Telescope (HST) imaging, such as CANDELS or COSMOS have provided a basis to study morphology as a function of redshift, but mostly based on 1-profile modeling (Mowla et al. 2019), or shape and texture characterization

(Whitney et al. 2021). Thanks to better angular resolution and redder rest-wavelengths, the early results from the stupendous deep images recently taken by the James Webb space telescope (JWST) show that the fraction of disk galaxies is higher than previously estimated at $z > 1.5$ from HST imaging (Jacobs et al. 2023), and even dominate to redshifts as high as 8, with most of the stars in the Universe being formed inside spiral galaxies up to $z \sim 6$ (Ferreira et al. 2022). The Hubble sequence therefore formed very early in the history of the Universe and this justifies the extensive use of bulge+disk modeling at all redshifts.

It therefore appears realistic and fundamental to trace the evolution of the Hubble sequence back in time. This could be performed by characterizing and determining the relative frequencies of the entire variety of morphological types in the local and distant Universe based on their bulge and disk characteristics. Major changes with redshift are expected as galaxies, when they evolve, take all morphologies from their initial state as small irregular building blocks, to spirals and lenticulars, and eventually giant ellipticals.

To this end, my adapted methodology for performing reliable bulge+disk modeling on deep galaxy images could be applied to existing HST data (CANDELS), as well as the recent and forthcoming surveys from the JWST and Euclid space missions. This will be essential to reconstruct the Hubble sequence and its evolution over time. One can expect to see an increase in the frequency of late-type

galaxies (late spirals and irregulars) with redshift, while early-types are expected to be rarer. I would also test whether the properties of the bulges and disks of a given type (effective radii, B/T...) change with redshift, or whether the evolution of galaxy populations over cosmic time is a varying mix of types, within a settled Hubble sequence.

In that regard, I am particularly interested in the galaxies that will be observed by the Euclid telescope, that was launched the 1^st of July of 2023. I intend to adapt and apply my bulge and disk modeling approach directly on galaxies from the first Euclid quick release Q1, with $\sim 5\,10^5$ galaxies over 50 deg^2. As a member of Euclid consortium, I will have access to these data in the summer of 2024. And I will be able to extend this analysis to the first data release DR1 ($\sim 10^7$ galaxies over 2500 deg^2) scheduled for December 2024 for consortium members (and December 2025 for the public release). The quality of these spatial images, with a 0.1 and 0.3 arcsec angular resolution in the optical and infrared respectively, and the large statistics should allow me to study the evolution of galaxy types as well as their relative frequencies using their bulge and disk size and luminosities up to $z \sim 3$ (Euclid Collaboration et al. 2022). I will also use extensive image simulations of the CFHTLS-Deep fields using Stuff and SkyMaker (Bertin 2009), to control the systematics in the bulge and disk sizes, as well as the type variations derived from the images. The ability to reliably measure galaxy morphology beyond the redshift of the peak of cosmic star formation at $z \sim 2$, called the "Cosmic Noon" (Madau & Dickinson 2014), will notably be key to decipher how the morphological transformations around this epoch are related to the inversion of the cosmic star formation rate at this peak redshift.

Morphologies of galaxies along the Cosmic Web

The large-scale environment of galaxies as defined by the cosmic web is shown in numerical simulations with dark matter and gas hydrodynamics (see Sect. 1.3.5 to contribute to determining their morphologies: mergers of spirals from walls induce their spin alignments with the filaments, but misaligned angular momenta of accreted material in nodes lead to spheroids (Sales et al. 2012; Dubois et al. 2014). I intend to examine where the various EFIGI and MorCat morphological types are located among the sheets, filaments and nodes (corresponding to clusters) of the large-scale structure in the SDSS volume, in collaboration with Katarina Kraljic who has expertise in applying the DISPERSE code (Sousbie 2011) for extracting these structures from galaxy surveys. Other maps of the cosmic web are already available (Jasche et al. 2015) and could also be used. This study may help to understand the quenching of galaxies in terms of changes in replenishment of the gas reservoir, maybe via the cosmic streams (Dekel & Birnboim 2006), and more generally, to identify where the morphological transformations from the Blue Cloud to the Red Sequence occur. Such an analysis would provide more stringent constraints than the mere type segregation effects in galaxy color along the cosmic web (Kraljic et al. 2018).

Bridging observations and simulations

Any observed trend in the morphological types of the EFIGI-MorCat galaxies detected along the present-time cosmic web structures would have to also be present in the numerical simulations. More generally, generating realistic simulations requires to constrain them with the observed galaxy properties at various redshifts, including the present time. The EFIGI-MorCat sample is therefore useful to test whether simulated galaxies resemble closely real objects in the present Universe. Moreover, simulations are not hampered by the drawback of observations that we only see each galaxy at its specific age and at a specific epoch since the Big Bang: simulations allow us to follow statistical samples of all galaxy types over their full cosmic history. In Quilley & de Lapparent (2022), we have already confronted the formation pathways seen in simulations to the evolutionary picture inferred from the EFIGI analysis. Deriving from cosmological volumes the color-mass diagram complemented by B/T and disk color would be a first simple, but critical test of the simulations. In a second stage, producing projected images of the simulated galaxies as they will be observed for example by the Euclid spatial telescope, and then performing reliable bulge+disk modeling using SourceXtractor++ would

allow to monitor the possible biases due to observational effects, and thus provide the most meaningful comparison between observed and simulated galaxies.

Varying dust extinction with disk inclination

It would be interesting to revisit the analysis of Driver et al. 2007 by studying the bulge and disk parameters of the EFIGI sample over all disk inclinations (as galaxies with `Inclination`=3 or 4 have been discarded in the analyses performed in this thesis). Indeed, measuring the varying luminosities of disks all the way from face-on to edge-on would allow one to estimate the varying dust extinction with inclination for the various morphological types. Although the bulge and disk decomposition is more prone to errors because of dust lanes that sometime obscure part of the bulge, there should be sufficient statistics for such a study, and even more with MorCat (see Sect. 6.2).

Improved modeling beyond the Sérsic and exponential profiles

In this thesis, I have confirmed using the EFIGI catalog that non-peculiar, hence the majority of galaxies in the nearby Universe are dominated by one or two components, a spheroid (or bulge) and a disk component, with specific profiles and colors that characterize the evolution of stars and their dynamical rearrangements with time. Because they correspond to first-order variations over the disk and bulge properties, spiral arms, bars, rings, and dust lanes are rarely modeled. I discuss below the potential interest of adding new components to the modeling of EFIGI galaxies, and address the limitations of the Sérsic bulge and exponential disk decomposition used here.

Is the Sérsic profile suited for all bulges and spheroids ?

The Sérsic model, and even more for large values of the Sérsic index, show huge variations in light intensity at its center, that are spread over a limited number of pixels, hence are poorly sampled by the PSF. In our model-fitting of EFIGI galaxies, this takes the form of many spheroids (either E or bulges) being improperly fitted at their center. In Fig. P.2 we see two examples of residuals showing an excess of light at the very center surrounded by a narrow black ring, indicating that the model overestimates surface brightness in this area. The presence of these structures in residual images points out to a limitation in correctly modeling the innermost parts of spheroid light profiles with the Sérsic profile. Modeling of some EFIGI bulges were successfully performed using two Sérsic profiles, and the obtained effective radii differ by 50% to a factor of 4.

Modeling galactic bars and rings

Throughout this thesis, I focus on the two main components of galaxies that are bulges and disks, but this work also provides evidence that dynamical features, such as bars and rings (see Sect. 4.5), may play a role in the evolution of galaxies (Quilley & de Lapparent 2022). This case was made through an extensive use of the EFIGI visual morphological attributes that measure the presence and strength of these features. To go beyond these visual indicators, one would like to obtain quantitative measurements of these features, so additional light profiles must be added in the SourceXtractor++ routine in order to model the bars and rings of galaxies. In the 0.16 release of SourceXtractor++ was added the possibility to include *ad hoc* models. We already mention this new feature in Sect. 3.1.5-b, which we used to implement inner-truncated disk profiles in our modeling.

In that regard, EFIGI provides us with an extensive sample of 1886 barred galaxies and 1229 ringed galaxies (counting either outer and inner rings, and with 236 galaxies actually exhibiting both) to be used to test and improve the modeling of these features. Therefore, it would be interesting and challenging to create a bulge+disk+bar, a bulge+disk+ring and a bulge+disk+bar+ring decomposition method. A proof of concept for the addition of such profiles is briefly presented in Kümmel et al. (2022) with a Sérsic+bar+ring model of the M95 galaxy i-band image, but the remaining structure seen in the residual indicates that the bar and ring models need to be improved (the ring model is too diffuse, and the bar too long and of insufficient flux, causing a residual bimodal structure). Moreover, there is

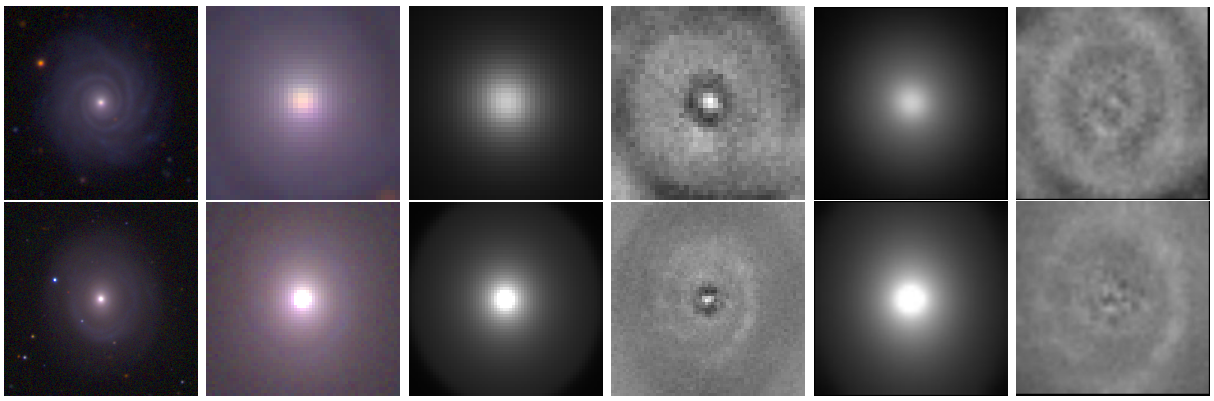

Figure P.2: From left to right: *gri* composite color image of the galaxy and of the bulge, model-fitting and residual of the bulge in the g band with a single Sérsic profile, and with two Sérsic profiles, for PGC0010108 and PGC0047678 in the top and bottom rows, respectively. Both examples show that with a single Sérsic profile there remains an excess of light in the very center of the bulge whereas the level of flux in its outskirts is over-estimated by the model. The modeling with two Sérsic profiles displays an improvement, as the amplitude of the residual structures at the location of the bulge are significantly lower.

an additional difficulty for the bars due to their "rectangular" shape, which would require that more complex profiles than the current pure radial variation with elliptical symmetry, and an aspect ratio to control the elongation, be developed in SourceXtractor++. The EFIGI visual morphological attributes present the strong advantage that they can be used to control the successes and possible failures of the high-dimensional fits beyond bulge and disk decomposition. If one intends to extend the fitting of bars and rings to MorCat galaxies, hence without prior information on the presence of these features, a criterion must be developed to assess if the added bar and ring profiles improve or not the modeling.

The parameters of the bar and ring profiles should provide one with exhaustive data about the share of flux (hence of mass) within these structures compared to the total galaxy, but also to examine the possible biases in the measure of B/T for barred galaxies, in which the bar and bulge components are difficult to disentangle, and which lead to the zoom-in procedure that I developed.

It would be particularly interesting to measure the colors of both bars and rings, in order to compare them with the bulge and disk colors of their host galaxy. Colors tell us about the stellar populations that constitute theses structures, and can therefore provide very valuable insight into their build-up, the star formation activity within them, as well as the stellar migrations within the galaxy, radial migration being already known to be related to the bar (Brunetti et al. 2011; Minchev et al. 2011; Di Matteo et al. 2013).

Visual examination of many EFIGI galaxies has lead us to notice some systematic color effects related to bars and rings, whose validity could be assessed by pursuing such an analysis. On the one hand, it seems that some rings are the locus of star formation while other are made up of old stars. One could measure the colors of the rings and compare them to the disk color to examine whether rings are simply rearrangement of disk stars, or trigger locally enhanced star formation as in spiral arms. On the other hand, it would be interesting to investigate the role of the bar in building the bulge and eventually quenching the galaxy (Khoperskov et al. 2018). In order to do so, one would need to examine the color of the bar in relation to bulge and disk colors as well as B/T. Moreover, measuring the bar length would allow one to probe the possible color gradients within the inner part of the disk spanned by the bar and the remaining outer part of the disk.

Bibliography

Abazajian, K. N., Adelman-McCarthy, J. K., Agüeros, M. A., et al. 2009, ApJS, 182, 543

Abdurro'uf, Accetta, K., Aerts, C., et al. 2022, ApJS, 259, 35

Abraham, R. G. & van den Bergh, S. 2001, Science, 293, 1273

Adelman-McCarthy, J. K., Agüeros, M. A., Allam, S. S., et al. 2008, ApJS, 175, 297

—. 2006, ApJS, 162, 38

Aguerri, J. A. L., Balcells, M., & Peletier, R. F. 2001, A&A, 367, 428

Aihara, H., Arimoto, N., Armstrong, R., et al. 2018, PASJ, 70, S4

Alam, S., Albareti, F. D., Allende Prieto, C., et al. 2015, ApJS, 219, 12

Allen, P. D., Driver, S. P., Graham, A. W., et al. 2006, MNRAS, 371, 2

Anderson, K. S. J., Baggett, S. M., & Baggett, W. E. 2004, AJ, 127, 2085

Ann, H. B., Seo, M., & Ha, D. K. 2015, ApJS, 217, 27

Athanassoula, E. 2005, MNRAS, 358, 1477

Athanassoula, E. 2008, in Formation and Evolution of Galaxy Bulges, ed. M. Bureau, E. Athanassoula, & B. Barbuy, Vol. 245, 93–102

—. 2013, in Secular Evolution of Galaxies, ed. J. Falcón-Barroso & J. H. Knapen, 305

Athanassoula, E., Rodionov, S. A., Peschken, N., & Lambert, J. C. 2016, ApJ, 821, 90

Baggett, W. E., Baggett, S. M., & Anderson, K. S. J. 1998, AJ, 116, 1626

Baillard, A., Bertin, E., de Lapparent, V., et al. 2011, A&A, 532, A74

Balcells, M. & Peletier, R. F. 1994, AJ, 107, 135

Baldry, I. K., Balogh, M. L., Bower, R., Glazebrook, K., & Nichol, R. C. 2004a, in American Institute of Physics Conference Series, Vol. 743, The New Cosmology: Conference on Strings and Cosmology, ed. R. E. Allen, D. V. Nanopoulos, & C. N. Pope, 106–119

Baldry, I. K., Balogh, M. L., Bower, R. G., et al. 2006, MNRAS, 373, 469

Baldry, I. K., Driver, S. P., Loveday, J., et al. 2012, MNRAS, 421, 621

Baldry, I. K., Glazebrook, K., Brinkmann, J., et al. 2004b, ApJ, 600, 681

Ball, N. M., Loveday, J., Fukugita, M., et al. 2004, MNRAS, 348, 1038

Balogh, M. L., Baldry, I. K., Nichol, R., et al. 2004, ApJLett, 615, L101

Barnes, J. E. & Hernquist, L. E. 1991, ApJLett, 370, L65

Bellanger, C., de Lapparent, V., Arnouts, S., et al. 1995, Astron. Astrophys. Suppl. Ser., 110, 159

Bertin, E. 2009, Mem. Soc. Astron. Italiana,, 80, 422

Bertin, E. & Arnouts, S. 1996, Astron. Astrophys. Suppl. Ser., 117, 393

Bertin, E., Schefer, M., Apostolakos, N., et al. 2020, in Astronomical Society of the Pacific Conference Series, Vol. 527, Astronomical Data Analysis Software and Systems XXIX, ed. R. Pizzo, E. R. Deul, J. D. Mol, J. de Plaa, & H. Verkouter, 461

Bertone, G., Hooper, D., & Silk, J. 2005, Physics Reports, 405, 279

Bianchi, L., Shiao, B., & Thilker, D. 2017, ApJS, 230, 24

Bielby, R., Hudelot, P., McCracken, H. J., et al. 2012, A&A, 545, A23

Binggeli, B., Sandage, A., & Tarenghi, M. 1984, AJ, 89, 64

Birnboim, Y. & Dekel, A. 2003, MNRAS, 345, 349

Blanton, M. R., Hogg, D. W., Bahcall, N. A., et al. 2003, ApJ, 592, 819

Blitz, L. 1993, in Protostars and Planets III, ed. E. H. Levy & J. I. Lunine, 125

Block, D. L., Bertin, G., Stockton, A., et al. 1994, A&A, 288, 365

Bluck, A. F. L., Conselice, C. J., Bouwens, R. J., et al. 2009, MNRAS, 394, L51

Bluck, A. F. L., Maiolino, R., Brownson, S., et al. 2022, A&A, 659, A160

Blumenthal, G. R., Faber, S. M., Primack, J. R., & Rees, M. J. 1984, Nature, 311, 517

Boquien, M., Burgarella, D., Roehlly, Y., et al. 2019, A&A, 622, A103

Bournaud, F., Combes, F., & Jog, C. J. 2004, A&A, 418, L27

Bournaud, F., Elmegreen, B. G., & Elmegreen, D. M. 2007, ApJ, 670, 237

Bournaud, F., Jog, C. J., & Combes, F. 2005, A&A, 437, 69

Bower, R. G., Benson, A. J., Malbon, R., et al. 2006, MNRAS, 370, 645

Breda, I., Papaderos, P., & Gomes, J.-M. 2020, A&A, 640, A20

Bridge, C. R., Carlberg, R. G., & Sullivan, M. 2010, ApJ, 709, 1067

Brinchmann, J., Charlot, S., White, S. D. M., et al. 2004, MNRAS, 351, 1151

Brooks, A. M., Solomon, A. R., Governato, F., et al. 2011, ApJ, 728, 51

Bruce, V. A., Dunlop, J. S., McLure, R. J., et al. 2014, MNRAS, 444, 1660

Brunetti, M., Chiappini, C., & Pfenniger, D. 2011, A&A, 534, A75

Bruzual, G. 1981, Spectral evolution of galaxies

Bundy, K., Bershady, M. A., Law, D. R., et al. 2015, ApJ, 798, 7

Buta, R. 1995, ApJS, 96, 39

Buta, R. & Combes, F. 1996, Fundamentals of Cosmic Physics, 17, 95

Buta, R., Laurikainen, E., Salo, H., & Knapen, J. H. 2010, ApJ, 721, 259

Buta, R. J. 2011, arXiv e-prints, arXiv:1102.0550

—. 2019, MNRAS, 488, 590

Cameron, E., Driver, S. P., Graham, A. W., & Liske, J. 2009, ApJ, 699, 105

Cappellari, M. 2016, An. Rev. Ast. Astroph., 54, 597

Cappellari, M., Emsellem, E., Krajnović, D., et al. 2011, MNRAS, 416, 1680

Cappellari, M., McDermid, R. M., Alatalo, K., et al. 2013, MNRAS, 432, 1862

Carassou, S., de Lapparent, V., Bertin, E., & Le Borgne, D. 2017, A&A, 605, A9

Cattaneo, A., Dekel, A., Devriendt, J., Guiderdoni, B., & Blaizot, J. 2006, MNRAS, 370, 1651

Chabrier, G. 2003, PASP, 115, 763

Cheng, T.-Y., Conselice, C. J., Aragón-Salamanca, A., et al. 2021a, MNRAS, 507, 4425

—. 2020, MNRAS, 493, 4209

Cheng, T. Y., Domínguez Sánchez, H., Vega-Ferrero, J., et al. 2023, MNRAS, 518, 2794

Cheng, T.-Y., Huertas-Company, M., Conselice, C. J., et al. 2021b, MNRAS, 503, 4446

Chevallard, J. & Charlot, S. 2016, MNRAS, 462, 1415

Ciotti, L., D'Ercole, A., Pellegrini, S., & Renzini, A. 1991, ApJ, 376, 380

Combes, F., Debbasch, F., Friedli, D., & Pfenniger, D. 1990, A&A, 233, 82

Combes, F. & Sanders, R. H. 1981, A&A, 96, 164

Conroy, C. 2013, An. Rev. Ast. Astroph., 51, 393

Conselice, C. J. 2003, ApJS, 147, 1

Conselice, C. J., Bershady, M. A., Dickinson, M., & Papovich, C. 2003, AJ, 126, 1183

Conselice, C. J., Mundy, C. J., Ferreira, L., & Duncan, K. 2022, ApJ, 940, 168

Costantin, L., Méndez-Abreu, J., Corsini, E. M., et al. 2018, A&A, 609, A132

Coupon, J., Ilbert, O., Kilbinger, M., et al. 2009, A&A, 500, 981

Croton, D. J., Springel, V., White, S. D. M., et al. 2006, MNRAS, 365, 11

Dahlen, T., Mobasher, B., Faber, S. M., et al. 2013, ApJ, 775, 93

Davé, R., Rafieferantsoa, M. H., Thompson, R. J., & Hopkins, P. F. 2017, MNRAS, 467, 115

Davidzon, I., Laigle, C., Capak, P. L., et al. 2019, MNRAS, 489, 4817

Davies, R. L., Efstathiou, G., Fall, S. M., Illingworth, G., & Schechter, P. L. 1983, ApJ, 266, 41

Davis, M., Efstathiou, G., Frenk, C. S., & White, S. D. M. 1985, ApJ, 292, 371

de Jong, R. S. 1996, A&A, 313, 45

de Jong, R. S. & Lacey, C. 2000, ApJ, 545, 781

de Lapparent, V. 2003, A&A, 408, 845

de Lapparent, V., Baillard, A., & Bertin, E. 2011, A&A, 532, A75

de Lapparent, V., Geller, M. J., & Huchra, J. P. 1986, ApJLett, 302, L1

De Rossi, M. E., Bower, R. G., Font, A. S., Schaye, J., & Theuns, T. 2017, MNRAS, 472, 3354

de Vaucouleurs, G. 1948, Annales d'Astrophysique, 11, 247

—. 1959, Handbuch der Physik, 53, 275

de Vaucouleurs, G., de Vaucouleurs, A., Corwin, Herold G., J., et al. 1991, Third Reference Catalogue of Bright Galaxies

Debattista, V. P., Mayer, L., Carollo, C. M., et al. 2006, ApJ, 645, 209

Deeley, S., Drinkwater, M. J., Sweet, S. M., et al. 2021, MNRAS, 508, 895

Dekel, A. & Birnboim, Y. 2006, MNRAS, 368, 2

—. 2008, MNRAS, 383, 119

Dekel, A., Lapiner, S., Ginzburg, O., et al. 2020, MNRAS, 496, 5372

Di Matteo, P., Gómez, A., Haywood, M., et al. 2015, A&A, 577, A1

Di Matteo, P., Haywood, M., Combes, F., Semelin, B., & Snaith, O. N. 2013, A&A, 553, A102

Di Matteo, P., Haywood, M., Gómez, A., et al. 2014, A&A, 567, A122

Di Matteo, T., Springel, V., & Hernquist, L. 2005, Nature, 433, 604

Dickinson, M., Giavalisco, M., & GOODS Team. 2003, in The Mass of Galaxies at Low and High Redshift, ed. R. Bender & A. Renzini, 324

Dimauro, P., Huertas-Company, M., Daddi, E., et al. 2018, MNRAS, 478, 5410

—. 2019, MNRAS, 489, 4135

Djorgovski, S. & Davis, M. 1987, ApJ, 313, 59

Domínguez Sánchez, H., Margalef, B., Bernardi, M., & Huertas-Company, M. 2022, MNRAS, 509, 4024

D'Onghia, E., Vogelsberger, M., & Hernquist, L. 2013, ApJ, 766, 34

Dressler, A. 1980, ApJ, 236, 351

Dressler, A., Oemler, Augustus, J., Butcher, H. R., & Gunn, J. E. 1994, ApJ, 430, 107

Driver, S. P., Hill, D. T., Kelvin, L. S., et al. 2011, MNRAS, 413, 971

Driver, S. P., Popescu, C. C., Tuffs, R. J., et al. 2007, MNRAS, 379, 1022

Dubois, Y., Pichon, C., Welker, C., et al. 2014, MNRAS, 444, 1453

Dunkley, J., Komatsu, E., Nolta, M. R., et al. 2009, ApJS, 180, 306

Elagali, A., Lagos, C. D. P., Wong, O. I., et al. 2018, MNRAS, 481, 2951

Emsellem, E., Cappellari, M., Krajnović, D., et al. 2011, MNRAS, 414, 888

—. 2007, MNRAS, 379, 401

Erroz-Ferrer, S., Carollo, C. M., den Brok, M., et al. 2019, MNRAS, 484, 5009

Euclid Collaboration, Bretonnière, H., Huertas-Company, M., et al. 2022, A&A, 657, A90

Ferrari, F., de Carvalho, R. R., & Trevisan, M. 2015, ApJ, 814, 55

Ferreira, L., Conselice, C. J., Sazonova, E., et al. 2022, arXiv e-prints, arXiv:2210.01110

Fioc, M. & Rocca-Volmerange, B. 1997, A&A, 326, 950

—. 1999, arXiv e-prints, astro

—. 2019, A&A, 623, A143

Fisher, D. B. & Drory, N. 2008, AJ, 136, 773

Fisher, D. B. & Drory, N. 2016, in Astrophysics and Space Science Library, Vol. 418, Galactic Bulges, ed. E. Laurikainen, R. Peletier, & D. Gadotti, 41

Fragkoudi, F., Di Matteo, P., Haywood, M., et al. 2018, A&A, 616, A180

Freedman, W. L., Madore, B. F., Gibson, B. K., et al. 2001, ApJ, 553, 47

Freeman, K. C. 1970, ApJ, 160, 811

Gadotti, D. A. 2009, MNRAS, 393, 1531

Gao, H., Ho, L. C., Barth, A. J., & Li, Z.-Y. 2019, ApJS, 244, 34

Geller, M. J. & Huchra, J. P. 1989, Science, 246, 897

Giavalisco, M., Ferguson, H. C., Koekemoer, A. M., et al. 2004, ApJLett, 600, L93

Gil de Paz, A., Boissier, S., Madore, B. F., et al. 2007, ApJS, 173, 185

González-García, A. C. & Balcells, M. 2005, MNRAS, 357, 753

Governato, F., Mayer, L., Wadsley, J., et al. 2004, ApJ, 607, 688

Graham, A. W. & Driver, S. P. 2005, PASA, 22, 118

Grazian, A., Castellano, M., Fontana, A., et al. 2012, A&A, 547, A51

Guiderdoni, B. & Rocca-Volmerange, B. 1987, A&A, 186, 1

Gunn, J. E. & Gott, J. Richard, I. 1972, ApJ, 176, 1

Häußler, B., Vika, M., Bamford, S. P., et al. 2022, A&A, 664, A92

Hogg, D. W. 1999, arXiv e-prints, astro

Hopkins, P. F., Cox, T. J., Younger, J. D., & Hernquist, L. 2009, ApJ, 691, 1168

Hubble, E. P. 1926, ApJ, 63, 236

Hubble, E. P. 1926, ApJ, 64, 321

Hubble, E. P. 1929, ApJ, 69, 103

Huchra, J., Davis, M., Latham, D., & Tonry, J. 1983, ApJS, 52, 89

Hudelot, P., Cuillandre, J. C., Withington, K., et al. 2012, VizieR Online Data Catalog, II/317

Huertas-Company, M., Gravet, R., Cabrera-Vives, G., et al. 2015, ApJS, 221, 8

Huertas-Company, M., Rouan, D., Soucail, G., et al. 2007, A&A, 468, 937

Huertas-Company, M., Rouan, D., Tasca, L., Soucail, G., & Le Fèvre, O. 2008, A&A, 478, 971

Illingworth, G. 1977, ApJLett, 218, L43

Jablonka, P., Martin, P., & Arimoto, N. 1996, AJ, 112, 1415

Jacobs, C., Glazebrook, K., Calabrò, A., et al. 2023, ApJLett, 948, L13

Jarrett, T. H., Chester, T., Cutri, R., et al. 2000, AJ, 119, 2498

Jarrett, T. H., Chester, T., Cutri, R., Schneider, S. E., & Huchra, J. P. 2003, AJ, 125, 525

Jasche, J., Leclercq, F., & Wandelt, B. D. 2015, JCAP, 2015, 036

Kartaltepe, J. S., Rose, C., Vanderhoof, B. N., et al. 2023, ApJLett, 946, L15

Katz, N. & White, S. D. M. 1993, ApJ, 412, 455

Kauffmann, G., White, S. D. M., Heckman, T. M., et al. 2004, MNRAS, 353, 713

Kaviraj, S., Laigle, C., Kimm, T., et al. 2017, MNRAS, 467, 4739

Kawamata, R., Ishigaki, M., Shimasaku, K., et al. 2018, ApJ, 855, 4

Kennicutt, Robert C., J. 1992, ApJS, 79, 255

—. 1998a, An. Rev. Ast. Astroph., 36, 189

—. 1998b, ApJ, 498, 541

Kereš, D., Katz, N., Weinberg, D. H., & Davé, R. 2005, MNRAS, 363, 2

Khoperskov, S., Haywood, M., Di Matteo, P., Lehnert, M. D., & Combes, F. 2018, A&A, 609, A60

Kim, K., Oh, S., Jeong, H., et al. 2016, ApJS, 225, 6

Kirby, E. N., Cohen, J. G., Guhathakurta, P., et al. 2013, ApJ, 779, 102

Klypin, A. A. & Shandarin, S. F. 1983, MNRAS, 204, 891

Koekemoer, A. M., Faber, S. M., Ferguson, H. C., et al. 2011, ApJS, 197, 36

Kormendy, J. 1977a, ApJ, 218, 333

—. 1977b, ApJ, 217, 406

—. 1979, ApJ, 227, 714

Kormendy, J. 1993, in Galactic Bulges, ed. H. Dejonghe & H. J. Habing, Vol. 153, 209

Kormendy, J. & Bender, R. 1996, ApJLett, 464, L119

Kormendy, J. & Ho, L. C. 2013, An. Rev. Ast. Astroph., 51, 511

Kormendy, J. & Illingworth, G. 1982, ApJ, 256, 460

Kormendy, J. & Kennicutt, Robert C., J. 2004, An. Rev. Ast. Astroph., 42, 603

Krajnović, D., Alatalo, K., Blitz, L., et al. 2013, MNRAS, 432, 1768

Krajnović, D., Bacon, R., Cappellari, M., et al. 2008, MNRAS, 390, 93

Kraljic, K., Arnouts, S., Pichon, C., et al. 2018, MNRAS, 474, 547

Kreckel, K., Faesi, C., Kruijssen, J. M. D., et al. 2018, ApJLett, 863, L21

Kreckel, K., Ho, I. T., Blanc, G. A., et al. 2019, ApJ, 887, 80

Kroupa, P. 2001, MNRAS, 322, 231

Kruijssen, J. M. D., Dale, J. E., & Longmore, S. N. 2015, MNRAS, 447, 1059

Kruk, S. J., Lintott, C. J., Bamford, S. P., et al. 2018, MNRAS, 473, 4731

Kumar, A., Das, M., & Kataria, S. K. 2021, MNRAS, 506, 98

Kümmel, M., Álvarez-Ayllón, A., Bertin, E., et al. 2022, arXiv e-prints, arXiv:2212.02428

Kümmel, M., Bertin, E., Schefer, M., et al. 2020, in Astronomical Society of the Pacific Conference Series, Vol. 527, Astronomical Data Analysis Software and Systems XXIX, ed. R. Pizzo, E. R. Deul, J. D. Mol, J. de Plaa, & H. Verkouter, 29

Laigle, C., Davidzon, I., Ilbert, O., et al. 2019, MNRAS, 486, 5104

Lange, R., Driver, S. P., Robotham, A. S. G., et al. 2015, MNRAS, 447, 2603

Larson, R. B., Tinsley, B. M., & Caldwell, C. N. 1980, ApJ, 237, 692

Laureijs, R., Amiaux, J., Arduini, S., et al. 2011, arXiv e-prints, arXiv:1110.3193

Le Borgne, D. & Rocca-Volmerange, B. 2002, A&A, 386, 446

Le Fèvre, O., Vettolani, G., Garilli, B., et al. 2005, A&A, 439, 845

Lee, B., Giavalisco, M., Williams, C. C., et al. 2013, ApJ, 774, 47

Lilly, S. J., Carollo, C. M., Pipino, A., Renzini, A., & Peng, Y. 2013, ApJ, 772, 119

Lilly, S. J., Le Fèvre, O., Renzini, A., et al. 2007, ApJS, 172, 70

Lin, C. C. & Shu, F. H. 1964, ApJ, 140, 646

Lin, L., Koo, D. C., Willmer, C. N. A., et al. 2004, ApJLett, 617, L9

Lintott, C., Schawinski, K., Bamford, S., et al. 2011, MNRAS, 410, 166

Lintott, C. J., Schawinski, K., Slosar, A., et al. 2008, MNRAS, 389, 1179

Livet, F., Charnock, T., Le Borgne, D., & de Lapparent, V. 2021, A&A, 652, A62

Loeb, A. & Barkana, R. 2001, An. Rev. Ast. Astroph., 39, 19

López-Sanjuan, C., Balcells, M., Pérez-González, P. G., et al. 2009, A&A, 501, 505

Lotz, J. M., Primack, J., & Madau, P. 2004, AJ, 128, 163

Madau, P. & Dickinson, M. 2014, An. Rev. Ast. Astroph., 52, 415

Makarov, D., Prugniel, P., Terekhova, N., Courtois, H., & Vauglin, I. 2014, A&A, 570, A13

Man, A. & Belli, S. 2018, Nature Astronomy, 2, 695

Martig, M., Bournaud, F., Teyssier, R., & Dekel, A. 2009, ApJ, 707, 250

Martin, D. C., Fanson, J., Schiminovich, D., et al. 2005, ApJLett, 619, L1

Martin, G., Kaviraj, S., Devriendt, J. E. G., Dubois, Y., & Pichon, C. 2018, MNRAS, 480, 2266

Martini, P., Regan, M. W., Mulchaey, J. S., & Pogge, R. W. 2003a, ApJS, 146, 353

—. 2003b, ApJ, 589, 774

Miller, G. E. & Scalo, J. M. 1979, ApJS, 41, 513

Minchev, I., Famaey, B., Combes, F., et al. 2011, A&A, 527, A147

Mo, H., van den Bosch, F. C., & White, S. 2010, Galaxy Formation and Evolution

Montero-Dorta, A. D. & Prada, F. 2009, MNRAS, 399, 1106

Mortlock, A., Conselice, C. J., Hartley, W. G., et al. 2013, MNRAS, 433, 1185

Mowla, L. A., van Dokkum, P., Brammer, G. B., et al. 2019, ApJ, 880, 57

Nair, P. B. & Abraham, R. G. 2010, ApJS, 186, 427

Nelson, D., Pillepich, A., Springel, V., et al. 2018, MNRAS, 475, 624

Noguchi, M. 1999, ApJ, 514, 77

Pacifici, C., Iyer, K. G., Mobasher, B., et al. 2023, ApJ, 944, 141

Park, M., Tacchella, S., Nelson, E. J., et al. 2021, arXiv e-prints, arXiv:2112.07679

Paturel, G., Fouque, P., Bottinelli, L., & Gouguenheim, L. 1995, VizieR Online Data Catalog, VII/119

Peletier, R. F. & Balcells, M. 1996, AJ, 111, 2238

Peng, C. Y., Ho, L. C., Impey, C. D., & Rix, H.-W. 2002, AJ, 124, 266

—. 2010a, AJ, 139, 2097

Peng, Y.-j., Lilly, S. J., Kovač, K., et al. 2010b, ApJ, 721, 193

Perlmutter, S., Aldering, G., Goldhaber, G., et al. 1999, ApJ, 517, 565

Petrosian, V. 1976, ApJLett, 210, L53

Pillepich, A., Nelson, D., Hernquist, L., et al. 2018, MNRAS, 475, 648

Pozzetti, L., Bolzonella, M., Zucca, E., et al. 2010, A&A, 523, A13

Quilley, L. & de Lapparent, V. 2022, A&A, 666, A170

—. 2023, arXiv e-prints, arXiv:2305.02069

Renzini, A. 1999, in The Formation of Galactic Bulges, ed. C. M. Carollo, H. C. Ferguson, & R. F. G. Wyse, 9

Riess, A. G., Filippenko, A. V., Challis, P., et al. 1998, AJ, 116, 1009

Rix, H.-W. & Rieke, M. J. 1993, ApJ, 418, 123

Robotham, A. S. G., Taranu, D. S., Tobar, R., Moffett, A., & Driver, S. P. 2017, MNRAS, 466, 1513

Rubin, V. C., Ford, W. K., J., & Thonnard, N. 1980, ApJ, 238, 471

Sachdeva, S., Saha, K., & Singh, H. P. 2017, ApJ, 840, 79

Sales, L. V., Navarro, J. F., Theuns, T., et al. 2012, MNRAS, 423, 1544

Salim, S. 2014, Serbian Astronomical Journal, 189, 1

Salim, S., Fang, J. J., Rich, R. M., Faber, S. M., & Thilker, D. A. 2012, ApJ, 755, 105

Salpeter, E. E. 1955, ApJ, 121, 161

Sandage, A. 1961, The Hubble Atlas of Galaxies

Scarlata, C., Carollo, C. M., Lilly, S., et al. 2007, ApJS, 172, 406

Schechter, P. 1976, ApJ, 203, 297

Schinnerer, E., Maciejewski, W., Scoville, N., & Moustakas, L. A. 2002, ApJ, 575, 826

Schlafly, E. F. & Finkbeiner, D. P. 2011, ApJ, 737, 103

Schlegel, D. J., Finkbeiner, D. P., & Davis, M. 1998, ApJ, 500, 525

Schmidt, M. 1959, ApJ, 129, 243

Schwarz, M. P. 1981, ApJ, 247, 77

Scoville, N., Aussel, H., Brusa, M., et al. 2007, ApJS, 172, 1

Semelin, B. & Combes, F. 2005, A&A, 441, 55

Sérsic, J. L. 1963, Boletin de la Asociacion Argentina de Astronomia La Plata Argentina, 6, 41

Shen, S., Mo, H. J., White, S. D. M., et al. 2003, MNRAS, 343, 978

Silk, J. & Rees, M. J. 1998, A&A, 331, L1

Simard, L. 1998, in Astronomical Society of the Pacific Conference Series, Vol. 145, Astronomical Data Analysis Software and Systems VII, ed. R. Albrecht, R. N. Hook, & H. A. Bushouse, 108

Simard, L., Mendel, J. T., Patton, D. R., Ellison, S. L., & McConnachie, A. W. 2011, ApJS, 196, 11

Simon, J. D. 2019, An. Rev. Ast. Astroph., 57, 375

Smith, D., Haberzettl, L., Porter, L. E., et al. 2022, MNRAS, 517, 4575

Sousbie, T. 2011, MNRAS, 414, 350

Springel, V., Di Matteo, T., & Hernquist, L. 2005a, ApJLett, 620, L79

—. 2005b, MNRAS, 361, 776

Springel, V. & Hernquist, L. 2005, ApJLett, 622, L9

Springel, V., Pakmor, R., Pillepich, A., et al. 2018, MNRAS, 475, 676

Springel, V., White, S. D. M., Jenkins, A., et al. 2005c, Nature, 435, 629

Steinmetz, M. & Navarro, J. F. 2002, New Astronomy, 7, 155

Strateva, I., Ivezić, Ž., Knapp, G. R., et al. 2001, AJ, 122, 1861

Tacchella, S., Diemer, B., Hernquist, L., et al. 2019, MNRAS, 487, 5416

Teyssier, R., Chapon, D., & Bournaud, F. 2010, ApJLett, 720, L149

Tinsley, B. M. 1972, ApJ, 178, 319

Torrey, P., Vogelsberger, M., Marinacci, F., et al. 2019, MNRAS, 484, 5587

Trayford, J. W., Theuns, T., Bower, R. G., et al. 2015, MNRAS, 452, 2879

Tremonti, C. A., Heckman, T. M., Kauffmann, G., et al. 2004, ApJ, 613, 898

Trujillo, I., Rudnick, G., Rix, H.-W., et al. 2004, ApJ, 604, 521

Tuccillo, D., Huertas-Company, M., Decencière, E., et al. 2018, MNRAS, 475, 894

Tully, R. B. & Fisher, J. R. 1977, A&A, 54, 661

van den Bergh, S., Abraham, R. G., Ellis, R. S., et al. 1996, AJ, 112, 359

Vega-Ferrero, J., Domínguez Sánchez, H., Bernardi, M., et al. 2021, MNRAS, 506, 1927

Vogelsberger, M., Genel, S., Springel, V., et al. 2014, Nature, 509, 177

Vogelsberger, M., Marinacci, F., Torrey, P., & Puchwein, E. 2020, Nature Reviews Physics, 2, 42

Weinmann, S. M., van den Bosch, F. C., Yang, X., & Mo, H. J. 2006, MNRAS, 366, 2

Whitney, A., Ferreira, L., Conselice, C. J., & Duncan, K. 2021, ApJ, 919, 139

Williams, J. P., Blitz, L., & McKee, C. F. 2000, in Protostars and Planets IV, ed. V. Mannings, A. P. Boss, & S. S. Russell, 97

Wyder, T. K., Martin, D. C., Schiminovich, D., et al. 2007, ApJS, 173, 293

Yang, L., Leethochawalit, N., Treu, T., et al. 2022a, MNRAS, 514, 1148

Yang, L., Morishita, T., Leethochawalit, N., et al. 2022b, ApJLett, 938, L17

Yoachim, P. & Dalcanton, J. J. 2006, AJ, 131, 226

York, D. G., Adelman, J., Anderson, John E., J., et al. 2000, AJ, 120, 1579

Zeldovich, I. B., Einasto, J., & Shandarin, S. F. 1982, Nature, 300, 407

Zwicky, F. 1937, ApJ, 86, 217